Modeling of grain structure and hot cracking for arc welding processes

Chengdan Xue

PSL UNIVERSITÉ PARIS

THÈSE DE DOCTORAT
DE L'UNIVERSITÉ PSL

Préparée à MINES ParisTech

Modeling of Grain Structure and Hot Cracking for Arc Welding Processes

Modélisation de la structure de grains et de la fissuration à chaud dans les procédés de soudage à l'arc

Soutenue par

Chengdan XUE

Le 15 Mars 2022

Ecole doctorale n° 364

SCIENCES FONDAMENTALES ET APPLIQUÉES

Spécialité

MECANIQUE NUMERIQUE ET MATERIAUX

Composition du jury :

Aude SIMAR Professeur, Université Catholique de Louvain	*Présidente*
Dominique DALOZ Professeur, Université de Lorraine	*Rapporteur*
Iryna TOMASHCHUK Maitre de conférences, Université Bourgogne Franche-Comté	*Rapportrice*
Cyril BORDREUIL Professeur, Université de Montpellier	*Examinateur*
Pierre-Emile LHUILLIER Ingénieur-Chercheur EDF R&D	*Examinateur*
Charles-André GANDIN Directeur de recherche, Mines ParisTech	*Directeur de thèse*
Michel BELLET Professeur, Mines ParisTech	*Co-Directeur de thèse*
Gildas GUILLEMOT Maître assistant, Mines ParisTech	*Examinateur*

MINES ParisTech | PSL

Acknowledgment

The three-year PhD experience is unforgettable in my life.

Firstly, I would like to express my sincere gratitude to my PhD supervisors, Charles-André GANDIN, Michel BELLET and Gildas GUILLEMOT. Without their guidance and helps, I couldn't achieve my PhD work. Besides, I would also like to thank Yancheng ZHANG, who helps me a lot in the solid mechanical.

Special thanks to the jury for evaluating my work. The final version of manuscript is improved thanks to their friendly and professional comments and propositions. Besides, it is truly a great honor to have all the jury members present in the thesis defense during the complicated period of Covid.

Special thanks also to the administration staff in CEMEF, Marie-Françoise GUENEGAN for the helps in my recruitment and the thesis defense, and also Geneviève ANSEEUW, for her organization of my work-related travels.

I would also thank all my colleges in the group 2MS, Oriane SENNINGER, Lucas RAVIX, Emile HAZEMANN, Tiphaine HOUDARD and Théophile CAMUS. I really appreciate discussion with them which can often bring me new ideas and directions to advance my work. Special thanks to those with whom I have shared the office for my first years in CEMEF, Hanadi Ettroudi, Vincent MAGUIN and Alexis Queva who help me a lot in all directions at my arrival in the office BE109, I won't forget the shared breakfast with you, the gift exchange for Christmas day and the gift you gave me for my birthday. Special thanks also to Paul MARTIN, Chloé GRANDJEAN, Geoffroy NAVARRE-LASNIER and Anas RASSANE with whom I shared the office during the writing of my manuscript the preparation of my defense. This was a time truly difficult for me but thanks to you, I achieved at last. Especially for Paul, your Chinese words is very good and very encouraging.

I would also express my thanks to all my Chinese friends here in CEMEF, Shaojie ZHANG, Feng GAO, Fangxin ZOU, Han WANG, Junfeng CHEN, Fuqiang ZHUANG, Yijian WU, Tianqi HUANG, Shengfei WANG, Hongxin GE, Zhongfeng XU and etc. It is really a pleasure to meet you and make friends with you. I won't forget the discussions, barbecues, badminton games, LOL games and etc. which give me the energy to continue in my research.

Special thanks to my best friends, or more precisely, my brothers, Fan XU, Xizhe LI, Xiao HU and Xiao GU. I think the word "brother" is quite appropriate to express what I want to say to you.

I would also thank the girl who encouraged me to come to France for my study, even though I missed you in the end, thank you for coming into my life.

The most important, I would express all my thanks to my whole family, especially to my father who always encourages me and cares for me from my childhood and gives me more than all he has, dad, thank you. And to my grandfather who supported me from the primary school until the master and encouraged me for doing the PhD one month before he passed away. Grandpa, I'm a doctor now and you can be proud of me!

Table of content

List of symbols

Acronyms

BM	Base Metal
BTR	Brittle Temperature Range
CAFE	Cellular Automaton Finite Element
CALB	Cellular Automaton Lattice Boltzmann
CND	Contrôle Non Destructive
CSF	Continuum Surface Force method
CST	Critical Strain Rate for Temperature Drop
FZ	Fusion Zone
GMAW	Gas Metal Arc Welding
GTAW	Gas Tungsten Arc Welding
GS	Gulliver-Scheil Transformation Path
HAZ	Heat Affected Zone
HCS	Hot Cracking Sensitivity
JWRI	Joining Welding Research Institute Test
KGT	Kurz-Giovanola-Trivedi model
LR	Lever Rule Transformation Path
LS	Level-Set method
MIG	Metal Inert Gas
MISO	Means of In-Situ Observation and Measurement
NDT	Non-destructive Control
NS	Navies-Stokes
PE	Partial Equilibrium Model
RDG	Rappaz, Drezet and Gremaud Criterion
TIG	Tungsten Inert Gas
UT	Ultrasonic Testing
VMS	Variational MultiScale
WYSO	Young Mok Won, Tae-Jung Yeo, Dong Jin Seol, And Kyu Hwan Oh Criterion

Roman alphabets

a_g	Gravitational acceleration	m s^{-2}
C	Kinematic hardening parameter	Pa
C_v	Cells center	-
C_p	Volumetric heat capacity	J K^{-1} m^{-3}
D	Geometry dimension of the mesh	-
D^l	Solute diffusion coefficient in liquid	m^2 s^{-1}
D_i^l	Solute diffusion coefficient in liquid of solute element j	m^2 s^{-1}
D_{min}	Minimum ductility	-
$d(x)$	Geometric distance to $\varphi = 0$	m

d_{NA}	Number of non-aligned edge vectors related to node *i*	-
E		
E_{CL}	Crystal lattice energy for Monte Carlo model	J
E_{LB}	Energy density in Lattice Boltzmann model	J m^{-3}
$\dot{E}(x)$	Cumulative average deformation rate	s^{-1}
E^{CA}	CA element	-
E^{FE}	FE element	-
e	Thickness of metal sheet	m
$\boldsymbol{e_k}$	Velocity vectors in Lattice Boltzmann model	m s^{-1}
F	Plasticity criterion	Pa
F^{WYSO}	WYSO hot cracking criterion	-
F_{HC}	Hot cracking criterion function	-
f	Scalar field	-
f^l	Mass fraction of liquid phase	-
f^s	Mass fraction of solid phase	-
f_d	Frequency of detachment of the droplets	s^{-1}
f_i	Value of scalar field f at node *i*	-
f_k	Lattice Boltzmann distribution function	-
f_z	Thickness attenuation factor	-
$\boldsymbol{f_V}$	Volumetric force	N m^{-3}
h	Specific enthalpy	J kg^{-3}
h_c	Heat transfer coefficient	W m^{-2} K^{-1}
h_K	Characteristic length of element in the direction of fluid flow	m
h_k	Energy density distribution function in Lattice Boltzmann model	J m^{-3}
h_{min}	Minimum element size	m
I	Current	A
Iv	Ivantsov function	-
g^l	Volume fraction of liquid phase	-
g^s	Volume fraction of solid phase	-
$g_{v,CA}^{en}$	Envelop fraction of CA cell	-
g^{ϕ}	Volume fraction of ϕ phase	-
$G_C^{l\,s/l}$	Solid-liquid interface solute gradient in the liquid	wt% m^{-1}
$G_i^{l\,s/l}$	Solid-liquid interface gradient of solute element j in the liquid	wt% m^{-1}
G	Temperature gradient	K m^{-1}
$\boldsymbol{G^G}$	Barycenter of grain G	-
K_p	Permeability	m^2
K	Consistence coefficient	Pa
K_c	Twice of the mean interface curvature	m^{-1}
k	Partition coefficient	-
k_e	Efficiency coefficient	-
k_j	Partition coefficient solute element j	-
k_B	Boltzmann constant	J K^{-1}
L	Volumetric latent heat	J m^{-3}

L_a	Length of the arc plasma	m
L_c	Height of the cavity	m
l_{CA}	Cell length of cellular automaton	m
M	Mobility	-
m^l	Liquidus slope	K wt%$^{-1}$
m_j^l	Liquidus slope of solute element j	K wt%$^{-1}$
m^M	Mass of the metal part during the simulation	kg
m^{theo}	Theoretic mass of the metal part during the simulation	kg
$\boldsymbol{\mathcal{M}}_i$	Metric tensor	m^{-2}
$\boldsymbol{\mathcal{M}}_C^G$	Covariance matrix of grain G	-
n	Hardening coefficient	-
NbE	Elements number in the mesh	-
NbN	Nodes number in the mesh	-
N_c^G	Total number of cells inside the grain G	-
p	Pressure	Pa
P_{Plasma}	Pffective power of the plasma arc	W
P_{Cr2Go}	Passage matrix from the crystal frame of reference to the global frame of reference	-
P_C	Critical pressure for hot cracking	Pa
P_{Tip}	Pressure of dendrite tip	Pa
P_{Root}	Pressure of dendrite root	Pa
p	Pressure	Pa
$\dot{Q}$	Volumetric heat source	W m^{-3}
$\dot{Q}_D$	Volumetric heat source of molten droplet	W m^{-3}
$\dot{Q}_{input}$	Volumetric input heat source	W m^{-3}
$\dot{Q}_P$	Surface input heat source of arc plasma	W m^{-2}
r_s	Radius of welding arc	m
R_c	Radius of the cavity	m
R_d	Radius of the droplet	m
R_w	Radius of the wire fire	m
$R_{\nu_1}^{en_0}$	Initial radius of envelop associated to cell ν_1	m
$R_{\nu_1}^{en}$	Radius of envelop associated to cell ν_1	m
$\mathcal{R}$	Rotation matrix	-
s	Truncation factor	m
$\bar{\bar{s}}$	Deviatoric stress tensor	Pa
S_ν^{en}	Apex of envelop associated to cell ν	-
T_c	Coherent temperature	K
T_d	Temperature of droplets	K
T_f	Fusion temperature	K
T_{liq}	Liquidus temperature	K
T_{sol}	Solidus temperature	K
T_s	Simulation temperature	K
$T^{l\,\infty}$	Far-field solute temperature	K

$T^{s/l}$	Solid-liquid interface temperature	K
T_t^i	Physical temperature for Monte Carlo model	K
$T_{\nu^{CA}}$	Temperature of cell ν in CA	K
$T_{n^{FE}}$	Temperature of FE node	K
$T_{n^{CA}}$	Temperature of CA node	K
t_v	Time spent in the BTR interval	s
t_r	Normalization time during which the deformations in the mushy zone can be fed by the liquid	s
U	Tension	V
V_c	Cavity volume of adding material	m^{-3}
V_T	Isothermal planes speed	$m\ s^{-1}$
V_ν^{en}	Current volume of the envelope associated to cell ν	m^3
$V_\nu^{en_0}$	Initial volume of the envelope associated to cell ν	m^3
$V_\nu^{en_{max}}$	Maximum volume of the envelope associated to cell ν	m^3
v_{tip}	Dendrite tip growing velocity	$m\ s^{-1}$
$\boldsymbol{v}$	Velocity	$m\ s^{-1}$
$\boldsymbol{v(n)}$	Normal component of the velocity	$m\ s^{-1}$
$\boldsymbol{v^l}$	Fluid flow velocity	$m\ s^{-1}$
$\boldsymbol{v^s}$	Solid deformation velocity	$m\ s^{-1}$
$v_{0,d}$	Initial droplet velocity	$m\ s^{-1}$
v_d	Velocity of the droplets falling into the melt pool	$m\ s^{-1}$
v_w	Velocity of the adding filler wire	$m\ s^{-1}$
$v_{\nu\ max}^{en}$	Maximum dendritic growth velocity	$m\ s^{-1}$
$v^{\langle 100 \rangle}$	Growth velocity of dendrite tip	$m\ s^{-1}$
w	Mass composition	wt%
w_B^0	Nominal solute mass composition of	wt%
w_B^l	Mass composition of element B in the liquid	wt%
w_B^s	Mass composition of element B in the solid	wt%
$w^{l\ s/l}$	Solid-liquid interface solute equilibrium mass composition in liquid	wt%
$w_j^{l\ s/l}$	Solid-liquid interface solute equilibrium mass composition in liquid of solute element j	wt%
$w^{s\ s/l}$	Solid-liquid interface solute equilibrium mass composition in solid	wt%
$w^{l\ \infty}$	Far-field solute mass composition	wt%
$w_j^{l\ \infty}$	Far-field solute mass composition of solute element j	wt%
w^0	Nominal solute mass composition	wt%
$\boldsymbol{X}$	Coordinate vector of a point	-
$\bar{\bar{X}}$	Kinematic hardening stress tensor	Pa
$\boldsymbol{X}_{ij}$	Desired edge vector between the node i and j	m
x_{ij}	Edge vector between the node i and j	m

Greek alphabets

α	Thermal diffusivity	$m^2\ s^{-1}$
$\bar{\bar{\alpha}}$	Kinetic hardening internal variables tensor	-
α_T	Thermal expansion coefficient	K^{-1}
$\gamma(\boldsymbol{n})$	Anisotropy surface tension coefficient	$N\ m^{-1}$
γ_{ab}	Interfacial energy	$J\ m^{-2}$
γ_{SL}	Solid-liquid interface energy	$J\ m^{-2}$
γ_s	Surface tension coefficient	$N\ m^{-1}$
$\Gamma^{s/l}$	Gibbs-Thomson coefficient	$K\ m$
Γ_{corr}	Restrained part of $\Gamma^{s/l}$ for mass correction	-
$\Gamma^{L/G}$	Liquid/gas interface	-
$\Gamma^{M/G}$	Metal/gas interface	-
$\Gamma(i)$	Set of nodes connected to node i	-
ΔS_f	Volumetric fusion entropy	$J\ m^{-3}\ K^{-1}$
ΔT	Undercooling	K
ΔT_{BTR}	Brittle temperature range	K
ΔT_b	Critical undercooling of the coalescence	K
ΔT_C	Solute undercooling	K
ΔT_K	Kinetic undercooling	K
ΔT_R	Curvature undercooling	K
ΔT_T	Thermal undercooling	K
Δt	Time step	s
δ	Dirac function associated to φ	m^{-1}
δ_D	Thickness of the diffusive solid-liquid interface	m
δ_{LS}	Correction distance applied	m
δm	Mass error of the metal part during simulation	kg
$\delta_{S_i S_i}$	Kronecker delta function	-
δt	Microscopic time step	s
ρ	Density	$kg\ m^{-3}$
ρ_w	Density of the wire file	$kg\ m^{-3}$
$\bar{\bar{\sigma}}$	Stress tenson	Pa
σ_0	Yield stress	Pa
σ_r	Stefan-Boltzmann constant	$kg\ s^{-3}\ K^{-4}$
ε	Half thickness of transition zone	m
$\dot{\bar{\varepsilon}}$	Generalized viscoplastic strain rate	-
$\dot{\bar{\bar{\varepsilon}}}$	Stain rate tensor	s^{-1}
$\dot{\bar{\bar{\varepsilon}}}^{th}$	Thermal stain rate tensor	s^{-1}
$\dot{\bar{\bar{\varepsilon}}}^{el}$	Elastic stain rate tensor	s^{-1}
$\dot{\bar{\bar{\varepsilon}}}^{vp}$	Viscoplastic stain rate tensor	s^{-1}
ε_{BTR}	Cumulative strain in the BTR	-
ε_c	Critical strain	-
ε_r	Emissivity	-
$\dot{\varepsilon}$	Strain rate	s^{-1}
$\dot{\varepsilon}_c$	Critical strain rate	s^{-1}

η	Heat source efficiency	-
η_{LD}	Low ductility zone thickness	m
$\dot{\theta}$	Expansion rate in the cavity	s^{-1}
κ_c	Interface curvature	m^{-1}
κ	Thermal conductivity	$W\ m^{-1}\ K^{-1}$
κ_t	Total curvature	m^{-1}
λ_{min}	Minimum wavelength destabilizing the planar solid-liquid interface	m
λ_2	Secondary dendrite arm spacing	m
μ	Dynamic viscosity	Pa s
μ_0	Kinetic undercooling coefficient	$m\ K^{-1}\ s^{-1}$
$\mu(\boldsymbol{n})$	Anisotropy kinetic mobility	$m\ K^{-1}\ s^{-1}$
ν	Kinematic viscosity	$m^2\ s^{-1}$
$\hat{\xi}$	Mixed value of property ξ over metal and gas subdomains	-
$\langle\xi\rangle$	Average volumetric property of ξ in a subdomain	-
$\langle\xi\rangle^{\phi}$	Volumetric property of ξ for ϕ phase	-
υ	Poisson coefficient	-
ϕ	Phase field variable	-
$\phi_{n^{FE}}(n^{CA})$	Interpolation function of FE node n^{FE} estimated for CA node n^{CA}	-
$\phi_{n^{CA}}(\nu)$	Interpolation function of CA node n^{CA} estimated for CA cell ν	-
φ	Level set function	m
Ω	Global simulation domain	-
Ω^{CA}	CA diomain	-
Ω^{G}	Gas subdomain of the simulation	-
Ω^{M}	Metal subdomain of the simulation	-
Ω^{S}	Supersaturation	-
Ω_i^{S}	Supersaturation of solute element *j*	-

Others

$\mathcal{H}$	Heaviside function
Pe_C	Peclet number
$Pe_{C,j}$	Peclet number of solute element *j*

Indices

I_ν	Cell indicator in cellular automaton method
$x_{\nu^{CA}}$	Value in CA cell

Exponents

x^{FE}	Value in FE model
x^{CA}	Value in CA model
x^{en}	Value of the envelope of the CA cells

Operators

$\cdot$	Inner product
$\langle x \rangle$	Average value in the representative volume element
x^T	Transposition
$\nabla \cdot$	Divergence
∇	Gradient
∇_s	Surface gradient operator
Δ_s	Surface Laplace operator

Study context

Welding is a process to joint permanently two parts through localized assembly of materials resulting from an appropriate combination of temperature, pressure, and metallurgical conditions [Kha07]. Nowadays, welding is an essential process for various industrial sectors, for example, aeronautic, aerospace, marine, automobile, petroleum etc. For example, in the transportation industry, welding is widely used to manufacture various vehicle body parts. In 2019, the transportation end-use industry constituted 34.42% of the total welding materials market. According to OICA (Organisation Internationale des Constructeurs d'Automobiles), the global production of passenger cars amounted to 67.14 million [Market].
Welding technology can determine the performance of these industries (for example automobile) mentioned above. For example, in 2018, Fiat and Ford had to recall over 30000 vehicles because of a faulty weld in the frame [Web1, Web2]. Furthermore, the welding materials market is projected to grow from USD 13.6 billion in 2020 to USD 17.3 billion by 2025[Market]. Hence, the study of welding process is of great importance for improving the final performance of welded parts in these industries.
According to Khan [Kha07], regarding the magnitude of temperature and pressure endured by materials, welding process can be classified in several categories, such as gas welding, arc welding, resistance welding, solid state welding, etc. In order to achieve the joint of the two parts, either plastic deformation (in solid-state-welding) or melting (in fusion welding) of their two surfaces can be implemented. The present research activity is focused on the fusion welding process applied to metallic materials in which the melting and specially the solidification stage are of great importance in the final properties of the jointed part. In the fusion welding processes, the workpieces are firstly melted by the heat source, with or without an adding filler metal. Thereafter, a pool of molten material, named *melt pool*, is formed. The molten material then begins to solidify to form a strong joint called *weld bead*. Finally, the two workpieces are joined by the weld.

1. Arc welding process

Arc welding is the most common version of welding, whereby the heat source is provided by a high-current electric arc between the supplied electrode material and the base metal [Rit03]. The Gas Tungsten Arc Welding (GTAW) and Gas Metal Arc Welding (GMAW) are of the common techniques among the Arc Welding. The present work is focused on these welding processes, especially the GTAW process.

GTAW

GTAW is sometimes referred to as tungsten inert gas (TIG) welding (Figure 1). In this process, assembly of metals is produced by heating with an arc between the base metal and a nonconsumable tungsten electrode. The tungsten electrode serves only to maintain the arc. Shielding from the atmosphere is obtained from a gas or gas mixture, usually helium, argon, or a combination of the two. A filler material may or may not be used depending on the joint

configuration. When a filler material is used, it is fed into the weld site from a separate rod or wire instead of feeding it through the electrode (different from the GMAW process). The filler material is melted by the arc and is added to the melt pool.

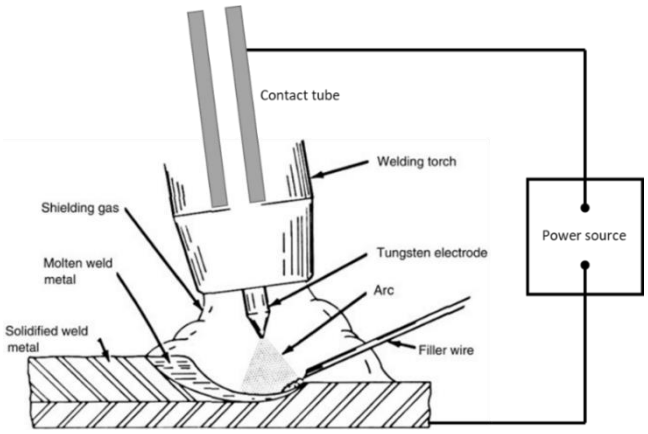

Figure 1. Schematic illustration of welding area in GTAW [Has14].

GTAW is best suited to weld thin sections of stainless steel and light metals, such as aluminum, magnesium, and copper alloys [Smi13]. The advantages of GTAW include inherently low-heat input which offers better control of weld filler dilution by the substrate and makes it suitable for welding thin sheets. The excellent shielding offered by argon, helium or their mixtures ensures the cleanliness of the process. However, its greatest limitation is its low deposition rate (0.5–1 kg h^{-1}) [Lum11] which leads to longer operation times than the GMAW process.
In order to improve the productivity of GTAW process especially the deposition rate, the hot-wire GTAW process is introduced Wroth and Manz in 1960s [Wro64, Man69]. The deposition rates possible are shown in Figure 2.

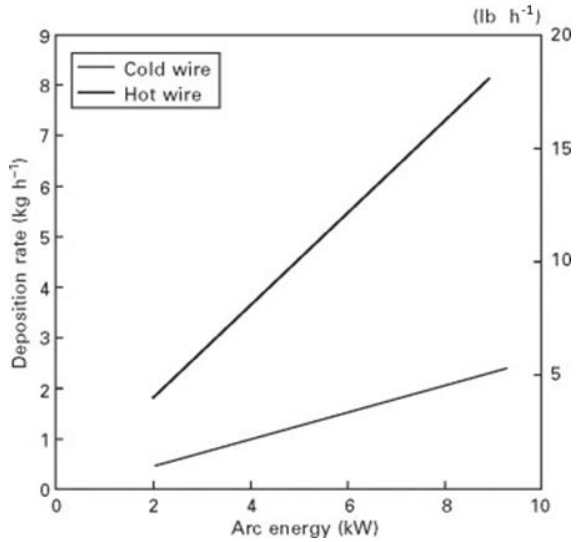

Figure 2. Deposition rate in GTAW, hot wire and cold wire [Nor06].

Although the equipment is more complex than GMAW it has been shown that deposition rates of 6-8 kg h^{-1} are possible (compared to 7-10 kg h^{-1} in GMAW) and high joint integrity may be expected [Nor06].

GMAW

In GMAW process, the heat is generated by an electric arc incorporating a continuous-feed consumable electrode that is shielded by an externally supplied gas, usually containing one of a mixture of the following gas: helium, argon, or carbon dioxide [Ozc03]. Compared to GTAW, the electrode wire which is the positive anode in GMAW is continuously fed into the arc and deposited as weld metal. It is also referred to as the Metal Inert Gas (MIG) process [Lin13]. A simple schematic diagram of the GMAW process is shown in Figure 3.

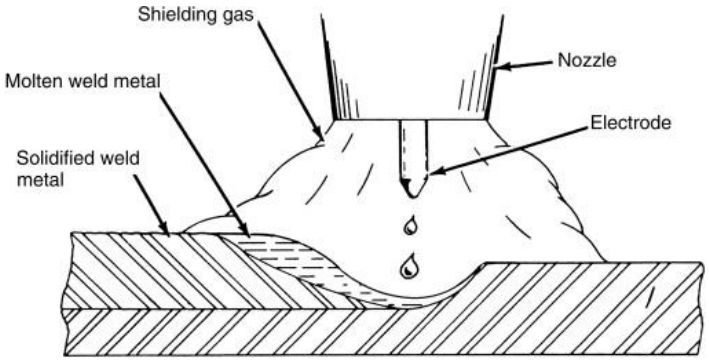

Figure 3. Schematic illustration of welding area in GMAW [Has14].

GMAW can be used to join a wide range of materials such as carbon steel, stainless steel, aluminum, magnesium, copper, bronze, titanium alloys and nickel alloys [Has14]. Compared to GTAW, GMAW is allowed to weld thicker workpieces at higher speeds due to the much higher deposition rate despite the difficulty to control the GMAW guns in small areas or corners [Lin13]. Nowadays, a preheating process involving heating the base metal in the region surrounding the joint prior to welding can be also applied during GMAW process to reduce the residual shrinkage stresses and increase the resistance to cracking in the weld area.

2. Defects during arc welding

During arc welding process, several types of defects could be observed which degrade the welding quality, such as decreasing the material properties, risk of premature break of welded part, failure during service and reduction of service life.

Undercut

The undercut is generally defined as groove or depression located at the toe of weld bead. The sharp weld bead profile may cause stress concentration or even crack, which severely deteriorates weld properties. Undercut is usually caused by inappropriate welding parameters, such as high welding speed, high welding current, large diameter electrode and incorrect

welding angle which will deliver more heat to the free edges. Figure 4 (a) presents the undercut after solidification of GTAW for welding current 250 A and welding speed 27.5 mm s^{-1} on the ASTM (American Society for Testing and Materials) 409L ferritic stainless steel sheet.

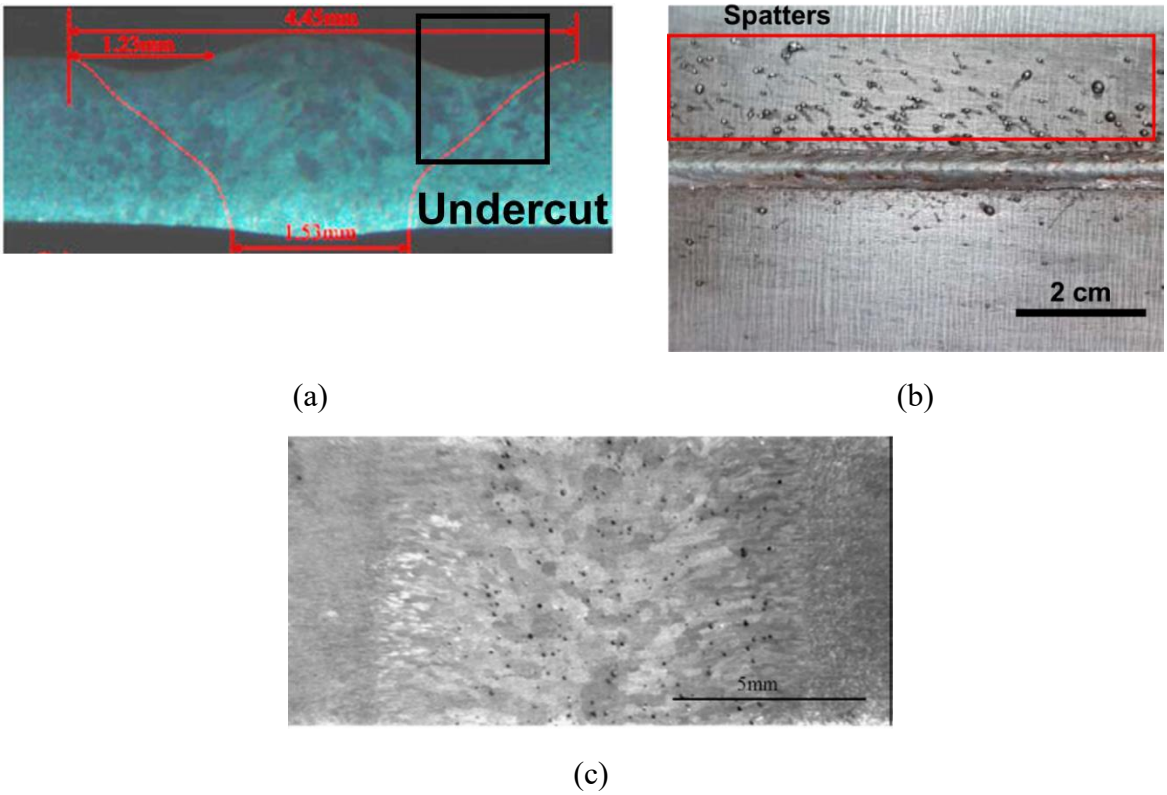

(a) (b)

(c)

Figure 4. Defects observed during welding process including (a) cross-section of solidified weld bead with undercut [Men16], (b) weld with spatters in GMAW [Kan20] and (c) observation of top surface after solidification showing microporosities as black spots [Liu12].

Slag inclusions

Slag inclusions are particles other than weld metal trapped in the weld or at its interface. Slag inclusions result from faulty welding technique, improper access to the joint, or both. With proper technique, slag inclusions rise to the surface of the molten weld metal. In GTAW process, inclusion corresponding to tungsten particles trapped in weld metal could be observed. Dipping the tungsten electrode in the molten weld metal or using too high current that melts the tungsten can cause inclusions [Sin20]. The most common cause of slag inclusions is failure to completely remove the slag from one weld pass before making another in multiple passes welding [Wem11].

Spatter

Spatter is defined as droplets of molten material that are formed near the welding arc during the welding process and ejected from the weld puddle. The ejection of molten material has numerous causes, for example, high welding current or inappropriate welding angle. In GMAW

process, the shielding gas CO_2 forms bubbles that explode during the welding process and can also be the cause of excess spatter [Sha20]. Figure 4 (b) presents the spatters observed in a GMAW process with a welding current 300 A with size of the order of 1 millimeter.

Microporosity

Microporosity corresponds to the presence of cavities in the weld metal because of solidification shrinkage or condensation of dissolved gas. It has a strong negative effect on mechanical properties, especially on ductility and fatigue life, because internal pores act as local stress concentrators and crack initiation sites. There are two main causes of microporosity in solidification: shrinkage porosity, due to the volume change upon solidification combined with restricted feeding of liquid to the final solidification stage; and gas porosity, due to the condensation of dissolved gases in the melt upon freezing, because of the difference in solubility of such gases in the liquid and solid phases [Dan09]. During welding process, gas porosity is more frequently observed because of the shielding gas and the vaporization of several metal elements at the base metal. For example, the zinc in zinc coated steels is more likely to vaporize and form the microporosity because of the weak boiling temperature (906 °C) compared with the fusion temperature of steels (usually above 1300°C) [Ahs16]. Figure 4 (c) presents the microporosity observed in GMAW process on aluminum alloy.

Hot cracking

Hot cracking (Figure 5) occurs during the last stages of solidification when the solid fraction is in the range of 90% to 99% and the alloy is in the mushy state, with a strong connection of the solid network. This region is critical because the solidification develops simultaneously with a high temperature gradient and a significant stress favoring the rupture of weak intergranular domains [Adi18, Dan09]. The cracks developed in the welded parts then reduce the mechanical properties and decrease the service life of the workpiece.

Figure 5 shows the hot cracking of a nickel base alloy for different welding powers (controlled by the welding current) of a GTAW process. Experimentally, no crack is observed when the welding current is lower than 159 A. This value can be determined as the minimum current intensity related to the occurrence of cracking. As the current of welding increases, hot cracking appears and the length of cracks is proportional to the intensity of the welding current, yet not discussed hereafter.

The hot cracking phenomenon will be precisely presented and analyzed thereafter in section 1.3 and chapter 5. It should also be pointed out that other defects are also observed in welding processes as dilution phenomena, underfill, incomplete fusion and incomplete penetration, get not discussed in this document.

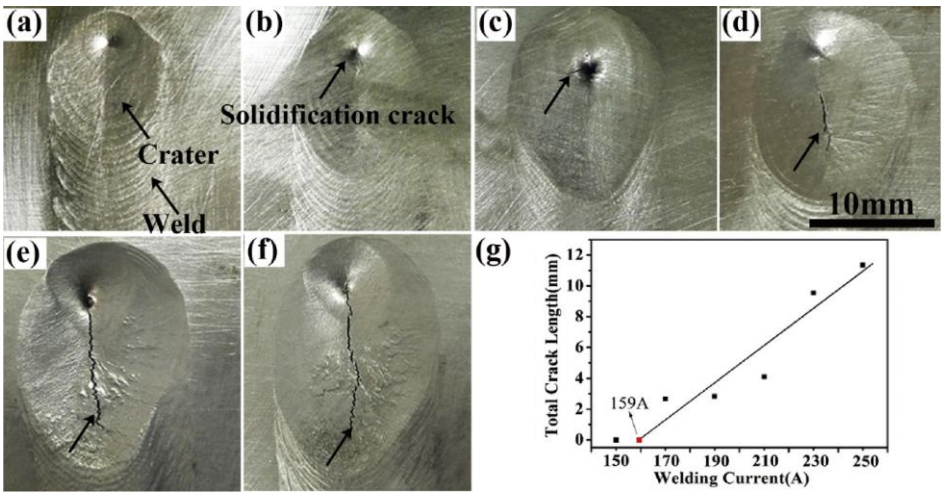

Figure 5. Hot cracking (a-f) during GTAW process of Ni-28W-6Cr alloy with (g) different working currents [Che19].

3. Non-Destructive Test (NDT)

Welded parts can have internal defects such as those mentioned above. NDT are therefore necessary to detect and characterize these defects and control the welding quality. Table 1 presents several NDT methods used to detect welding defects with their capabilities and limitations.

Table 1. Comparison of NDT methods [Dee21].

NDT method	Capabilities	Limitations
Visual inspection	More visible surface defects	Lack of reliability, difficult to detect small defect
Ultrasonic testing	Surface and internal defects	Testing material should be sound conductive
Magnetic particle test	Surface and layer defects	Suitable only for magnetic material
Radiography	Internal defects	Limited to detect thick cracks
Liquid penetration	Surface defects	Not suitable for porous material

As shown, for a welded metal part, the ultrasonic test is capable to detect at the same time the internal and surface defects which increase the inspect efficiency. This is also the reason why ultrasonic testing (UT) is often used in the industry to detect, localize and estimate welding defects. UT is based on the transmission, reflection and absorption of an ultrasonic wave propagating in the workpiece. The discontinuity in the workpiece is detected by the reflection of transmitted sounds waves, as shown in Figure 6.

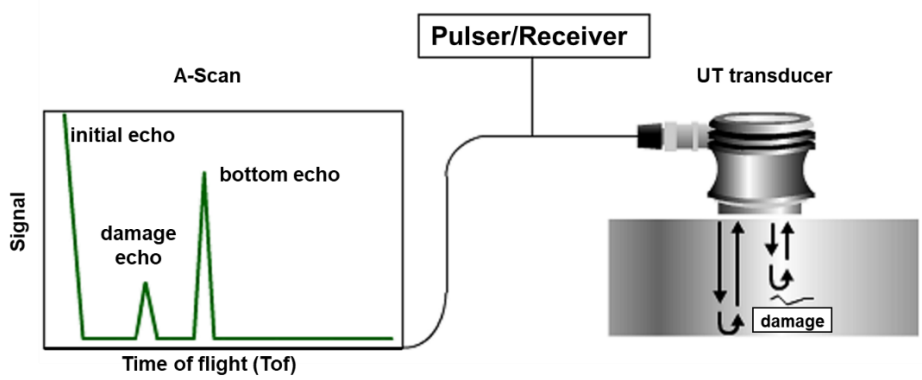

Figure 6. Principle of ultrasonic testing [Wro16].

During the inspection, the Pulser/Receiver produce high voltage electrical pulses driving the transducer to generate high frequency ultrasonic waves (usually between $0.5 - 20$ MHz [Man88]). The sound energy is then introduced and propagates through the materials by the ultrasonic waves. When a discontinuity (for example a damage) is presented inside the material, part of the ultrasonic waves will be reflected from the flaw surface ('damage echo'). This reflected wave signal is then transformed into an electrical signal by the transducer and then displayed (on the left of Figure 6). As the velocity of the waves is known and the travel time can be determined directly, the damage can be localized [Wro16]. UT is very precise in determining the position of the defect and in estimating its size and shape, usually at the magnitude of micrometers [Olympus]. It is also sensitive to surface and subsurface discontinuities. On the one hand, UT can provide instant results and the equipment can be portable and automated easily. On the other hand, certain microstructures, such as those with coarse grains, can induce significant disturbances of the waves and reduce the reliability of the control [Lhu13].

Since years of 2010, EDF R&D and the CEA have been developing software tools and NDT (especially ultrasonic testing) analyzes to increase the reliability and quality of control in welding by modeling the scattering phenomena and consider the attenuation and noise associated with microstructure.

For example, ATHENA developed by EDF R&D is a finite element code that simulates waves propagation in all kinds of elastic media including heterogeneous and anisotropic structures. By applying the fictitious domain method, the interaction between the beam and a defect can be simulated. As the mesh of the defect is independent of the structured mesh of the calculation zone, the arbitrary modeling of shape and orientation of defect can be also achieved [Cha09]. Besides, CIVA developed by CEA-LIST is another modeling software of ultrasonic propagation in materials used worldwide. CIVA is based on a semi-analytical model which can use input data provided by finite element or finite difference methods [Civ16].

These numerical studies must be based on precise input data for the microstructural description of the welded material. The precision of the simulation results thus strongly depends on the model used [Lhu13].

Figure 7 presents the ultrasonic wave intensity simulated by ATHENA. In the homogeneous structure (Figure 7 (a)), neither reflection nor attenuation phenomenon exists. The ultrasonic wave can go through the workpiece with an elevated intensity (Figure 7 (c)). To compare, the grain structure presented in Figure 7 (b) introduces the reflection and attenuation of the ultrasonic wave, therefore, the ultrasonic wave intensity is much lower at the bottom surface of the workpiece and could not go through it (Figure 7 (d)).

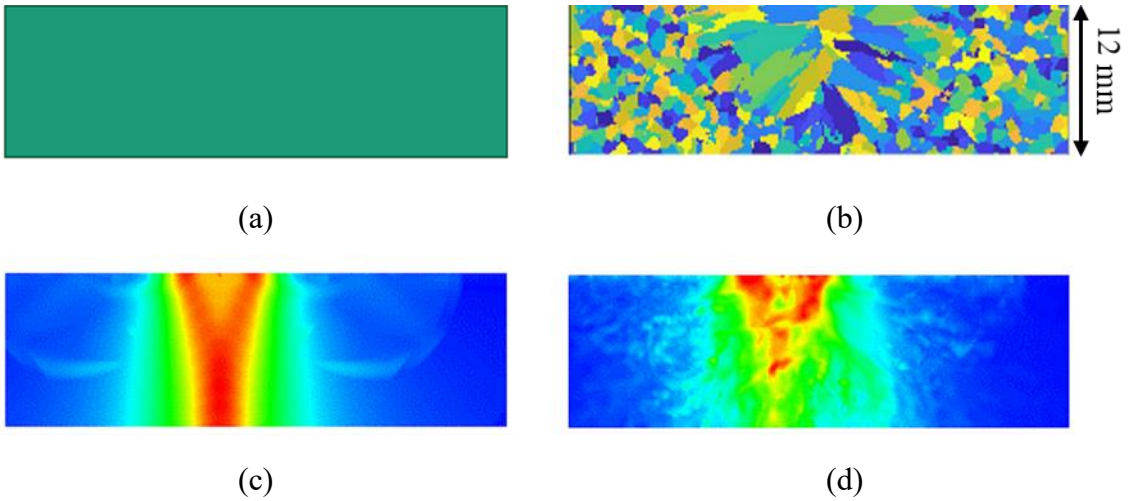

Figure 7. Structure (a) homogeneous and (b) inhomogeneous as a result of welding simulation and (c, d) associated ultrasonic wave intensity simulated using ATHENA software.

4. NEMESIS project

Under the context presented above, the project of "Agence Nationale de la Recherche" (ANR) NEMESIS*: Numerical metallurgy supporting arc welding processes: Virtual materials for mastering defects* is established. The present PhD activity is part of the ANR project NEMESIS. The objectives of the NEMESIS project are presented below:

Scientific:

1. Understand the development of microstructure and associated defects (notably hot cracking) during arc welding processes on industrial steels.
2. Modeling the development of grain structures and predict the occurrence of hot cracking by a CAFE multi-scale model (presented in chapter 2).
3. Provide partners with realistic grain structures for the study of ultrasonic wave/structure interaction for the improvement of NDT defect control.

Technical and technological:

1. Achieve relevant analysis to track rapid solidification and surface strain measurement on dedicated equipments.
2. Validate simulated grain structure by comparison with experimental results (e.g., Metallographic and EBSD analyses)

3. Provide a generalized numerical software enable to determine the limit welding conditions (welding speed, power of heat source, etc.) to avoid the welding defects for the industrial steels.
4. Connect the simulated grain structure with UT simulation tools (ATHENA/EDF R&D, CIVA/CEA-LIST) to estimate the influence of simulated microstructures in the modeling of UT.

The work packages and partners in NEMESIS project are presented below:

- WP1: Project management and coordination
- WP2: hot cracking investigation and grain structure development
- WP3: Modeling of grain structure and defect (hot cracking) during arc welding
- WP4: Industrial validation of numerical development
- WP5: NDT modeling on simulated virtual material

Figure 8 presents the 7 partners and their activities in the NEMESIS project. This PhD research activity is mainly related to WP3. On the one hand, the simulated grain structure should be firstly validated by the experimental results developed in WP2, then the simulation results will be used in WP5 to enhance NDT modeling. On the other hand, the simulation of welding defect notably hot cracking should also be validated by experimental results in WP2. At the end of the project, all the simulation results could be integrated in the welding software: TRANSWELD developed in TRANSVALOR.

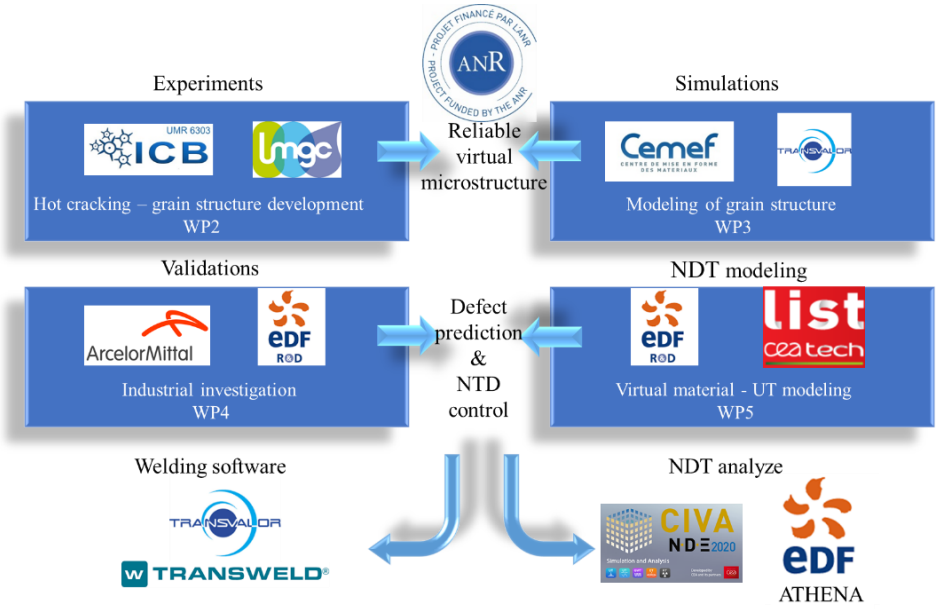

Figure 8. Presentation of the WPs activities and organization between the partners.

The context of the present manuscript is distributed in chapters as follows:

- Chapter 1, the fundamental theory related to the solidification in fusion welding process is presented, including the micro scale solidification theories required to understand the formation of the grain structure. Then the simulation methods commonly used

nowadays to model the solidified microstructure are presented. At the end of this chapter, the hot cracking phenomenon is presented with the current state of art related to this welding defect.

- Chapter 2, the Cellular Automaton Finite Element (CAFE) method for the modeling of grain structure is presented, including the fundamental theory of CAFE method and resolution of energy conservation, mass conservation and moment conservation equations.
- Chapter 3, the first validation of grain structure of single passe GTAW upon steel sheet without adding material. Comparisons for two different welding parameters (welding speed) are achieved. Fluid flow velocity and deformation of steel sheet after solidification are also included.
- Chapter 4 presents a second validation of grain structure simulation for multiple passes GTAW with a chamfer configuration and adding material. Comparison is focused on temperature field and EBSD map.
- Chapter 5, hot cracking simulations during GTAW process. A strain based hot cracking criterion is applied to compute the risk of hot cracking. The validation with experimental results is achieved by comparison with literature.

It should be noted that all the simulations presented in this work are achieved by the internal code (libraries) developed at CEMEF called *Cimlib*. The simulation is carried out on the internal cluster of computers at CEMEF containing 2016 computing cores interconnected by a very high speed and low latency network. More precisely, the configuration of each computation nodes is made of 28 cores (2×14) Bullx R424 Intel Xeon E5-2680v4 with Ram of 128 Go.

1 Introduction

1.1 Solidification in welding

1.1.1 Dendritic grain growth

Ivantsov [Iva47] first proposed a solution for the evolution of the diffusion field in front of a dendrite growing in a pure undercooled melt substance. The dendrite develops in an infinite medium (Figure 1-1) in a steady state regime with constant velocity v_{tip}. Heat flows are driven by the sole diffusion processes with far-field temperature, $T^{l\infty}$. The dendrite tip is assumed as a paraboloid (a parabolic shape in 2D and paraboloid of revolution in 3D). The paraboloidal dendrite tip is characterized by its curvature radius, R_{tip}.

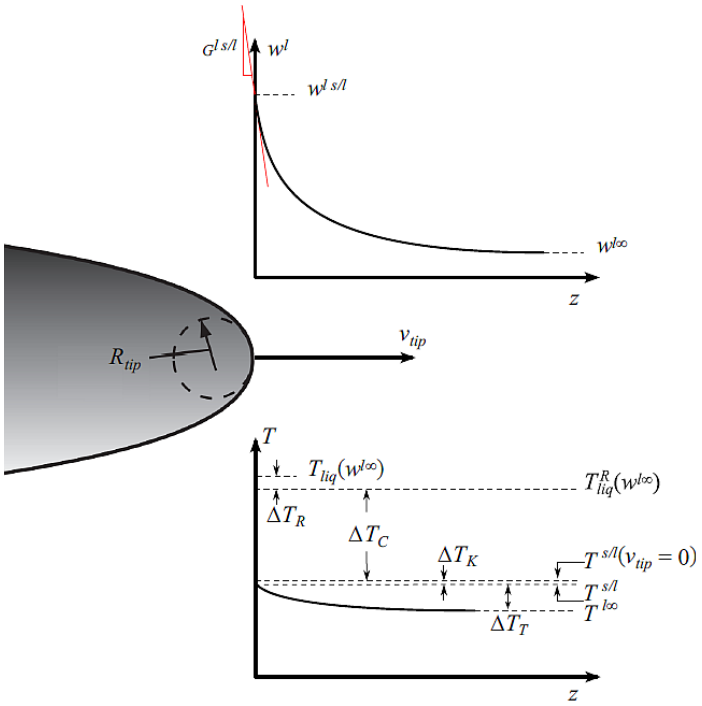

Figure 1-1. Dendrite tip growth with undercooling [Dan09].

Extension of the Ivantsov solution to the solute diffusion field links the supersaturation, Ω, at the dendrite tip by the following function.

$$\Omega = \frac{w^{l\,s/l} - w^{l\infty}}{w^{l\,s/l} - w^{s\,s/l}} = \frac{w^{l\,s/l} - w^{l\infty}}{w^{l\,s/l}(1-k)} = \mathrm{Iv}(Pe_C) \qquad (1\text{-}1)$$

where $w^{s\,s/l}$ is the solute equilibrium mass composition at the solid-liquid interface in the solid, $w^{l\infty}$ is the far-field solute mass composition in the melt, which can also be considered as the nominal solute mass composition of the melt w^0, $w^{l\,s/l}$ is the solute equilibrium mass composition at the interface in the liquid, k is the partition coefficient of the solute between the liquid and solid phases at the interface, defined by $w^{s\,s/l} = k\,w^{l\,s/l}$, Pe_C is the solute Péclet

number, $Pe_C = R_{tip} v_{tip}/2D^l$, with D^l the solute diffusion coefficient in liquid, and Iv(.) is the Ivantsov function defined by:

$$\mathrm{Iv}(x) = x \exp(x)\, \mathrm{E}_1(x) \tag{1-2}$$

where E_1 is the exponential integral function:

$$\mathrm{E}_1(x) = \int_x^{\infty} \frac{e^{-t}}{t} dt \tag{1-3}$$

1.1.1.1 Dendrite tip kinetic law in binary alloys

As shown in Figure 1-1, the total undercooling ΔT can be separated into four contributions: the thermal undercooling, ΔT_T, the solute undercooling, ΔT_C, the kinetic undercooling ΔT_K, and the curvature undercooling, ΔT_R.

$$\Delta T = \Delta T_T + \Delta T_C + \Delta T_K + \Delta T_R \tag{1-4}$$

At the dendrite tip, *i.e.* $z = 0$ in Figure 1-1, $\Delta T = T_{liq}(w^{l\infty}) - T^{s/l}$

The thermal undercooling, ΔT_T is defined as:

$$\Delta T_T = T^{s/l} - T^{l\infty} \tag{1-5}$$

where $T^{s/l}$ is the temperature of the solid-liquid interface at the dendrite tip.

The solute undercooling, ΔT_C can be estimated by:

$$\Delta T_C = T^R_{liq}(w^{l\infty}) - T^R_{liq}\left(w^{l\,s/l}\right) \simeq m^l\left(w^{l\infty} - w^{l\,s/l}\right) \tag{1-6}$$

where T^R_{liq} is the liquidus temperature of the alloy, neglecting kinetic effect but considering curvature effect, m^l is the approximation of the liquidus slope of the alloy. Generally, ΔT_C accounts for the most amount of the total undercooling for alloys.

At the solid-liquid interface, the driving force for the solute attachment of the liquid phase to the solid crystal is the deviation from the equilibrium temperature corresponding to a zero speed of the advance of the interface [Les86]. The kinetic undercooling ΔT_K is defined as:

$$\Delta T_K = T^R_{liq}\left(w^{l\,s/l}\right) - T^{s/l} = \frac{v_{tip}}{\mu_0} \tag{1-7}$$

where μ_0 denotes the kinetic undercooling coefficient. This parameter is usually of the order of 0.01 m K^{-1} s^{-1}[Les86]. During welding process, the growth velocity v_{tip} is usually small (less than 0.01 m s^{-1} in the cases studied in the present work). The magnitude of ΔT_K is less than 1 K, compared with the total undercooling which is much larger for the alloys studied in the present work. ΔT_K will thus be neglected thereafter.

The last curvature undercooling, ΔT_R can be estimated by the Gibbs-Thomson expression $\Gamma^{s/l}$. This parameter defines the difference between liquidus temperature and the interface temperature of curvature $2/R_{tip}$

$$\Delta T_R = T_{liq}(w^{l\infty}) - T_{liq}^R(w^{l\infty}) = \frac{2\Gamma^{s/l}}{R_{tip}} \quad (1\text{-}8)$$

where $\Gamma^{s/l}$ defined by the ratio of the specific solid/liquid interface energy to the melting entropy. Where the radius of the dendrite tip becomes smaller than a fraction of micrometers, the curvature effect could represent an important contribution to the total undercooling for small value of R_{tip}. Regarding the set of previous equations, also illustrated in (Figure 1-1), the total undercooling at the dendrite tip is consequently equal to:

$$\Delta T = T_{liq}(w^{l\infty}) - T^{s/l} \quad (1\text{-}9)$$

Combining equation (1-1)-(1-3) and (1-6), a relationship between the solute undercooling ΔT_C and the Péclet number Pe_C which characterize the dendrite growth can be obtained. However, the solution of these equations can not determine R_{tip} and v_{tip} separately, which means another relationship between R_{tip} and v_{tip} should be considered.

Langer [Lan78] proposed that the minimum wavelength that destabilizes the planar solid-liquid interface of a binary alloy, λ_{min}, provides a good approximation for the working point of the dendrite tip radius, where λ_{min} is deduced from the stability analysis developed by Mullins and Sekerka [Mul64]. The so-called *marginal stability criterion* writes as:

$$R_{tip} \approx \lambda_{min} \quad (1\text{-}10)$$

Kurz et al. [Kur86] proposed the following expression of λ_{min} in the KGT model:

$$\lambda_{min} = 2\pi \sqrt{\frac{\Gamma^{s/l}}{m^l G_C^{l\,s/l} - G}} \quad (1\text{-}11)$$

where $G_C^{l\,s/l}$ is the solute gradient in the liquid at the solid-liquid interface:

$$G_C^{l\,s/l} = -\frac{(1-k)w^{l\,s/l}v_{tip}}{D^l} \quad (1\text{-}12)$$

and G is the mean temperature gradient at the interface.

Finally, by combining equation (1-10)-(1-12), and neglecting the temperature gradient, G, the relationship between R_{tip} and v_{tip} is found as:

$$R_{tip}^2 v_{tip} = \frac{4\pi^2 D^l \Gamma^{s/l}}{m^l (k-1) w^{l\,s/l}} \quad (1\text{-}13)$$

For a binary alloy, R_{tip} and v_{tip} can then be calculated for a given undercooling ΔT for a binary alloy.

1.1.1.2 Dendrite tip kinetic law in multicomponent alloys

Based on the works mentioned for the binary alloy, Bobadilla [Bob88] and Rappaz [Rap99] have extended the KGT model for the growth kinetics of a multicomponent dendrite tip. To summarize, the following hypothesis are made [Hun01]:

- no thermal gradient at the grain scale;
- the thermal and kinetic undercooling are neglected;

- dendrite growth at steady state;
- independent solute fields given by the Ivantsov solution, *i.e.* neglect off-diagonal diffusion terms.

Based on the hypothesis above, and considering a multilinear phase diagram associated to each solute element $j \in [1, n]$, the total undercooling is given by:

$$\Delta T = \Delta T_C + \Delta T_R = \sum_{j=1}^{n} m_j^l \left(w_j^{l\,\infty} - w_j^{l\,s/l} \right) + \frac{2\Gamma^{s/l}}{R_{tip}} \tag{1-14}$$

with $w_j^{l\,\infty}$ and $w_j^{l\,s/l}$ the far-field mass composition of j in the liquid and the equilibrium mass composition of j at the solid-liquid interface in the liquid, respectively. For each solute element j, the corresponding supersaturation is defined as:

$$\Omega_j = \frac{w_j^{l\,s/l} - w_j^{l\,\infty}}{w_j^{l\,s/l}\left(1 - k_j\right)} = \mathrm{Iv}\left(Pe_{C,j}\right) \tag{1-15}$$

where k_j is the partition coefficient of element j and the solute Péclet number $Pe_{C,j}$ associated with element j is:

$$Pe_{C,j} = \frac{R_{tip} v_{tip}}{2D_j^l} \tag{1-16}$$

with D_j^l the diffusion coefficient of element j in the liquid.

Accordingly, the marginal stability condition becomes, neglecting the temperature gradient:

$$R_{tip} = 2\pi \sqrt{\frac{\Gamma^{s/l}}{\sum_{j=1}^{n} m_j^l G_j^{l\,s/l}}} \tag{1-17}$$

where m_j^l is the slope of the liquidus line corresponding to element j, $G_j^{l\,s/l}$ is the gradient of element j in the liquid at the dendrite tip, which can be calculated by:

$$G_j^{l\,s/l} = -\frac{\left(1 - k_j\right) w_j^{l\,s/l} v_{tip}}{D_j^l} \tag{1-18}$$

Finally, the combination of equation (1-14)-(1-18) enables an estimation of the R_{tip} and v_{tip} values in a multicomponent alloy for a fixed undercooling ΔT.

It should be mentioned that all the dendrite growth models presented above focus on the analytical solution weakly coupled with thermodynamic data. However, in the literature, thermodynamic coupled models are already developed and applied for multicomponent alloys, examples are available in [Gil96, Wan13, Zha13, Lah19]. The principal idea is to compute the partition coefficients and liquidus slopes based on the preexisting phase diagram calculations which can be easily obtained by several commercial software such as Thermo-Calc [The18] or JMatPro [JMa], examples are available in [Gil96, Wan13, Zha13, Lah19]. In this work, PhysalurgY [Phy], a library of physical metallurgy modules coupled with Thermo-Calc software [The18] developed at CEMEF, is applied. The numerical tool KIND [Gui22] in PhysalurgY is used to compute the dendrite tip kinetics.

1.1.2 Microsegregation

During solidification, an important phenomenon is the redistribution of solute between solid and liquid phases also named segregation. Solute segregation can significantly affect the material properties and microstructure, and even lead to enhanced defect formations. Depending on the scale of segregation, it can be distinguished as macrosegregation or microsegregation. Macrosegregation develops at scales larger than several hundred micrometers, is mainly due to solute transport caused by the convection effect or grains movement in the liquid domain. The microsegregation refers to segregation depending on solute diffusion in the liquid and solid between dendrite arms within the range 10 to 100 µm [Deb95]. Microsegregation mainly defines the solidification path, which gives the relationship between the temperature, the solute concentrations, and the fraction of each phase. Several microsegregation models depending on the underlying assumptions are reported in the literature. The Lever Rule (LR), Gulliver-Scheil (GS) and Partial Equilibrium (PE) models are presented hereafter considering a binary alloy.

1.1.2.1 Lever Rule

The Lever Rule (LR) model is based on the assumption that complete diffusion in solid and liquid occurs also considering interfacial equilibrium. As a result, the composition is uniform in the solid and liquid phases.

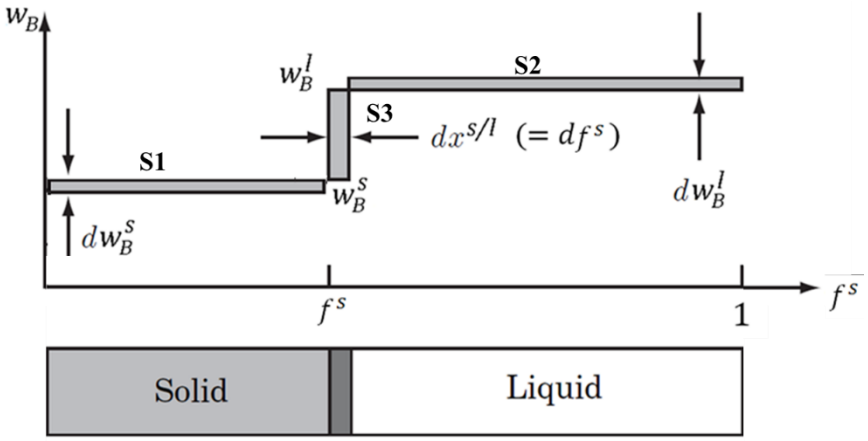

Figure 1-2. Solute partitioning for L-R microsegregation model.

Figure 1-2 represents a closed domain where solidification occurs. The mass balance derived from differential consideration is (S1 + S2 = S3):

$$f^s dw_B^s + (1 - f^s) dw_B^l = (w_B^l - w_B^s) df^s \tag{1-19}$$

also leading to

$$f^s w_B^s + f^l w_B^l = Constant = w_B^0 \tag{1-20}$$

with $f^l = 1 - f^s$ and w_B^0 the nominal solute mass composition.

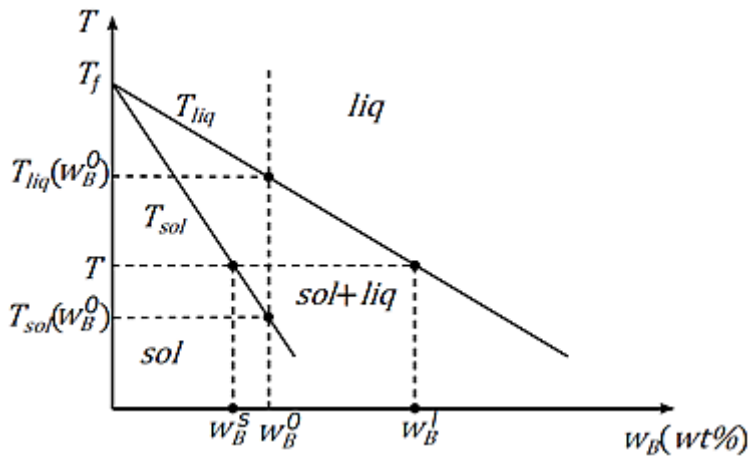

Figure 1-3. Linear phase diagram for a binary alloy with solute weight concentration w_B^0. The liquidus and solidus curves are approximated by straight lines.

Assuming a linear phase diagram as shown in Figure 1-3, the liquidus and solidus temperature can be deduced:

$$T_{liq}(w_B^0) = T_f + m^l w_B^0 \tag{1-21}$$

$$T_{liq}(w_B^l) = T = T_f + m^l w_B^l \tag{1-22}$$

$$T_{sol}(w_B^s) = T = T_f + m^s w_B^s \tag{1-23}$$

where T_f present the melting temperature of the pure component, m^l and m^s are the liquidus and solidus slope respectively. As mentioned in section 1.1.1.1, a constant partition coefficient $k = w_B^s / w_B^l$ is considered to simplify the equations. So that $w_B^s = w_B^l / k$. By combining equation (1-20)-(1-23), the mass fraction of solid is:

$$f^s = \frac{1}{1-k}\frac{T - T_{liq}(w_B^0)}{T - T_f} \tag{1-24}$$

In consideration of constant and identical density for each phase, the volume fraction of liquid can be obtained with the same expression.

With equation (1-24), the volume fraction of the solid phase can be deduced by the temperature T and $f^s = 1 - f^l$, which means that if the temperature evolution is known, the volume fraction of each phase can be explicitly computed. This provides the possibility to link the heat transfer at macro scale to the structure evolutions at micro scale regarding a specific solidification path. The same principle can be applied for another analytical model as presented below.

1.1.2.2 Gulliver-Scheil

The Gulliver-Scheil (GS) model is based on the assumption of a complete solute diffusion in liquid and no diffusion in the solid. Besides, it assumed that partitioning of solute obeys the phase diagram in equilibrium condition at the solid-liquid interface.

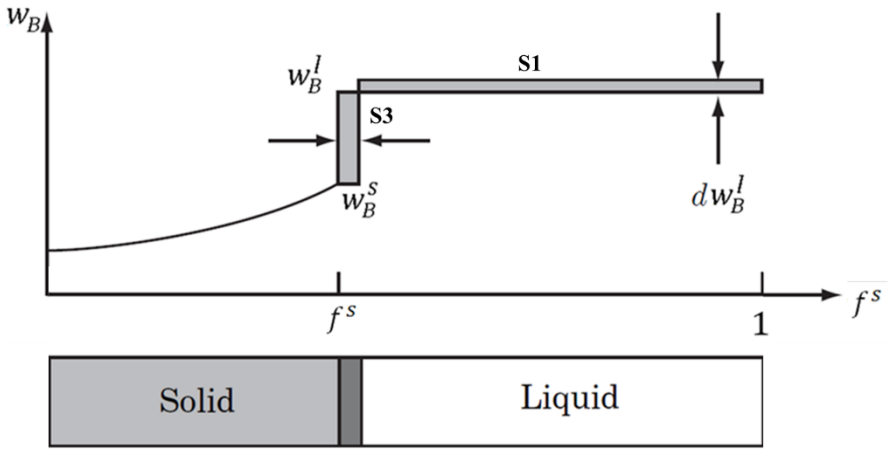

Figure 1-4. Solute partitioning for GS microsegregation model [Dan09].

As shown in Figure 1-4, the mass balance derived from differential consideration is (S1 = S2):

$$(1-k)w_B^l df^s = (1-f^s)dw_B^l \tag{1-25}$$

Equation (1-25) implies that the solute rejected by the moving interface is balanced by the increase of the solute concentration in the liquid. In the absence of undercooling, the initial condition is $w_B^l = w_B^0$ and $f^l = 1$. By rearrangement, (1-25) becomes for fixed partition coefficient:

$$\int_1^{f^l} \frac{df^l}{f^l} = -\frac{1}{1-k}\int_{w_B^0}^{w_B^l} \frac{dw_B^l}{w_B^l} \tag{1-26}$$

$$w_B^l = w_B^0 (f^l)^{k-1} \tag{1-27}$$

Assuming constant and identical density for each phase (the mass fraction f can be replaced by volume fraction g) and a linear liquidus curve with slope m^l (as shown in Figure 1-3), by combining equation (1-21), (1-22) and (1-27), the mass fraction of liquid and solid can be obtained for $T < T_{liq}(w_B^0)$:

$$g^l = \left(\frac{T - T_f}{T_{liq}(w_B^0) - T_f}\right)^{1/(k-1)} \tag{1-28}$$

Same as for the LR model, the volume fraction of each phase can be explicitly computed by considering the temperature evolution.

Besides the analytical models mentioned above applied to two phase solidification, models based on thermodynamic consideration for multiphase and multicomponent alloys have also been developed in the literature [Che02, Zha10, Zha13-2, Kos16]. In this work, the numerical tool PATH coupled with thermodynamic equilibrium calculations based on Thermo-Calc [The18] of library PhysalurgY [Phy] is applied to compute the phase transformations for steels.

1.1.2.3 Partial equilibrium

The Partial Equilibrium (PE) model assumes negligible diffusion in solids for substitutional elements and complete diffusion in solids for interstitial elements such as carbon, oxygen, nitrogen, hydrogen, and boron [Zha13-2, Kos16], so that the chemical potential of the latter becomes equal everywhere throughout the whole system. The liquid phase has still a homogeneous composition. In the GS model, the composition is frozen and a slight amount of solid phase is added to the previously formed solid phases of same nature. In the PE model, the compositions and the amounts of the existing phases are adjusted in order to obtain a homogeneous chemical potential for the interstitial elements present in the alloy.

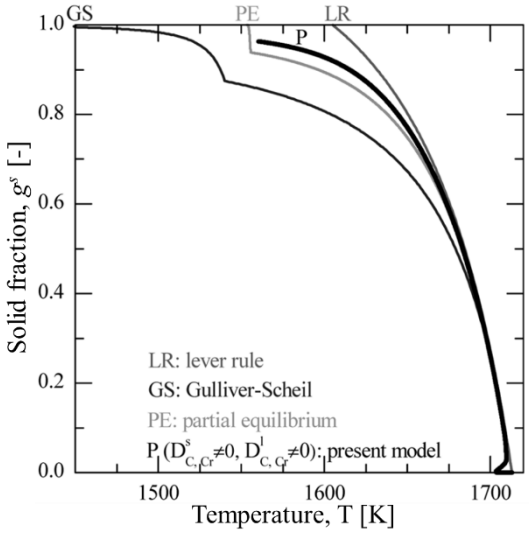

Figure 1-5. Predicted solid fraction, g^s, versus temperature, T, for a Fe–1wt%C–10wt%Cr alloy using different models of the solidification path [Zha10].

Figure 1-5 shows the solidification paths of different models (LR, PE, GS and P). The PE model is placed between the GS and LR model because it takes account the complete diffusion of C. The P model is proposed by Zhang *et al* [Zha10] by considering the growth of the dendrite tip as well as finite diffusion in the liquid and solid phase.

1.1.3 Microstructure of solidification in welding

The grain structure evolution during welding processes has also to be considered in the solidification stage. When the heat source passes and the melt pool solidifies, grains develop by epitaxial mechanism and compete to grow. The grains with preferred growing directions perpendicular to the melt pool boundary overgrowth the others. This preferential growing direction is the <100> direction in cubic system as 316L stainless steel alloy. Besides, during welding process, nucleation of new grains may occur by fragmentation or intentional inoculation.

1.1.3.1 Epitaxial grain growth

During the welding process, the existing base metal at the fusion line firstly acts as the substrate in an epitaxial grain growth mechanism. As the liquid metal is in direct contact with the substrate grain, the grains grow epitaxially from the existing grains to the liquid by keeping the original grain orientation (Figure 1-6 (a)). Besides, as shown in Figure 1-6 (b), the grain G1 stops growing and is eliminated by the growth of G2 through the grain growth competition. The reason is that the <100> direction of G2 is more perpendicular to the weld pool boundary than G1, as shown in Figure 1-6 (a) which prefers the growth of G2 than G1. The grain growth competition is presented in detail in 1.1.3.2.

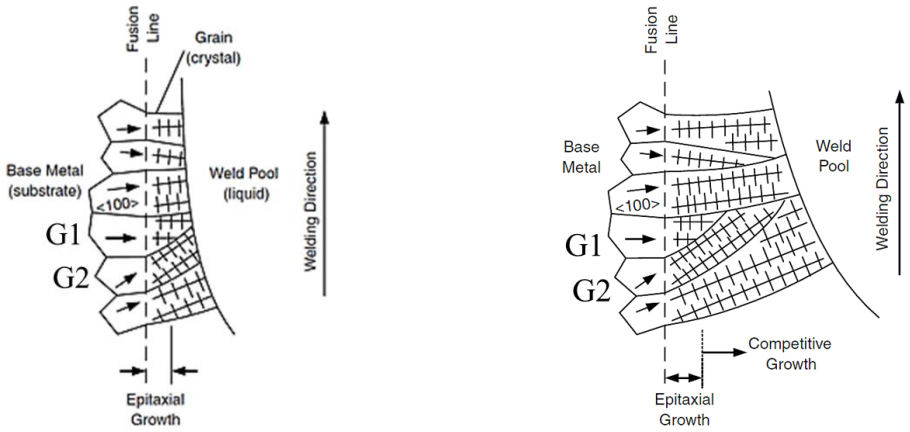

(a) (b)

Figure 1-6. (a) Epitaxial grain growth near the fusion line, and (b) grain competition in the fusion zone [Kou03].

1.1.3.2 Grain growth competition

The grain growth competition begins in the fusion zone after the epitaxial grain growth as shown in Figure 1-6 (b). The mechanism is well explained in [Rap93] in the casting process.
The principle of grain growth competition can be summarized as proposed by Rappaz [Rap93]: "The 'best alignment' selection criterion for dendritic grains corresponds to a minimum undercooling criterion". As shown in Figure 1-7, the dendrites in the left and right grains have the crystallographic direction <100> aligned with the temperature gradient, namely perpendicular to the liquidus isotherm (dashed line). Thus, these two grains grow with the same velocity as the liquidus isotherm (with the assumption of an established stationary regime), v_L. However, for the middle grain contains dendrites with <100> direction misoriented from the temperature gradient with an angle θ, the growth velocity v_θ, is larger than the velocity of the liquidus isotherm ($v_\theta = v_L/cos\theta$). As a result, based on the dendrite tip kinetics, the undercooling at the dendrite tip of the middle grain is larger than that of the side grains.

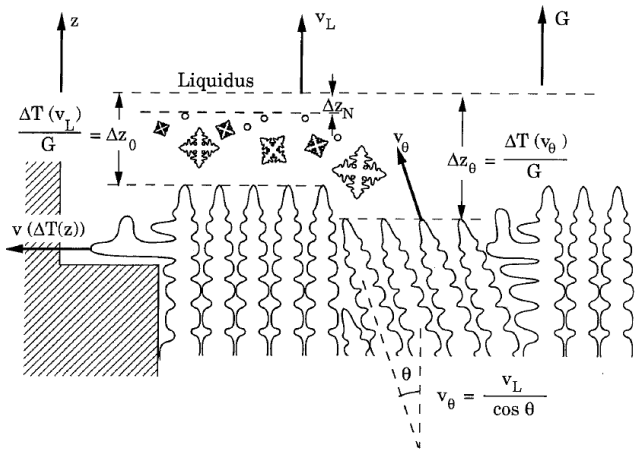

Figure 1-7. 2D schematic of the growth mechanisms occurring in a dendritic alloy with a non-uniform temperature [Rap93].

Therefore, the middle grain is out-grown by the side grains:

-The middle grain reaches the left grain and finally cannot grow any more.

-The right grain extends to the free liquid due to the diverging between the two grain directions.

Finally, the middle grain stops growing while the other grains containing the most favorable dendrite growth direction keep growing.

1.1.3.3 Nucleation in the melt pool

During welding process, nucleation can take place in the melt pool if local condition is sufficient to promote this mechanism, before epitaxial grains develop. Intentional addition of particles of inoculant to the melt can cause the heterogeneous nucleation in the weld pool. As shown in Figure 1-8, the inoculation with titanium in C-Mn steel inoculation increases the nucleation in the melt pool and restrains the growth of the columnar grains in the fusion zone. This heterogeneous nucleation refined the grains in the weld bead and significantly increases the ductility of the weld bead [Hei86, Pet73]. Besides, Chiocca [Chi19] has shown that the consideration of nucleation can largely change the final grain structure after the solidification of GTAM process in the simulation.

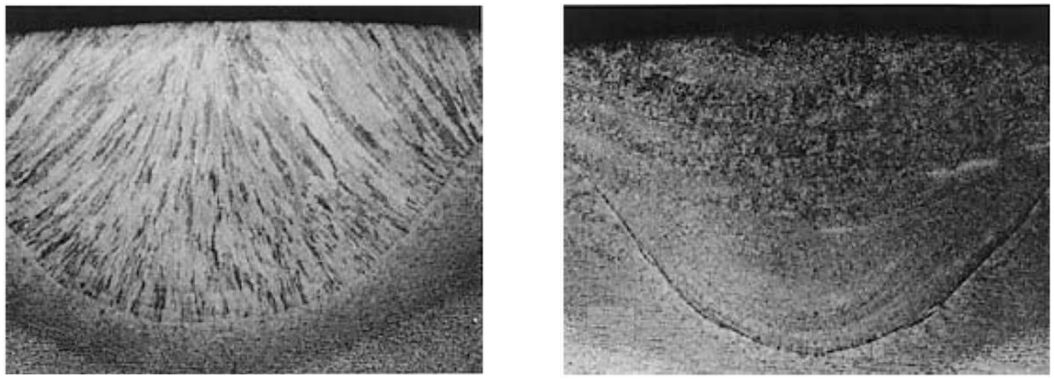

(a) (b)

Figure 1-8. Effect of inoculation on grain structure in submerged arc welding of C-Mn steel (magnification 6×), (a) without inoculation, (b) inoculation with titanium [Hei86, Kou03].

Another main cause of the nucleation in the melt pool is the detachment of the existing dendrite arms in the weld pool. Figure 1-9 presents a dendrite fragmentation occurring in solidification during casting. The fragmentation will continue to grow while it is transported away from the front of the columnar region. This fragment could form a new grain inside the undercooled melt pool [Ruv07]. This detachment nucleation refines the grains in the weld bead and thus improves mechanical properties such as ductility, hardness and strength [Che17].

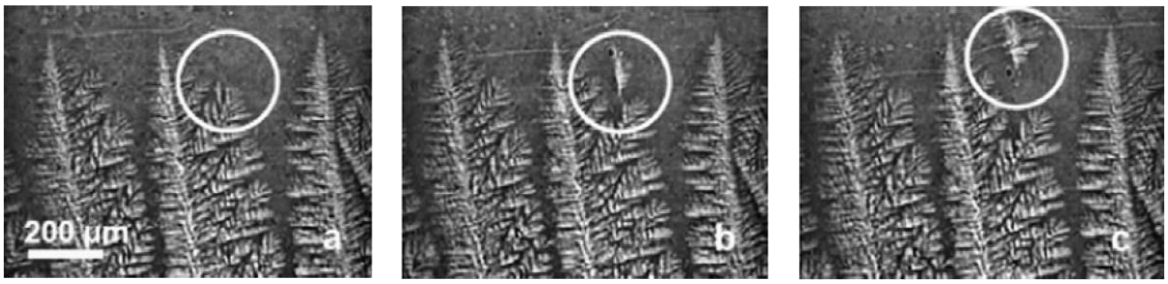

(a) (b) (c)

Figure 1-9. In situ observation of localized fragmentation during solidification of an Al-20wt.%Cu alloy at (a) t=0s, (b) t=2.25s, and (c) t=4.50s [Ruv07].

1.1.3.4 Grain structure during welding

The final grain structure after welding depends on the welding parameters, for example, welding speed. The welding speed can influence the melt pool shape. As the columnar grains growing from the base material aligned with the temperature gradient, the grain structure is strongly affected by the melt pool shape.

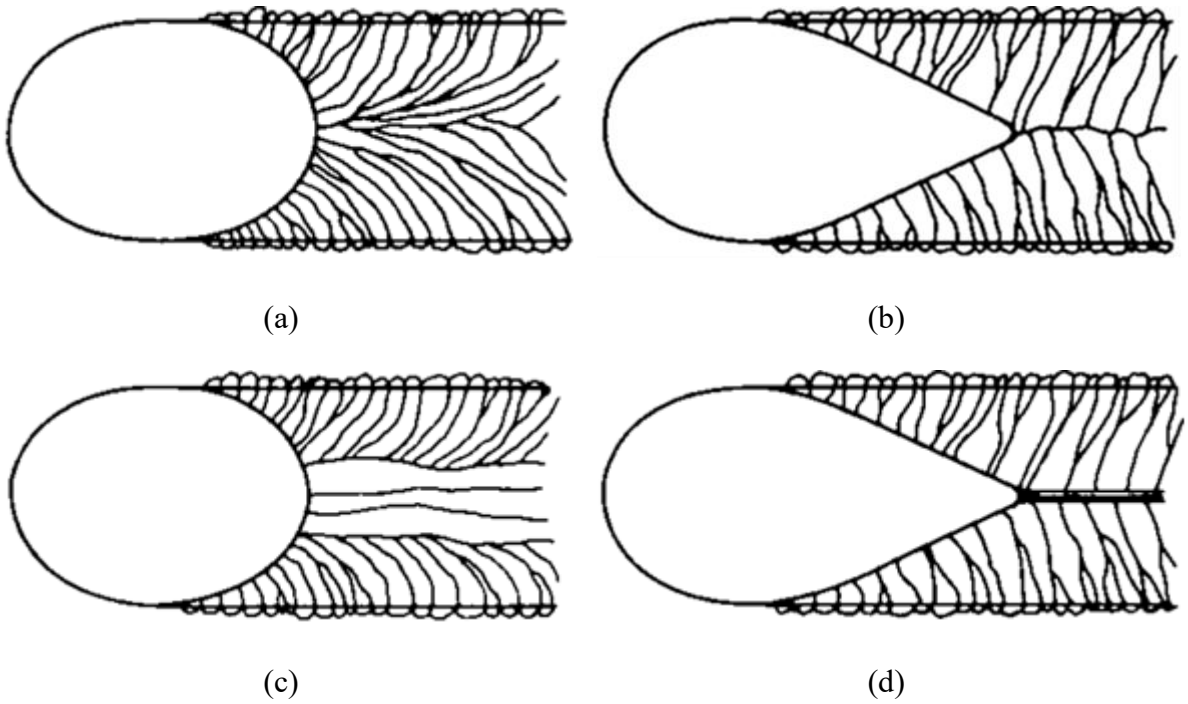

Figure 1-10. Effect of welding speed on columnar-grain structure in weld metal: (a) regular structure at low welding speed, (b) regular structure at high welding speed, (c) structure with axial grains at low welding speed and (d) structure with axial grains at high welding speed [Kou03].

Figure 1-10 and Figure 1-11 illustrate in details the welding speed influence on the final grain structure. The weld pool is elliptical (Figure 1-10 (a) and (c)) at low welding speeds and becomes teardrop shaped at high welding speeds (Figure 1-10 (b) and (d)). On the one hand, as the trailing boundary of an elliptical weld pool is curved, the columnar grains are also curved in order to grow perpendicular to the pool boundary, as shown in Figure 1-11 (a). On the other hand, because the trailing pool boundary of a teardrop-shaped weld pool is essentially straight, the columnar grains are also essentially straight in order to grow perpendicular to the pool boundary, as shown schematically in Figure 1-11 (b).

In addition, in the welding process, axial grains with grain growth directions aligned with the welding direction can also exist in the fusion zone. These axial grains can initiate from the fusion boundary at the starting point of the bead, in the domain with higher undercooling, and continue along the length of the bead, blocking the columnar grains growing inward the center of the fusion zone. However, the section of the axial grain layer can variate with the welding speed. As shown in Figure 1-10 (c) and Figure 1-11 (c), at low welding speed, the elliptical weld pool has a significantly longer section of the trailing pool boundary which can be perpendicular to the axial direction. This trailing pool boundary induces a region of axial grains significantly wider than a teardrop weld pool in Figure 1-10 (d) and Figure 1-11 (d): at high welding speed, only a relatively small section of the trailing pool boundary has the possibility to be perpendicular to the axial direction, therefore, a small section of axial grains can be formed.

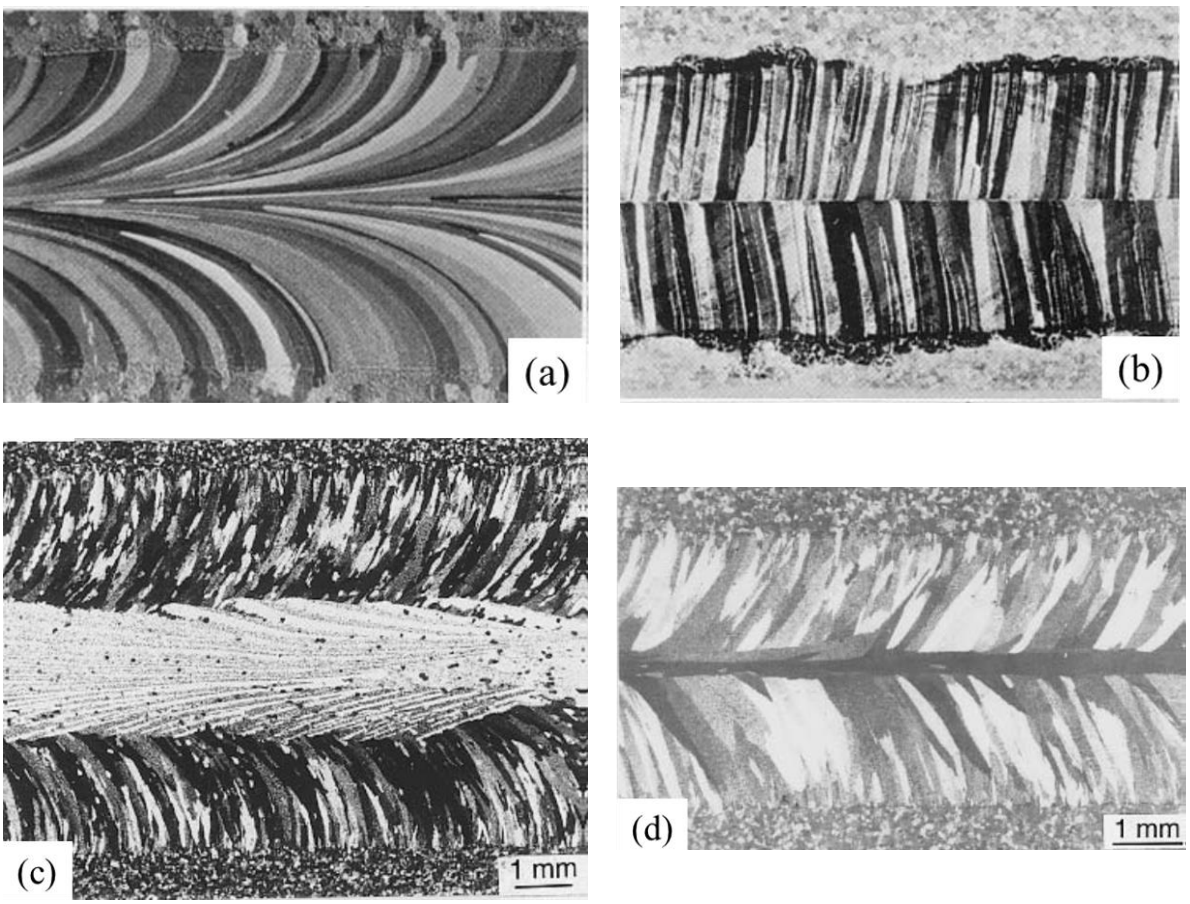

Figure 1-11. Grain structures in GTAW for (a) 99.96% aluminum at welding speed 4.17 $mm \cdot s^{-1}$ [Ara73], (b) 99.96% aluminum at welding speed 16.67 $mm \cdot s^{-1}$ [Kou03], (c) 5052 aluminum at welding speed 4.2 $mm \cdot s^{-1}$ [Kou03], and (d) 1100 aluminum at welding speed 12.7 $mm \cdot s^{-1}$ [Kou03].

1.2 Modeling of microstructural evolutions

In this section, several models applied in the literature to simulate the grain structure evolution during welding process are presented. A pertinent model should be chosen among these models to achieve the grain structure simulation in this work.

1.2.1 Cellular Automaton Finite Element (CAFE) model

The Cellular Automaton-Finite Element (CAFE) model is described in detail in the following chapters and is discussed here in order to situate it in relation to the other solidification models, and to reproduce its various evolutions.
The CAFE model was firstly proposed by Rappaz and Gandin to simulate the grain structures during the solidification process. It was then enriched by Guillemot [Gui04], Carozzani [Car12] and Chen [Che14]. The principal idea of CAFE model is to model the structure of grains rather than the internal morphology of grains. Two fundamental assumptions are done:

- the shape of the envelope of a grain is locally given by a simple geometric shape usually square in 2D and octahedron in 3D for cubic materials,

- the growth of this geometric shape can be calculated according to the preferred directions by a tip kinetics model.

These simplifications make it possible to model the growth of grains, neglecting the microscopic description of the dendrite arms, which define it as a mesoscopic model, as shown in Figure 1-12.

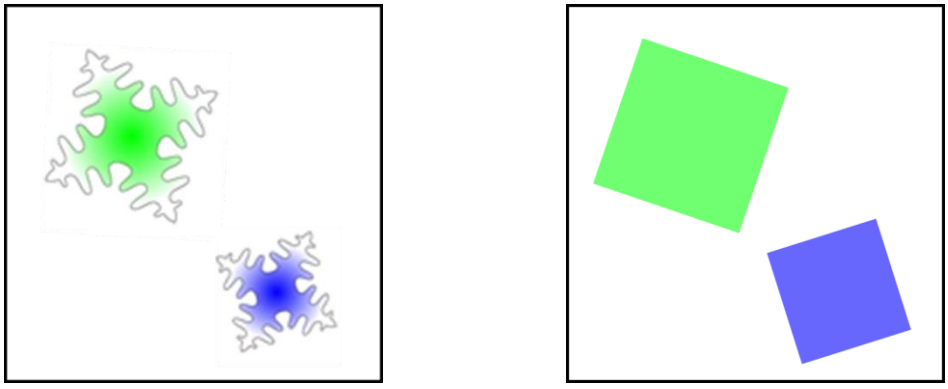

(a) (b)

Figure 1-12. Schematic representation in a representative elementary volume (REV) (a) of an equiaxial dendritic grain growth, (b) of the corresponding envelopes introduced in the CAFE model.

The CAFE model is based on the coupling of several resolution scales:

- Macroscopic scale: the resolution of the global conservation equations of mass, momentum, and energy,
- Mesoscopic scale: the development of the grain envelope is followed by a regular grid of cells in 2D or cubes in 3D, the temperature field can be transported between the macroscopic and the mesoscopic scales as part of the coupling of the resolution scales.
- Microscopic scale: models of dendrite tip kinetics to calculate the dendritic growth in order to obtain the evolution of the grain structure indirectly.

In the continuity of the work, Chen and co-workers [Che14-2, Che16] carried out an initial coupon structure storage method which allowed to predict the grain structure for welding process. Other research groups [Chi19, Han14, Han15, Che20] have also implemented the CAFE model to predict the morphological evolution of grain structure in welding. Besides. the CAFE model can also be implemented in the grain microstructure prediction during additive manufacturing processes [Koe19, Zha16, Zha19, Tef21, Xio21].

1.2.2 Monte Carlo model

The Monte Carlo model is well described by Sieradzki [Sie13]. Sista [Sis00] has developed this model for welding applications to simulate the grain evolution in the heat affected zone (HAZ) during the welding process, also considering the physical phenomena occurring during melting and cooling stages. In the Monte Carlo model, a random orientation number is assigned to each

site among the total number of orientations accessible to the grains. The energy for this crystal lattice is thus calculated locally for a given environment:

$$E = -J \sum_{j=1}^{n} (\delta_{S_i S_j} - 1) \tag{1-29}$$

with J the energy between two crystal lattices belonging to different grains (grain boundary energy), n the number of neighbors adjacent to the chosen crystal lattice, S_i is the orientation of the randomly chosen site i, S_j is the orientation of the neighbors of site j, δ is the Kronecker function. The kinetics of grain boundary migration are simulated by randomly selecting a site and changing its orientation to one of the closest orientations, based on the energy variation due to the change in orientation. The associated probability of change is:

$$\begin{cases} p = 1 \ if \ \Delta E \leq 0 \\ p = e^{\frac{-\Delta E}{k_B T_s}} = e^{\frac{-(n_1 - n_2)J}{k_B T_s}} \ if \ \Delta E > 0 \end{cases} \tag{1-30}$$

with ΔE the energy variation, k_B the Boltzmann constant, T_s the simulation temperature, which is not directly connected to the physical temperature of the system, and the value $J/(k_B T_s) = 1$ for grain growth [Tik10]. n_1 and n_2 represent the number of neighbors with different orientations before and after the reorientation test. It could be noted that, in the first approach proposed by Sieradzki [Sie13], $p = 0$ for equation (1-30) if $\Delta E > 0$ because no physical phenomena such as temperature is considered.

In welding process simulation, a non-uniform mobility term is added to modify the Monte Carlo probability at each given network site by Rodgers [Rod16]:

$$\begin{cases} p = M \ if \ \Delta E \leq 0 \\ p = M e^{\frac{-\Delta E}{k_B T_s}} = M e^{\frac{-(n_1 - n_2)J}{k_B T_s}} \ if \ \Delta E > 0 \end{cases} \tag{1-31}$$

where

$$M = M_0 \, e^{\frac{-Q}{k_B T_t^i}} \tag{1-32}$$

with M the mobility, Q the activation energy for grain boundary movement and M_0 a user defined factor. The temperature T_t^i represents the physical temperature (different from the simulation temperature T_s) as a function of the real time t and the position i.

In the HAZ, grain growth is simulated by the mobility of grain boundaries. It is high near the fusion zone (FZ) and decreases as the temperature moves away from this zone to $M = 0$ at room temperature. In the FZ, as the heat source moves, previously solid regions are melted. As the heat source advances, the FZ cools and the grains grow with grain boundary mobility M. So, melting, solidification and growth of the grains are simulated during the welding process, in this global model.

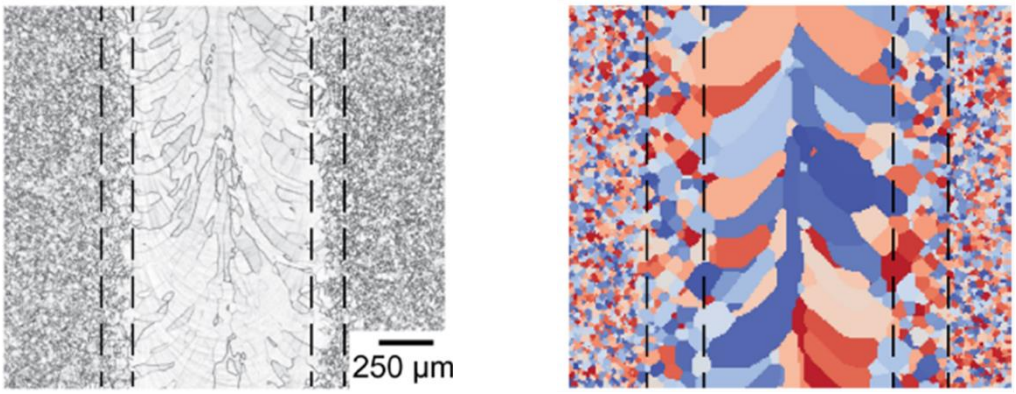

(a) (b)

Figure 1-13. Bead of electron beam welding (a) experimental result,
(b) simulation result [Rod16].

Figure 1-13 shows a very good consistency between experimental and simulation results. However, the simulation can only predict qualitative characteristics, the difficulty is to coincide the physical time with the simulation time for the temperature field, which demands a calibration of a great number of complex parameters. Much more development remain to be done to discover the physics of grain nucleation and growth during solidification [Fra17].

1.2.3 Cellular Automaton Lattice Boltzmann (CALB) model

The CALB model was initially used for the simulation of the grain structure evolution during additive manufacturing processes based on a powder bed fusion [Rai17]. This model is also developed at mesoscopic scale as it is applied at the grain scale. The CALB model is a coupling between the Lattice Boltzmann model solving the dynamic problems (the equations associated to mass, moment, and energy conservation) in the melt pool and the Cellular Automaton model which simulates the grain growth. The principles of the cellular automaton method and the transport between the LB model and CA model are identical to the CAFE method. The characteristics of the LB model are recalled here.
The Lattice Boltzmann model solves the physical problems by simulating the temporal evolution of the distribution functions of a particle $f\ (\boldsymbol{x}, \boldsymbol{v}, t)$ where f represents the probability of finding a particle at position $\boldsymbol{x}$, at time t and moving at velocity $\boldsymbol{v}$. The Lattice Boltzmann distribution function f_k is the discretization of the continuous function f, where the space is divided by crystal sites and the velocity is represented by a finite number of displacement vectors. k parameter evolves between 0 and 8 for two dimensional applications [Rai17]. The macroscopic quantities are given by the discretized functions:

$$\rho = \sum_k f_k \tag{1-33}$$

$$\rho u = \sum_k e_k f_k \tag{1-34}$$

$$E_{LB} = \sum_k h_k \tag{1-35}$$

where $h_k$is the energy density distribution function for each crystal site. Macroscopic equations (1-36)-(1-38) can be solved to follow physical evolution:

$$\nabla \cdot u = 0 \tag{1-36}$$

$$\frac{\partial u}{\partial t} + (u \cdot \nabla)u = -\frac{1}{\rho}\nabla p + \nu \nabla^2 u + g \tag{1-37}$$

$$\frac{\partial E_{LB}}{\partial t} + \nabla \cdot (u E_{LB}) = \nabla \cdot (\alpha \nabla E_{LB}) + \dot{Q} \tag{1-38}$$

with ν the kinematic viscosity, α the thermal diffusivity and $\dot{Q}$ the thermal source. Solution of these equations gives the temperature and the velocity fields, which can be transported into the CA model to simulate thereafter the grain structure evolution. Figure 1-14 shows the result of a simulation applied to the additive manufacturing process. The orientation of the developed grains is well presented.

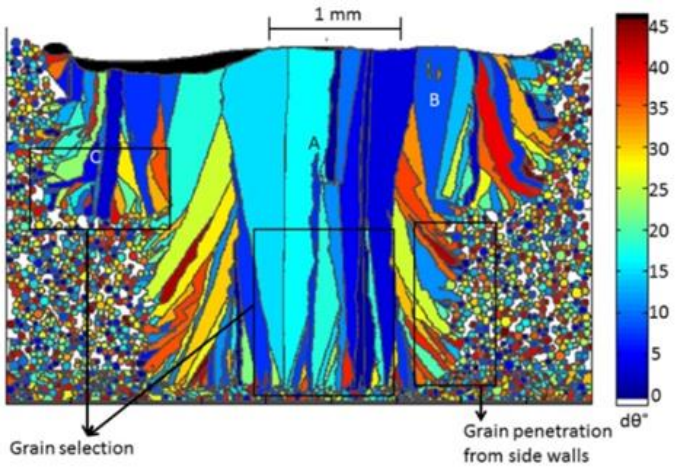

Figure 1-14. Simulation of grains structure in additive manufacturing of a T-shaped part in IN718 [Rai17].

This CALB model is currently restricted to 2-dimensional computational domain [Rai17] for additive manufacturing or welding process. The implementation of the CALB approaches in 3-dimension should be possible in the future as the LB model was already implemented in 3-dimensional computation of the electron beam fusion process [Amm14].

1.2.4 Mesoscopic envelope model

The mesoscopic envelope model is firstly proposed by Steinbach et al [Ste99, Ste05] for diffusion-controlled dendritic growth in pure substances. It was then extended by Delaleau [Del10] to binary alloys and convection by Delaleau [Del11] and Olmedilla1 [Olm19].
The essential idea of the envelope model is quite similar as the CA model. The dendritic grain is described by its envelop: a virtual smooth surface that links the tips of the actively growing dendrite branches. The velocities of envelop growth can then be deduced by the velocities of dendrite tips. For example, in an alloy, the growth of the dendrite tips is governed by the solute flux that the tips eject into the liquid. The branched dendritic structure inside the envelope is only implied and its details are not concerned (as shown in Figure 1-15); the interior of the envelope is instead described in a volume-averaged sense by a phase-fraction field. The phase solute concentrations are also described in a volume averaged sense. The phase change that determines the evolution of the structure, *i.e.*, of the phase fraction field, inside the growing envelope is controlled by the exchange of solute with the surroundings of the grain. The transport of solute at the mesoscopic scale is described by volume-averaged transport equations.

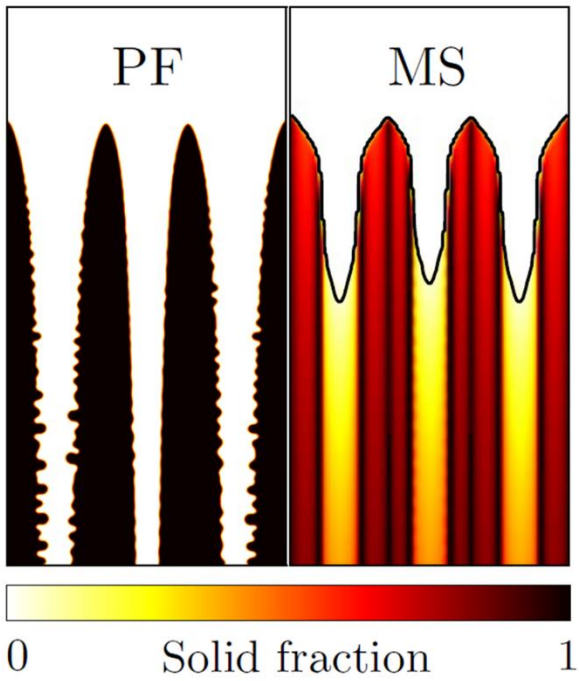

Figure 1-15. Solid fraction for phase field (PF) and mesoscopic (MS) simulations of the columnar grains during directional solidification initiated from two nuclei placed in the bottom corner. model. The envelope of the mesoscopic model is shown as a black line. The domain width is 250 μm [Via17].

1.2.5 Phase field method

The phase field method is used to model the solidification by an approach of continuous media. The space is divided into 3 areas: the liquid, the solid and the solid / liquid interface. The interface is diffuse with a defined thickness and the phase field variable ϕ allows continuous change from solid to liquid. The ϕ function depends on both time and position and evolves in the range [0,1]. This function is used to describe at a given position the belonging of the material to the liquid or solid phase. This approach allows the description of evolution for complex liquid \ solid interface, also considering diffusion and convection phenomena in both phases.
The phases are identified by the constant phase field ϕ in each phase which varies continuously in the interface. For example, the location of material belongs to liquid when $\phi = 1$ while it belongs to solid when $\phi = 0$. The principle of phase field method is to minimize the free energy E of the simulated domain Ω through the temporal evolution of the interface which allows this energy to be reduced. E is defined by Boettinger et al. [Boe02] as:

$$E = \int_{\Omega} \left[e(\phi, c, T) + \frac{\varepsilon_c^2}{2} |\nabla c|^2 + \frac{\varepsilon_\phi^2}{2} |\nabla \phi|^2 \right] d\Omega \tag{1-39}$$

where $e(\phi, c, T)$ is the free energy density which depends on the temperature, T the concentration, c, and the phase field variable, ϕ. ε_ϕ and ε_c are the gradient energy coefficient related to phase field and concentration gradients, respectively, mainly induced by interface.
The behavior of ϕ is governed by an equation which is coupled to equations for heat and solute transport proposed by Boettinger *et al*. and Chen *et al*. [Boe02, Che02-2]

$$\frac{\partial \phi}{\partial t} = -M_\phi \left[\frac{\partial e}{\partial \phi} - \varepsilon_\phi^2 \nabla^2 \phi \right] \tag{1-40}$$

$$\frac{\partial c}{\partial t} = \nabla \cdot \left[M_c c(1-c) \nabla \left(\frac{\partial e}{\partial c} - \varepsilon_c^2 \nabla^2 c \right) \right] \tag{1-41}$$

where M_ϕ and M_c are the positive mobilities related to the interface kinetic coefficient and solute diffusion coefficient, respectively. The definition of the function $e(\phi, c, T)$ coupled with equations (1-40) and (1-41) determines the final solution of the phase field.
Figure 1-16 illustrates the result of the solidification phase field simulation of a 3D dendritic grain. Moreover, the phase field method can be coupled with the Lattice Boltzmann model to take in account the convection during solidification [Tak20, Sak20], or coupled with cellular automata model to increase the simulation efficiency [Liu21].

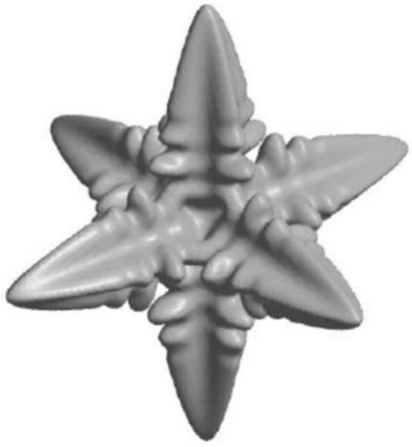

Figure 1-16. Phase field simulation of the growth of a dendritic grain in 3D [Hoy04].

1.2.6 Dendritic needle network

The dendritic needle network was initially introduced by Tourret and Karma [Tou13] in 2D for a binary alloy. The dendrites are represented by a network of needles with zero thickness, as presented in Figure 1-17. The method was then extended to 3D [Tou16].
In the dendritic needle network method, each dendrite is represented by a parabola (Figure 1-17 (b)), the diffusion of the composition field of solute is resolved only in the liquid domain and the composition is imposed inside the parabolas by the phase diagram of a front plane. Therefore, the dendritic needle network model does not verify the conservation of the solute mass in the simulation domain.

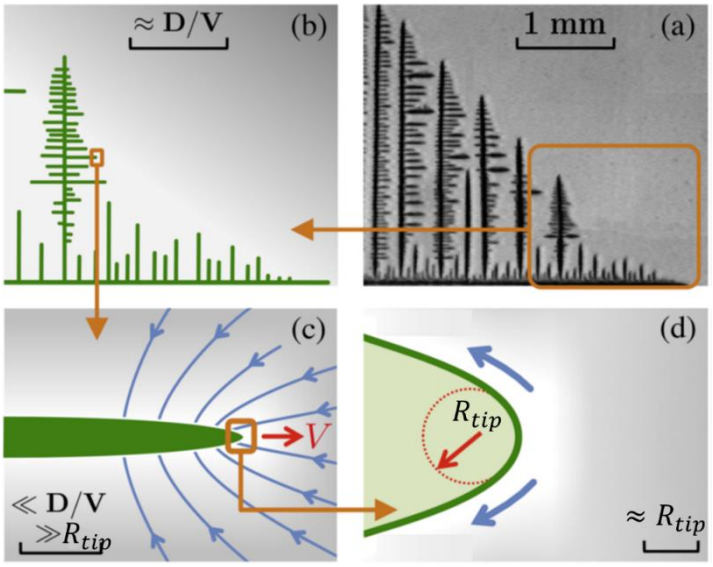

Figure 1-17. Schematic illustration of the dendritic needle network approach [Tou13], (a) an ammonium-bromide crystal in a supersaturated aqueous solution [Cou05], (b) representation of dendrite by a skeleton of thin needles, (c) solute diffusion and (d) a marginal stability condition on the inner scale of the dendrite tip

Unlike other models which assume the shape of the composition field and apply an analytical formula to determine the dendritic growth kinetics, the dendritic needle network model solves the solute flux ahead of the tip by integration. The marginal stability (equation (1-42)) is assumed to be valid, with d_0 the capillary distance. This equation (1-42) gives a relationship between the curvature radius of the tip of the parabola and its speed.

$$R_{tip} \approx \lambda_{min} = 2\pi \sqrt{\frac{d_0 D^l}{v_{tip}}} \tag{1-42}$$

The second equation explicitly compute the diffusion flux at the tip by integrating the solute field near the tip:

$$R_{tip} {v_{tip}}^2 = \frac{1}{8a} \left(\frac{-D^l}{(1-k) w^{l/s}} \right)^2 \left(\int_{\Gamma'} \nabla w|^{l/s} \cdot \boldsymbol{n} \, d\Gamma' \right)^2 \tag{1-43}$$

where $\nabla w|^{l/s}$ is the composition gradient at solid/liquid interface (Γ'), $\boldsymbol{n}$ is the normal direction of the interface (from solid to liquid). a is a distance defined as given in Figure 1-18.

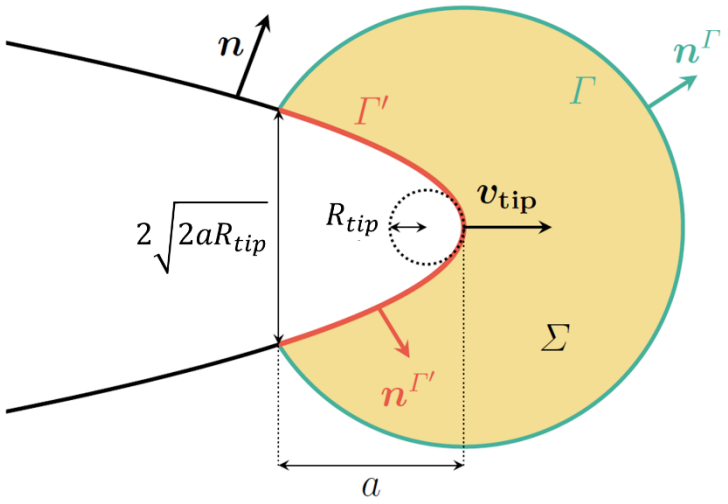

Figure 1-18. Illustration of integration zone defined by a in front of the dendrite tip [Fle19].

Details of the integration could be found in [Tou16, Fle19].

1.2.7 Front tracking method

The front tracking method was introduced by Juric *et al.* [Jur96] to simulate time dependent two-dimensional dendritic solidification of pure substances. The method can easily handle discontinuous material properties between the liquid and solid phases, topology changes and anisotropy of interfacial energy and kinetics. The location of the solid-liquid interface is explicitly always provided. In this method, the interface solution is directly controlled by the undercooling, surface tension, kinetic mobility, thermal conductivity, and volumetric heat

capacity of the liquid and solid phases. By ignoring the volume contraction expansion as well as fluid convection, the energy conservation equation can be written as proposed by Juric *et al* [Jur96]:

$$\frac{\partial(C_p T)}{\partial t} - \nabla \cdot (\kappa \nabla T) = Q \tag{1-44}$$

with C_p the volumetric heat capacity, κ the thermal conductivity, Q the energy source term which accounts for the liberation or absorption of latent heat at the solid-liquid interface with the expression:

$$Q = \int_f q\delta(\boldsymbol{x} - \boldsymbol{x_f})dS \tag{1-45}$$

where $\delta(\boldsymbol{x} - \boldsymbol{x_f})$ is a three-dimensional delta function that is non-zero only at the solid-liquid interface where $\boldsymbol{x} = \boldsymbol{x_f}$, which means the heat source Q localizes at the solid-liquid interface. Assuming that the heat capacity is equal in both liquid and solid, the interface heat source related to the latent heat liberation/absorption q can be described as

$$q = Lv(\boldsymbol{n}) \tag{1-46}$$

where L is the volumetric latent heat, $v(\boldsymbol{n})$ is the component of the velocity normal to the interface. Besides, at the interface, the Gibbs-Thomson temperature condition should be satisfied also with the assumption of identical heat capacity in both liquid and solid:

$$T^{s/l} = T_f - \frac{\gamma(\boldsymbol{n})T_f}{L}\kappa_c - \frac{v(\boldsymbol{n})}{\mu(\boldsymbol{n})} \tag{1-47}$$

where $T^{s/l}$ is the temperature at the interface, T_f is the equilibrium melting temperature, $\gamma(\boldsymbol{n})$ is the anisotropy surface tension as a function of the local surface normal orientation, κ_c is the interface curvature and $\mu(\boldsymbol{n})$ accounts for the effect of the anisotropy kinetic mobility.

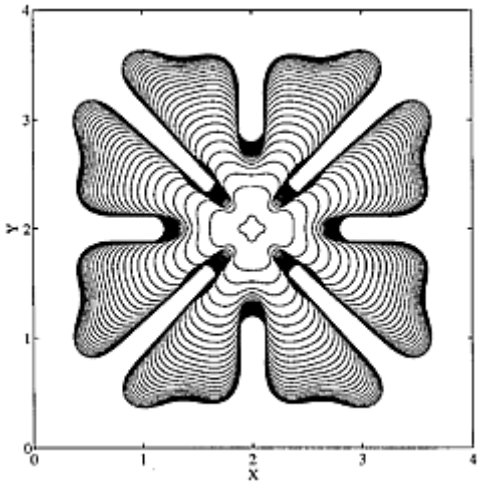

Figure 1-19. Simulation of dendritic solidification in an insulated cavity by front tracking method in 2D [Jur96].

Figure 1-19 presents a dendrite simulated by front tracking method in 2D. The time evolving interfaces from an initial perturbed circle with four lobes are plotted at non-dimensional time increments of 0.03. It shows that the four initial protrusions grow and become wider and then split reflecting the growth of a dendrite.
This front tracking method is then enriched to simulate the dendrite by taking consideration of liquid convection in 2D [Jur98, Al-R02] and 3D [Al-R04]. Results show that the melt flow leads to an increase of the growth rate of the arm growing into the flow and promotes more side branch formation on the upstream side. In addition, the flow results in a reduction of the growth rate of the downstream arm.

1.2.8 Conclusion of microstructure modeling

As shown in these section 1.2 , several models exist to investigate microstructure evolution during solidification. Among all these models presented above, the phase field and front tracking method focus on the microscopic scale, which provide precise morphological description and evolution of the dendrite interface. However, these two methods in microscopic scale can be very expensive in calculation time and storage memory if used in the modeling of microstructure evolution in welding processes. The dendritic needle network method can be applied at a larger scale than phase field and front tracking method, however, it is still not sufficient for the welding process. In other words, a mesoscopic scale simulation approach would be more suitable and would allow to model microstructure evolution at welding scale. Among the three mesoscopic scale simulation model, on the one hand, the CALB model has not yet a mature application in 3D modeling for welding process. On the other hand, although the 3D Monte Carlo model is well coupled with finite element [Sun20] and finite difference method [Rod21] to simulate grain structure evolution in additive manufacturing process, the physical description of grain nucleation and growth is still unclear.
Conversely, in CAFE model, the grain growth follows the KGT [Kur86] law, or a correlated law, also considering possible extension to multicomponent alloy [Hun01]. Besides, the grain nucleation can be computed by a heterogenous nucleation model. Furthermore, the CAFE model is well developed in the 3D simulation of welding process [Chen14, Chen14-2, Chen16]. Therefore, in this work, the CAFE model will be applied to simulate microstructure evolution in fusion welding processes.

1.3 Hot cracking during welding

The hot cracking phenomenon is investigated in the NEMESIS project in order to master and control fusion welding processes both for nuclear and automotive applications. The first part of this section presents the physical phenomena as the origin of the cracking mechanisms and the second part details the criteria of hot cracking proposed in the literature.

1.3.1 Physical phenomena related to hot cracking

1.3.1.1 Liquid circulation during solidification

The solidification process can be separated into four stages, presenting different behaviors during mechanical loading, in order to investigate the origin of cracking phenomenon, as described in Figure 1-20. The temperature gradient and the strain rate during solidification are shown consequently as they are of prime importance in crack occurrence.

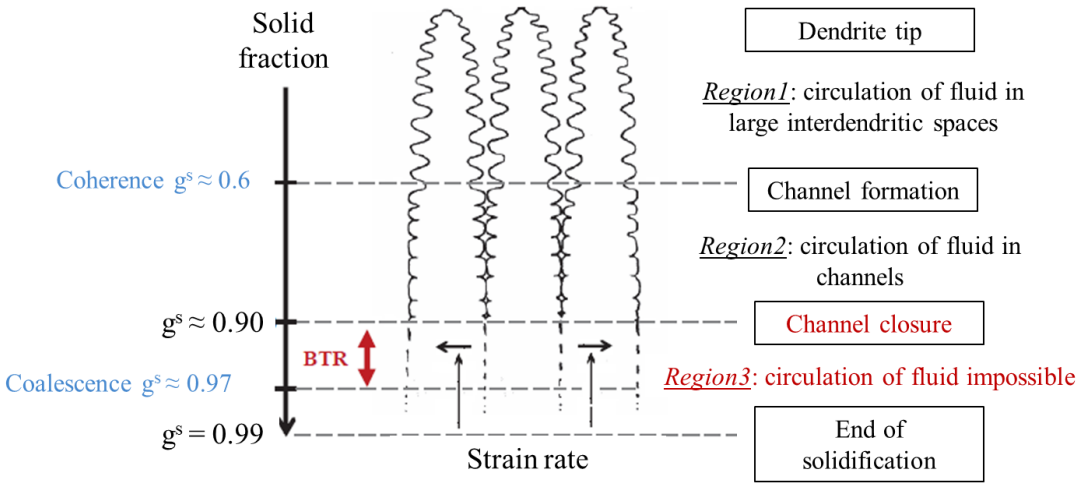

Figure 1-20. Evolution of columnar dendritic solidification [Bou13].

- The first stage corresponds to the area of formation of primary dendrites between which the liquid circulates easily (Region 1). The solid phase is dispersed, and the liquid phase is continuous. In this region, there is no cohesion or continuous solid network due to the high liquid fraction.
- As solidification continues, the dendrites grow until they meet each other and form a cohesive solid network (Region 2). The temperature (or the solid fraction) of coherence formation is defined as the coherency point [Dan09] ($g^s \sim 0.6$ in present scheme). The solid phase and the liquid phase are continuous, but the permeability remains sufficient so that the liquid can still circulate in the growing solid network. In this region, the deformations of the solid network can be compensated by the free circulation of the liquid phase.
- In region 3, the dendrites form bridges between the grains and the liquid film transforms into isolated pockets, reducing the permeability of the solid network and blocking the liquid circulation in the channels. Consequently, the deformations are no longer fed by the circulation of the liquid. In addition, the solid network has not yet coalesced (see the last step) and does not have sufficient mechanical strength to resist high stresses developed during welding and induced by thermal stresses. Accordingly, region 3 includes the area which is susceptible to hot cracking. The temperature range of this zone corresponds to the brittleness interval of the alloy, called the BTR ("Brittle Temperature Range") [Dan09] with, usually, $0.9 < g^s < 0.99$.

- At the last stage of solidification, the solid bridges between the grains are reinforced, the mechanical properties increase strongly and are sufficient to withstand the stresses generated by welding. Coalescence is achieved and the alloy then continues to solidify and strengthen until it reaches 100% solid phase.

1.3.1.2 Origins of the constraints developed

During welding, the non-uniform temperature field produced by the heat source is the origin of thermomechanical stress leading to hot cracking. Figure 1-21 presents the part deformation associated with thermomechanical stresses, T_{sol} is the solidus temperature and T_{liq} is the liquidus temperature. We suppose that the welding is limited to a heating step followed by a cooling step. Figure 1-21 (a) presents the initial state of the part in plan with a temperature T_0 and free stress.

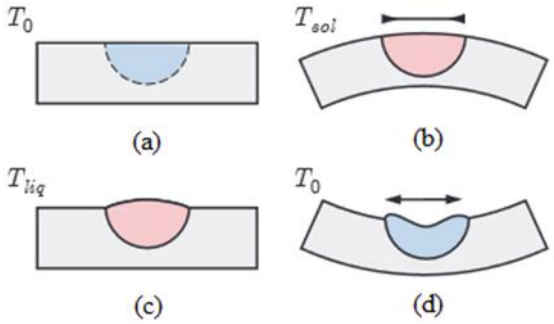

Figure 1-21. Deformation related to thermomechanical stresses [Dan09].

As the heat source passes, the workpiece is heated, the top surface expands and tends to flame (Figure 1-21 (b)). The bead undergoes a compressive stress. When the temperature reaches the liquidus, the heated part melts and the compressive stress is relaxed, the part returns to a planar state and the weld pool is slightly larger than the initial volume (Figure 1-21 (c)). Then, the unconstrained solidification begins at the solid-liquid interface, the bead is no longer plane (Figure 1-21 (d)). It shrinks and undergoes tensile stress. It should be noted that under this condition, the center of the bead is more susceptible to hot cracking.
Hot cracking is a combined phenomenon. On the one hand, the existence of the BTR during solidification leads to a domain of susceptibility to cracking. On the other hand, the stresses during welding act as the driving force of these cracks.

1.3.1.3 Parameters influencing hot cracking

In the previous section, the causes of hot cracking have been presented and detailed. In this section, the parameters influencing hot cracking will be detailed.

Chemical composition

Many studies have demonstrated the influence of chemical composition on hot cracking. For example, a pure metal, which passes directly from a liquid state to a solid state, without a mushy zone does not present the risk of hot cracking [Dan09]. Indeed, the chemical composition determines the solidification interval, that is, the difference between the solidus and the liquidus temperatures. The larger the solidification interval is, the higher the sensitivity to hot cracking becomes, since the time spent in a vulnerable state (BTR) is longer. Therefore, hot cracking depends on the chemical composition. For the 316L steel used in the NEMESIS project (alloy of interest for EDF R&D partner), elements such as sulfur, phosphorus and boron decrease the solidus and increase the sensitivity to hot cracking [Kos16]. As shown in Figure 1-22, for a steel at a given ferrite phase fraction, the increase of sulfur and phosphorus content could lead to cracking during welding process.

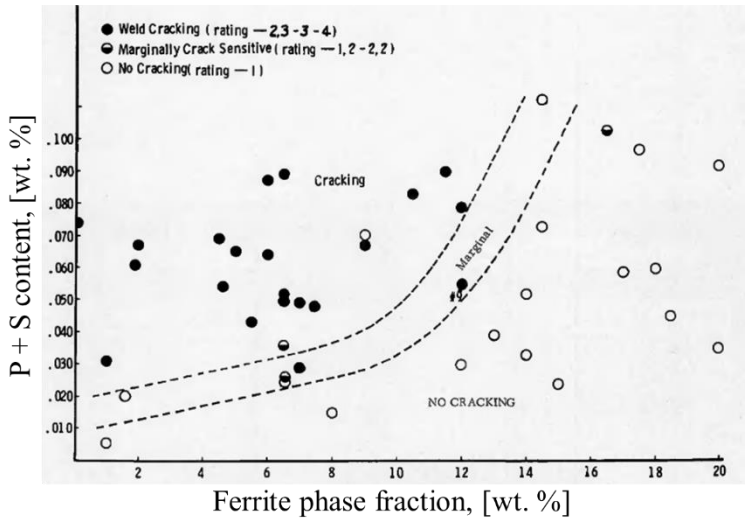

Figure 1-22. Weld test results showing the relationship between phosphorus and sulfur (P+S) content, ferrite phase fraction and weld cracking [Bro78].

However, the addition of manganese makes it possible to avoid the effect of sulfur. The effect of carbon is not so clear. Although carbon causes a widening of the solidification interval, in an Fe-C alloy greater than 0.3%, a high carbon mass composition decreases the risk of hot cracking [Pie07].

Microstructure

The microstructure also influences hot cracking. A fine microstructure decreases the sensitivity to hot cracking by adapting more easily the deformation at the mechanical level. The slip at the grain boundary can thus absorb the deformation [Pie07]. In addition, the microstructure also influences the permeability in the mushy zone, thus the circulation of the liquid in the BTR. The metallurgical phases can also influence hot cracking during solidification. This influence on steels is demonstrated regarding the sulfur and phosphorus elements. These two elements are easily soluble in ferrite but not in austenite: this means that the kinetics of the disappearance

of the liquid at the end of solidification depends on the amount of austenitic phase formed previously: the more the austenitic phase is formed, the more of these impurities of sulfur and phosphorus elements are rejected upon solidification and tend to build up at interdendritic boundaries [Kot93]. Moreover, the contraction corresponding to the transformation of ferrite into austenite generates an additional deformation in the mushy zone modifying the sensitivity to hot cracking [Kos16].

The disorientation angle at grain boundaries also influences the hot cracking during solidification [Wan04] (Figure 1-23 (a)). The result shows that a critical grain boundary angle exists for hot cracking of a two-phase alloy (Al – Cu). Above this angle, the susceptibility to cracking increases due to the decrease in the coalescing temperature leading to a larger BTR, because greater undercooling is required.

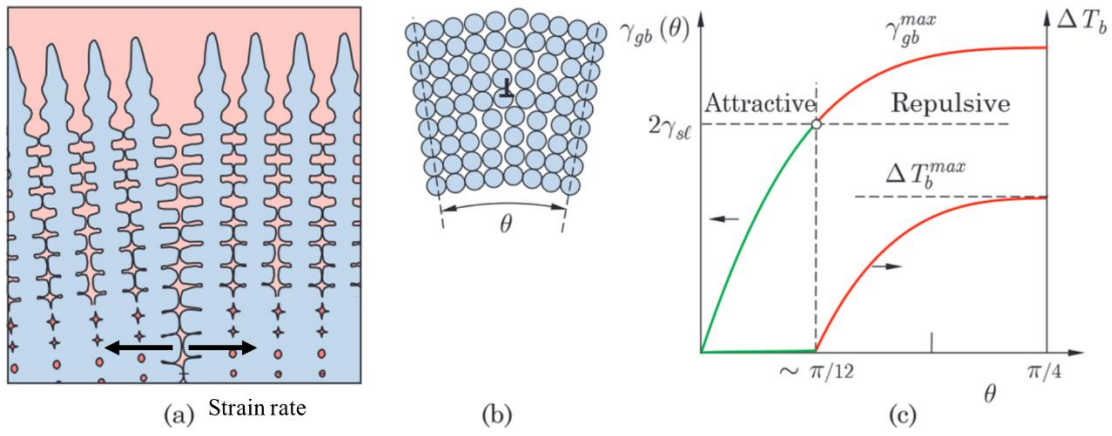

Figure 1-23. (a) Columnar dendritic grains exhibiting a disorientation angle, (b) configuration of the atoms located at the grain boundary after solidification, (c) surface energy of a supercooled grain boundary, as a function of disorientation angle θ. [Dan09]

When the dendritic structure forms at the grain boundary, an interfacial energy $\gamma_{gb}(\theta)$, (Figure 1-23 (c)), related to the angle of the grain boundaries θ is to be overcome. When the angle θ is small, $\gamma_{gb}(\theta) < 2\gamma_{SL}$ (where γ_{SL} is the solid-liquid interface energy), the liquid film is morphologically unstable and the dendrites join as soon as their interfaces reach a distance of interaction, the grain boundaries are "attracted" and the formation of the grain boundary is favorable. When the angle θ increases up to an angle such as $2\gamma_{SL} < \gamma_{gb}(\theta)$, the liquid film remains stable at a critical undercooling of the coalescence $\Delta T_b(\theta)$. The grain boundaries are "pushed back", the formation of grain boundary is unfavorable. $\Delta T_b(\theta)$ is defined as [Dan09]:

$$\Delta T_b(\theta) = \frac{\gamma_{gb}(\theta) - 2\gamma_{SL}}{\Delta S_f \delta} \tag{1-48}$$

with ΔS_f the volume fusion entropy, δ the thickness of the diffusive solid-liquid interface. Increasing the disorientation angle θ leads to an increase in the BTR during solidification, therefore to an increase in the risk of hot cracking.

Wetting angle

The wetting angle at the solid-liquid interface also influences the sensitivity to hot cracking. In fact, this wetting angle can affect the ability of the liquid to spread over the solid surface [Bra00]. This angle α which is related to the interfacial energies by the relationship: $cos\alpha = \gamma_{gb}/\gamma_{SL}$ determines the distribution of the liquid film at the grain interface (Figure 1-24). It thus influences the intergranular mechanical resistance and therefore the sensitivity to hot cracking.

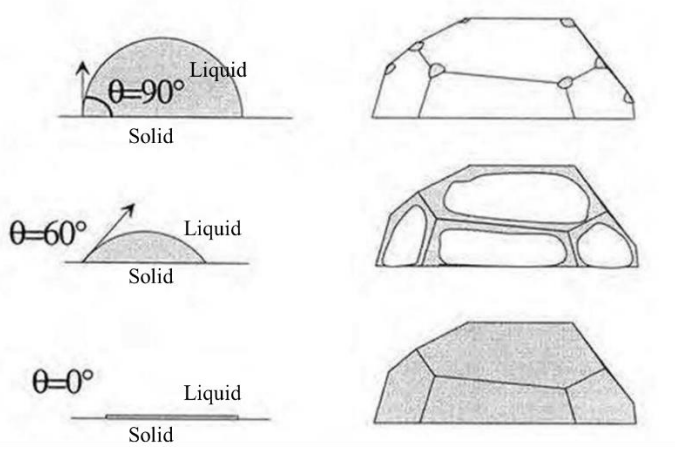

Figure 1-24. Liquid distribution at the solid-liquid interface for various wetting angle [Bra00].

In fact, when the wettability of the liquid on the grains at the end of solidification is low, there are no continuous liquid films between the grains. Isolated liquid droplets ($\alpha = 90°$) are formed and are not likely to participate in the risk of cracking. However, when the wettability is high ($\alpha = 0°$), continuous liquid films between the grains are easily formed, leading to an increased risk of cracking [Nie11].

Thermomechanical stress

The parameters presented above are alloy properties (chemical composition, microstructure, and wetting angle). During the welding process, the thermomechanical stress also plays an important role in the cracking. This stress acting as the driving force depends on the thermomechanical properties of the alloy (expansion rate in particular), the geometry of the part and even more importantly, the process parameters. For example, if the welding speed increases, the cooling speed in the mushy zone will also increase. This can lead to an increase of mechanical stresses and therefore the risk of hot cracking. Likewise, if the power of the heat source increases, the risk of hot cracking also increases (Figure 5).

1.3.2 Hot cracking criterion

Several criteria are presented in the literature to determine the risk of cracking occurrence related to the material and process parameters influencing this phenomenon. The more relevant criterions are presented hereafter.

1.3.2.1 Criterion based on chemical composition

An illustration of such a criterion is presented by deVito [Vit00] on nickel base alloys by carrying out hot cracking tests in GTAW. Phases highly enriched in niobium, magnesium and silicon are observed in crack propagation and within open cracks. They represent the trace of a residual liquid which spread out during the opening of the solid network.
The magnitude and importance of hot cracking phenomenon are possibly characterized by considering the solidification interval, the residual liquid fraction deduced from measurements by microprobe and the length of the mushy zone (function of the thermal gradient and of the solidification speed). The influence of certain chemical elements on hot cracking for this type of alloy can be then appreciated. For example, the niobium content is a determining factor in the development of hot cracking since it increases the liquid fraction over a wide temperature range. This liquid will have a longer time penetrating easily into the openings of the solid network, therefore reducing the risk of hot cracking. Regions 1 and 2 in Figure 1-20 are increased while the region 3 which is susceptible to hot cracking is decreased. In addition, in steels containing silicon, the solidification interval increases strongly and a small fraction of residual liquid can remain over extended temperature intervals, thus increasing the sensitivity to hot cracking. According to such a chemical based criterion, many parameters must therefore be controlled and analyzed. In addition, the combined effects of the elements make the compositional criterion still difficult to implement to control the start of cracking.

1.3.2.2 Criterion based on the evolution of solid fraction

This model proposed by Clyne and David [Cly81] is based on the evolution of the solid fraction g^s with time t and considers the solidification duration. The authors established that hot cracking is due to a fracture of the dendritic network in a vulnerable area (BTR in section 1.3.1.1), where the dendritic arms can be easily separated. The hot cracking sensitivity: HCS *(Hot Cracking Sensitivity)* is defined from a ratio of times: duration necessary for interdendritic separation compared to that necessary to fight against cracking:

$$HCS = \frac{t_v}{t_r} = \frac{t_{g^s=0.99} - t_{g^s=0.9}}{t_{g^s=0.9} - t_{g^s=0.4}} \tag{1-49}$$

with t_v the time spent in the BTR interval, and t_r a normalization time during which the deformations in the mushy zone can be compensated by the liquid feeding (the cracking can be filled by the flow of the liquid). Both times can be determined by a thermal calculation. This model gives good consistency with the experimental results for the Al-Si alloy. However, this model does not reproduce the expected trend when a constant cooling rate is imposed [Dan09].

1.3.2.3 Rappaz, Drezet et Gremaud (RDG) criterion

The RDG criterion proposed by Rappaz, Drezet and Gremaud [Rap99-2] is the most widespread criterion applied in the literature. This model considers in a stationary approach, the combined effect of the problems of liquid supply between the dendrites due to solidification shrinkage and of the positive strain rate perpendicular to the direction of dendritic growth. This criterion leads to the determination of a cavitation pressure linked to the liquid supply to compensate for the solidification shrinkage and the deformation of the solid skeleton. Figure 1-25 shows two grains growing in different crystallographic directions. Figure 1-25 (a) highlights the intergranular deformation perpendicular to the thermal gradient direction, Figure 1-25 (b) presents the depression induced by the solidification shrinkage and the deformation of the skeleton. This model illustrates the deformations suffered by the grains in the direction perpendicular to the dendritic growth and the difficulty of the liquid supply due to the relative permeability of the interdendritic domain.

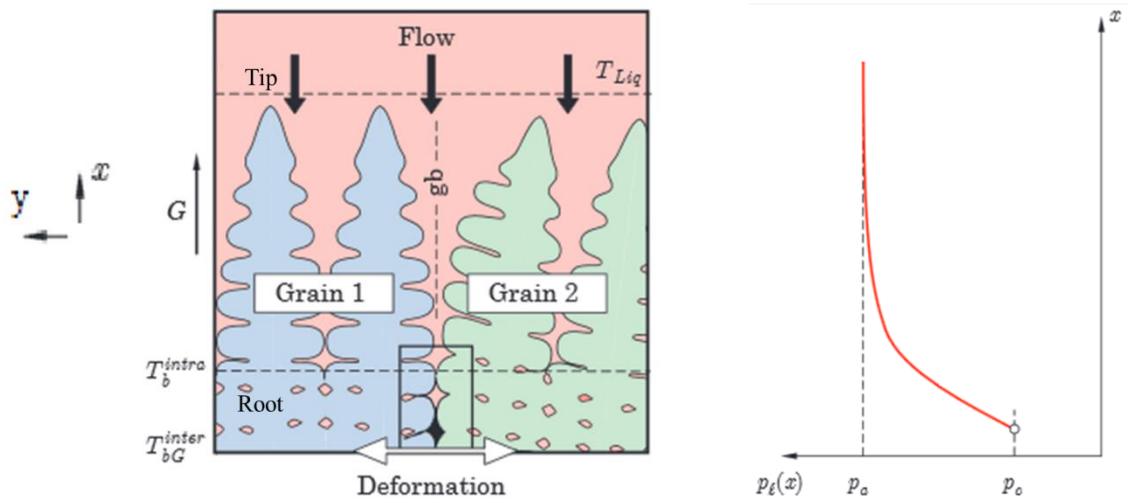

(a) (b)

Figure 1-25. Schema of hot cracking illustrating the RDG criterion induced by liquid depression [Dan09].

This model is based on the mass conservation. The conservation equation expressed with the averaged quantities (noted, $\langle . \rangle$) on a REV of the mushy zone is written:

$$div\langle \rho \boldsymbol{v} \rangle + \frac{\partial}{\partial t}\langle \rho \rangle = 0 \qquad (1\text{-}50)$$

This equation is applied to the columnar solidification zone, as schematically represented in 2D in Figure 1-25 with the following assumptions:

- the fluid flow velocity $\boldsymbol{v_l}$ takes place only in the direction $\boldsymbol{x}$ which is also the solidification direction defined by the thermal gradient $\boldsymbol{G}$,
- the solid displacement $\boldsymbol{v_s}$ takes place only in the $\boldsymbol{y}$ direction,
- the solid fractions g^s and liquid fraction g^l depend only on the x position.

Darcy's law is also used in the form below:

$$g^l v_l = -\frac{K_p}{\eta}\frac{\partial P}{\partial x} \tag{1-51}$$

K_p is a function of $g^s(x)$ and represents the permeability of the skeleton and η is the fluid viscosity. The permeability is usually presented by the Carman-Kozeny model associated to a dendritic structure:

$$K_p = \frac{\lambda_2^2(1-g^s)^3}{180 \times g^{s2}} \tag{1-52}$$

where λ_2 is the secondary dendrite arm spacing.
The pressure drop in the liquid between the tip and the roots of the dendrites can be expressed by:

$$\Delta P = P_{tip} - P_{root} = (1+\beta)\eta \int_0^L \frac{E(x)}{K_p\,(x)}dx + V_T\,\beta\eta \int_0^L \frac{g^l(x)}{K_p\,(x)}dx \tag{1-53}$$

with $\beta = (\rho_s/\rho_l) - 1$, V_T is the speed of isothermal planes. And:

$$E(x) = \int_0^x g^s \dot{\varepsilon} dx \tag{1-54}$$

the cumulated deformation rate on the segment $[0, x]$ of the mushy zone.
The first term on the right-hand side represents the pressure drop due to skeleton deformation between the grains and the second term is related to solidification shrinkage. The cracking criterion is then defined from a critical pressure value P_C called “cavitation pressure” below which a crack can be initiated at the root of the dendrites. The cracking criterion corresponds to the situation where: $P_{root} < P_C$, therefore $\Delta P > \Delta P_C$ with $\Delta P = P_{tip} - P_{root}$, $\Delta P_C = P_{tip} - P_C$.
The temperature T is the variable of integration along the solidification zone varying over the solidification interval $[T_{sol}, T_{liq}]$ of amplitude $\Delta T = T_{liq} - T_{sol}$. It is related to the gradient G. Therefore:

$$\frac{180\eta}{\lambda_2^2 G}\left[(1+\beta)\int_{T_{sol}}^{T_{liq}} \frac{E\,g^{s2}}{(1-g^s)^3}dT + V_T\,\beta\int_0^L \frac{g^{s2}}{(1-g^s)^2}dT\right] > \Delta P_C \tag{1-55}$$

Assuming that the strain rate is homogeneous over the entire length of the solidification zone, (1-55) becomes:

$$\frac{180\eta}{\lambda_2^2 G}\left[A\,\beta\,V_T\,\Delta T + \frac{B(1+\beta)}{G}\dot{\varepsilon}\Delta T^2\right] > \Delta P_C \tag{1-56}$$

with: $A = \frac{1}{\Delta T}\int_{T_s}^{T_l}\frac{g^{s2}}{(1-g^s)^2}dT$, $B = \frac{1}{\Delta T}\int_{T_s}^{T_l}\frac{g^{s2}G_s}{(1-g^s)^3}dT$ and $G_s = \frac{1}{\Delta T}\int_{T_s}^{T} g^s dT$

with the expression (1-56), another formulation of the criterion relating to a critical strain rate $\dot{\varepsilon}_{local}^{max}$ that the mushy zone can withstand is proposed, also depending on the possibility of liquid supply. In other words, cracking occurs if:

$$\dot{\varepsilon} > \frac{G}{\Delta T^2 B}\left[\frac{\Delta P_C \lambda_2^2 G}{180(1+\beta)\eta} - V_T A \Delta T \frac{\beta}{\beta+1}\right] \equiv \dot{\varepsilon}_{local}^{max} \quad (1\text{-}57)$$

The determination of the critical pressure was studied thereafter by Drezet [Dre04] by experimental tests. Its value remains imprecise and therefore the model can be considered as semi empirical. In summary, even if the RDG criterion is the most used in the literature, this criterion is essentially based on the critical deformation rate which does not take into consideration the cumulated deformation [Bel09]. Moreover, the criterion based on a critical strain by considering the cumulated deformation (which will be presented in next section) would show a better coherence with the experimental results for the prediction of hot cracking [Bel16].

1.3.2.4 Criterion based on critical strain

These models consider the ductility drop that takes place in the BTR. The appearance of the defect would be the consequence of a strain reached in the BTR which would exceed the strain required to induce material crack:

$$F_{HC} = \varepsilon_{BTR} - \varepsilon_c \quad (1\text{-}58)$$

where ε_{BTR} is the cumulated local strain in the mushy zone during solidification in the BTR, and ε_c is the critical strain at which the cracks form. From equation (1-58), a positive value of the F_{HC} criterion function indicates cracking due to the excess of the cumulated strain compared to the critical strain. Nagata [Nag90] summarized many experimental results obtained on steels and concluded that the critical strain is related to the strain rate by a power law:

$$\varepsilon_c = A\dot{\varepsilon}^{-m^*} \quad (1\text{-}59)$$

with m^* a constant and A a function of the chemical composition of the steel. In addition, the author introduces a parameter η presenting the thickness of the zone of low ductility. Equation (1-59) becomes:

$$\varepsilon_c = \frac{\phi}{\eta^{n^*}}\left(\frac{\dot{\varepsilon}}{3\times 10^{-4}}\right)^{-m^*} \quad (1\text{-}60)$$

$$\begin{cases} \phi = 0.0602, n^* = 2.13 \; if \; \eta \in [1\text{mm},\ 3\text{mm}] \\ \phi = 0.0077, n^* = 0.258 \; if \; \eta > 3 \text{ mm} \end{cases} \quad (1\text{-}61)$$

Won *et al*. [Won00] proposed a similar expression considering the temperature interval associated with the BTR called hereafter the WYSO criterion:

$$\varepsilon_c = \frac{\phi}{\dot{\varepsilon}^{m^*}{\Delta T_{BTR}}^{n^*}} \quad (1\text{-}62)$$

where the three parameters can be deduced by experimental analyzes carried out on different steels. According to the authors, ϕ = 0.02821, m^* = 0.3131 and n^*= 0.8638.
A great influence of the value of the BTR on the critical strain predicted by the WYSO criterion is studied [Bel09]. Indeed, two problems are raised:

1. The calculation of the solidification path, from which the value of BTR is determined, is clearly critical: the prediction of the criterion is very different depending on the microsegregation model used,
2. The definition of the BTR has an important influence on the value injected into the criterion and can then lead to values very different from the critical limits of theoretical strain.
By considering these two problems, a new criterion based on the WYSO criterion is proposed by Bellet *et al*. [Bel09] called hereafter the CBC criterion:

$$\varepsilon_c = \frac{\varphi}{\dot{\varepsilon}^{m^*} {\Delta T_{BTR}}^{n^*}} \Big/ \left(a e^{b\, w_C} \left(\frac{w_{Mn}}{w_S} \right)^c (w_P)^d \right) \tag{1-63}$$

where a = 736.5, b = 2.195, c = -0.857, and d = 0.851. The w values refer to the percent mass compositions of chemical species. In addition, the calculated BTR value corresponds to the solid fraction interval g^s between 0.85 and 0.97.

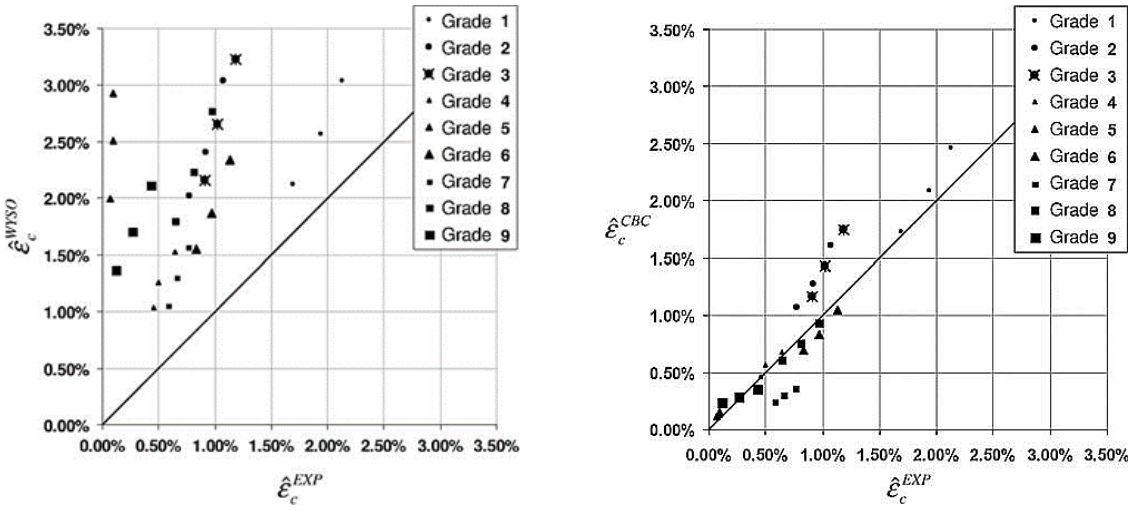

(a) (b)

Figure 1-26. Comparison between the experimental critical strain and the theoretical critical strain (a) WYSO criterion (b) CBC criterion [Bel09].

The Figure 1-26 presents the comparison of the experimental critical strain (obtained by buckling test) and the theoretical critical strain for 9 steel grades, the straight line implies consistency between the simulated result and the experimental result. A better consistency is observed with the CBC criterion. Indeed, this criterion considers mass content of some specific chemical element (carbon, manganese, sulfur and phosphorus) which are known to influence the solidification path and therefore the BTR.

1.3.2.5 Conclusion on hot cracking criterion

Several studies of hot cracking criteria have been reviewed aiming at predicting the appearance of this defect. It appears that it is difficult to correctly and quantitatively reproduce cracking defects observed on an industrial scale. The most relevant models require a good knowledge of

the thermophysical and thermomechanical data of the material at high temperature and in the mushy zone [Bou13].

The phenomenological criteria such as the criterion based on chemical composition, criterion based on fraction solid evolution, and the RDG criterion, offer a good view of the physical phenomena involved and lead to encouraging results. They have the advantage of considering the microstructural aspects of alloys (size of dendrites, thickness of liquid films, etc.). However, their implementation involves knowledge of several material properties in mushy zone which remain difficult to determine. Moreover, they are not always very suitable to be coupled with a finite element modeling method (however some criteria leading to "mechanical" quantities like the criterion RDG (critical strain rate) can be integrated easily into a numerical model).

The mechanical criterion based on critical strain can also lead to quite adequate results. However, they do not consider the supply of liquid to the initiation of cracks and have the major drawback of not being directly linked to the microstructure of the alloy. One weak points of these criterions is that they are generally associated with the use of a specific constitutive law to determine the deformations within the test specimens, but these laws are not always well mastered, more particularly at high temperature. The experimental identification of the parameters of these laws in the mushy zone remains delicate. Nevertheless, the mechanical criterions have the notable advantage to be easily introduced into a numerical simulation code. The CBC criterion proposed by Bellet [Bel09] has the advantage of a high-performance mechanical model that can be easily implemented in a computer code and considers the influence of the most harmful elements (for steels).

In this NEMESIS project, the objective is to predict the appearance of hot cracking by a numerical tool based on a critical strain in a finite element computer code. Therefore, the mechanical criterion based on critical strain/strain rate will be applied in this work.

1.3.3 Hot cracking test in welding

The tests described below address the characterization of the sensitivity to hot cracking in welding. These tests allow classifying the alloys according to their sensitivity, but do not develop a quantitative criterion for each material. Variant parameters are the type of force (constant or progressive), the type of bead (remelting or assembly), the material, the geometry of the test piece and the conditions for carrying out the test. According to the type of test, the temperatures, the forces, the deformations, as well as the length and the number of cracks obtained can be measured.

1.3.3.1 Self-restrained test

In these self-restrained tests, the origin of the stresses is the shrinkage of the metal.

Houldcroft Test

The Houldcroft test is proposed by [Hou55] to provide a simple test to assess the sensitivity to hot cracking of different alloys. A thin parallelepipedal specimen is used to design the test. In order to observe the stop of the crack initiated at the start of the bead, stresses in the specimen

should be modified. In the Houldcroft test, this is achieved by making grooves in the specimen (Figure 1-27(b)).

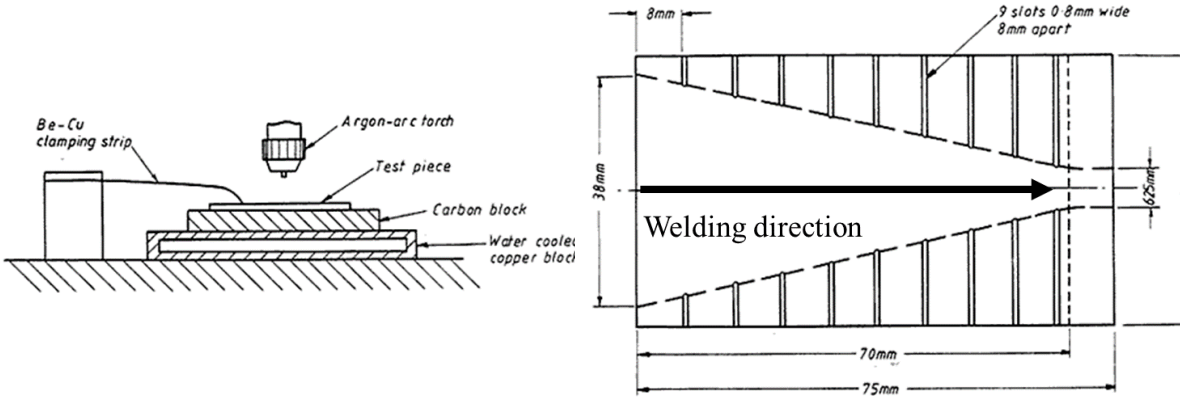

(a) (b)

Figure 1-27. Experiment set up (a) and specimen dimensions (b) of the Houldcroft test [Hou55].

The entire device sits on a carbon block and is held in position with a clip (Figure 1-27(a)). The bead is initiated from the left edge and advances to the right (Figure 1-27(b)). One of the advantages of the Houldcroft test, like all other self-restrained tests, is its significantly lower cost than tests requiring special installations. It is therefore simple to set up and provides a useful result. However, Houldcroft noticed poor reproducibility in his tests. A significant variation in the length of the crack is observed and reduces the interest of the results obtained [Hou55].

Taper shape cracking test

The taper shape cracking test is proposed by [Mat82] to study the crack susceptibility in the electron-beam welding. This test is based on the inverted Houldcroft test.

The specimen (Figure 1-28) is welded from the smallest width (W_S) to the largest width (W_F). The dimensions of the test piece are defined such that the hot cracking defect is observed at the start of the bead and stops for a width W_C with $W_S < W_C < W_F$. This width W_C is called the critical width. The authors found that a slight decrease in the thickness of the specimen in the area where the bead begins can exacerbate the sensitivity to hot cracking and thus increase the chances of observing the defect at the start of the bead.

In the taper shape cracking test, the influence of melt pool dimensions on the sensitivity to hot cracking was observed: for a melt pool with large width (5mm), the crack lengths are greater than in that of smaller width (3.7mm) [Mat82].

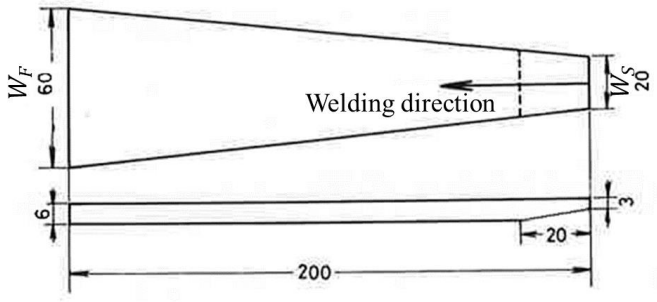

Figure 1-28. Specimen dimensions of taper shape cracking test [Mat82].

Joining Welding Research Institute (JWRI) Test

The JWRI test (named after the Joining Welding Research Institute in Osaka, Japan) consists in making a fusion line emerging on a flat specimen restrained at one edge while the other edge is free (Figure 1-29).

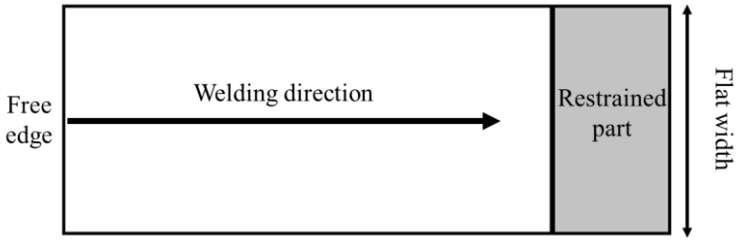

Figure 1-29. Illustration of JWRI test specimen.

The initiation of the crack is on the free edge of the specimen. The longitudinal cracking of the bead then propagates and is then stopped due to the more favorable deformation state created by the clamping. The parameters of the test are the dimensions of the specimen and the welding conditions (ex. power of thermal source or welding speed). It has been found that the more the width of the specimen increases, the less the crack propagates. Besides, the welding speed has also an influence on hot cracking: when the welding speed is low, the appearance of the hot cracking defect is not clear regardless of the width of the specimen [Car95]. This test can therefore be simulated to estimate the distribution of strains by a finite element modeling thanks to the simple geometry of the specimens used and the easily modeled boundary conditions of the problem [Nie11].

1.3.3.2 Test with external force

Varestraint test

The Varestraint test is widely used to classify filler materials for their susceptibility to hot cracking. This test makes it possible to generate hot cracking of a material regardless of its

sensitivity to this phenomenon by imposing a suitable strain rate. The experimental set-up consists of a folding die block on which a parallelepipedal test piece is held.

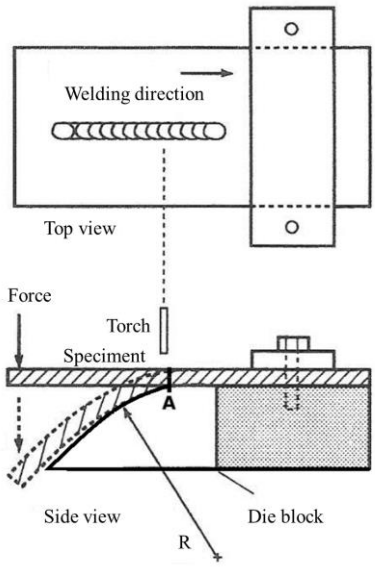

Figure 1-30. Illustration of Varestraint test set up [Wis09].

A GTAW fusion line is made on the upper face of the specimen along its symmetry axis. Welding takes place from the free edge of the specimen to the restrained edge. When the front face of the liquid zone reaches the mark A, the specimen is bent against the cylindrical part of the die block (force F applied to the free end of the specimen). The folding time is adjustable. The radius of curvature of the die block is chosen according to the average target deformation. The tensile deformation imposed on the face is determined according to the geometry of the system:

$$\varepsilon_{max} = \frac{E_p}{2R + E_p} \tag{1-64}$$

with E_p the thickness of the specimen and R the radius of curvature of the die block.
The imposed deformation can thus be modified by changing the thickness of the specimen or the radius of curvature of the die block. The characterization of the hot cracking sensitivity is done by measuring the number of cracks, the cumulated crack length, and/or the maximum crack length. A comparison between the different materials can thus be made. However, the Varestraint test is not easy to be achieved in simulation in particular because of the representation of the contacts with the die block (ex. heat transfer, stress and strain on an evolving surface) and the control of the deformation speed. A variant of this test exists in the literature, named the Trans-varestraint test. In this test, the bending is done in the transverse direction to the welding direction [Wei06].

Means of In-Situ Observation and measurement (MISO) test

This test is proposed by [Mat83] using an observation technique (high speed camera and microscope) coupled with a tensile hot cracking test Figure 1-31(a). A GTAW fusion line is achieved on a specimen with dimensions specified in Figure 1-31 (b). The holes placed on either side of the specimen allow the traction of the sample. During welding, a tensile stress is applied when the weld bead (dotted line in Figure 1-31 (b)) is halfway to the edges of the specimen. This approach makes it possible to create a single crack in the middle of the bead (hot cracking of solidification). Images of the specimen are taken throughout welding. Analysis of these images can determine the strain and strain rate.

A great advantage of the MISO test is the possibility of observing the initiation of cracks in real time (in-situ test), which makes it possible to determine the strain and deduce the strain rate with high precision compared to most other tests ex-situ where these important values are roughly determined. However, the MISO test demands a good performance of the image treatment methods and a good quality of images which limit the choice of materials. In addition, a problem remains to be discussed concerns the choice of reference points to calculate the critical cracking strain: different choices give a large range of possible results and it is not easy to determine them according to a simple criterion.

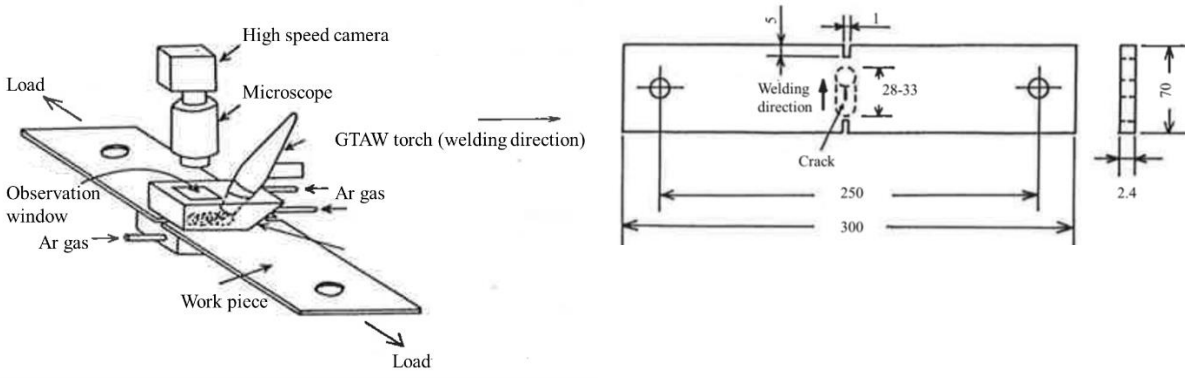

(a) (b)

Figure 1-31. Experimental set up (a) and specimen dimension (b) of MISO test [Mat83].

1.4 Conclusions

During welding process, melting of the materials occurs in the fusion zone leading thereafter to a solidification domain during cooling. The grains develop from the partially melted grains previously formed in an epitaxial mechanism. The grains growth along their preferred growth directions leading to grain competition. As shown in Figure 1-10, the final grain structure is significantly affected by the temperature gradient caused by the moving heat source and cooling conditions.

Several numerical methods are proposed in the literature to model the dendrite growth in the melt pool. Methods developed at micro scale (ex. the front tracking method, the phase field

method) focus on the solid-liquid interface evolution for the dendrites. However, it is difficult for these models to predict the whole welding microstructure due to the computation costs and simulation durations. Therefore, a mesoscale method should be applied in the welding process to model the microstructure evolution, as the CAFE method detailed in section 1.2.8.
Hot cracking is one of the common defects observed in welding. The origin of hot cracking is a coupling between a susceptible temperature zone (BTR) as presented in section 1.3.1.1 and the thermal stress (Figure 1-21) developed during solidification. Several criteria are proposed in the literature to predict the risk of hot cracking. Among all these criterions, the mechanical criterions based on critical strain/strain rate can be applied to predict the occurrence of this defect by a numerical tool in a finite element computer code.
In conclusion, the NEMESIS project has two objectives in the modeling of welding processes. On the one hand, the CAFE approach will be applied to simulate the microstructure evolution and the results will be compared with the experimental observations of LMGC and ICB laboratories. Reliable microstructure will be thereafter provided to NEMESIS partners (CEA and EDF R&D) for NDT modeling. On the other hand, the hot cracking risk during the welding process will be also estimated based on the WYSO criterion with the stress and strain calculated by a finite element solid mechanic solver (presented in chapter 5). The grain structure, considering growth direction of grains, will be also introduced in the WYSO criterion to analyze its influence on the prediction of hot cracking occurrence.

1.5 French summary

Durant le procédé de soudage, un domaine de fusion apparait, au niveau de la source de chaleur, avant qu'une étape de solidification n'intervienne, liée au refroidissement du métal. La croissance des grains pendant l'étape de solidification débute à partir des grains partiellement fondus dans un mécanisme de croissance épitaxial. Les grains se développent le long de leurs directions de croissance privilégiées, ce qui entraîne une compétition entre les grains, comme montré dans la Figure 1-10. La microstructure finale est fonction du gradient de température lié à la source de chaleur en mouvement, et aux conditions de refroidissement.
Plusieurs méthodes numériques sont proposées dans la littérature pour modéliser la croissance des dendrites. Les méthodes à l'échelle micro, tels le suivi de front ou le champ de phase, s'attachent à suivre l'évolution de l'interface solide-liquide aux frontières des dendrites. Cependant, la prédiction de la microstructure à l'échelle du procédé de soudage est rendue difficile par ces méthodes en raison des coûts et durée de calcul. Par conséquent, une méthode à l'échelle méso doit être appliquée dans ces procédés pour modéliser l'évolution de la microstructure sur l'ensemble du domaine d'intérêt, telle la méthode CAFE comme expliqué dans la section 1.2.6.
La fissuration à chaud est l'un des défauts les plus couramment observés en soudage. Elle tire son origine de l'existence d'une zone de température 'fragile' (BTR), sensible à la fissuration, comme présenté dans la section 1.3.1.1, et du développement d'une contrainte thermique (Figure 1-21) pendant la solidification. Plusieurs critères sont proposés dans la littérature pour prédire le risque de fissuration à chaud. Parmi tous ces critères, ceux, mécaniques, basés sur la déformation cumulée au regard d'un taux de déformation critique peuvent être appliqués pour

prédire la fissuration à chaud par le développement et l’exploitation d’un code de calcul éléments finis.
En conclusion, dans le projet NEMESIS, d'une part, la méthode CAFE sera appliquée pour simuler l'évolution de la microstructure et les résultats de la modélisation seront comparés aux observations expérimentales afin de fournir, par la suite, une microstructure fiable aux partenaires du projet pour la modélisation du contrôle non destructif (CND) et de l’interaction ondes - structures. D'autre part, le risque de fissuration à chaud pendant le soudage sera également déterminé, basé sur le critère WYSO, avec les contraintes et les déformations calculées par un solveur éléments finis de mécanique solide (présenté dans le chapitre 5). Les orientations et directions de croissance privilégiées du grain seront également considérées dans le critère WYSO amélioré, proposé par la suite, pour analyser son influence sur la prédiction du risque de fissuration à chaud.

2 Multiphysical CAFE modeling of grain structure and fluid flow in welding

2.1 Presentation of CAFE model

As mentioned in section 1.2.1, the CAFE model is based on the coupling of several approaches which are implemented at different scales. Carozzani [Car11, Car12] has developed the use of two meshes in the CAFE model referring to FE mesh and CA mesh respectively. Scale and mesh concepts used in the CAFE model are summarized below to clarify the presentation:

- Figure 2-1 (a)
  Blue : FE mesh: the adaptive mesh for the Finite Element resolution of the average conservation equations,
- Orange : FE element E^{FE}: element in FE mesh;
- Black : FE node n^{FE}: node in FE mesh;

- Figure 2-1 (b)
- Red: CA mesh: the fixed mesh for Cellular Automaton resolution to transport information between FE mesh and CA grid;
- Green: CA element E^{CA}: element in CA mesh;
- Black: CA node n^{CA}: node in CA mesh;

- Figure 2-1 (d)
- CA grid: grid made of regular lattice of cells;

- Figure 2-1 (c)
- CA cell: cell in the CA grid in pink.

As showed in Figure 2-1 (a) and (b), two meshes are used in the CAFE model leading to the use of computational resource to transport information between these meshes, however, the advantages of the use of two meshes are presented below:

- Firstly, the use of a restricted CA domain. As shown in Figure 2-1 (a) and (b), the CA mesh is smaller than the FE mesh as the welded domain is usually smaller than the workpiece. In the simulation, the global conservation equations of mass, momentum, and energy are solved on the FE mesh which corresponds usually to the size of the workpiece. The CA mesh is used to generate the CA grid (Figure 2-1 (d)) and compute the grain structure on a reduced domain corresponding to the actual welding dimension.
- Secondly, the use of two meshes allows the adaptative remeshing on the FE mesh to optimize the resolution of global conservation equations while the CA mesh is fixed. The CA mesh is dedicated to field transportation as temperature from the FE mesh to the CA grid. No equation resolution is achieved onto the CA mesh. Besides, as the CA grid is generated on the CA mesh, the fixed CA mesh ensures a unique CA grid during the simulation and a fixed location of cells inside CA elements.

All these advantages aiming at reducing the computation time and resource can totally compensate the transportation time of information between meshes and, at the same time, improve the simulation efficiency.

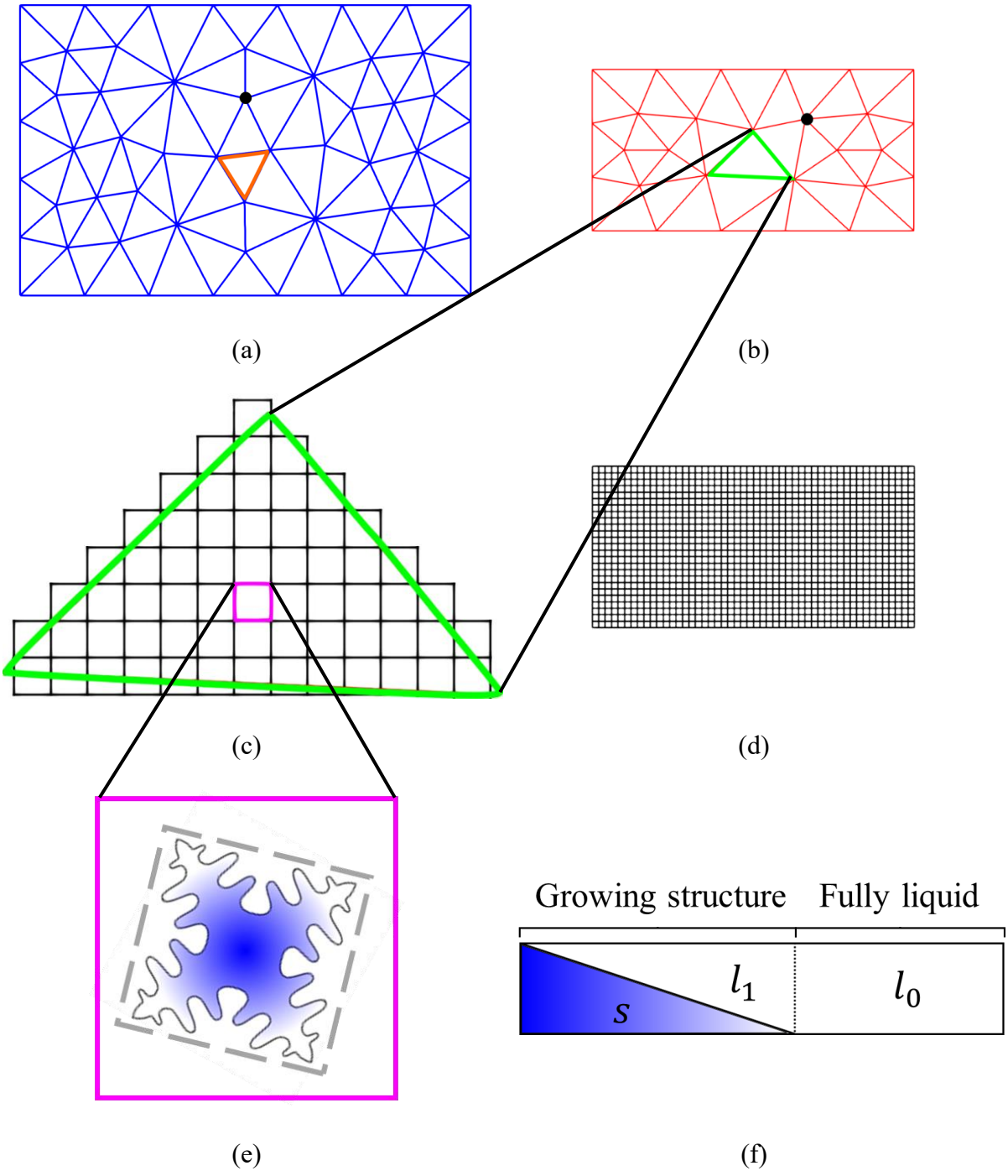

Figure 2-1. Different scales of CAFE modeling according to [Car13] (a) FE mesh for the FE model, a FE element in orange, a FE node in black (b) CA mesh for the CA model, a CA element in green, a CA node in black (c) CA grid on CA mesh, (d) global view of CA grid generated and superimposed on the CA mesh, (e) Growth envelope of the dendritic grain in a CA cell, (f) phases considered in the solidification.

2.2 FE model

2.2.1 Level-Set method

The Level-Set (LS) method is firstly introduced by Osher [Osh88] in order to follow moving interfaces. At CEMEF, thanks to the preliminary activities of Hamide [Ham08] and Desmaison [Des13], the LS method can be applied to the welding process to track the metal/gas interface during the process.

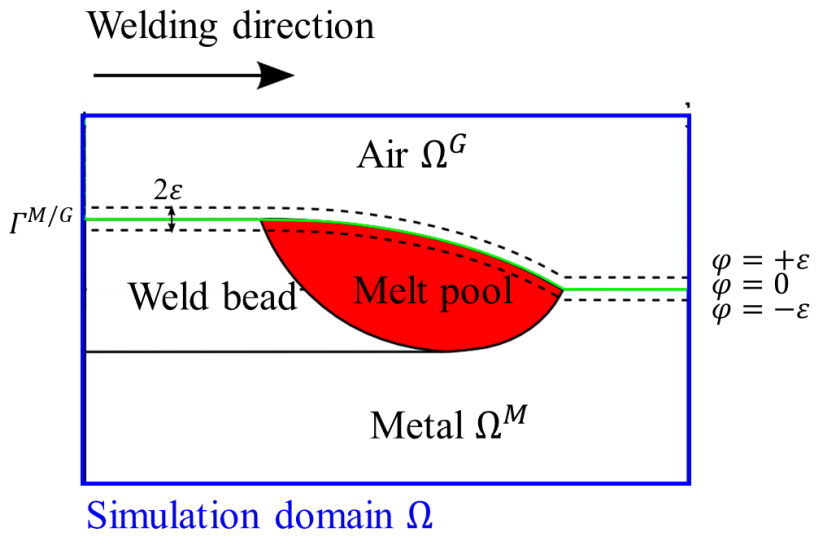

Figure 2-2. Modeling schematic of 2D GMAW process with the LS method tracking the metal/gas interface.

As presented in Figure 2-2, the global simulation domain (Ω) contains the metal subdomain (Ω^M) (workpiece) and the surrounding gas subdomain (Ω^G). Besides, a distance function, namely the level set function, φ is defined on Ω.
These metal and gas subdomains are separated by the metal/gas interface ($\Gamma^{M/G}$, green in Figure 2-2) defined as distance function $\varphi = 0$. At any time of the process, the value of φ for a given point B is defined as the signed distance between B and the metal/gas interface. In the present work, negative values of φ are assigned to the points in the metal while positive values correspond to those in the gas, presented as:

$$\begin{cases} \varphi = -d(x) & \text{if } B \in \Omega^M \\ \varphi = 0 & \text{if } B \in \Gamma^{M/G} \\ \varphi = d(x) & \text{if } B \in \Omega^G \end{cases} \quad (2\text{-}1)$$

where $d(x)$ refers to the geometric distance between B and $\Gamma^{M/G}$.
During welding simulation, the iso level-set $\varphi = 0$ follows the metal/gas interface driven by the fluid flow velocity $\widehat{\boldsymbol{v}^{\boldsymbol{F}}}$ determined by solving the mass and momentum conservation equations (details of expression $\widehat{\boldsymbol{v}^{\boldsymbol{F}}}$ will be presented in section 2.2.5), the transport equation is solved to update the level set function:

$$\frac{\partial \varphi}{\partial t} + \widehat{\boldsymbol{v}^{\boldsymbol{F}}} \cdot \nabla \varphi = 0 \qquad (2\text{-}2)$$

However, such transport does not preserve the eikonal property (unitary gradient) of the level set function. Among other, Shakoor *et al.* [Sha15] have developed a reinitialization method based on the geometrical computation of the distance function between each FE node and the transported iso level-set associated to $\varphi = 0$. It is performed after each transportation step of the level set function. Besides, a smoothed Heaviside function $\mathcal{H}^M(\varphi)$ related to the metal subdomain defined over a distance 2ε (Figure 2-2) is introduced to vary the material properties along the interface. $\mathcal{H}^M(\varphi)$ continuously evolves from 1 in the metal subdomain, for $\varphi < -\varepsilon$, to0 in the gas subdomain, for $\varphi > +\varepsilon$:

$$\mathcal{H}^M(\varphi) = \begin{cases} 1 & \text{if } \varphi < -\varepsilon \\ \frac{1}{2}\left(1 + \frac{\varphi}{\varepsilon} + \frac{1}{\pi}\sin\left(\frac{\pi\varphi}{\varepsilon}\right)\right) & \text{if } |\varphi| \leq +\varepsilon \\ 0 & \text{if } \varphi > +\varepsilon \end{cases} \qquad (2\text{-}3)$$

Hence, $\mathcal{H}^M$ and $\mathcal{H}^G = 1 - \mathcal{H}^M$ are presence functions in the metal and gas subdomains, respectively, with φ-dependencies dropped for simplicity. One then directly generalizes a property ξ at any point of the simulation domain by the arithmetic mean $\hat{\xi}$:

$$\hat{\xi} = \mathcal{H}^M(\varphi)\xi^M + (1 - \mathcal{H}^M(\varphi))\xi^G \qquad (2\text{-}4)$$

where ξ^M and ξ^G denote the same properties respectively associated to the metal and gas subdomains. The Dirac function δ can be then deduced by the derivation of the Heaviside function:

$$\delta(\varphi) = \begin{cases} 0 & \text{if } \varphi < -\varepsilon \\ \frac{1}{2\varepsilon}\left(1 + \cos\left(\frac{\pi\varphi}{\varepsilon}\right)\right) & \text{if } |\varphi| \leq +\varepsilon \\ 0 & \text{if } \varphi > +\varepsilon \end{cases} \qquad (2\text{-}5)$$

Figure 2-3 presents the evolution of Heaviside function $\mathcal{H}^M(\varphi)$ and the Dirac function δ.

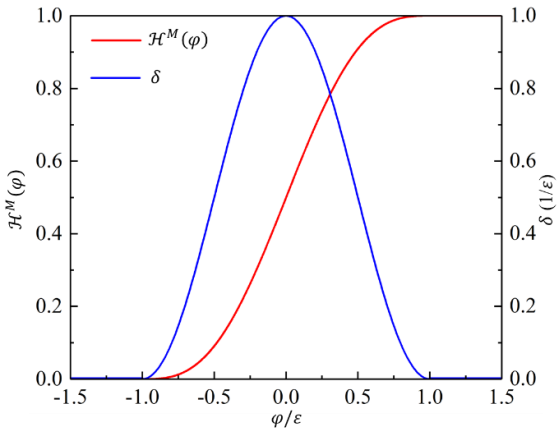

Figure 2-3. Heaviside function and the Dirac function.

By applying the LS method, an interface is assumed and replaced by the position of the level set function $\varphi = 0$ in the mesh. Consequently, in order to apply surface conditions at the metal/gas interface, a Continuum Surface Force (CSF) method [Bra92] is carried out to transform these surface conditions into volumetric conditions:

$$\int_{\Gamma^{M/G}} F\, dS = \int_{\Omega} F\delta\, dV \tag{2-6}$$

where F present an interfacial field (scalar field or vector field) imposed at the metal/gas interface. The equivalent volumetric contribution $F\ \delta$ added to the whole simulation domain Ω thus only acts around the boundary $\Gamma^{M/G}$ to impose the nominal surface field F.

2.2.2 Adaptive remeshing method

The quality of mesh is of prime importance in the finite element resolution. For example, meshes should be fine enough in the transition zone where gradients of material properties across the metal/gas interface are very high and may derive severe numerical oscillations [Saa16]. Besides, the melt pool and mushy zone should also be refined to provide precise estimation of the solution field of fluid mechanical equations. All the potential zone of melt pool and mush zone should be meshed finely in addition. For a single pass welding with a weld bead of dimension $50 \times 5 \times 5\ \text{mm}^3$ with mesh size 0.05 mm, the number of meshes would be 10 million only for the weld bead, and the total number of elements of the global domain would be larger. Therefore, the definition of a mesh strategy allowing the adapted remeshing during the simulation is required to save calculation time and resources. In this work, an error based remeshing method developed at CEMEF by Coupez *et al*. [Cou11, Cou13] is applied to achieve the adaptive remeshing. It should be noted that the adaptive remeshing is only applied on the FE mesh.

2.2.2.1 Error based remeshing method

The mesh size is controlled by the metric tensor $\mathcal{M}_i$ defined on any node *i* of the FE mesh. This tensor $\mathcal{M}_i$ is symmetric, positive thus diagonalizable in an orthonormal basis ($\boldsymbol{e}_1$, $\boldsymbol{e}_2$, $\boldsymbol{e}_3$) of the 3D Euclidean space $\mathbb{R}^3$, and its eigenvalues are related explicitly to the mesh sizes required in the directions associated to eigenvectors,

$$\boldsymbol{\mathcal{M}}_i = \mathcal{R}^T \begin{pmatrix} \frac{1}{h_{\boldsymbol{e}_1}^2} & & \\ & \frac{1}{h_{\boldsymbol{e}_2}^2} & \\ & & \frac{1}{h_{\boldsymbol{e}_3}^2} \end{pmatrix} \mathcal{R} \tag{2-7}$$

$\mathcal{R}$ is the rotation matrix corresponding to the change of the reference frame to diagonalize $\boldsymbol{\mathcal{M}}_i$. $h_{\boldsymbol{e}_1}$, $h_{\boldsymbol{e}_2}$ and $h_{\boldsymbol{e}_3}$ are the desired mesh size in the direction of $\boldsymbol{e}_1$, $\boldsymbol{e}_2$ and $\boldsymbol{e}_3$ respectively. The

method is based on the definition of the metric for which the length of the edge vector $\boldsymbol{x}_{ij}$ connecting the nodes *i* and *j* must be unitary:

$$\left\|\boldsymbol{x}_{ij}\right\|_{\boldsymbol{\mathcal{M}}_i} = \sqrt{\boldsymbol{x}_{ij}{}^T \boldsymbol{\mathcal{M}}_i \boldsymbol{x}_{ij}} = 1 \tag{2-8}$$

Geometrically, to satisfy equation (2-8), all the edge connected to the node *i* should be located in an ellipsoid (3D) with axes of length $h_{\boldsymbol{e}_1}$, $h_{\boldsymbol{e}_2}$ and $h_{\boldsymbol{e}_3}$. Therefore, the definition of metric $\boldsymbol{\mathcal{M}}_i$ is important to define the mesh size of FE mesh during the simulation to provide a good resolution of equations. An optical metric at node *i* can be obtained by minimizing the following function:

$$\boldsymbol{\mathcal{M}}_i = arg\min_{\boldsymbol{\mathcal{M}}} \sum_{j\in\Gamma(i)} \left(\boldsymbol{X}_{ij}{}^T \boldsymbol{\mathcal{M}} \boldsymbol{X}_{ij} - 1\right)^2 \tag{2-9}$$

where $\boldsymbol{X}_{ij}$ is the desired edge vector between the node *i* and *j*. The metric tensor at the node *i* can be defined as [Cou11]:

$$\begin{aligned} \boldsymbol{\mathcal{M}}_i &= \frac{1}{d_{NA}} \left(\frac{1}{|\Gamma(i)|} \sum_{j\in\Gamma(i)} \boldsymbol{X}_{ij} \otimes \boldsymbol{X}_{ij} \right)^{-1} \\ &= \frac{1}{d_{NA}} \left(\frac{1}{|\Gamma(i)|} \sum\nolimits_{j\in\Gamma(i)} s_{ij}^2 \boldsymbol{x}_{ij} \otimes \boldsymbol{x}_{ij} \right)^{-1} \end{aligned} \tag{2-10}$$

with d_{NA} is the number of non-aligned edge vectors related to node *i*, $\Gamma(i)$ denotes the set of nodes connected to node *i* and $|\Gamma(i)|$ is the cardinality of this set. $s_{ij} = \left\|\boldsymbol{X}_{ij}\right\| / \left\|\boldsymbol{x}_{ij}\right\|$ is the edge stretching factor. It is defined with a total error e_{tot} and the local error e_{ij}:

$$s_{ij} = min\left(\left(\frac{e_{tot}}{e_{ij}} \right)^{\frac{1}{p+2}}, \frac{\left|\boldsymbol{X}_{ij}\right|}{h_{min}} \right) \tag{2-11}$$

where $p = 1.5$ is a constant coefficient and h_{min} the minimal mesh size defined by the user. As shown by the definition of s_{ij}, the metric is correctly estimated when $s_{ij} = 1$. The total error of estimation e_{tot} is then calculated as:

$$e_{tot} = \left(\frac{\sum_1^{NbN} \sum_{j\in\Gamma(i)} e_{ij}{}^{\frac{p}{p+2}}}{D(D-1)NbE} \right)^{\frac{p+2}{p}} \tag{2-12}$$

with D the geometry dimension, NbN the number of nodes and NbE the number of elements contained in the mesh. Considering a scalar field f, f_i and f_j present the value of f at node *i* and *j*. The gradient ∇f is constant per element and discontinuous from element to element. The gradient field $\boldsymbol{G}$ at node *i* that minimizes the total error of edges connected corresponds to minimizing the following function:

$$\boldsymbol{G}_i = arg\,\min_{G}\left(\sum_{j\in\Gamma(i)}\left|(\boldsymbol{G}-\nabla f)\cdot\boldsymbol{X}_{ij}\right|^2\right) \tag{2-13}$$

The local edge error e_{ij} is defined as:

$$e_{ij} = max\left(\left|\boldsymbol{G}_{ij}\cdot\boldsymbol{x}_{ij}\right|, \epsilon_{err}\left\|\boldsymbol{x}_{ij}\right\|^2\right) \tag{2-14}$$

with $\boldsymbol{G}_{ij} = \boldsymbol{G}_i - \boldsymbol{G}_j$ present the gradient difference. ϵ_{err} is a coefficient defined by the user and is also equivalent to the Hessian matrix (second derivative). Figure 2-4 shows the influence of this coefficient ϵ_{err} on the mesh in a chamfer type sample geometry.

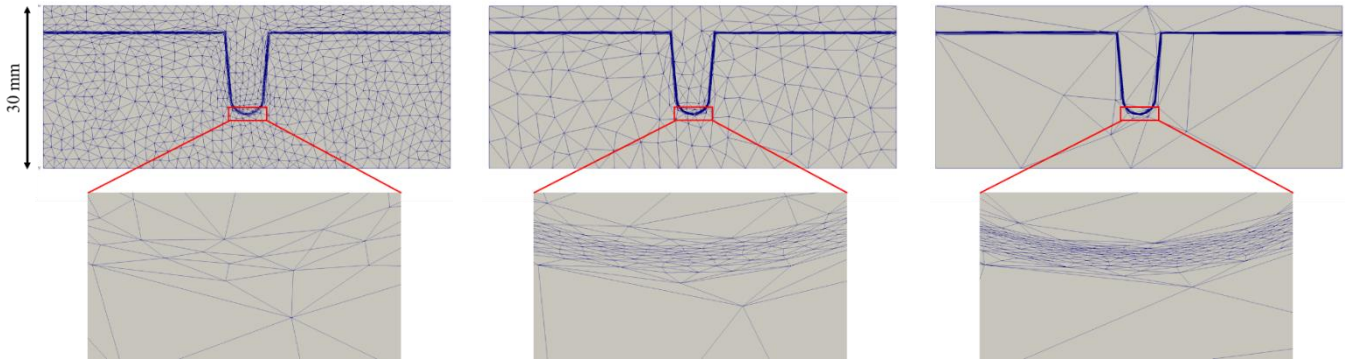

(a) (b) (c)

Figure 2-4. Mesh adaptation in a chamfer. Half thickness of transition zone 0.1 mm. This function is used for the mesh adaptation with ϵ_{err} = (a) 1, (b) 0.01, and (c) 0.001. The total element number NbE is defined at 500 000 and the final mesh element number is (a) 481 862, (b) 436 636, and (c) 425 661. The minimum element size h_{min} is defined at 0.01 mm.

As shown in Figure 2-4, with the same total element number NbE and the minimum element size h_{min}: the lower the coefficient ϵ_{err}, the more refined the meshes in the interested zone (inside the transition zone presented in Figure 2-4). And contrarily, the meshes are coarsed out of the interest zone. Thus, ϵ_{err} is an important coefficient to be defined during the simulation. In the simulation of welding process, the fields considered in the error based remeshing method are:

- Heaviside function to ensure the transition of physical properties at metal/gas interface;
- Interface liquid/solid in the metal in order to track the melt pool shape and the mushy zone;
- Temperature to assure fine resolution at position associated to important temperature gradient.

2.2.3 Intersection of metrics

As presented in Figure 2-4, the requirement of fine meshes in the zone of interest can sometimes introduce coarse mesh outside. To avoid too coarse global meshes, the intersection method between metrics is available. This method aims at finding the eigenvalues of two metrics in a

common basis. Considering two metrics $\boldsymbol{\mathcal{M}}_1$ and $\boldsymbol{\mathcal{M}}_2$, the common basis $(\boldsymbol{e}_1, \boldsymbol{e}_2, \boldsymbol{e}_3)$ can be obtained by the diagonalization of $\boldsymbol{\mathcal{M}}_1{}^{-1}\boldsymbol{\mathcal{M}}_2$. Then these two metrics can be written as:

$$\boldsymbol{\mathcal{M}}_1 = \mathcal{P}^T \begin{pmatrix} \lambda_1 & 0 & 0 \\ 0 & \lambda_2 & 0 \\ 0 & 0 & \lambda_3 \end{pmatrix} \mathcal{P}, \boldsymbol{\mathcal{M}}_2 = \mathcal{P}^T \begin{pmatrix} \mu_1 & 0 & 0 \\ 0 & \mu_2 & 0 \\ 0 & 0 & \mu_3 \end{pmatrix} \mathcal{P} \tag{2-15}$$

where $\lambda_i = \boldsymbol{e}_i{}^T \boldsymbol{\mathcal{M}}_1 \boldsymbol{e}_i$ and $\mu_i = \boldsymbol{e}_i{}^T \boldsymbol{\mathcal{M}}_2 \boldsymbol{e}_i$, $i = (1,2,3)$ and $\mathcal{P} = (\boldsymbol{e}_1, \boldsymbol{e}_2, \boldsymbol{e}_3)$. Then the intersection of these two metrics are:

$$\boldsymbol{\mathcal{M}}_1 \cap \boldsymbol{\mathcal{M}}_2 = \mathcal{P} \begin{pmatrix} max(\lambda_1, \mu_1) & 0 & 0 \\ 0 & max(\lambda_2, \mu_2) & 0 \\ 0 & 0 & max(\lambda_3, \mu_3) \end{pmatrix} \mathcal{P}^T \tag{2-16}$$

2.2.4 Mass correction strategy

When using the Level Set method, the reinitialization of the distance function after transport (section 2.2.1) may cause mass deviations by the introduction of errors in nodes distance function in the neighborhood of the interface [Sha15]. Besides, with the need of regular remeshing strategy, the conversation of mass is more difficult [Che18]. Therefore, a mass correction method proposed by Zhang and Queva [Zha20, Que21] is used at each time step to ensure mass conservation. At each time step, the current mass of the metal can be expressed as:

$$m^M = \int_\Omega \mathcal{H}^M \langle \rho \rangle^M dV \tag{2-17}$$

As the theoretical mass m^{theo} at each time step is always known, the current mass error is $\delta m = m^M - m^{theo}$. As current mass depends from the Heaviside $\mathcal{H}^M$, the mass error δm can be then corrected by adjusting the position of a restrained part Γ_{corr} (normally for the elements with average temperature above the solidus, presented as $H(T - T_S) = 1$) of the metal/gas interface $\Gamma^{M/G}$ by a uniform distance δ_{LS} through modifying the distance function φ artificially as follows:

$$\begin{cases} \delta_{LS} = \dfrac{\delta m}{\int_{\Gamma_{corr}} \langle \rho \rangle^M dS} \\ \varphi^{new} = \varphi^{old} - H(T - T_S)\delta_{LS} \end{cases} \tag{2-18}$$

The second equation expresses that the correction of distance function is restricted to elements with average temperature above the solidus, in other words, at the liquid/gas and mushy zone/gas interface. Figure 2-5 gives a detailed illustration of the calculation of Γ_{corr}. For an element located at the metal/gas interface with average temperature above the solidus, as shown in Figure 2-5, the nodes of the element present both positive and negative values of distance function. The intersection interface Γ_e of this element by the metal/gas interface $\Gamma^{M/G}$(presented as $\varphi = 0$), is then identified and easily calculated. The total restricted surface Γ_{corr} is the sum of all Γ_e calculated at all selected tetrahedral elements: $\Gamma_{corr} = \sum_e \Gamma_e$.

The mass correction strategy is a pure numerical treatment to fix the mass conservation deviation caused by the transport of level set function and the remeshing. In fact, in the welding simulations presented in the next chapters, the correction distance δ_{LS} is usually about 1% (magnitude of 10^{-3} mm) of the half thickness of the transition zone (magnitude of 10^{-1} mm). Therefore, the influence of the application of this mass correction method is insignificant to the global simulation results while keeping a good metal mass conservation.

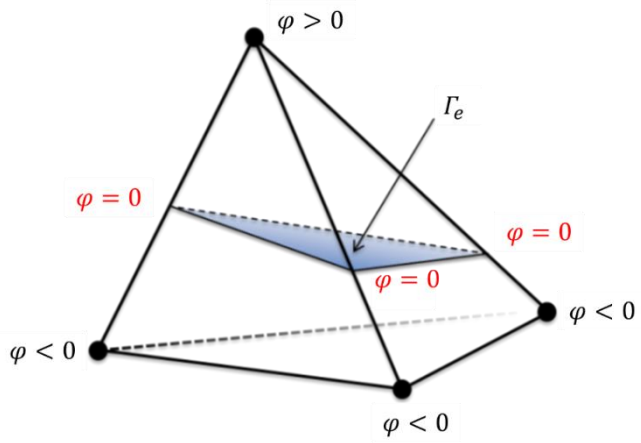

Figure 2-5. A tetrahedral element with average temperature above the solidus and illustration of Γ_e in this element cut by the metal/gas interface presented by level set function $\varphi = 0$ [Zha20].

2.2.5 Heat transfer resolution

2.2.5.1 Energy conservation equation

When solving the energy conservation equation, the standard volume averaging method [Rap10] is applied to the conservation of energy over the metallic subdomain as it is composed of several thermodynamic phases (presented in chapter 3). More details can be found in [Rap10, Saa16]. The principle of the volume averaging method is presented here. For a value of field ξ, the average volumetric property is presented as:

$$\langle \xi \rangle = \sum_{\phi} \langle \xi^{\phi} \rangle = \sum_{\phi} g^{\phi} \langle \xi \rangle^{\phi} \tag{2-19}$$

It should be noted that this average volumetric property is not needed for the gas subdomain as it is made of a single gas (usually argon) phase, its volume fraction in the gas subdomain is $g^{G} = 1$. As mentioned in section 2.2.1, by using the level-set method, the properties of a specified point B in the system are the averaged value of metal and gas properties by the space mixing law. Following Saad [Saa16] the intrinsic energy conservation equation for the metal and the gas can be established, respectively:

$$\begin{cases} \dfrac{\partial \langle \rho h \rangle^M}{\partial t} + \nabla \cdot \langle \rho h \boldsymbol{v} \rangle^M - \nabla \cdot (\langle \kappa \rangle^M \boldsymbol{\nabla} T) = \dot{Q}^M \\ \dfrac{\partial \langle \rho h \rangle^G}{\partial t} + \nabla \cdot \langle \rho h \boldsymbol{v} \rangle^G - \nabla \cdot (\langle \kappa \rangle^G \boldsymbol{\nabla} T) = \dot{Q}^G \end{cases} \quad (2\text{-}20)$$

With $\langle \quad \rangle^{M/G}$ present the average volumetric property of metal or gas.
Following hypothesis are considered in the resolution of heat transfer equation:
1. The average value of product equals the product of average value which means for example $\langle \rho h \rangle^M = \langle \rho \rangle^M \langle h \rangle^M$
2. Incompressibility of liquid metal and gas fluid (for this work, density of liquid metal is considered as a constant), which means $\nabla \cdot \langle \boldsymbol{v} \rangle^G = \nabla \cdot \langle \boldsymbol{v} \rangle^M = 0$
3. Static solid phase, which means $\langle \rho h \boldsymbol{v} \rangle^M = \langle \rho \rangle^l \langle h \rangle^l \langle \boldsymbol{v^l} \rangle + \langle \rho \rangle^s \langle h \rangle^s \langle \boldsymbol{v^s} \rangle = \langle \rho \rangle^l \langle h \rangle^l \langle \boldsymbol{v^l} \rangle$
By applying the space mix law (2-4) and rearranging the equation, the energy conservation equation in level-set method is as follow:

$$\frac{\partial \widehat{\rho h}}{\partial t} + \widehat{\boldsymbol{v^F}} \cdot \nabla \widehat{\rho h^F} = \nabla \cdot (\hat{\kappa} \nabla T) + \dot{Q} \quad (2\text{-}21)$$

with

$$\widehat{\rho h} = \mathcal{H}^M (g^l \rho^l h^l + g^s \langle \rho \rangle^s \langle h \rangle^s) + \mathcal{H}^G \rho^G h^G \quad (2\text{-}22)$$

$$\widehat{\rho h^F} = \mathcal{H}^M \rho^l h^l + \mathcal{H}^G \rho^G h^G \quad (2\text{-}23)$$

$$\hat{\kappa} = \mathcal{H}^M (g^l \kappa^l + g^s \langle \kappa \rangle^s) + \mathcal{H}^G \kappa^G \quad (2\text{-}24)$$

$$\widehat{\boldsymbol{v^F}} = \mathcal{H}^M g^l \boldsymbol{v}^l + \mathcal{H}^G \boldsymbol{v}^G \quad (2\text{-}25)$$

As presented in equation (2-25), only the energy over the liquid metal and the gas $\widehat{\rho h^F}$, is transported at velocity $\widehat{\boldsymbol{v^F}}$.

2.2.5.2 Heat source modeling

In the present model of welding simulation, the total volume power $\dot{Q}$ in equation (2-21) is divided in two parts:

$$\dot{Q} = \dot{Q}_{input} + \dot{Q}_{cooling} \quad (2\text{-}26)$$

$\dot{Q}_{cooling}$ presents a surface cooling induced by the heat convection and thermal radiation effect at the metal/gas interface, corresponding to the Fourier flux condition plus the Stefan-Boltzmann law:

$$\dot{Q}_{cooling} = \delta\left(h_T (T - T_{ext}) + \sigma_B \varepsilon_r (T^4 - T_{ext}^4)\right) \quad (2\text{-}27)$$

with h_T the heat transfer coefficient, ε_r the emissivity and σ_B the Stefan–Boltzmann constant at 5.67×10^{-8} W m^{-2} K^{-4} and δ the dirac function introduced by equation (2-5). For the GTAW process without adding material, $\dot{Q}_{input}$ is the volume input power induced by the arc plasma:

$$\dot{Q}_{input} = \delta \dot{Q}_P \tag{2-28}$$

$\dot{Q}_p$ is described by a Gaussian angular heat source as initially proposed by [Des13] and exploited by [Che14]:

$$\dot{Q}_P = \frac{3P_{Plasma}}{K_P \, 2\pi \, d^2 \, (1 - \cos\alpha)} \mathrm{e}^{-3\left(\frac{\beta}{\alpha}\right)^2} \cos\gamma \tag{2-29}$$

with $P_{Plasma} = \eta UI$ (η the efficiency of the heat source) the total effective power of the plasma arc of aperture angle α as defined in Figure 2-6:

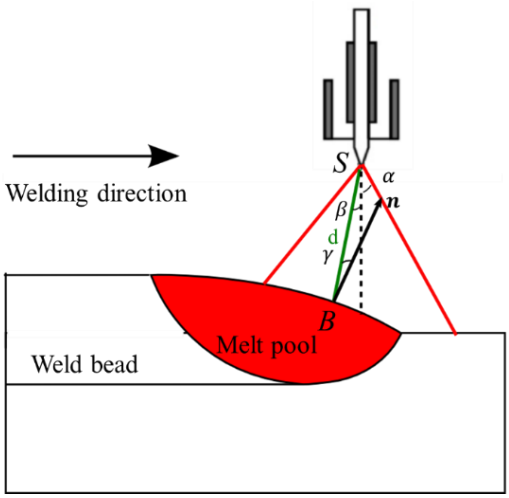

Figure 2-6. Gaussian angular heat source [Che14].

Equation (2-29) is valid for any point B located at the metal/gas boundary. This point is defined by its half-angle, β, between SB and the heat source direction (dashed line), necessarily smaller than α, its distance d from the origin of the heat source, S, and the angle γ between SB and the local normal $\boldsymbol{n} = \nabla\varphi$ (as $\|\nabla\varphi\| = 1$) of the metal/gas boundary. The normalization factor K_P is introduced to ensure that the requested effective power is well retrieved by an energy balance:

$$K_P = 0.95 + 0.0347\alpha^2 \tag{2-30}$$

For the GTAW process with adding material or GMAW process, the expression of $\dot{Q}_{input}$ should contain the volumetric heat source associated to the molten droplet $\dot{Q}_D$.

$$\dot{Q}_{input} = \delta \dot{Q}_P + \dot{Q}_D \tag{2-31}$$

$\dot{Q}_D$ is applied only inside the volume of the cavity of the adding material V_c. Details regarding calculation of V_c will be presented thereafter in section 2.2.6.1. During the process, the adding material is melted by the arc, consuming a part of the welding power, $\eta \; U \; I$. $\dot{Q}_{Plasma}$ (Eq. (2-29) is, consequently, no longer the total effective power of the process. The expression of $\dot{Q}_{Plasma}$ of GTAW process with adding material or GMAW process is:

$$P_{Plasma} = \eta UI - \dot{Q}_D V_c \tag{2-32}$$

2.2.5.3 FE implementation

The energy conservation equation (2-21) is solved by the Finite Element method. The principle is presented here: firstly, multiplying equation (2-21) by a test function $\mathfrak{w}$ belonging to the Sobolev space $\mathbb{H}^1(\Omega)$ and integration at the sole domain Ω. Secondly, using the finite element to discretize Ω to Ω^E. In this work, simple linear elements ($P1$) will be used, which corresponds to tetrahedra in 3D cases. A Fourier boundary condition is considered on the domain boundary $\partial\Omega^E$. The weak form of equation (2-21) can be written as:
Find,

$$T \in \mathcal{T} = \left\{ T \in \mathbb{H}^1(\Omega^E), T|_{\partial\Omega_T^E} = T_{imp} \right\} \tag{2-33}$$

for

$$\forall \mathfrak{w} \in \mathcal{W} = \left\{ \mathfrak{w} \in \mathbb{H}^1(\Omega^E), \mathfrak{w}|_{\partial\Omega_T^E} = 0 \right\} \tag{2-34}$$

satisfying:

$$\int_{\Omega^E} \mathfrak{w} \frac{\partial H}{\partial t} dV + \int_{\Omega^E} \mathfrak{w} \widehat{\boldsymbol{v}^F} \cdot \nabla \widehat{\rho h^F} dV = \int_{\Omega^E} \mathfrak{w} \nabla \cdot (\hat{\kappa} \nabla T) dV + \int_{\Omega^E} \mathfrak{w} \dot{Q} dV \tag{2-35}$$

with $H = \widehat{\rho h}$ to simplify the presentation. In the *Cimlib*, the Streamline Upwind Petrov-Galerkin (SUPG) scheme is implemented in order to stabilize the standard Galerkin scheme when advection phenomena dominate heat transfers. This stabilization is carried out by adding a diffusion term depending on the mesh size and the speed of the fluid in the element [Hac09]. Then equation (2-35) can be formed by assembling the local matrix contributed by each element E at time t [Saa16]:

$$(R_i^E)^t = M_{ij}^E \left(H_j^t - H_j^{t-\Delta t} \right) + A_{ij}^E H_j^t + \left(K1_{ij}^E + K2_{ij}^E \right) T_j^t - F_i^E - Q_i^E = 0 \tag{2-36}$$

with $i, j \in [1, D+1]$, D the dimension of the problem (3 for 3D), Δt the time step. The matrices in equation (2-36) are defined here:

$$M_{ij}^E = \int_{\Omega^E} \frac{1}{\Delta t} N_i N_j dV \tag{2-37}$$

$$A_{ij}^E = \int_{\Omega^E} N_i \widehat{\boldsymbol{v}^F} \nabla N_j dV \tag{2-38}$$

$$K1_{ij}^E = \int_{\Omega^E} \hat{\kappa} \nabla N_i \cdot \nabla N_j dV \tag{2-39}$$

$$K2_{ij}^{E} = \int_{\partial\Omega^{E}} h_c N_i N_j dS \tag{2-40}$$

$$F_i^{E} = \int_{\partial\Omega^{E}} h_c N_i T_{ext} dS \tag{2-41}$$

$$Q_i^{E} = \int_{\Omega^{E}} \dot{Q} N_i dV \tag{2-42}$$

with N_i the interpolation functions. The local matrix is computed by considering, in a loop, all the volumetric and surface elements. They are assembled into a global matrix, leading to a final linear system to be solved:

$$(R_i)^t = M_{ij}\left(H_j^t - H_j^{t-\Delta t}\right) + A_{ij}H_j^t + \left(K1_{ij} + K2_{ij}\right)T_j^t - F_i - Q_i = 0 \tag{2-43}$$

This system (Eq. (2-43)) can be expressed as the same form as equation (2-36) while it is applied to the whole domain rather than the element E and the global numbering will be used for node index i, j. The difficulty relates to the non-linearity of the minimization problem, as the volumetric enthalpy, H, is a non-linear function of the temperature, T. This difficulty is overcoming by using the Newton-Raphson method [Rap10]. Besides, a coupling of the energy conservation equation resolution with microsegregation by the enthalpy-temperature relation has been developed in the *Cimlib* library by [Saa16], more details can be found in this reference.

2.2.6 Fluid mechanics inside the melt pool

2.2.6.1 Cavity model for droplets fall

In GMAW process, added metal is considered induced by the melting of droplets falling from the consumable electrode. In GTAW, metal can also be added to the melting zone developed by the tungsten electrode, using a filler wire. Added metal (GTAW / GMAW) impinges in the melt pool to form the weld bead. As the formed weld bead determines the new metal/gas interface, the volume of the droplet V_c should be clearly defined.

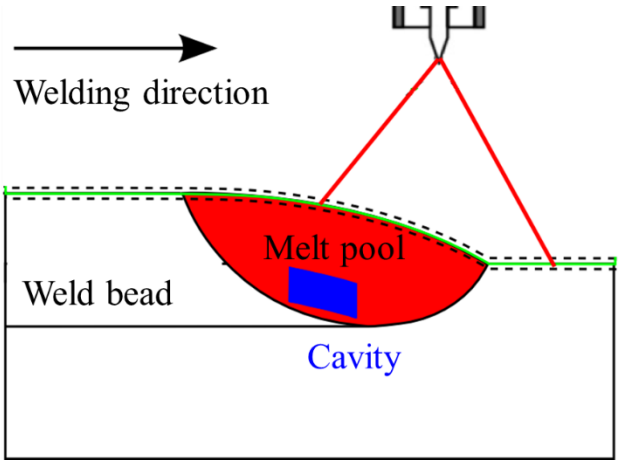

Figure 2-7. In blue the zone of droplet impingement, in the view of the longitudinal section of the workpiece [Che14].

In the approach developed in *Cimlib* to follow welding processes and addition of metal, the molten droplet fallen in the melt pool is modelled by a limited cylindrical or *cavity* region [Des13, Bel13], as shown in Figure 2-7 in blue. The shape of cavity is defined by level-set function φ, therefore, it follows the shape of the interface. The radius of the cavity R_c, is considered as twice as that of the droplet:

$$R_c = 2R_d = 2\left(\frac{3\rho_w(T_{0,w})R_w^2 v_w}{4f_d\rho_w(T_d)}\right)^{\frac{1}{3}} \tag{2-44}$$

where $\rho_w(T_{0,w})$ is the density of the filler wire at its initial temperature $T_{0,w}$. $\rho_w(T_d)$ corresponds to the density of the filler wire at the temperature assumed for droplets, T_d ($T_d = 2500\text{K}$ [Des13]). In the present work, the density of the filler wire is considered to be the same at different temperatures ($\rho_w(T_{0,w}) = \rho_w(T_d)$) due to the fact that the shrinkage of the material is not modeled. R_w is the radius of the filler wire, and v_w is the velocity of the adding filler wire. f_d is the frequency of detachment of the droplets defined by Kim [Kim03]:

$$f_d = \frac{-243.44}{1 + exp\left(\frac{I - 291.086}{6.06437}\right)} + 323.506 - 0.8741I + 0.0025I^2 \tag{2-45}$$

where I is the current intensity.
Besides, the height of the cavity, L_c, is modeled as Kumar *et al* [Kum94] and later corrected by Desmaison [Des13]:

$$L_c = -\frac{2\gamma_s}{R_c\rho(T_{dro})a_g} + 2\sqrt{\left(\frac{\gamma_s}{R_c\rho(T_{dro})a_g}\right)^2 + \frac{R_c v_d^2}{24a_g}} \tag{2-46}$$

where γ_s is the surface tension coefficient, $\rho(T_{dro})$ is the local density of the liquid metal of the droplets, a_g is the gravitational acceleration (9.81 m s^{-2}) and v_d is the velocity of the droplets falling into the melt pool. v_d is defined by:

$$v_d = \sqrt{v_{0,d}^2 + 2a_d L_a} \tag{2-47}$$

where $v_{0,d}$ is the initial droplet velocity. a_d is the acceleration of the droplet, which is assumed to be constant through the arc plasma (55 m s^{-2} [Des13]), L_a is the length of the arc plasma (3.45 mm [Des13]). $v_{0,d}$ is computed by [Lin01, Des13]:

$$v_{0,d} = \sqrt{-0.33692 + 0.00854(I/2R_d)} \tag{2-48}$$

Then the volume of the cavity can be expressed as:

$$V_c = \pi R_c^2 L_c \tag{2-49}$$

2.2.6.2 Mass conservation inside the cavity

In the cavity impinged by droplets, a term related to the adding material should be added at the right hand side of the mass conservation equation. As shown in Figure 2-7, this cavity is in the melt pool, the mass conservation equation inside the cavity writes:

$$\frac{\partial \langle \rho \rangle^l}{\partial t} + \nabla \cdot \langle \rho \boldsymbol{v} \rangle^l = \frac{\dot{m}_w}{V_c} = \frac{\rho_w(T_{0,w}) R_w^2 v_w}{R_c^2 L_c} \tag{2-50}$$

where $\dot{m}_w = \rho_w(T_{0,w})\pi R_w^2 v_w$ the mass flow rate of the filler metal. The density variation of the liquid phase is then neglected in the present relation related to added material in cavity (ρ is constant). Equation (2-50) is consequently simplified as:

$$\nabla \cdot \langle \boldsymbol{v} \rangle^l = \frac{\dot{m}_w}{\rho V_c} = \frac{\rho_w(T_{0,w})}{\rho} \frac{R_w^2 v_w}{R_c^2 L_c} \tag{2-51}$$

As mentioned above, no shrinkage is considered in the present approach which means the density of the filler is constant at different temperature: $\rho_w(T_{0,w}) = \rho$. Equation (2-51) becomes:

$$\nabla \cdot \langle \boldsymbol{v} \rangle^l = \frac{R_w^2 v_w}{R_c^2 L_c} = \dot{\theta} \tag{2-52}$$

Considering in the whole FE domain:

$$\begin{cases} \dot{\theta} = 0 & outside\ the\ cavity \\ \dot{\theta} = \dfrac{R_w^2 v_w}{R_c^2 L_c} & inside\ the\ cavity \end{cases} \tag{2-53}$$

2.2.6.3 Mass conservation equations

The mass conservation in the metal and gas writes:

$$\begin{cases} \dfrac{\partial \langle \rho \rangle^M}{\partial t} + \nabla \cdot \langle \rho \boldsymbol{v} \rangle^M = \dot{\theta} \\ \dfrac{\partial \langle \rho \rangle^G}{\partial t} + \nabla \cdot \langle \rho \boldsymbol{v} \rangle^G = \dot{\theta} = 0 \end{cases} \tag{2-54}$$

supposing the incompressibility of metal and gas, equation (2-54) becomes:

$$\begin{cases} \nabla \cdot \langle \boldsymbol{v} \rangle^M = \dot{\theta} \\ \nabla \cdot \langle \boldsymbol{v} \rangle^G = \dot{\theta} = 0 \end{cases} \tag{2-55}$$

The monolithic mass conservation by applying the space mix law (2-4) writes:

$$\nabla \cdot \hat{\boldsymbol{v}} = \dot{\theta} \tag{2-56}$$

with $\hat{\boldsymbol{v}} = \mathcal{H}^M (g^l \langle \boldsymbol{v} \rangle^l + g^s \langle \boldsymbol{v} \rangle^s) + \mathcal{H}^G \boldsymbol{v}^G$. It should be noted that $\dot{\theta}$ is non-equal to zero only in the cavity when added metal is considered. Consequently $\nabla \cdot \hat{\boldsymbol{v}} = 0$ for GTAW process when no addition of metal is considered.

2.2.6.4 Momentum conservation equations

The momentum conservation equation is the same for the process with or without adding material, the monolithic equation writes:

$$\hat{\rho} \left(\frac{\partial \hat{\boldsymbol{v}}}{\partial t} + (\hat{\boldsymbol{v}} \cdot \nabla) \hat{\boldsymbol{v}} \right) = \nabla \cdot \bar{\bar{\sigma}} + \boldsymbol{f_V} \tag{2-57}$$

The stress tensor is

$$\bar{\bar{\sigma}} = 2\hat{\mu} \left(\bar{\bar{\dot{\varepsilon}}} - \frac{1}{3} tr\left(\bar{\bar{\dot{\varepsilon}}}\right) \bar{\bar{\mathrm{I}}} \right) - p\bar{\bar{\mathrm{I}}} = 2\hat{\mu} \left(\bar{\bar{\dot{\varepsilon}}} - \frac{1}{3} \dot{\theta} \bar{\bar{\mathrm{I}}} \right) - p\bar{\bar{\mathrm{I}}} \tag{2-58}$$

with $tr\left(\bar{\bar{\dot{\varepsilon}}}\right) = \nabla \cdot \hat{\boldsymbol{v}} = \dot{\theta}$, $\bar{\bar{\dot{\varepsilon}}} = 1/2(\nabla \cdot \hat{\boldsymbol{v}} + (\nabla \cdot \hat{\boldsymbol{v}})^{\boldsymbol{t}})$, $p = \mathcal{H}^M \langle p \rangle^M + \mathcal{H}^G p^G$ is the pressure. $\boldsymbol{f_V}$ is the volumetric driving force which will be presented in section 2.2.6.5. Combined with the mass conservation equation (Eq. (2-56), the Navier-Stokes (NS) equation writes:

$$\begin{cases} \nabla \cdot \hat{\boldsymbol{v}} = \dot{\theta} \\ \hat{\rho} \left(\dfrac{\partial \hat{\boldsymbol{v}}}{\partial t} + (\hat{\boldsymbol{v}} \cdot \nabla) \hat{\boldsymbol{v}} \right) - 2\nabla \cdot \left(\hat{\mu} \bar{\bar{\dot{\varepsilon}}} \right) + \nabla p + \dfrac{2}{3} \hat{\mu} \nabla \dot{\theta} \ = \boldsymbol{f_V} \end{cases} \tag{2-59}$$

It can be noted that $\hat{\boldsymbol{v}}$ is the velocity field of the global domain which is different from $\widehat{\boldsymbol{v}^{\boldsymbol{F}}}$ in equation (2-25) used for the transport of level set function and the heat convection. To obtain $\widehat{\boldsymbol{v}^{\boldsymbol{F}}}$ in Eq. (2-25), a post treatment is applied after the resolution of equation (2-57) to neglect the velocity in the solid metal part ($\langle \boldsymbol{v} \rangle^s$). In fact, this velocity in the metal solid is very weak about (10^{-4} mm s^{-1}) compared with the velocity of the metal liquid inside the melt pool (several mm s^{-1}) and can be considered as negligible. Details on the velocity field is presented

and discussed in next chapter (chapter 3). $\hat{\mu}$ and $\hat{\rho}$ denote the average viscosity and density over the global domain according to equation (2-60) and (2-61) respectively.

$$\hat{\mu} = \mathcal{H}^M \langle \mu \rangle^M + \mathcal{H}^G \mu^G \tag{2-60}$$

$$\hat{\rho} = \mathcal{H}^M (g^l \langle \rho \rangle^l + g^s \langle \rho \rangle^s) + \mathcal{H}^G \rho^G \tag{2-61}$$

2.2.6.5 Driving forces

In the welding process, the driving forces in the melt pool are surface tension, Marangoni force and gravity forces. The recoil pressure is neglected in both GTAW and GMAW processes due to the low power density compared with laser welding or additive manufacturing [Jar01].

$$\boldsymbol{f_V} = \boldsymbol{f_V}^{\boldsymbol{T}} + \boldsymbol{f_V}^{\boldsymbol{M}} + \boldsymbol{f_V}^{\boldsymbol{G}} \tag{2-62}$$

with $\boldsymbol{f_V}^{\boldsymbol{G}} = \hat{\rho}\boldsymbol{g}$.

The surface tension is caused by the cohesive forces between liquid molecules [Joh04]. For each molecule inside the liquid, all cohesive forces from neighboring liquid molecules are in local equilibrium. However, at the liquid/gas interface, these forces are partly contributed by gas molecules. As the intermolecular distance in gas is higher than that in liquid, the cohesive forces induced by gas molecules are smaller than those induced by liquid molecules. Consequently, internal pressure is created, and the interface has tendency to bend towards the gas. This is described by the Young-Laplace equation:

$$p_g - p_l = -\gamma_s \nabla \cdot \boldsymbol{n} = \gamma_s \kappa_t \tag{2-63}$$

with p_g and p_l pressures in liquid and gas respectively. γ_s is the surface tension coefficient and $\kappa_t = -\nabla \cdot \boldsymbol{n}$ the total curvature. $\boldsymbol{n}$ is the unit normal direction pointing out of liquid:

$$\boldsymbol{n} = \nabla\varphi \ \ (\|\varphi\| = 1) \tag{2-64}$$

where φ is the LS function associated to the melt pool boundary. The resulting surface tension force acting on the liquid surface by applying the CSF method is:

$$\boldsymbol{f_V}^{\boldsymbol{T}} = \gamma_s \kappa_t \boldsymbol{n} \delta \tag{2-65}$$

This is the volume force, using CSF method, acting in the normal direction toward the liquid at the liquid/gas interface. The tangential effect of surface tension is Marangoni effect which is due to the shear stress at the liquid/gas interface induced by the gradient of surface tension coefficient along this interface. Supposing that γ essentially depends on temperature, we obtain:

$$\boldsymbol{f_V}^{\boldsymbol{M}} = \delta \nabla_s \gamma_s = \delta \frac{\partial \gamma_s}{\partial T} \nabla_s T \tag{2-66}$$

where ∇_s represent the surface gradient operator. $\nabla_s T$ is the tangential component of the gradient at the interface:

$$\nabla_s T = \nabla T - (\nabla T \cdot \boldsymbol{n})\boldsymbol{n} \tag{2-67}$$

According to (2-66) with a given surface temperature gradient, the Marangoni force depends only on the Marangoni coefficient $\partial\gamma_s/\partial T$, which is a property of the liquid material. The sign of $\partial\gamma_s/\partial T$ plays an important role as the direction of the convection flow depends on it, as shown in Figure 2-8. Consequently, the temperature distribution and the shape of melt pool will be modified [Mil98].

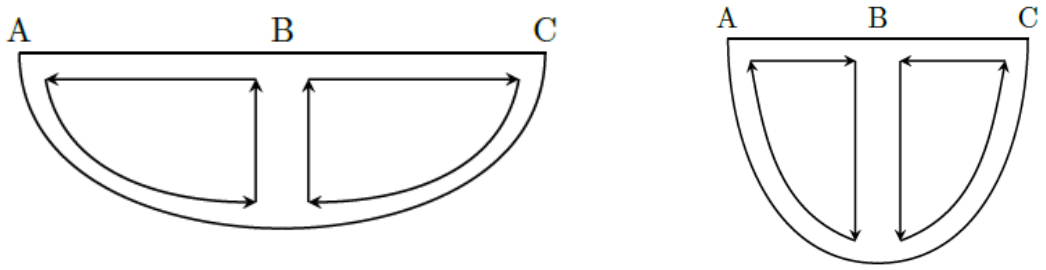

(a) $\frac{\partial\gamma_S}{\partial T} < 0$ (b) $\frac{\partial\gamma_S}{\partial T} > 0$

Figure 2-8. Convection flow induced by different Marangoni coefficients having opposite signs with T_A and T_C lower than T_B [Mil98].

2.2.6.6 Semi-implicit formulation of surface tension

The calculation of the surface tension depends on the total curvature κ_t and the normal direction $\boldsymbol{n}$ (Eq. (2-65)). However, these two parameters are not known a priori as the interface moves over time. Considering a point with coordinate vector $\boldsymbol{X}$ at the liquid/gas interface $\Gamma^{L/G}$, the total curvature and normal direction can be calculated as:

$$\kappa_t \boldsymbol{n} = \Delta_{\boldsymbol{s}} \boldsymbol{X} = \nabla_{\boldsymbol{s}} \cdot (\nabla_{\boldsymbol{s}} \boldsymbol{X}) \tag{2-68}$$

the $\Delta_{\boldsymbol{s}}$ and $\nabla_{\boldsymbol{s}}$ present the surface Laplace and Nabla operators respectively. Besides, $\nabla_{\boldsymbol{s}}\boldsymbol{X}$ can be presented in relation of $\nabla\boldsymbol{X}$**:**

$$\nabla_{\boldsymbol{s}} \boldsymbol{X} = \nabla \boldsymbol{X} - (\nabla \boldsymbol{X} \cdot \boldsymbol{n})\boldsymbol{n} \tag{2-69}$$

A simple explicit formulation, consists of computing this term by using the interface calculated at the previous time increment, however, a CLF (Courant-Friedrichs-Lewy) condition related to the mesh size, the time step and the material properties should be satisfied [Hys06]:

$$\Delta t < {h_{min}}^{\frac{3}{2}} \sqrt{\frac{\rho}{2\pi\gamma_s}} \tag{2-70}$$

For a steel type 316L used in this work, $\rho = 7800\ \mathrm{kg\ m^{-3}}$, $\gamma_s = 1.943\ \mathrm{N\ m^{-1}}$ [Tra11], for a typical minimum mesh size 20 µm, the limit time step Δt is about 5×10^{-4} s. For a welding process for 20 seconds, 40000 time steps would be necessary which would lead to a non-sustainable computation time. Therefore, a semi-implicit formulation is introduced and integrated in the *Cimlib* library by Hamide [Ham08] and Chen [Che18]:

$$\kappa_t \boldsymbol{n} = \Delta_s \boldsymbol{X} = \Delta_s \boldsymbol{X}^- + \Delta_s \widehat{\boldsymbol{v}} \Delta t = \kappa_t \boldsymbol{n}^- + \Delta_s \widehat{\boldsymbol{v}} \Delta t \tag{2-71}$$

The minus sign represents the previous time step. Compared with the explicit formulation, the second term at right hand side related to the surface diffusion of velocity is added in this semi-implicit formulation. More details on this semi-implicit formulation can be found in [Ham08, Che18, Que21].

2.2.6.7 FE implementation

In the *Cimlib* library, a Variational MultiScale (VMS) method proposed by [Hug95] is used to ensure the stability in the FE resolution. This method is briefly introduced here. Coarse and fine scales are considered in the solution. As presented by the NS equation (2-59), the resolution is carried out in the framework of a mixed velocity-pressure formulation. Thus, in the VMS method, both the velocity and pressure are decomposed into these two scales. Then the resolution of NS equation is separated into two scales, and the final resolution at coarse scale is obtained by using the solution at fine scale. More details can be found in [Hac09, Kha16]. Only the final equations to be solved with semi-implicit surface tension and compressible behavior (existence of $\dot{\theta}$) are presented here:
Above all, the functional spaces could be defined:

$$\begin{aligned} \mathcal{V} &= \left\{ \widehat{\boldsymbol{v}} \in \mathbb{H}^1(\Omega^E), \widehat{\boldsymbol{v}}|_{\partial\Omega_v^E} = \widehat{\boldsymbol{v}}_{imp} \right\} \\ \mathcal{V}_0 &= \left\{ \widehat{\boldsymbol{v}} \in \mathbb{H}^1(\Omega^E), \widehat{\boldsymbol{v}}|_{\partial\Omega_v^E} = 0 \right\} \\ \mathcal{P} &= \{ p | p \in L_2(\Omega) \} \end{aligned} \tag{2-72}$$

The resolution is to find $\widehat{\boldsymbol{v}} \in \mathcal{V}$ and $p \in \mathcal{P}$, for $\forall \mathfrak{w} \in \mathcal{V}_0$ and $q \in \mathcal{P}$

$$
\begin{cases}
\left(\hat{\rho}\dfrac{\widehat{\boldsymbol{v}}}{\Delta t}, \mathfrak{w}_{supg}\right) & \text{Unsteady term} \\
+\left(\hat{\rho}(\widehat{\boldsymbol{v}}\cdot\nabla)\widehat{\boldsymbol{v}}, \mathfrak{w}_{supg}\right) & \text{Convection term} \\
+2\left(\hat{\mu}\bar{\bar{\varepsilon}}(\widehat{\boldsymbol{v}}):\bar{\bar{\varepsilon}}(\mathfrak{w}), \mathfrak{w}_{supg}\right) & \text{Viscous term} \\
+\left(\nabla p, \mathfrak{w}_{supg}\right) + (\tau_C \nabla\cdot\widehat{\boldsymbol{v}}, \nabla\cdot\mathfrak{w}) & \text{Pression term} \\
+\Delta t[(\delta\gamma_s\nabla\widehat{\boldsymbol{v}}:\nabla\mathfrak{w}) - (\delta\gamma_s\nabla\widehat{\boldsymbol{v}}\cdot\boldsymbol{n}, \nabla\mathfrak{w}\cdot\boldsymbol{n})] & \text{Surface tension term} \\
-\dfrac{2}{3}(\hat{\mu}\nabla\cdot\widehat{\boldsymbol{v}}, \nabla\cdot\mathfrak{w}) & \text{Compressibility terms} \\
= \left(f_t, \mathfrak{w}_{supg}\right) + \left(\tau_C\dot{\theta}, \nabla\cdot\mathfrak{w}\right) & \text{External forces + contributions of explicit term} \\
\\
(\nabla\cdot\widehat{\boldsymbol{v}}, q) & \text{Continuity term} \\
+\left(\hat{\rho}\dfrac{\widehat{\boldsymbol{v}}}{\Delta t}, \tau_K\nabla q\right) + (\hat{\rho}(\widehat{\boldsymbol{v}}\cdot\nabla)\widehat{\boldsymbol{v}}, \tau_K\nabla q) + (\nabla p, \tau_K\nabla q) & \text{Stabilization term} \\
= \left(\dot{\theta}, q\right) + (f_t, \tau_K\nabla q) & \text{Compressibility + stabilization term}
\end{cases}
\tag{2-73}
$$

with $(*\,,*) = \int_\Omega (*\,,*)dV$ and $(*:*) = \int_\Omega (*:*)dV$ and

$$
\mathfrak{w}_{supg} = \mathfrak{w} + \tau_K\hat{\rho}\nabla\mathfrak{w}\cdot\widehat{\boldsymbol{v}} \tag{2-74}
$$

$$
f_t = \hat{\rho}\boldsymbol{g} + \delta\gamma_s(\kappa_t\boldsymbol{n})^- + \delta\frac{\partial\gamma_s}{\partial T}[\nabla T - (\nabla T\cdot\boldsymbol{n})\boldsymbol{n}] + \hat{\rho}\frac{\widehat{\boldsymbol{v}}^-}{\Delta t} \tag{2-75}
$$

τ_C and τ_K are stabilization coefficient in [Cou13, Kha16]:

$$\tau_C = \left(\left(\frac{\hat{\mu}}{\hat{\rho}} \right)^2 + \left(\frac{c_2 \|\hat{\boldsymbol{v}}\|}{c_1 h_K} \right)^2 \right)^{1/2} \tag{2-76}$$

$$\tau_K = \left(\left(\frac{2\hat{\rho}}{\Delta t} \right)^2 + \left(\frac{2\hat{\rho}\|\hat{\boldsymbol{v}}\|}{h_K} \right)^2 + \left(\frac{4\hat{\mu}}{h_K^2} \right)^2 \right)^{-1/2} \tag{2-77}$$

where c_1 and c_2 are constants independent to the characteristic length h_K of element in the direction of fluid flow [Tez03]:

$$h_K = \frac{2\|\hat{\boldsymbol{v}}\|}{\sum_{i=1}^{i=D} |\hat{\boldsymbol{v}} \cdot \nabla N_i|} \tag{2-78}$$

with N_i the interpolation function of node i of the local element and D is 4 for 3D simulation. It should be noted that, the compressibility term with $\dot{\theta}$ is nonzero only in the cavity in the welding process with adding material and equal to zero elsewhere. In GTAW process without adding material, $\dot{\theta}$ is equal to zero on the whole domain.

2.3 CA model

The CA model was developed in the *Cimlib* library during previous research activities by various authors [Car12, Chen14, Pin19]. The main principle related to the welding process are presented here. More details can be found in these references for a detailed description of the methodology.

2.3.1 Definition of cells

As presented in Figure 2-1, the CA mesh is discretized into a regular lattice of square cells in 2D or cubic cells in 3D. All the cells have the same size and are kept fixed during the simulation. The cellular automaton method is based on the definition (1) of a neighborhood, (2) of several variables per cell, evolving according to physical and/or statistical models, (3) of a transition function allowing changing the state of a cell according to the state of its neighborhood.
Each cell has 26 neighbors in 3D (8 in 2D). For each cell, a I_v status indicator is given:

- $I_v = 0$ if the cell is completely liquid, called liquid cell;
- $I_v = 1$ if the cell is located in the growing mushy zone, one or several grain envelopes is growing locally, called growing cell;
- $I_v = 2$ if the growth of the cell has reached a local maximal size of growth (will be presented in section 2.3.4), called fully mushy cell;
- $I_v = -10$ to represent the cells located in the air, called air cell.

In the growing cell with $I_v = 1$, an envelope which locally coincide with the grain shape and crystallographic orientation is associated to present the growing grain. Considering the 316L used in this work for example, the preferred dendritic growth direction is <100> for both austenite (δ-BCC) and ferrite (α-FCC). The trunks and arms of the dendritic grains are then supposed to be aligned along the <100> directions. The envelopes associated with the cells are

defined as an octahedron in 3D (square in 2D) with the main half diagonals along the <100> crystallographic directions of the corresponding grains. Besides, the apices of the envelopes are considered as the dendrite tip of the crystal. This octahedron may be subsequently deformed if the <100> crystallographic directions do not grow at the same velocity. For each octahedron, a triplet of Euler angle, named $(\varphi_1, \phi, \varphi_2)$ in 3D, in the Bunge convention is associated to present the crystallographic directions.

2.3.2 Remelting of initial grain structure

Differently from the casting process, in welding, an initial grain structure is preexisted. When the heat source passes and heats the work piece, the preexisted grain structure is melted in forming a melt pool and the solidification takes place by the partially melted grain at the solid-liquid interface. Even though the nucleation caused by fragmentation or intentional inoculant can take place in the melt pool (presented in Section 1.1.3.3), this phenomenon is not considered in the present CAFE model for welding and only re-melting / re-solidification stage is assumed presently. Hence, the remelting should be presented for the welding process.

The cell state in remelting of the initial grain structure can be separated into two situations:

- the cell is in the metal part fully melted (melt pool);
- the cell is in the partially melted metal (solid-liquid interface) serving for epitaxial growth.

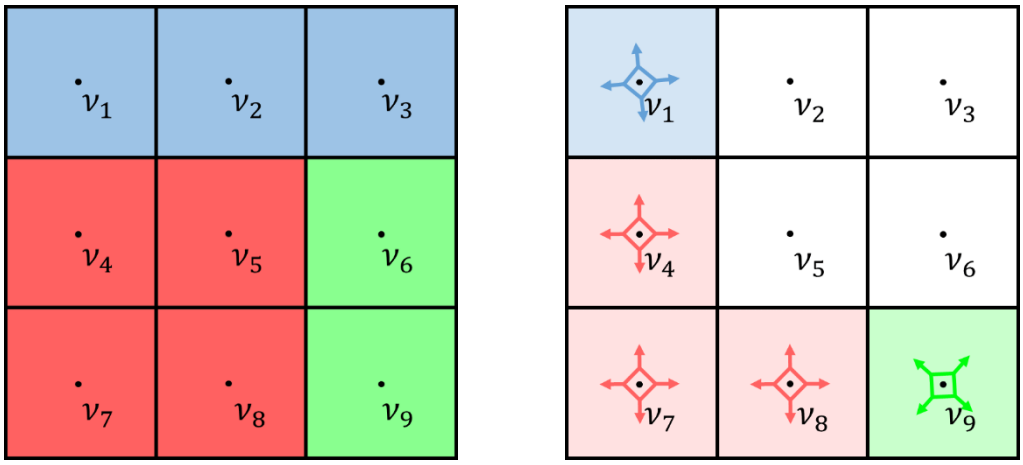

(a) Initial grain structure at time $\boldsymbol{t}$ (b) Remelting at time $t + \Delta t$

Figure 2-9. Cell states transition during remelting [Che14].

Considering a cluster of 9 cells representing the initial grain structure (Figure 2-9 (a)) with initial fully mushy state ($I_{\nu_i} = 2, i \in [1,9]$) and temperature $T_{\nu_i}, i \in [1,9]$ below the liquidus T_{liq}, *i.e.* $T_{\nu_i} < T_{liq}, i \in [1,9]$. These 9 cells belong to 3 different grains marked in blue, red, and green. At time $t + \Delta t$, the temperature of cells ν_2, ν_3, ν_5 and ν_6 becomes higher than T_{liq} because of the heat source, *i.e.* $T_{\nu_i} > T_{liq}, i = \{2,3,5,6\}$, as shown in Figure 2-9 (b). The states

of these four cells are therefore changed to be fully liquid, *i.e.*, $I_{\nu_i} = 0, i = \{2,3,5,6\}$. And the color of these cells is therefore changed into white.
For other cells, their temperature is still under T_{liq}, *i.e.* $T_{\nu_i} < T_{liq}, i = \{1,4,7,8,9\}$. As they have at least one neighbor cell with temperature higher than the liquidus (for example, for cell, ν_1, $T_{\nu_1} < T_{liq}$, and its neighbor cell ν_2 has $T_{\nu_2} > T_{liq}$), these 5 cells are considered to be located at the solid-liquid interface. As a consequence, they are changed to the growing state, i.e., $I_{\nu_i} = 1, i = \{1,4,7,8,9\}$. New envelopes are created in the center of $\nu_i, i = \{1,4,7,8,9\}$ as shown in Figure 2-9 (b). The information of crystallographic orientations (Euler angle) and the grain numbers is kept as their initial values. Note that the arrows represent the preferred growth direction <100> in 3D (<10> in 2D).

2.3.3 Grain growth and cell capture principle

The algorithm of grain growth and capture is proposed and detailed in [Gan97], here the principle of the algorithm is presented and illustrated in 2D. In the welding process, the solidification takes place when the heat source moves away. As mentioned above, the partially melted grains at the solid-liquid interface grow epitaxially followed by the grain growth competition.
The envelope of a cell can be created if:

- the cell is a neighbor of a liquid cell formed due to the melting;
- the cell is itself a liquid cell and captured by neighboring growing cells.

The growth of a grain is achieved by the enlargement of the envelope growth in crystallographic directions <100> in 3D (<10> in 2D). As shown in Figure 2-10, $R_{\nu_1}^{en}$ presents the radius of envelop (half diagonal for the square envelop) associated to cell ν_1, the envelope growth is indicated by the evolution of radius from the initial value $R_{\nu_1}^{en_0}$ to $R_{\nu_1}^{en}$.

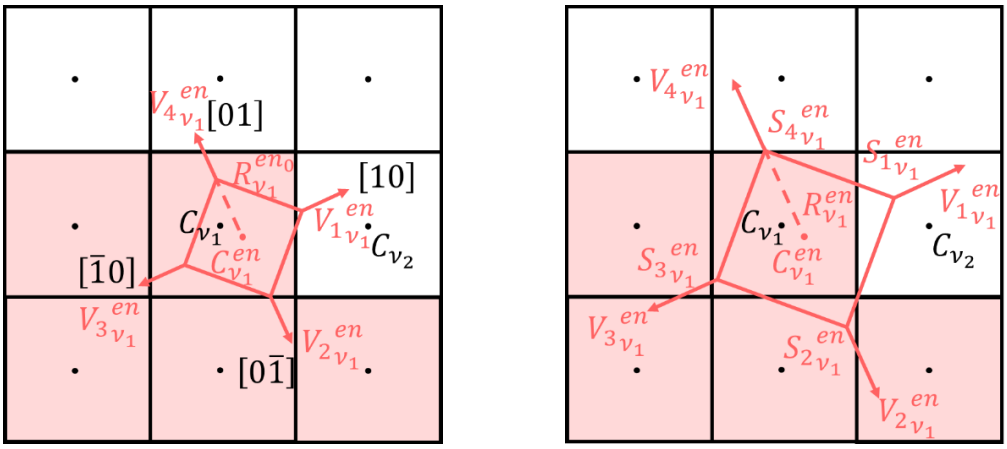

(a) t (b) $t + \Delta t$

Figure 2-10. 2D presentation of the envelope growth associated to cell ν_1 at time t (a) and time $t + \Delta t$ (b). With fully liquid cell in white and growing cell in color [Che14].

A dendrite tip law such as the one deduced from the use of the KGT model [Kur86] is applied at the four apexes $\left(S_{i_{\nu_1}}^{en}, i \in [1,4]\right)$ of the envelope to get the growth velocities, $V_{i_{\nu_1}}^{en}, i \in [1,4]$ which are related to the temperature (undercooling) chosen. One classic method is to choose the temperature in the center of the cell C_{ν_1}, which means the same value for the four apexes, when the growth law only depends on the cell temperature. In this situation, the velocities of radius growth are also the same at the four apexes and the envelope is quadratic and is kept during its growth. Another method is to compute the temperature for each apex, in this case, if the temperature field is not uniform, the envelope is no longer quadratic. In the present work, the second method is applied. The reason is the non-uniform thermal gradient in the welding process, thus, each apex of the envelope should be considered separately. More details and comparison of the temperature choices can be found in [Car12, Pin19], authors show that the consideration of temperature for each apex carries out better simulation results compared to analytical ones. As long as the envelope of ν_1 is large enough to encompass the center of a neighbor liquid cell, ν_2 ($I_{\nu_2} = 0$), ν_2 is then considered to be "captured". The growth of a grain occurs through successive local capture of cells. An example of the capture process is presented in Figure 2-11

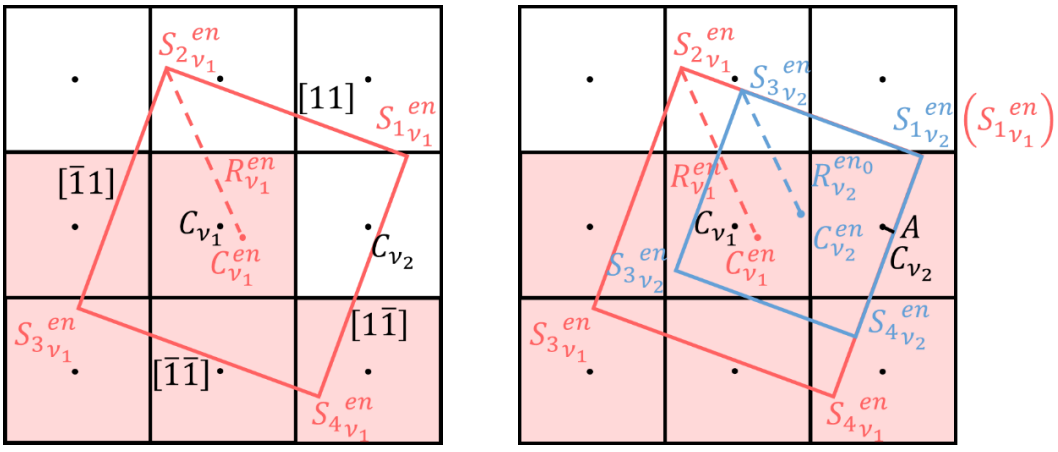

(a) t (b) $t + \Delta t$

Figure 2-11. 2D presentation of the cell capture process (a) time t before the capture of ν_2, and (b) time $t + \Delta t$ the cell ν_2 is captured [Che14].

Once the growing envelope associated to cell ν_1 captures the cell ν_2, the state of cell ν_2 is then changed from 0 to 1 (presented in Figure 2-11 by the change of cell color). At the same time, a new decentered envelope (blue one in Figure 2-11 (b)) is created to associate to ν_2, positioned in such a way that one of its apexes coincides with the apex of envelope of ν_1 nearest to ν_2 (*e.g.* $S_{1_{\nu_2}}^{en} = S_{1_{\nu_1}}^{en}$). The grain number and crystallographic orientation (Euler angle) associated to ν_1 are set to be identical with those of ν_2. In order to limit the dimensions of the new growth envelope and therefore to avoid a continuous increase in radius at each capture event, the envelope is truncated as presented in [Gan97]:

$$R_{\nu_2}^{en_0} = \frac{\sqrt{2}}{2}\left[Min\left(AS_{1_{\nu_2}}^{en}, \sqrt{2}l_{cell}\right) + Min\left(AS_{4_{\nu_2}}^{en}, \sqrt{2}l_{cell}\right)\right] \quad (2\text{-}79)$$

A is the point where the center of ν_2, C_{ν_2}, projects on the $(1\bar{1})$ face of the square envelope of ν_1, defined at the time of capture. $(1\bar{1})$ is indeed considered as the capturing face regarding the position of the grain envelope and the cell center, C_{ν_2}. $AS_{1_{\nu_2}}^{en}$ and $AS_{4_{\nu_2}}^{en}$ are equivalent to the distances between C_{ν_2} and (11) and $(\bar{1}\bar{1})$ faces, respectively. l_{cell} is the cell size. $R_{\nu_2}^{en_0}$ is the initial value of the radius of this envelope.
Once the position and the radius of the new envelope is defined, its center, $C_{\nu_2}^{en}$ can be therefore defined. Then the new envelope associated to ν_2 grows based on the dendrite tip kinetic law.
During the solidification, a cell can be captured by several neighbor growing cells in the same time step, in this case, the neighbor cell with the most grown envelope is favored. Which means, a cell is only captured by the neighbor cell having the largest envelop.

2.3.4 Mushy zone fraction (envelope fraction)

As mentioned above in section 2.3.1, each envelope has a local maximal size of growth. The state of the cell changes to $I_\nu = 2$, when this maximum size is reached. To better present the cell states, an envelope faction $g_{\nu^{CA}}^{en}$ is defined:

$$g_{\nu^{CA}}^{en} = Min\left(\frac{V_\nu^{en} - V_\nu^{en_0}}{V_\nu^{en_{max}} - V_\nu^{en_0}}, 1\right) \quad (2\text{-}80)$$

where V_ν^{en} is the volume of the envelope at current time, $V_\nu^{en_0}$ is the initial volume of the envelope in 3D (created at the time of the capture of the cell), $V_\nu^{en_{max}}$ is the maximum volume of the envelope growth. It could be noted that all the volumetric parameters in 3D correspond to the surface parameters in 2D.
Several methods to compute the maximum volume $V_\nu^{en_{max}}$ are presented by Carozzani [Car11, Car12]. Here only the applied method referred as "compute by neighbor" is presented: an envelope associated with a cell ν has reached its maximum growth when it encompassed the center of all the neighbor cells. As presented in equation (2-80), there are three cases of g_ν^{en}:

- $g_{\nu^{CA}}^{en} = 0$, the envelope does not exist. The cell ν is in liquid state, *i.e.* $I_\nu = 0$;
- $0 < g_{\nu^{CA}}^{en} < 1$, the envelope is growing, while it does not reach the maximum value. The cell ν is in the growing state, *i.e.* $I_\nu = 1$;
- $g_{\nu^{CA}}^{en} = 1$, the envelope reaches the maximum size and encompasses all the centers of the neighbor cells. The envelope stops growing, and the cell ν is in the fully mushy state, *i.e.* $I_\nu = 2$.

Therefore, $g_{\nu^{CA}}^{en}$ can be used to determine the transition of cell from growing state to fully mushy state. When $g_{\nu^{CA}}^{en}$ reaches to 1, the state of a growing cell $I_\nu = 1$ can be changed to $I_\nu = 2$, and the growth is stopped.

2.3.5 Transformation between air cell and metal cell

In welding process, the metal/gas interface evolves due to the addition of metal or the subsidence of the metal plate (detailed in section 3), induced when melt pool is developed

through the entire thickness of the piece. In the FE model, this phenomenon is presented by the evolution of the level-set function, and in the CA model, it is reflected by the transformation between the air cell and metal cell ($I_\nu \geq 0$).
Considering the first case of adding material. As presented in section 2.3.1, the cell ν is defined as an air cell when it is located in the air subdomain, *i.e.* $\varphi_\nu > 0$. Once the value of φ_ν changes to be negative or zero, ν is considered to be encompassed by the weld bead, consequently, state of ν is changed from $I_\nu = -10$ to $I_\nu = 0$. Here, the air cell is considered to be changed to a liquid cell because the adding material is achieved in the cavity inside the melt pool (Figure 2-7). When melt pool is developed on the entire thickness of the plate with subsidence of the liquid, part of the metal subdomain is replaced by air subdomain and vice versa. The initial metal cell ν with $I_\nu \geq 0$ has its level-set function $\varphi_\nu < 0$, once the value of φ_ν changes to be positive, the state of ν is changed from $I_\nu \geq 0$ to $I_\nu = -10$ to present the transition from metal cell to air cell.

2.4 Coupling between Macro-Meso

In the CAFE method, the coupling of Macro-Meso-Micro scales is achieved by the transport of information between FE mesh (Macro), CA mesh (Macro) and CA grid (Meso), as presented in section 2.1

2.4.1 Transport FE mesh => CA mesh => CA grid

Some variables computed at FE nodes as solutions of equations presented in section 2.2 (in this work, the variables transported from FE mesh to CA cell are the temperature T and the level-set function φ) must be interpolated at first to the CA nodes. The relations between FE mesh, CA mesh and CA grids are detailed in Figure 2-1. The CA mesh is superimposed onto the FE mesh and may correspond to a lower volume. A specific CA node n_j^{CA} is located inside one FE element E^{FE} composed by FE nodes $n_i^{FE}, i \in [|1,4|]$ for 3D. The transported value of the variable $x^t_{n_j^{CA}}$ for the CA node n_j^{CA} at time t is interpolated from the variable $x^t_{n_i^{FE}}$ of the FE node $n_i^{FE}(n_i^{FE} \in E^{FE})$:

$$x^t_{n_j^{CA}} = \sum_{n_i^{FE} \in E^{FE}} \phi_{n_i^{FE}}\left(n_j^{CA}\right) x^t_{n_i^{FE}} \tag{2-81}$$

where $\phi_{n_i^{FE}}\left(n_j^{CA}\right)$ is the interpolation coefficient of FE node n_i^{FE} estimated for CA node n_j^{CA}. The temperature on CA node can be applied to determine the temperature for the apex of the grain growth envelope by interpolation.
Then for a cell ν inside the CA element E^{CA} composed by $n_j^{CA}, j \in [|1,4|]$ for 3D, the transported value of x_ν^t for the cell ν is:

$$x_\nu^t = \sum_{n_j^{CA} \in E^{CA}} \phi_{n_j^{CA}}(\nu)\, x^t_{n_j^{CA}} \tag{2-82}$$

where $\phi_{n_j^{CA}}(\nu)$ is the interpolation function of CA node n_j^{CA} estimated for cell ν.

For example, the level-set function on the cell is used to determine the cells states (air or metal) as mentioned in section 2.3.5.
Besides, any other variables calculated such as fluid flow velocity [Car11, Car12] can be also transported to enrich the CA resolution.

2.4.2 Transport CA grid => CA mesh => FE mesh

As mentioned in section 2.3.4, an envelope fraction $g_{v^{CA}}^{en}$ is computed for each cell. The envelope fraction $g_{v^{CA}}^{en}$ represents the fraction of the mushy structure (*i.e.* the mixture of the interdendritic liquid (l_1), and solid (s), as presented in Figure 2-1). Therefore, it can be used to determine the mushy zone fraction associated to FE node n^{FE}, $g_{n^{FE}}^{m}$ (details will be presented in section 2.4.3). In order to obtain the $g_{n^{FE}}^{m}$, a mushy zone fraction associated to CA node n^{CA}, $g_{n^{CA}}^{m}$ should be firstly computed using a reassignment method covering the entire set of cells surrounding the node:

$$g_{n_j^{CA}}^{m} = \frac{\sum_{v^{CA} \in E^{CA}} \phi_{n_j^{CA}}(v^{CA})\, g_{v^{CA}}^{en}}{\sum_{v^{CA} \in E^{CA}} \phi_{n_j^{CA}}(v^{CA})} \tag{2-83}$$

where $g_{n_j^{CA}}^{m}$ is the mushy fraction associated to the CA node n_j^{CA}. Then this mushy zone fraction at CA node is interpolated to FE node, with the same principle introduced in section 2.4.1:

$$g_{n_i^{FE}}^{m} = \sum_{n_j^{CA} \in E^{CA}} \phi_{n_j^{CA}}(n_i^{FE})\, g_{n_j^{CA}}^{m} \tag{2-84}$$

where $\phi_{n_j^{CA}}(n_i^{FE})$ is the interpolation function of CA node n_j^{CA} estimated for FE node n_i^{FE}.

2.4.3 Chaining and coupling method

Two coupling schemes are used thereafter in the proposed simulations and summarized as chaining and coupling methods, as shown in Figure 2-12. The main difference relies on the communications between the CA and FE methods and the resulting solution of the energy conservation. The chaining scheme (Figure 2-12 left) simply makes use of the temperature field computed on nodes n^{FE} of the FE mesh, $T_{n^{FE}}$, projected on nodes n^{CA} of the CA mesh, $T_{n^{CA}}$, and then interpolated on cell v of the CA grid, $T_{v^{CA}}$. As presented in section 2.4.1. Based on this temperature field, the growth velocity of the grain envelope along the ⟨100⟩ directions, $v^{\langle 100 \rangle}\left(\Delta T_{v^{CA}}\right)$, is therefore computed by applying the kinetic dendrite tip law. As no coupling occurs, the mushy fraction at cell scale is not considered in FE resolution and its fraction has no influence on the solution of the heat conservation equation computed on nodes of the FE mesh. The temperature field itself, $T_{n^{FE}}$, is consequently computed using the uniquely pre-defined solidification path as detailed in chapter 3. The fraction of the solid phase $g_{n^{FE}}^{s}$ uniquely depends on the temperature, $g^{s}\left(T_{n^{FE}}\right)$ given by the solidification path.
Coupling approach (Figure 2-12 right) is more sophisticated as the fraction of the solid phase onto FE mesh now depends on the existence of the grains and on the amount of the mushy zone, defined by the mushy fraction $g_{n^{FE}}^{m}$ (section 2.4.2). Therefore, the fraction of phases becomes $g_{n^{FE}}^{s} = g^{s}\left(T_{n^{FE}}\right) \times g_{n^{FE}}^{m}$. Thus, the temperature depends on the existence of grains and on the

amount of mushy domain. This coupling scheme is required when the temperature field is expected to depend on the microstructure development [Gan94, Gui04, Car12].

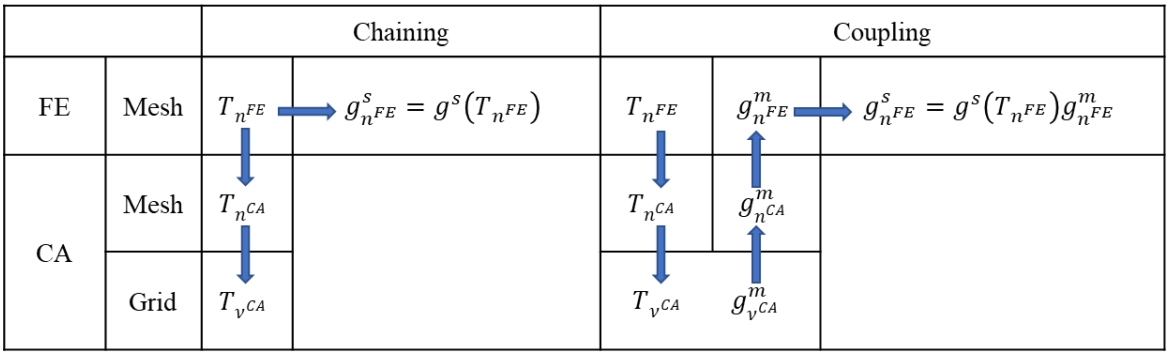

Figure 2-12. Chaining and coupling strategies developed for the CAFE model.

Influence of the chaining and coupling method on the grain structure is investigated in chapter 3 regarding the results obtained with various strategies.

2.4.4 Microscopic time step

In the CAFE model, two time steps are defined: the FE time step, Δt refered as macroscopic time step, is used to for the resolution of mass, momentum, and energy conservation at macroscopic scale onto the FE mesh; the CA time step, δt referred as microscopic time step, is used for the CA resolution in order to follow grain growth envelope evolution. In fact, the growth and capture algorithm require that during a time step, a given cell can only capture its direct neighbors. In other words, the maximum development of the envelope during a time step must be at most equal to the cell size l_{CA}. The value of macroscopic time step, Δt ($0.1 \sim 1\ s$), currently used can rarely fulfill this condition, also considering cell size ($10\ \mu m \sim 100\ \mu m$). This requires the use of a smaller time step, δt, to follow grain structure evolution defined as:

$$\delta t = Min\left(\frac{l_{CA}}{v^{en}_{v\,max}}, \Delta t\right) \tag{2-85}$$

where $v^{en}_{v\,max}$ is the maximum dendritic growth velocity. In could be noted that during a macroscopic time step Δt, the global fields as temperature and velocity do not evolve. More details are provided by Carozzani [Car12].

2.5 Grain structure data operation

2.5.1 Storage of initial structure

A preexisting structure is required before the simulation of welding process, which is also named the initial grain structure. Normally, the initial grain structure is equiaxed and deduced from a first CAFE simulation of the structure formed during casting assuming nucleation and growth of grains in a uniform temperature domain [Car12, Che14]. This initial grain structure is stored as a binary file [Cam19]. More details are provided by Chen [Che14], despite some

clear improvements have been proposed to improve the management and registration of the description of the initial structure. The structure of the file is presented here after.
The whole binary file contains three parts of data: the header, the information of cells and the information of grains:

- Header:
  - Total number of the CA element NbE^{CA},
  - Dimension of the problem,

  - Center of element number 1,
  - Rank of the cells in element number 1,
  - Element mark of element number 1,

  - Center of element number 2,
  - Rank of the cells in element number 2,
  - Element mark of element number 2

    …
  - Center of element number NbE^{CA},
  - Rank of the cells in element number NbE^{CA},
  - Element mark of element number NbE^{CA}

    …
  - Empty line
  - End row of the cells' information
  - Empty line
- Cell information:
  - Cell information for the cells inside the element number 1,
    - Grain number of cell number 1 in the element number 1,
    - Grain number of cell number 2 the element number 1,

    …
  - Cell information for the cells inside the element number 2,
    - Grain number of cell number 1 in the element number 2,
    - Grain number of cell number 2 the element number 2,

    …
  - Cell information for the cells inside the element number NbE^{CA},
    - Grain number of cell number 1 in the element number NbE^{CA},
    - Grain number of cell number 2 the element number NbE^{CA},
    - …
- Grain information (i.e. angle : 1 angle in 2D and 3 angles in 3D)
  - Euler angle for grain number 1,
  - Euler angle for grain number 2,
  - …

Element mark (*boolean*) defined in the first lines are used to determine if the element contains already cells information associated to grain structure as Euler angles. This Boolean is equal to

0 (*false*) before the creation of the initial grain structure and 1 (*true*) once the initial grain structure is created. In order to keep compatibility with the storage strategy, all the air cells are associated to a grain number -10 and Euler angles are fixed with $\varphi_1 = \phi = \varphi_2 = 181°$.
It could be clearly noted that the size of the binary file for a fixed CA mesh is related to the total number of elements, depending from the CA mesh size, total number of cells, depending from the cell size, and the total number of grains, depending from the grain density of the initial grain structure. However, the total number of cells is the main factor defining the file length.

2.5.2 Dynamic allocation

A dynamic allocation algorithm is proposed by Carozzani [Car12, Che14] to reduce the resources required in the CAFE resolution especially in the CA model. In fact, for a typical welding domain of $100 \times 50 \times 30\ mm^3$, assuming a cell size of the order of 50 to 100 μm [Gan94], the total number of cells is about $0.15 - 1.2$ billions. This can cause a lot of compute resource wasting if all the cells are allocated into the memory of the computer as only a small part should be considered in the growing structure (basically the mushy zone and the melt pool). Therefore, a dynamic allocation algorithm is used in CA computations developed with the *Cimlib* library [Car14, Che14] to solve this problem. All the cells inside the same CA element E^{CA} are allocated or deallocated at the same time. Consequently, the dynamic allocation is achieved at the CA element scale. A CA element will be activated and the cells inside will be allocated when at least one of the below conditions is fulfilled:

- At least one node of the element is above the liquidus temperature,
- At least one of its neighbor elements fulfills the previous condition.

In order to save computation time, the elements located in the gas (*i.e.* all the element nodes located in the gas subdomain) will never be activated as no grain structure will growth inside, the cell information (Euler angles) of air cell is always kept. This is not contradictory with the transformation between air cell and metal cells presented in 2.3.5. In fact, the transformation takes place always in an element with at least one node in the metal subdomain. Once a CA element is activated, the corresponding information in the binary file will be read into the memory and be rewriten until this CA element is deactivated, which occurs when both the conditions below are fulfilled simultaneously:

- All the nodes of the element are below the liquidus temperature,
- The mushy fractions of all the nodes of the element are equal to 1.

More details of the dynamic allocation can be found in [Car12, Che14, Che14-2].

Besides the grain structure date operations presented above, some other grain structure analyses tools such as grain structure reconstruction and grain statistical analyses are also developed for the NEMESIS project, aiming at the exploitation of simulated grain structure in the CND software (*e.g.* ATHENA and CIVA [Civ16]). Details of these tools are presented in Appendix 1.

2.6 Conclusions

In this chapter, the CAFE approach dedicated to model welding process has been detailed. In the FE model, the mass, momentum and energy conservation equations are solved by finite element method. Besides, other numerical methods are also coupled with the CAFE model to better simulate the welding process: the level-set method is applied to track the metal/gas interface, the adaptive remeshing method is used to reduce the computation time by keeping a good quality of resolution, the mass correction method is carried to correct the numerical problem of mass conservation. In the CA model, the grain structure is simulated by changing the states of cells defined in a CA grid associated to the CA mesh. The dynamic allocation is developed to reduce the required computational resource. The reconstruction of grain structure and the grain statistical analyses give the possibility to implement the virtual microstructure (especially grain structure) of CAFE model in the NDT simulation software to investigate the relationship between the ultrasonic wave and grain structure.

2.7 French summary

Dans ce chapitre, le modèle CAFE utilisé dans ce travail pour la modélisation des procédés de soudage est présenté en détail. Dans l'approche FE, les équations de conservation globales associées à la masse, la quantité de mouvement et l'énergie sont résolues par la méthode des éléments finis. Par ailleurs, d'autres méthodes numériques sont également couplées au modèle CAFE pour mieux simuler le procédé de soudage: la méthode level-set est appliquée pour suivre l'interface métal/gaz, la méthode de remaillage adaptatif est exploitée pour réduire le temps de calcul en gardant une bonne qualité de résolution, la méthode de correction de masse permet de s'assurer de la conservation de la quantité de matière. Dans le modèle CA, la structure des grains est simulée par le changement des états de cellules définies dans une grille de cellules associée au maillage CA. L'allocation dynamique est développée pour réduire la ressource de calcul requise. La reconstruction de la microstructure et les analyses statistiques des grains donnent la possibilité d'implémenter le résultat (en particulier la structure des grains) du modèle CAFE dans le logiciel de simulation CND pour étudier la relation entre l'onde ultrasonore et la structure des grains.

3 Single pass GTAW upon sheet without added material

In this chapter, the 3D CAFE model is applied to a single pass GTAW without adding material on a 316L steel sheet. A comparison of macroscopic field (such as melt pool shape, fluid flow velocity) and microstructure between experiment and simulation result is achieved.

3.1 Material properties

Because of its superiority in resisting pitting and stress corrosion cracking [Kov02], 316L steel is widely used in chemical and petrochemical industry. As an austenite steel of low-carbon composition, the sensitization in the heat affect zone is minimized during welding [AISI]. The chemical composition of 316L used in this work is presented in Table 3-1 and corresponds to a standard composition.

Table 3-1. Chemical composition of 316L steel (according to EN10088-4 [EN09]).

Element	Fe	C	Cr	Mn	Mo	Ni
Composition (wt. %)	balance	0.016	16.765	1.383	2.044	10.07
Element	P	S	Si	N	Co	
Composition (wt. %)	0.031	0.001	0.389	0.041	0.187	

Figure 3-1(a) describes the transformation path computed with the TCFE9 thermodynamic database [TCFE9] by software Thermo-Calc [The18] assuming partial equilibrium during solidification [Kos16] with activation of the peritectic transformation where liquid, l, and ferrite, α, transform into austenite, γ. It shows the evolution with temperature, T, of the volume fraction of phases, g^{φ} with $\varphi = \{l, \alpha, \gamma\}$. Hence, all the average volumetric properties for the solid $g^s\langle\xi\rangle^s$ can be expressed as: $g^s\langle\xi\rangle^s = g^\alpha\langle\xi\rangle^\alpha + g^\gamma\langle\xi\rangle^\gamma$ with $g^s = g^\alpha + g^\gamma$. Upon cooling, solidification starts at the liquidus temperature, $T_{liq} = 1452$ °C, and ends at the solidus temperature, $T_{sol} = 1301$ °C. The latter value is chosen for a remaining fraction of liquid lower than 1%. For simplicity, no other solid phases, as intermetallic phases, have been considered in the present simulations. The remaining fraction of ferrite is $g^\alpha = 13\%$.
The choice of the partial equilibrium solidification path is motivated by experimental observations showing that austenite is dominant at room temperature after completion of solidification [Li21, Elm00]. Yet a full equilibrium lever rule (LR) transformation path predicts that ferrite is the dominant phase at room temperature as austenite resulting from the peritectic transformation retransforms into ferrite at low temperature, reaction being preventing by the high cooling rate inherent to the present welding process, as shown in Figure 3-2 (a). It could also be noted that for the LR path, the peritectic transformation is similar to the one observed

for the partial equilibrium path. At the same time, a Gulliver-Scheil (GS) approximation cannot predict the peritectic transformation [Kos16] as shown in Figure 3-2 (b) as the solid phase transformation are prevented. So, the partial equilibrium with peritectic transformation seems the more reasonable approximation. Tabulations of the volumetric enthalpies are also extracted at the corresponding temperature and phase composition by multiplying the density, ρ^{φ}, by the enthalpy per unit mass, h^{φ}, for all phases $\varphi = \{l, \alpha, \gamma\}$ using the PhysalurgY library [Phy].

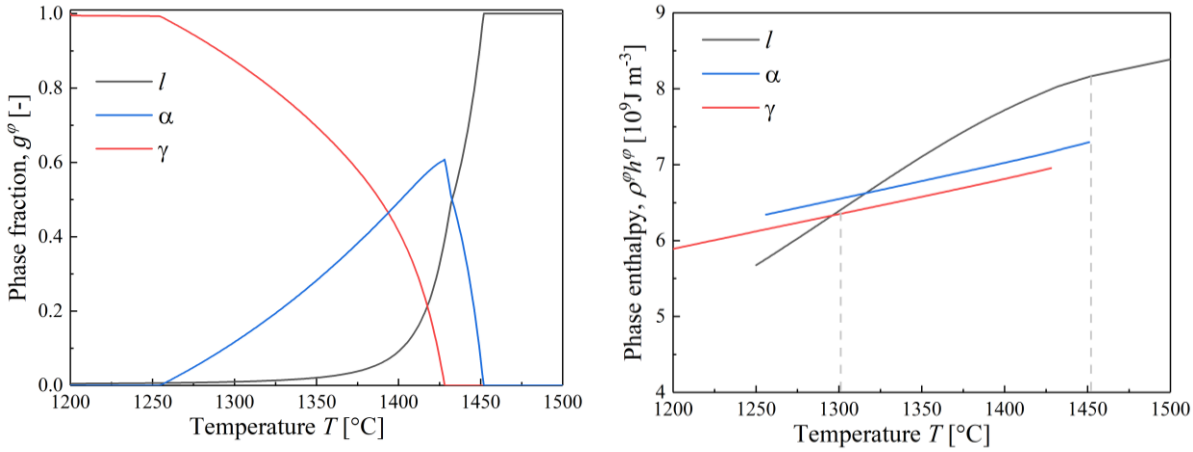

(a) (b)

Figure 3-1. Temperature evolution of (a) the volume fraction of the phases involved during solidification, g^{φ} with $\varphi = \{l, \alpha, \gamma\}$, corresponding to liquid, l, ferrite, α, and austenite, γ, phases and (b) their volumetric enthalpy, $\rho^{\varphi}h^{\varphi}$ [Phy].

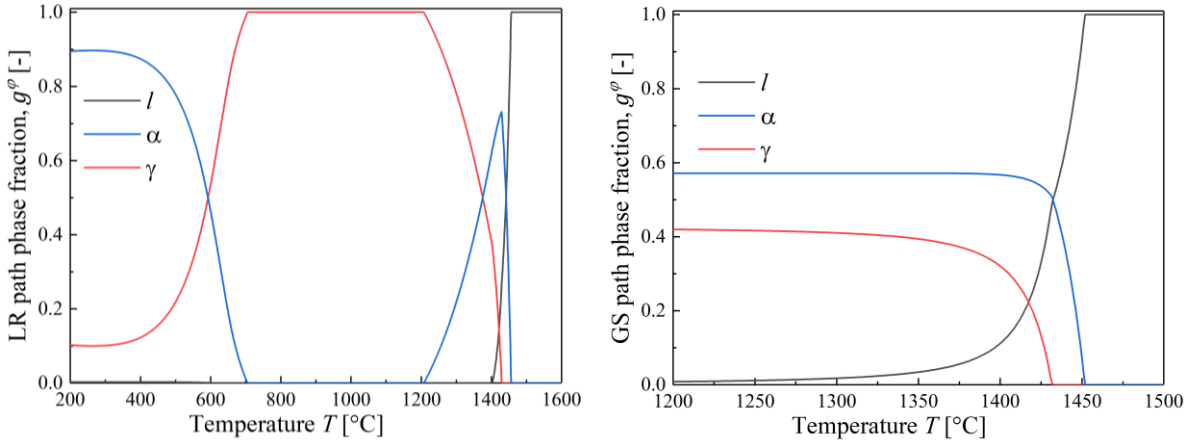

(a) (b)

Figure 3-2. Temperature evolution of the volume fraction of the phases involved during solidification, (a) full equilibrium lever rule path, (b) Gulliver-Scheil path [Phy].

Besides, the thermal conductivity $\langle\kappa\rangle^{\varphi}$ for all phases $\varphi = \{l, \alpha, \gamma\}$ is expressed by the relationship $\langle\kappa\rangle^{\varphi} = 0.0143T + 13.803$ for T in °C within the interval $[20, 1400]$ °C [Mur11],

as presented in Figure 3-3 (a). In present simulations, the value of thermal conductivity at 1400 °C (33.8) is kept for higher temperature.

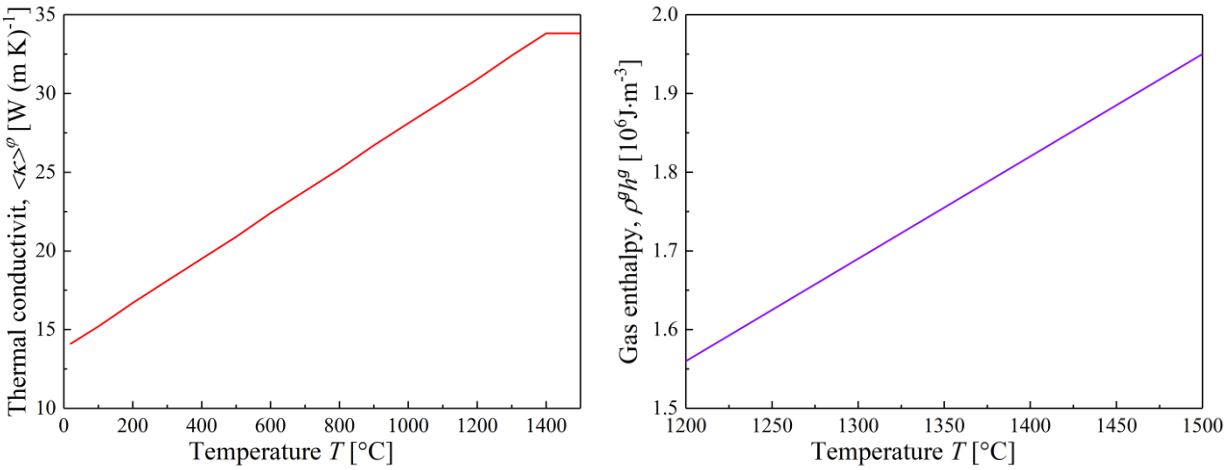

(a) (b)

Figure 3-3. (a) thermal conductivity $\langle\kappa\rangle^{\varphi}$ of 316L steel for $\varphi = \{l, \alpha, \gamma\}$ [Mur11]. (b) temperature evolution of gas volumetric enthalpy, $\rho^g h^g$.

The evolution of gas enthalpy with temperature is linear and associated to a volumetric heat capacity, presented in Figure 3-3 (b).

The other properties used for 316L steel grade and gas in present simulations are listed in Table 3-2. In could be noted that the physical properties of gas are mostly taken as constant and are not of the expected order regarding the values proposed in the literature (*i.e.* the gas thermal conductivity is increased by a factor of almost 100). This choice has been done to reduce numerical difficulties and computing time. However, thermodynamic properties of gas are of few influences on the simulation results [Che14]. Another point to mention is the dynamic viscosity of metal and gas. The Navier-Stokes equations, (equation 2-59), are solved on the whole domain, that is for gas, liquid and solid metal. Having in mind that the main objective of the mechanical resolution is to predict fluid flow in the melt pool, this justifies i) the use of a Newtonian behavior (and Navier-Stokes equations) in the solid, as the objective is not to address the plastic deformation of the solid metal, and ii) the use of viscosity values that will be the nominal one in the liquid metal, but that could be arbitrarily adjusted in the gas and the solid. Those arbitrary values should comply with two constraints: the solution velocities in the solid should be small enough, compared to the liquid velocities, and the global viscosity range should be as small as possible, in order to allow a rapid convergence of the iterative solvers in charge of the resolution of the linear sets of equations. Therefore, as indicated in Table 3-2, the viscosities of solid phases are identically chosen equal to 1000 Pa s, while the gas viscosity is chosen 10 times smaller than the liquid viscosity, as the present model does not aim at a

quantitative prediction of gas flow. Finally, equation (2-60) is used to model the viscosity change within the metal/gas interfacial region, while the viscosity change between solid and liquid is modelled by the following logarithmic mixing rule: $\langle\mu\rangle^M = (\mu^l)^{g^l}(\mu^\alpha)^{g^\alpha}(\mu^\gamma)^{g^\gamma}$. Taking the same dynamic viscosity value for both solid phases, $\mu^s = \mu^\alpha = \mu^\gamma$, one can rewrite $\langle\mu\rangle^M = (\mu^l)^{g^l}(\mu^s)^{(1-g^l)}$.
Besides, the Marangoni coefficient chosen in the simulation is twice than reported in the literature:$-4.3 \cdot 10^{-4}$ N m^{-1} K^{-1} [Sah88]. The aim is to reduce the underestimation of fluid flow caused by the increased viscosity for gas and liquid.

Table 3-2. Properties used for the simulations for the 316L steel grade and for argon gas.

Property	Variable	Value	Unit
Marangoni coefficient	$\partial\gamma/\partial T$	$-8 \cdot 10^{-4}$	N m^{-1} K^{-1}
Surface tension coefficient [Tra11]	γ_s	1.943	N m^{-1}
Metal density	$\rho^\varphi, \varphi = \{l, \alpha, \gamma\}$	7800	kg m^{-3}
Gas density	ρ^g	1.3	kg m^{-3}
Liquid metal dynamic viscosity	μ^l	$5 \cdot 10^{-2}$	Pa s
Solid metal dynamic viscosity	$\mu^\varphi, \varphi = \{\alpha, \gamma\}$	1000	Pa s
Gas dynamic viscosity	μ^g	$5 \cdot 10^{-3}$	Pa s
Gas thermal conductivity	κ^g	1	W m^{-1} K^{-1}

As presented in chapter 2, the growth of grain assumes that primary solidification takes place with a dendritic microstructure along the main ⟨100⟩ crystallographic directions. A continuously dendrite kinetic law for growth velocity, $v^{\langle 100\rangle}$, depending on the undercooling, ΔT, is applied. The dendrite tip kinetics law used in the simulation with CAFE model are presented in Table 3-3. The law K_1 is proposed in order to obtain similar melt pool sizes compared with experiments. Details are presented in section 3.4 . Law K_2 is deduced from PhysalurgY [Phy], The module used in present application corresponds to the computation of dendrite tip growth kinetic in multicomponent alloy based on the model proposed by Hunziker [Hun01]. Thermodynamic equilibrium at the solid/liquid interface are obtained using the TCFE9 [TCFE9] database and chemical diffusion in liquid phase is provided by the MOBFE6 [MOBFE6] database.

Table 3-3. Dendrite tip kinetics law.

K_1	$v_1^{\langle 100 \rangle} = 1.8 \cdot 10^{-6} \Delta T^{2.7}$	mm s^{-1}
K_2	$v_2^{\langle 100 \rangle} = 1.01 \cdot 10^{-3} \Delta T^{3.26} + 1.32 \cdot 10^{-6} \Delta T^{5.19}$	mm s^{-1}

Figure 3-4 presents the undercooling dependence of these laws based on power law relations. The blue and purple horizontal line presents two welding speeds V_1 and V_2, (3.3 and 4.3 mm. s^{-1}) applied in the welding experiments detailed in section 3.2. Corresponding undercoolings are respectively equal to 208°C and 230°C for K_1, 12°C and 12.5°C for K_2. The influences of these two growth laws on the grain structure is discussed in section 3.5

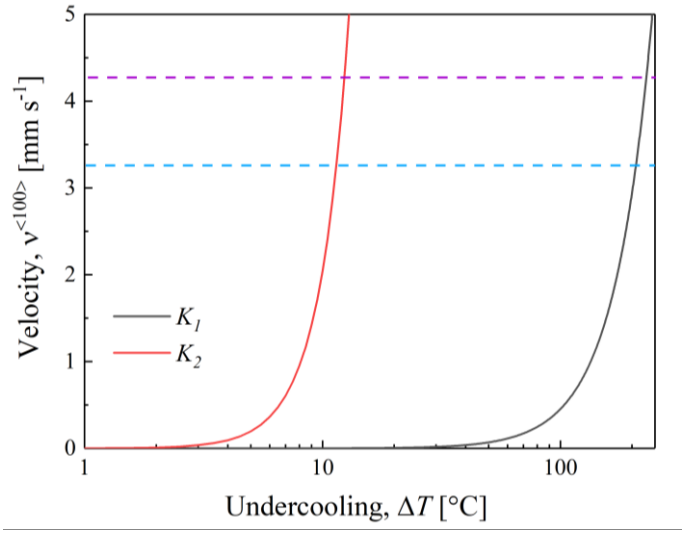

Figure 3-4. Growth velocity, v, as a function of dendrite tip undercooling, ΔT. Evolution of investigated laws K_1 and K_2

3.2 Experiment set up of single pass GTAW

All the experimental work presented hereafter is established and achieved in LMGC (Laboratoire de Mécanique et Génie Civil) of the University of Montpellier who is a partner of the NEMESIS project. Details of the experimental work was presented by Nicolas Blanc [Bla20, Bla21] who was in charge of these experimental developments and associated analysis. This experiment aims at investigating grain structure development and melt pool evolution in welding processes using direct observations developed in GTAW processes. Results and details can also be found in [Xue21].

3.2.1 Experimental device and parameters

The experimental device is designed to carried out full penetration weld on sheet-metal plates [Bla20, Bla21]. The device was designed to have a static heat input in the lab frame in order to

simplify the observation. It is composed of a GTAW station with arc voltage and welding current measurement systems. A mobile support is used with controlled motion speed. It is made of an open rectangular metallic stand with dimensions 150×75×1.5 mm closed at its top by the sheet metal plate that serves as sample coupon and at its bottom by a glass plate. The volume encompassed between these elements creates a gas chamber continuously filled with argon for the protection of the lower side of the weld pool from air oxidation. Similarly, an argon flow rate of 15L/min is applied during processing through the static welding torch in order to protect the upper side of the weld pool (Figure 3-5(b)). A static camera (Mako models from Allied Vision Technologies), labelled AVT Cameras in Figure 3-5 (a), offer a global view of the weld pool from its lower side through the glass plate at 300 frames per second. The region of interest is illuminated by a 15 W laser diode that is fixed at the lower side of the metal plate. Thanks to the differences of reflexion between solid and liquid parts, the liquid zones are identified. In addition, it is possible to measure the size and shape of the melt pool and to estimate fluid flow by following the trajectories of floating particles at the molten metal/gas surfaces. Welding is carried out along the X direction by moving the mobile support in the opposite direction at velocity V. The vertical direction through the thickness of the sheet metal plate is Z so the complementary transverse direction of the reference frame is Y as presented in Figure 3-5. The origin of the system, labelled O in Figure 3-5, is chosen at the center of the lower surface of the plate.

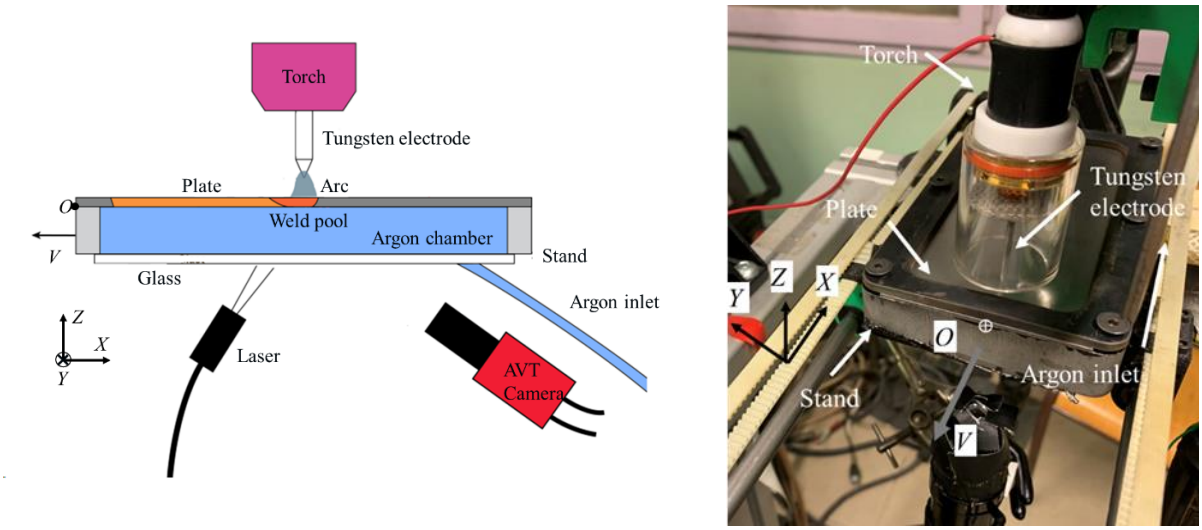

(a) (b)

Figure 3-5. Experimental setup with (a): schematics of the various devices including diagnostics apparatus and sheet-metal plate sample, and (b): picture of the GTAW torch and stand of the sample.

The arc is initiated by lift-arc in a motionless configuration at the beginning of the experiment and the support begins to move 0.4 s after. The sample dimensions are 150×75×1.5 mm. Values of the welding parameters are chosen to obtain fully penetrated weld pool and given in Table 3-4. Two welding speeds are investigated, referenced with $V_1 = 3.3$ mm s^{-1} and $V_2 =$

4.3 mm s^{-1}. The weld pool dimension and the shape of the solidification interface are expected to be changed by modulating the welding speed leading to an evolution of the heat transfer and fluid flows motions. It is worth noting that the welding parameters, *i.e.* the welding voltage and the current intensity, are maintained constant for the two reported experimental configurations so as to simplify comparisons. The total welding length is 100 mm. This was found sufficient to reach a steady regime for the melt pool shape over a sufficiently large distance, *i.e.* an established and fixed melt pool shape in the reference associated to the cameras. The measures are realized during the last 35 mm excluding the arc extinction stage.

Table 3-4. Welding parameters.

Parameter	Value		Unit
	V_1	V_2	
Welding voltage, U	8.76	8.67	V
Current intensity, I	81.3	81.5	A
Welding speed	3.3	4.3	mm s^{-1}
Welding length	100		mm
Start point of welding	$(X_S, Y_S, Z_S) = (20, 0, 1.5)$		mm

3.2.2 In-situ observations and characterizations

Characterizations are first conducted by analyses of the in-situ video recording of the melt pool by the cameras. More than two thousand frames were analyzed by N. Blanc per experiment in order to extract the evolution of weld pool geometry. Some little variations of shapes or positions can be observed probably due to the fluctuation of heat and to the fluid flows reflecting the dynamic of the weld pool. On the base of these data, N. Blanc has defined the average weld pool contour during the steady state.

Figure 3-6 presents the steady shape of the melt pools at established welding regimes for speeds V_1 and V_2 as observed on the bottom surface of the plate. The contrast and the reflection of the light is sufficient to clearly distinguish between the surface of the molten metal, with smooth distribution of the grey levels, and the solid-containing regions where modulations of the grey color appear due to surface roughness. Delimitations of the molten pools can thus be highlighted in yellow in Figure 3-6. Typical teardrop shapes are observed, with smaller dimensions as velocity increases while maintaining constant welding voltage and current intensity (Table 3-4). The fluid flow velocity is also evaluated thanks to visible moving particles which are present at the surface of the melt pool. The particle trajectories are obtained by PTV method [All21]. A typical tracking of the particles with time is superimposed in Figure 3-6 (b) in the frame of reference attached to the heat source. The PTV method is based on moving particles or bubbles located at the surface of the weld pool. The direction of liquid circulation can be evaluated and

the lower bound of velocities of the particles are obtained by the time derivative of their positions. Flows were observed from the center towards the border of the melt pools, in a typical direction induced by the negative Marangoni coefficient associated to surface tension. More details on the experimental setup, in-situ diagnostics techniques and exploitation methodologies are available in reference [Bla20, Bla21].

Post-mortem metallography is also achieved in transverse cross sections of the weld bead. This gives access to the weld bead profile and measurement of its deflection toward gravity due to the flow of the matter during its phase changes. Consequently, polishing is required in order to prepare the samples for EBSD measurements conducted in XY planes above the top surface of the plate. Beside the texture of the grain structure produced upon solidification of the melt pool, it gives the initial grain density in the sheet-metal plates.

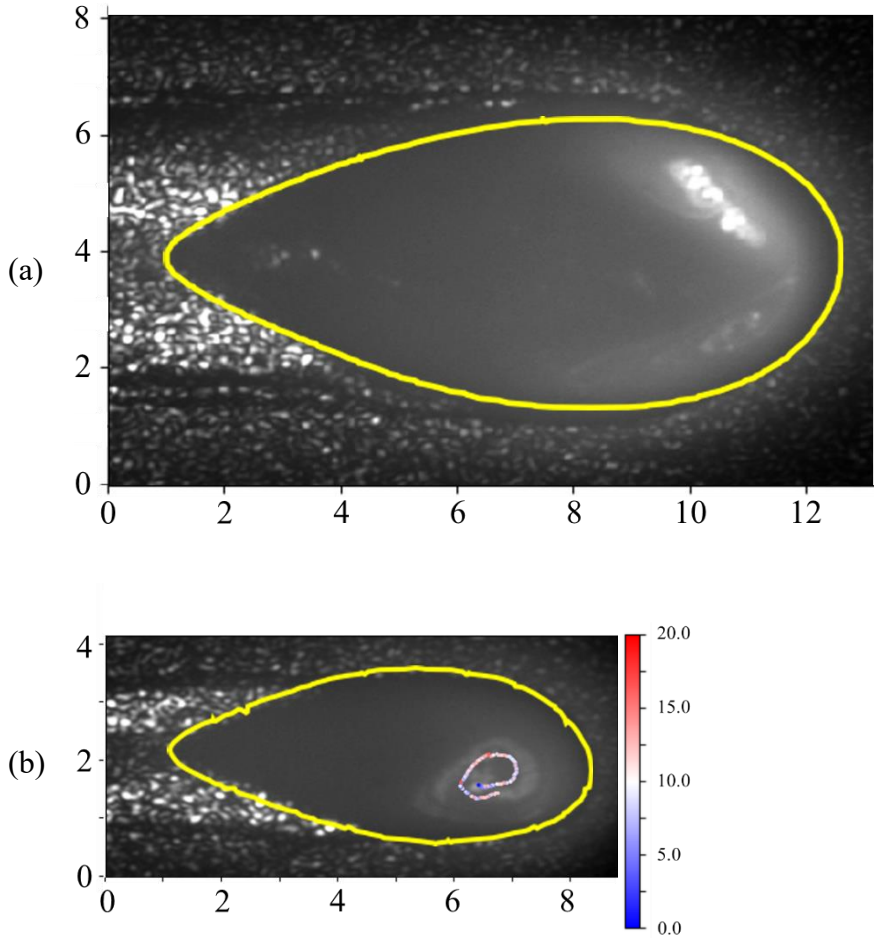

Figure 3-6. Surface melt pool as recorded by video imaging at the bottom surface of the samples for welding speed (a) V_1 , (b) V_2 (see Table 3-4). Scales are reported in mm [Bal21]. Moving particles are only represented in (b) V_2, particle velocity scale in mm s^{-1}.

As presented in Figure 3-7, two square zones of $100\ \mu m \times\ 100\ \mu m$ in the domain of base metal containing the equiaxed grains is chosen. In these two square zones, the grains totally inside (except for too small grains, *i.e.* two grains between grain number 14 and number 16 for

Figure 3-7 (a)) and the grains at the top and left boundary is counted as the grains inside the zone. The average number of grains is counted as 19, giving an average grain surface (2D) at $526\ \mu m^2$. Supposing the grains are equiaxed, an average grain size is $27\ \mu m$. The estimated initial grain density is $6.4 \cdot 10^{13}\ \mathrm{m}^{-3}$ grains per cubic meter.

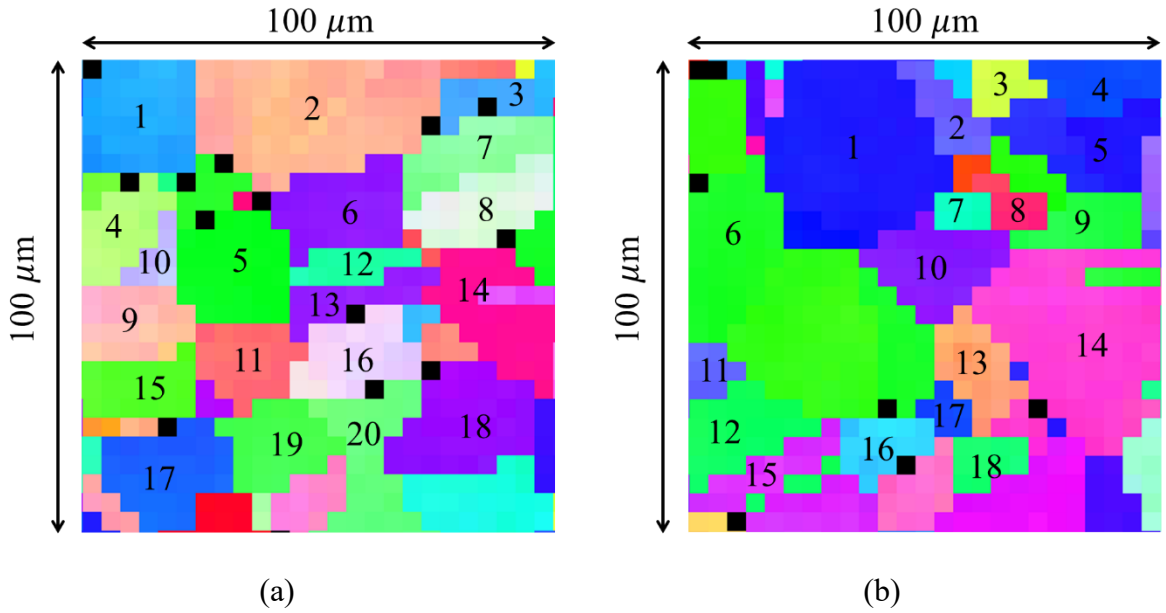

(a) (b)

Figure 3-7 EBSD measurements of base metal of the weld part with grains separated in different colors and numerate, black pixels present the EBSD patterns that could not be indexed.

3.3 Simulation parameters

These two welding tests, previously presented, associated to velocities V_1 and V_2 are simulated in order to compare numerical results associated to the thermo-mechanical evolutions of pieces and the final grain structures to the experimental observations. The global simulation domain contains the metal subdomain Ω^M and the surrounded gas subdomain Ω^G on the top and bottom surface of the metal plate. As presented in Figure 3-8 by the FE mesh.

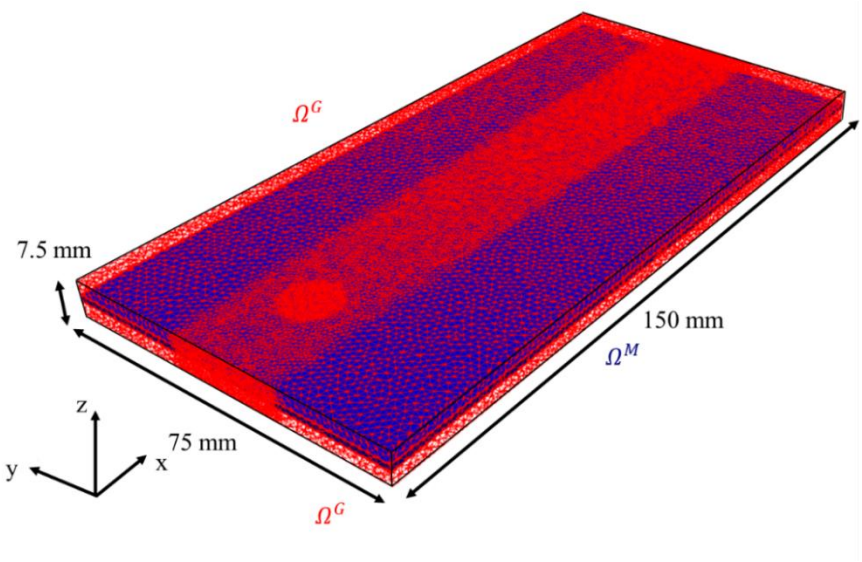

Figure 3-8. Simulation domain with (blue) metal subdomain Ω^M between (red) the top and bottom gas subdomains Ω^G.

A zoom of the initial FE mesh is presented in Figure 3-9 (a), and the CA mesh is highlighted in the center of the FE mesh in Figure 3-9 (b). As presented in Chapter 2, the CA domain and its associated mesh are smaller compared with the FE mesh in order to save computation time. Besides, the CA mesh is chosen to be thicker than the metal plate containing initial gas subdomain. The aim is to follow and investigate the deformation of metal plate due to the fully penetration melt pool. Details of the mesh size and the dimension of domain are given in Table 3-5. As shown in Figure 3-9 (a), the meshes around the heat source (Zone HS) is refined to better solve the FE problem in this zone where temperature gradient is large. During the simulation, this zone of refined mesh will advance with the heat source by the adaptive remeshing strategy presented in Chapter 2.

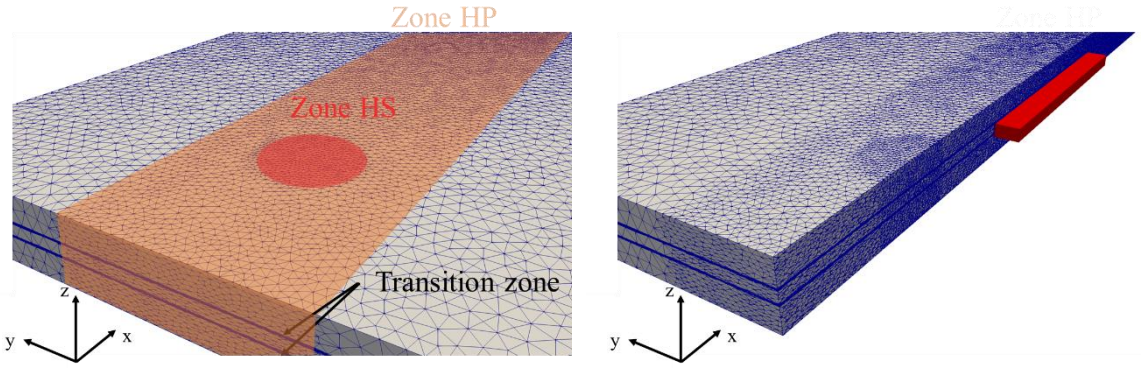

(a) (b)

Figure 3-9 (a) zoom of initial FE mesh, (b) cut of initial FE mesh by plan Y=0 (blue) and CA mesh (red).

Table 3-5. Mesh parameters.

Parameter	Value
Global simulation domain, Ω	$150 \times 75 \times 7.5$ mm
Metal subdomain, Ω^M	$150 \times 75 \times 1.5$ mm
Top and bottom gas subdomain, Ω^G	$150 \times 75 \times 3$ mm
Half thickness of transition zone, ε	0.1 mm
FE mesh size in the transition zone (Figure 3-9 (a))	20 µm
FE mesh size along the heat source path (Zone HP, Figure 3-9 (a))	1(X), 1(Y), 0.4(Z) mm
FE mesh size around the heat source (Zone HS, Figure 3-9 (a))	0.5 mm
FE mesh size elsewhere	1.5 mm
CA domain Ω^{CA}	$40 \times 7 \times 1.8$ mm
CA mesh size (fixed)	0.2 mm
CA cell size	20 µm

The welding parameters used in the simulation are similar to the experimental ones (Table 3-4), except for the welding length. In the experiment, a weld bead of length 100 mm is achieved to measure the result in steady state (measurement is done at the last 35 mm [Bla20, Bla21]). The simulation shows that, the steady state arrives much earlier at about 45 mm. Therefore, in order to save the computation time, a welding time of 15s is chosen which leads to a weld bead of $49.5\,mm$ for $V_1 = 3.3\,mm\,s^{-1}$ and a weld bead of $64.5\,mm$ for $V_2 = 4.3\ \mathrm{mm\ s^{-1}}$. Other details of welding parameters are presented in Table 3-6.

Table 3-6. Welding parameters in simulation.

Parameter	Value	
	V_1	V_2
Welding speed	$3.3\ \mathrm{mm\ s^{-1}}$	$4.3\ \mathrm{mm\ s^{-1}}$
Start point of welding	$(X_S, Y_S, Z_S) = (20, 0, 1.5)$	
Welding duration	$15\ s$	
End point of welding	$(X_E, Y_E, Z_E) = (69.5, 0, 1.5)$	$(X_E, Y_E, Z_E) = (84.5, 0, 1.5)$
Weld bead length	49.5 mm	64.5 mm
Efficiency, η	0.65	0.6
Heat source power, $\eta \times U \times I$	463 W	424 W

In the simulation, the initial temperature considered in the heat conservation problem equation (2-21) is room temperature (20℃). For Navier-Stokes equations (2-59) the velocity field for the global system is equal to zero at initial time. Besides, the GTAW process is simulated without adding material, $\dot{\theta} = 0$ for the global system during the simulation.

Boundary surfaces are adiabatic regarding energy conservation equation (2-21) in order to simplify the identification of parameters such as heat transfer coefficient h_T and emissivity ε_r. For Navier-Stokes equations (2-59), zero velocity and free pressure are applied for all the 4 metal side surfaces. For each time step, the computation process is presented in Figure 3-10, the remeshing is achieved each 20 time steps in order to limit remeshing time while keeping sufficient mesh quality.

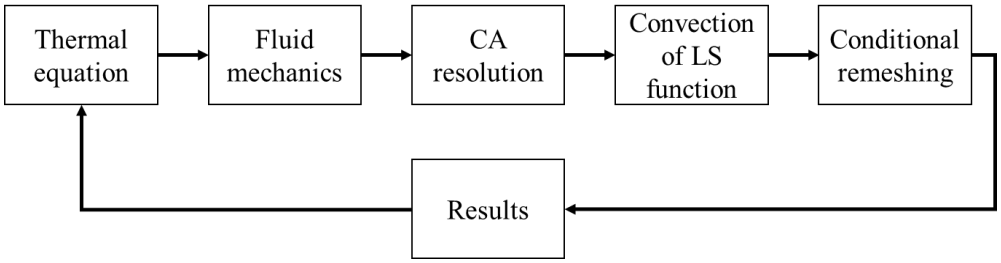

Figure 3-10. Compute process for each time step.

3.4 Simulation results

Simulations results associated to the coupling scheme are presented hereafter, for the two welding configurations V_1 and V_2 reported in Table 3-4. The dendrite tip kinetics law K_1 has been used firstly. These two simulations are hereafter referred to as cases RV_1K_1CO and RV_2K_1CO, here, R refers to random initial grain structure in order to be distinguished with the T, "textured" grain structure presented in section 3.5.3. Comparisons are conducted considering the melt pool shape observed by the AVT camera and the measured texture of the grain structure as deduced from EBSD measurements. Results will serve for comparison with two additional simulations reported in the following discussion part. All configurations of the simulations are summarized in Table 3-7, all these simulations are launched on 56 processors in a parallelized simulation, the total simulation time is about 20 hours.

Table 3-7. Simulation configurations.

Case	Welding velocity	Growth kinetics law	CAFE scheme
RV_1K_1CO	V_1	K_1	$COupling$
RV_2K_1CO	$\boldsymbol{V_2}$	K_1	$COupling$
RV_1K_2CO	V_1	$\boldsymbol{K_2}$	$COupling$
RV_1K_1CH	V_1	K_1	$\boldsymbol{CHaining}$
$\boldsymbol{T}V_1K_1CO$	V_1	K_1	$COupling$
$\boldsymbol{T}V_2K_1CO$	$\boldsymbol{V_2}$	K_1	$COupling$

3.4.1 Welding configuration V_1, kinetics law K_1, coupling scheme CO

At first, the computed temperature field and fluid flow velocity are presented in Figure 3-11 for the welding configurations V_1. The air regions have been omitted to offer a better view of the metal subdomain. As presented in Table 3-6, the efficiency of the heat source is considered to take account of the partial transfer of energy from the heat source to the metal, and the associated energy loss. Both values are obtained by calibration when comparing the simulated melt pool width with measurements using the images recorded at the bottom of the plate (Figure 3-6). The value $\eta = 0.65$ was retained for the present configuration V_1 and $\eta = 0.6$ for V_2, as reported in Table 3-6.

The color maps in Figure 3-11 gives the temperature distribution using T_{liq} as the maximum value. The arrows represent the direction and intensity of the liquid velocity vectors. In Figure 3-11 (b), the top view reveals a radial outward liquid flow from a central point that corresponds to the hottest region of the melt pool located just below the heat source. The surface temperature gradient, radial and inward, creates a surface force that drives the matter towards the boundaries of the melt pool. This is typical of Marangoni-driven convection with a negative value of the $\partial\gamma/\partial T$ coefficient. The pool extends further and the liquid velocity reaches its higher value behind the heat source where the heat is preferentially transported. The flow then progressively decreases at lower temperature due to interaction of melt flow with the mushy domain as discussed later. At the lower surface of the plate, shown in Figure 3-11 (c), a similar flow pattern is observed, with lower intensity. The velocities observed at mid-thickness ($Z = 0.75$ mm) in the longitudinal cut ($Y = 0$ mm) in Figure 3-11 (a) reveals a flow in the welding direction at the rear of the pool and in the opposite direction ahead of the heat source. So in summary, the predicted convection loops consist of two toroidal flows, one above the other, with opposite flow directions. Both toroidal flows are due to radial outward Marangoni forces created at the top and bottom liquid-gas surfaces, the top one being more intense. The maximum computed velocity at the top and bottom surfaces reaches 43 mm s^{-1} and 13 mm s^{-1}, respectively.

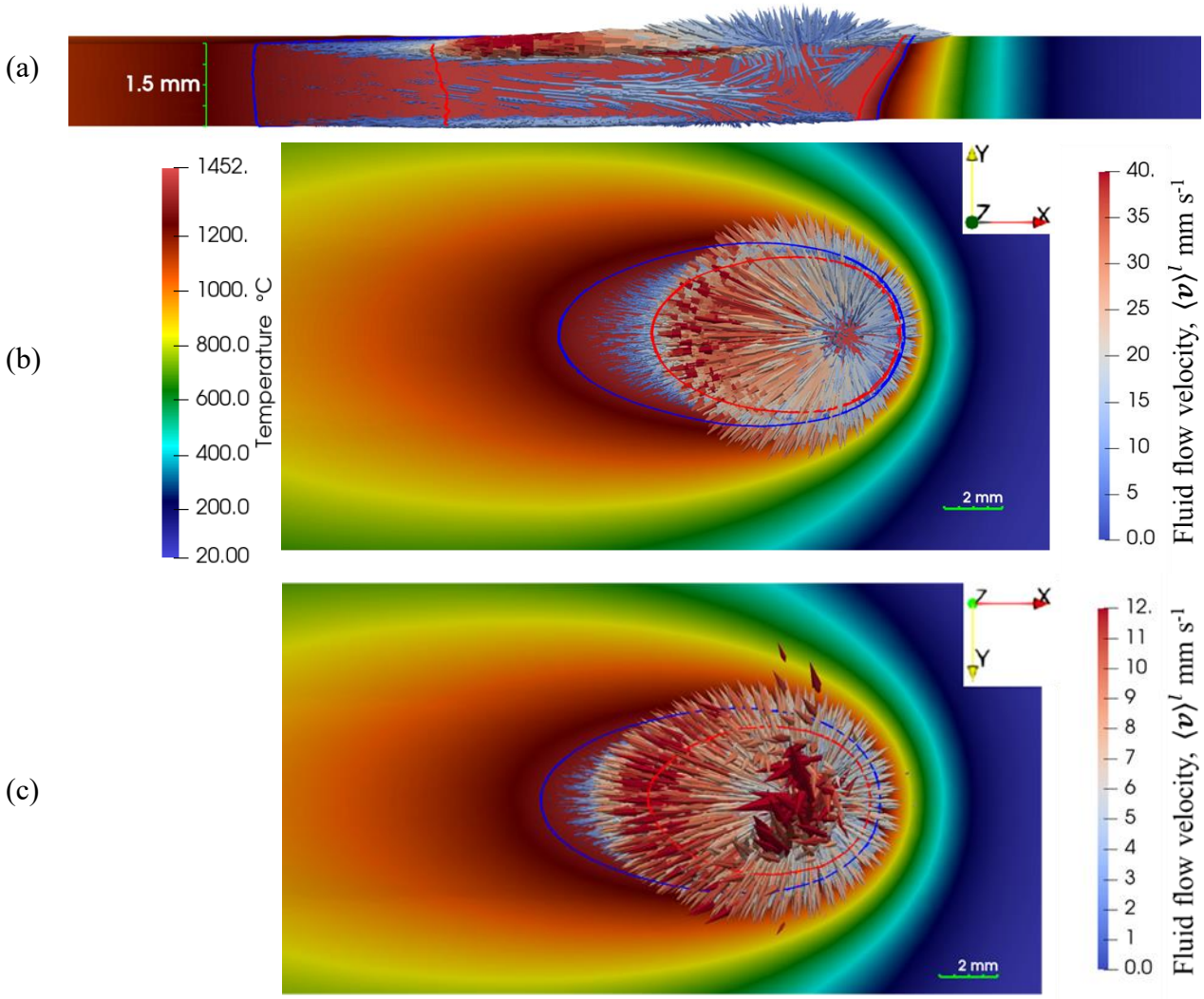

Figure 3-11. RV_1K_1CO simulation at time 14 s. Temperature field, with (red lines) liquidus isotherm and (blue lines) solidus isotherm, and (colored arrow) liquid velocity field (see Table 3-8) as observed (a) in the $Y = 0$ mm longitudinal cross section through the plate, as well as from (b) the top and (c) the bottom surfaces of the metallic subdomain. The gas subdomains have been omitted for clarity. Note that the temperature scale is the same for all images and the velocity scale in (b) also applies to (a) but a different velocity scale is used in (c) as the velocity field is weaker.

The maximum and average velocities deduced from the AVT camera viewing the lower side of the molten pool are reported in Table 3-8. The maximum recorded value, 34.4 mm s^{-1}, is clearly higher than in the simulation, while the average, 13.6 mm s^{-1}, is close to the maximum predicted value. One could explain these discrepancies by the monolithic approach chosen here to solve the momentum and mass conservation equations in the whole simulation domain encompassing the gas, liquid and solid regions, with viscosities varying by several orders of magnitudes. In addition, the liquid viscosity (Table 3-2) is clearly larger by – at least – one order of magnitude compared with expected values (~ 1 mPa.s). However, the use of realistic viscosity values lead to poor conditioning of the matrices arising when solving the momentum conservation equations, preventing a solution to be found. The pragmatic choice is then to reduce the huge gap between viscosity values. This is presently done by decreasing the apparent

viscosity of the solid and increasing the viscosity of the liquid and gas phases (Table 3-2), leading to underestimated fluid flow. One solution is to increase the Marangoni coefficient (as presented in Table 3-2). However, the value used in present computation is equal to $-8 \cdot 10^{-4}$ N m^{-1} K^{-1} and already twice larger compared to values reported in literature. The simulation done with a Marangoni coefficient of $-4.3 \cdot 10^{-4}$ N m^{-1} K^{-1} [Sah88], gives a maximum computed velocity at the top and bottom surfaces at 20 mm s^{-1} and 4.9 mm s^{-1}, which are more underestimated. Besides, other numerical problems arised when the Marangoni coefficient is chosen higher than the actual value $-8 \cdot 10^{-4}$ N m^{-1} K^{-1}. Therefore, this method could just compensate the underestimation rather than propose a definitive solution for the problem.

Another solution could have consisted in solving the set of equations with momentum interactions between metallic phases modelled by the Darcy law [Aal20, Zha19-2] . With the latter approach, no viscosity value is required in the solid region so that the solution is purely fluid oriented with less variations in viscosities between the gas and liquid fluids. However, such methodology is more demanding in computing ressources and could not be conducted in the present context of welding simulations. Indeed the simulation taking into consideration Darcy law in present configuration would require a time step 10 times smaller than the actual value (0.01s). A simple simulation can take 8-10 days which makes it impossible to calibrate the simulation paramaters such as efficiency and dendrite tip kinetic law.

Table 3-8. Comparison between measured and simulated fields at the lower side of the plate for cases V_1K_1CO and V_2K_1CO.

Parameter			Measured	Computed	Unit
Liquid velocity	Maximum	V_1	34.4	13.2	mm s^{-1}
	Average		13.6		
	Maximum	V_2	18.5	5.9	
	Average		5.2		
Plate deflection		V_1	190	120	µm
		V_2	40	40	
Melt pool length		V_1	11.7	11.7	mm
		V_2	7.13	7.42	
Melt pool width		V_1	4.89	5.01	mm
		V_2	2.86	2.86	

The melt pool shape observed on the bottom surface of the plate is presented in Figure 3-12 (a). At first, the elements of the FE mesh with all nodes reaching a fraction of solid higher than 99 % are displayed in grey color. Secondly, the grain structure colored using first Euler angle, φ_1, is represented on the CA grid, revealing the position of the growth front with the liquid cells in white. Note that the small white gap appearing between the growth front and the fully liquid region identified in grey is a numerical artefact of the representation due to the interpolation

between the FE mesh and the CA mesh and the choice of the threshold value 99 % liquid to draw the molten pool. It appears larger where the temperature gradient is lower, *i.e.* at the rear of the melt pool. Finally, the experimental melt pool contour deduced from the in-situ camera observations is superimposed as a yellow contour. The melt pool clearly extends further than the isotherm liquidus temperature also superimposed as a red contour as a simulation result. The liquid region between the red contour and the melt pool shape is in metastable state. In this latter domain, the grain structure is not developed until a local undercooling ΔT $(= T_{liq} - T)$ corresponding to the growth undercooling associated to dendritic structure development for the K_1 law (Table 3-3). Table 3-8 compares the length and width of the melt pool as measured and computed according to simulation V_1K_1CO, showing very good agreement. This is due to the fact that law K_1 was adjusted so as to retrieve the experimental contour. It was also verified that the melt pool dimensions are stable, *i.e.* do no longer change considering the time used in Figure 3-12 (a). In fact, the width of the images is only half the length of the CA mesh and CA grid. The heat and mass transfers as well as the computed grain structure on the left of the image displayed in Figure 3-12 (a) include transient regimes that are not considered in the comparisons with experimental results. Grain structure is not made of grains aligned in the $\pm Y$ −directions regarding the transverse cross section (Figure 3-12 (b)) unlike what seems to be the case in the Figure 3-12 (a). In fact, a section at constant X coordinate in Figure 3-12 (a) shows that, within the weld bead, several grains are indeed encountered, thus explaining the distribution of the transverse cut. The solidified width is found to be almost stable in Figure 3-12 (b) in the thickness direction, *i.e.* across the whole plate thickness. This means that the teardrop shape of the melt pool in Figure 3-12 (a) is only two-dimensional. This is the result of a simple two-dimensional heat flow configuration thanks to the fully penetrated weld pool condition, that shall ease interpretation of the results. Said differently, the temperature gradient and hence the heat flow mainly lie in the plane of the plate, explaining the similar temperature fields computed at the top and bottom surfaces of the plate shown in Figure 3-11.

Simulations also include the plate subsidence with maximum deflection located at the center of the weld bead. Indeed, the total deflection of the metal-sheet plate is made visible in the transverse section by comparison with the initial planar sheet surface marked with black horizontal lines. Figure 3-12 (b) shows the result as observed after it was transferred to the CA mesh and used by the CA grid to compute the grain structure. The computed value, 120 µm, is lower compared with the measurement reported in Table 3-8, reaching 190 µm. As discussed before, underestimation could be linked to the monolithic solver using too large viscosity, underestimating the flow intensity.

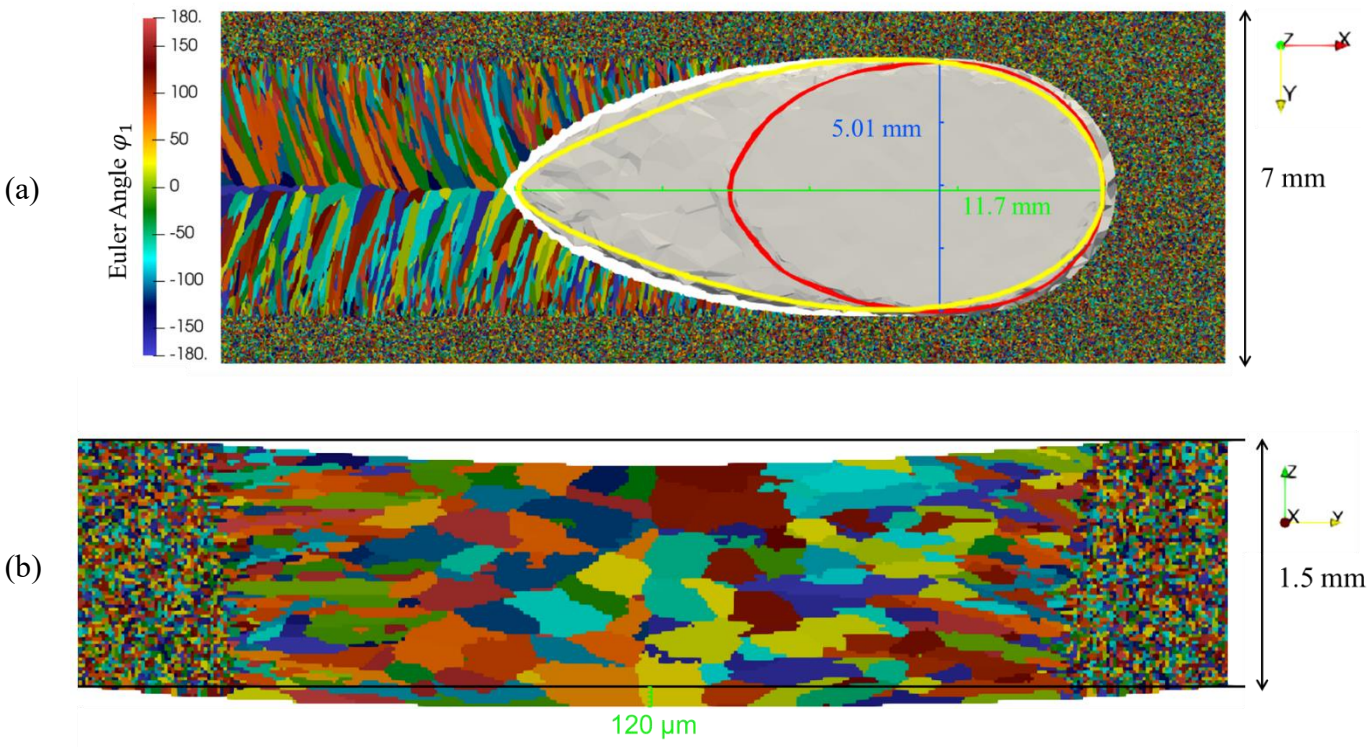

Figure 3-12. V_1K_1CO simulation. Snapshots of (colored using the first Euler angle φ_1) the grain structure (a) from the bottom surface ($t = 14$ s) and (b) in a transverse cross section after solidification. The melt pool shape is (grey surface) deduced from the FE simulations by considering the FE elements with nodes such that $g^l_{n^{FE}} > 0.99$, (yellow contour) deduced from in-situ camera observations (Figure 3-6) and (boundary between colored\white cells) identified by the growth front. The liquidus isotherm is added as a red contour.

Quantitative comparison is also done for the grain structure in Figure 3-13. The representation is complementary to the structure displayed in Figure 3-12 where the colors were only used to distinguish grains, without texture presentation. Only a small part of the simulation domain is displayed in the right-hand-side images of Figure 3-13, corresponding to the same dimensions as the scanned surfaces using EBSD displayed in the left-hand-side images. Three inverse pole figures (IPF) are made available corresponding to the orientation of the grains projected along the (a) $X-$, (b) $Y-$ and (c) $Z-$ directions. The three figure permit a full displayed of the grain crystallographic orientations. One first observation is that the grain size in the base plate, far from the heat affected zone, is very fine and well represented by the simulation, showing the relevance of the estimation proposed for the initial grain density in simulations (section 3.2.2). Overall, an elongated solidification grain structure is observed, typical of columnar growth, with a center line marked around $Y = 0$ mm. This observation valid the choice made to neglect nucleation events in the melt pool. The overall colors of the grains are also compared, starting with the IPF-Y maps (Figure 3-13 (b)). A dominance of red, orange, and pink colors is found close to the weld bead boundaries, that turn to orange and pink towards the centerline (*i.e.* the red grains get eliminated). These grains have one of their $\langle 100 \rangle$ directions slightly misaligned with the $Y-$direction. According to the melt pool shape displayed in Figure 3-12 (a), the temperature gradient close to the bead boundaries is indeed not far from the $\pm Y-$directions, explaining the selection of those grains. As a consequence, grains in blue, green or very light

colors do not survive to the grain growth competition. Going from the boundaries to the centerline of the weld bead, Figure 3-12 (a) shows that the normal to the growth front (or melt pool boundary) progressively turns toward the $\pm X$ −direction up to around 30°. This explains the elimination of the red grains (with well aligned $\langle 100 \rangle$ direction along the $\pm Y$ −directions) at the centerline of the weld, and subsistence of only the orange and pink grains. Very few light green and blue grains remain at the centerline of the experimental EBSD IPF-Y map (Figure 3-13 (b) left), and are not present in the simulation. Similarly, even if the trend of grain selection is well reproduced by the model, it occurs faster compared to the measurements when going from the boundaries to the centerline of the weld bead. The grain density is also slightly higher in the measurements as the grains appear thinner. It is suggested that these observations could be the results of a small source of new grains formed by either nucleation or fragmentation in the undercooled liquid, that contribute to growth competition with the other grains coming from the initial plate structure, as presented in the literature [Chi19]. This source of additional grains has not been added to the simulations. Additionally, while the color distribution is the same for the simulated grain structure in Figure 3-13 (a)-(c) right, *i.e.* for IPF-X, IPF-Y and IPF-Z, revealing random orientations, it is slightly different in the measurements. The grain structure in the base plates appear more purple, blue and green in Figure 3-13 (a)-(c), respectively. This deviation means that a small initial texture exists in the base plate, that is not considered in the simulation. As presented in Figure 3-14, the $\langle 100 \rangle$ pole figure plotted in the base metal (white rectangle in Figure 3-13) for the experiment shows a preexisting texture (Figure 3-14 (a)) compared with the simulation results (Figure 3-14 (b)) where the random texture of the base metal is retrieved. The role of this initial anisotropy is discussed in section 3.5.3.

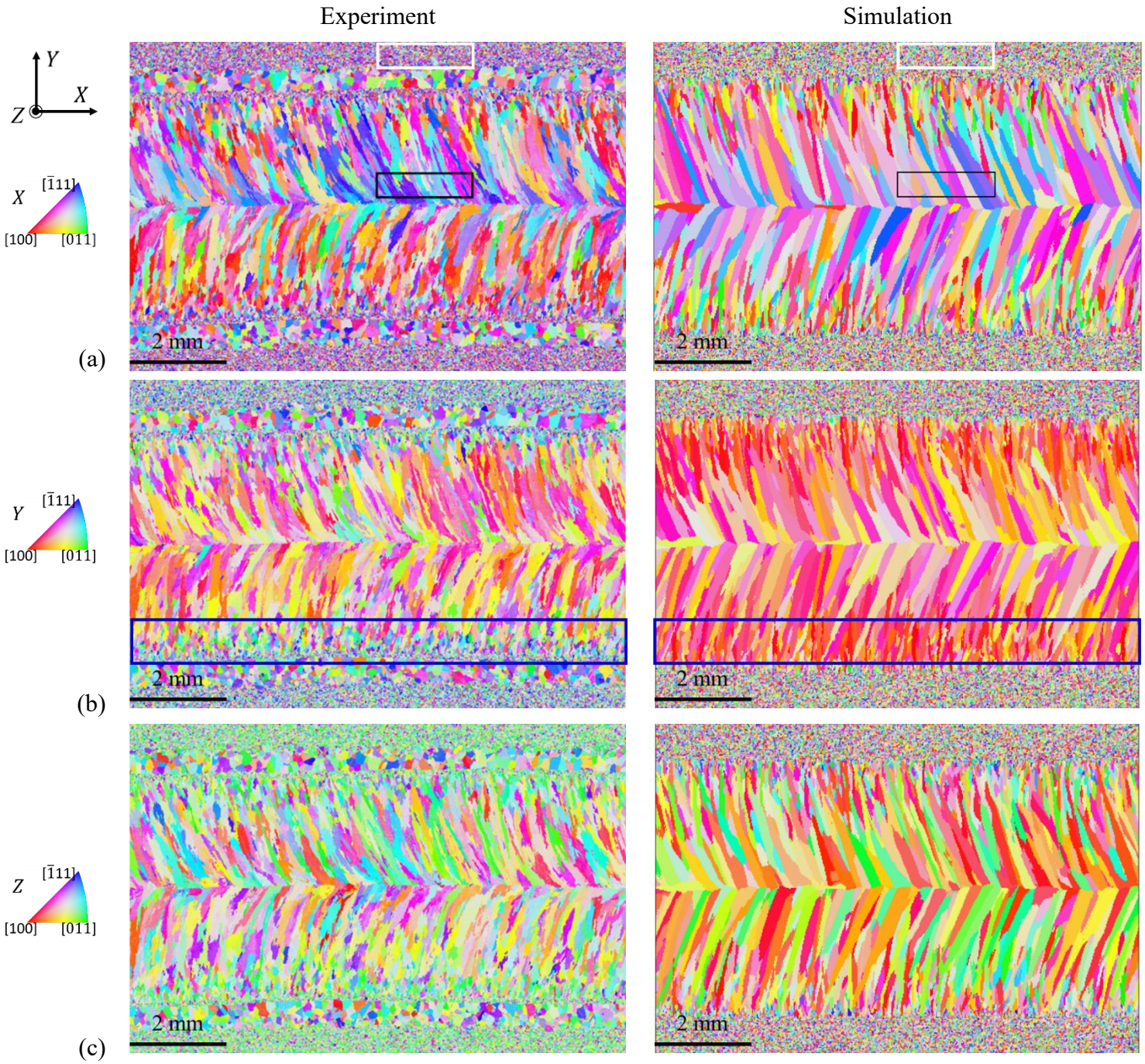

Figure 3-13. V_1K_1CO simulation. EBSD maps of the grain structure in a $Z-$ plane 0.3 mm under the top surface (left) measured and (right) simulated with the CAFE model. The inverse pole figure color codes used are with respect to the (a) $X-$, (b) $Y-$ and (c) $Z-$ directions.

The overall-colored grain structures drawn for IPF-X and IPF-Z maps also compare favorably. A more quantitative information is provided in Figure 3-15. The $\langle 100 \rangle$ pole figures of the grains located in the black rectangles windows drawn in Figure 3-13 are plotted from (left) the recorded and (right) the simulated orientation maps. The windows are chosen close to the center of the weld (small Y value) in the $+Y$ mid-plane where the temperature gradient at the growth front takes positive X and negative Y components. A strong fiber texture is revealed that coincides with selected grains having a $\langle 100 \rangle$ direction along the corresponding direction of the temperature gradient at the growth front. Besides, a grain coarsening phenomenon is experimentally observed in the border of the melt pool in the heat affected zone as reported in the literature [Bla21]. This coarsening phenomenon is not considered in the present modelling.

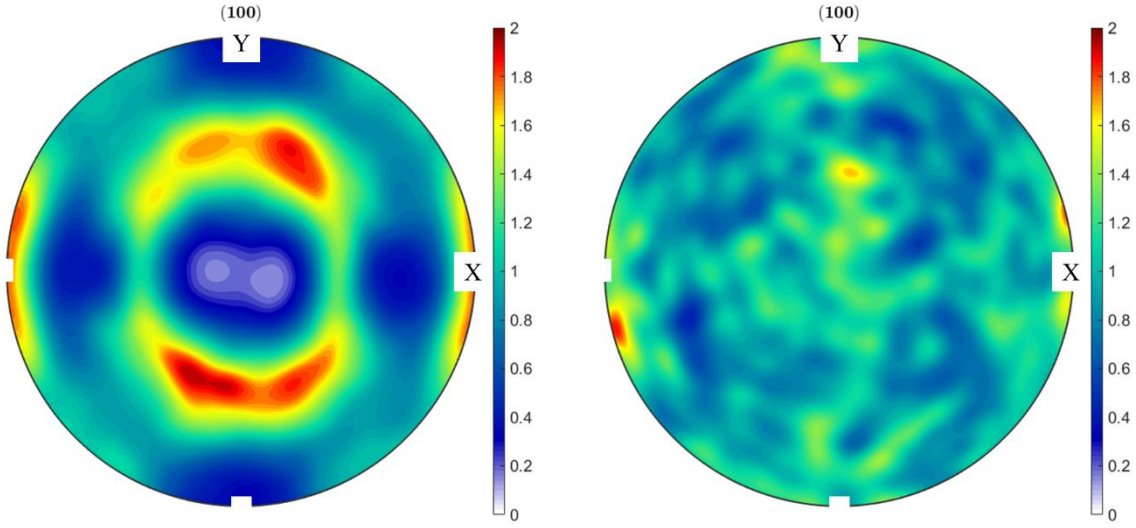

(a) (b)

Figure 3-14. $\langle 100 \rangle$ pole figure plotted in the based matel (white rectangle in Figure 3-13) for (a) experimental observation, (b) simulation results. The normal direction of the pole figures is the $Z-$ direction.

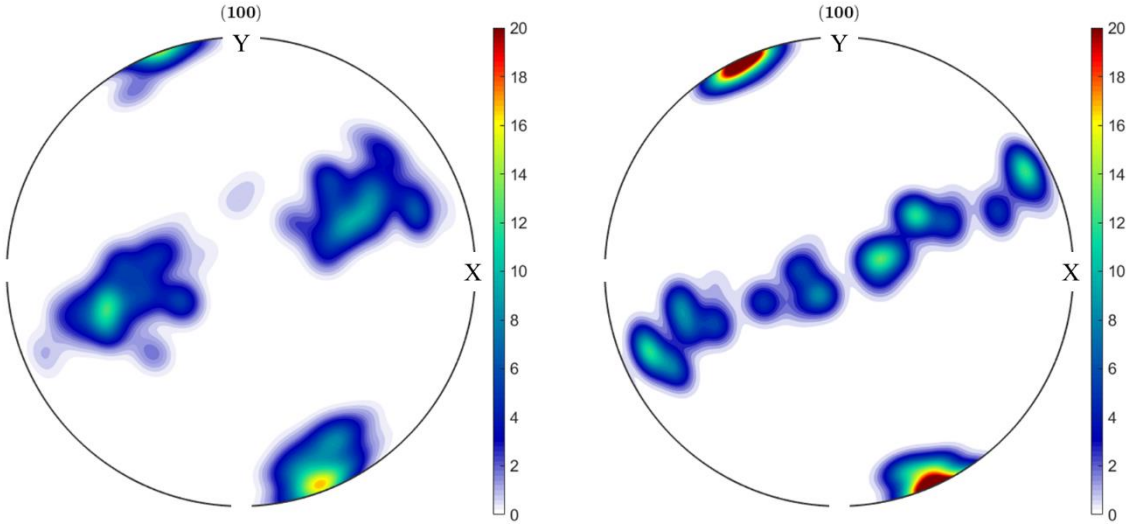

(a) (b)

Figure 3-15. ⟨100⟩ pole figure plotted in the weld bead (black rectangle in Figure 3-13) for (a) experimental observation, (b) simulation results. The normal direction of the pole figures is the $Z-$ direction.

3.4.2 Welding configuration V_2, kinetics law K_1, coupling scheme CO

Configuration V_2K_1CO proposes to investigate a slightly higher welding speed, $V_2 = 4.3$ mm s^{-1}. The effective power of the plasma arc is almost similar, with $\dot{Q}_{Plasma} = 424$ W (V_2K_1CO) compared with $\dot{Q}_{Plasma} = \eta\, U\, I = 463$ W (V_1K_1CO) and for case (Table 3-6). As a consequence, the linear energy $\dot{Q}_{Plasma}/V$ is decreased and a smaller melt pool is expected. It could be noted that for the configuration V_2, the heat source efficiency η is decreased to 0.6 rather than 0.65 for V_1. This value $\eta = 0.6$ is obtained with the same calibration of melt pool width. As this value is unknow in the experiment, the influence of 5% is considered to be acceptable. One can note that the efficiency value is weak compared with that reported in the literature (*e.g.* $\eta = 0.85$ [Des13]), one reason could be the adiabatic boundary condition applied in this simulation and another reason could be the underestimated fluid flow velocity which underestimate the thermal convection.

Figure 3-16 clearly shows a smaller melt pool compared with Figure 3-12. Two toroidal flows are observed in simulations, as in previous case, with a decreased intensity of the maximum liquid velocity. Table 3-8 again gathers information for comparison with measurements. As for the previous case, the maximum computed liquid velocity, 5.9 mm s^{-1}, is very close to the average measurement, 5.2 mm s^{-1}.

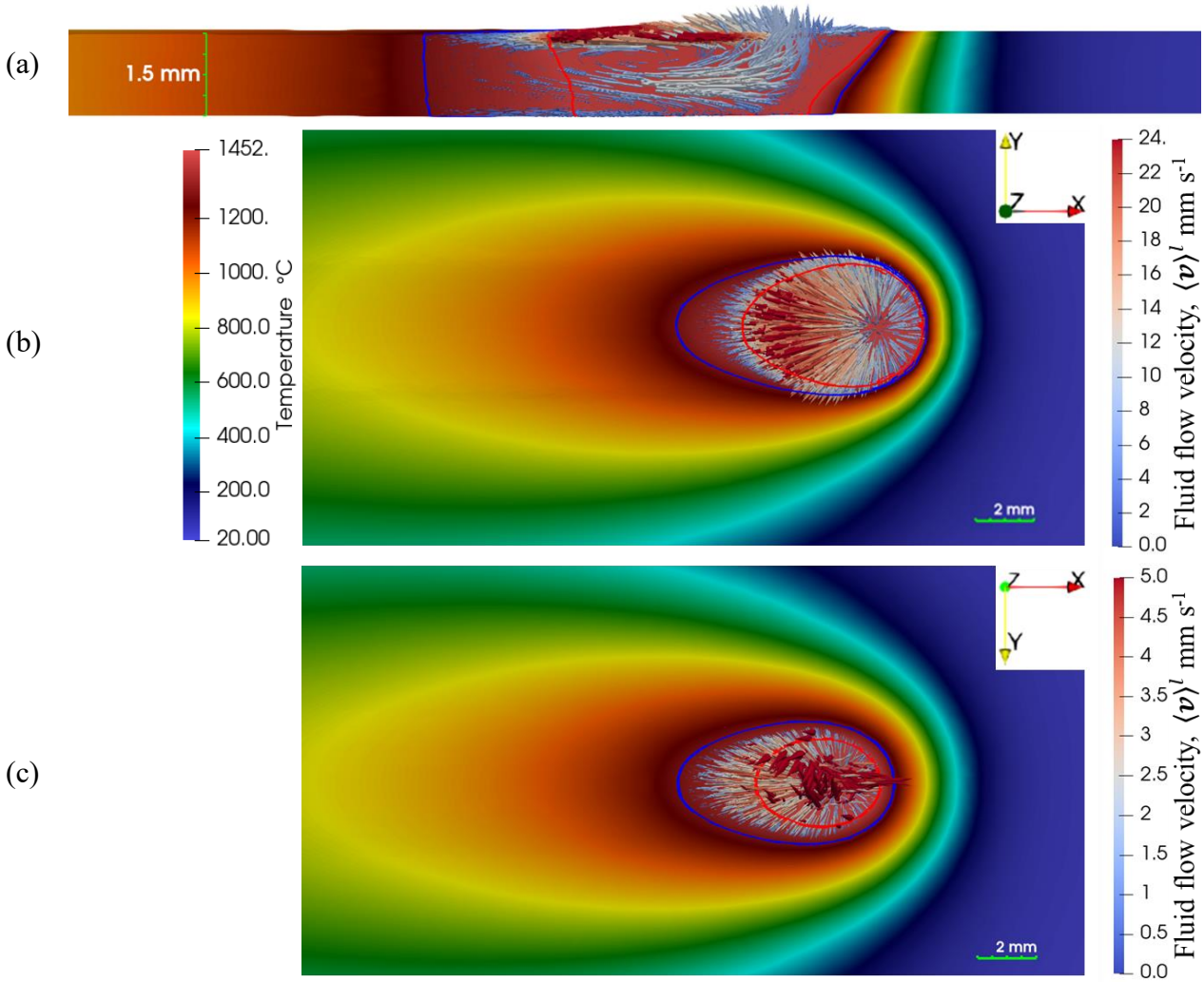

Figure 3-16. V_2K_1CO simulation at time 14 s. Same as Figure 3-11 caption.

Figure 3-17 again shows the shape and dimensions of the melt pool to be compared with measurement (Table 3-7 (b), Table 3-8). The length and width of the met pool, 11.7 mm and 7.42 mm, but also the maximum computed deflection shown in Figure 3-17 (b), 40 µm, retrieve the measured values. A smaller subsidence is observed both experimentally and numerically due to a smaller pool leading to faster solidification. Considering that no simulation parameter is changed compared to V_1K_1CO expect the welding velocity, these results are consistent.

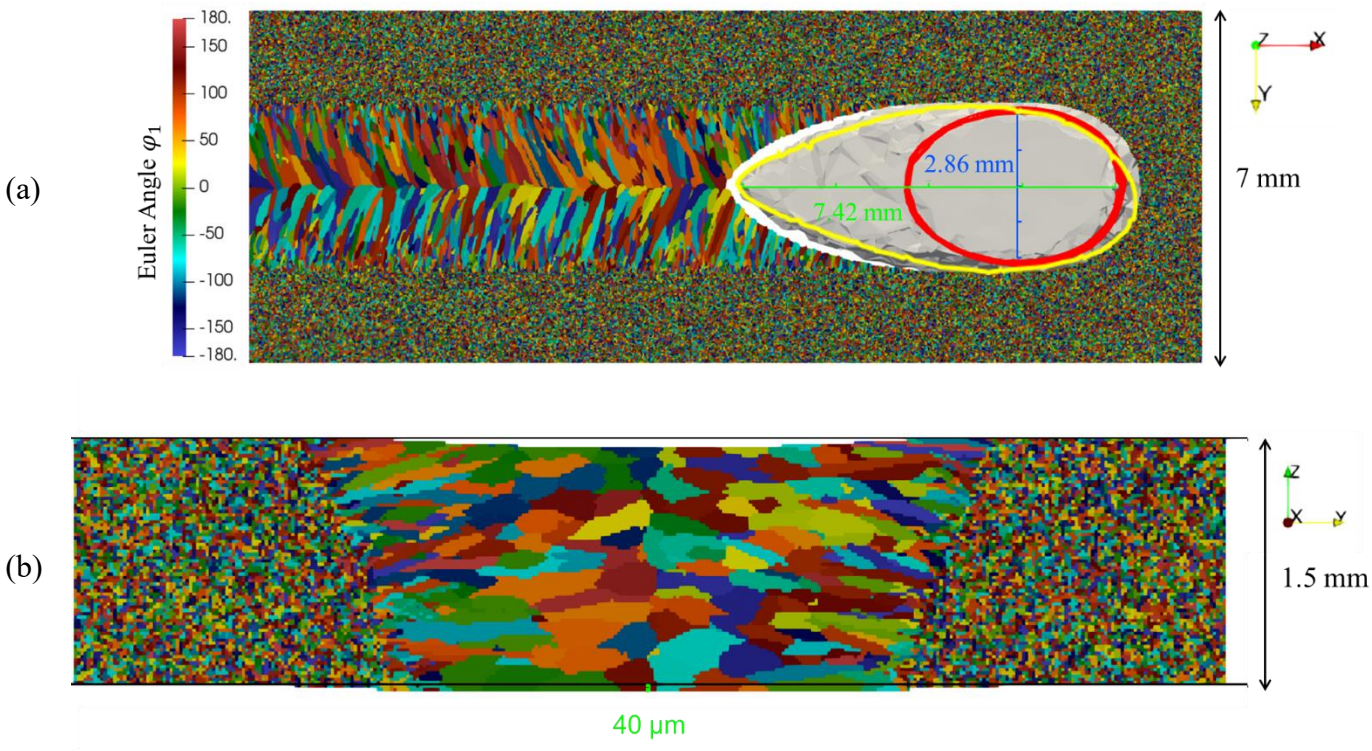

Figure 3-17. V_2K_1CO simulation at time 14 s. Same as Figure 3-12 caption.

The experimental and numerical EBSD map for V_2 case are presented in Figure 3-18. Considering firstly the IPF-X, the same observations as for Figure 3-13 can be made. The grain size is smaller as the melt pool width has decreased compared to case V_1. This is also observed in the simulation as the grains have less distance to compete prior to interact at the centerline. Another consequence is a less texture and oriented grain structure compared to the lower velocity case V_1K_1CO. This is quantitatively shown in Figure 3-19 where the $\langle 100 \rangle$ pole figure is drawn, corresponding to the grains falling in the rectangle window displayed in Figure 3-18. The fiber texture is retrieved in the direction of the temperature gradient at the growth front, with a positive X and negative Y components as for the reference case V_1K_1CO. However, the experimental intensity of the texture is slightly weaker as revealed by comparing the colors in the experimental data drawn in Figure 3-15 (intensity $= 17$) and Figure 3-19 (intensity $= 16$). The $\langle 100 \rangle$ pole figure for the V_2 experiment also shows that the texture has a small Z component, not well retrieved by the simulation. However, no clear $\langle 100 \rangle$ texture is found, with more well distributed crystal orientation perpendicular to the fiber direction.

However, the IPF-Y and IPF-Z present a difference of color which is not negligible. For example, the IPF-Y for the simulation result (Figure 3-18 (b) right) has a dominance color of red, orange, and pink in the weld bead which is coherent with the lower velocity case V_1K_1CO as presented in Figure 3-13 (b) right. Even though, experimental observation does not retrieve similar tendency. Indeed, in Figure 3-18 (b) left, more green, blue and violet color can be observed presenting a different texture from the simulation result (Figure 3-18 (b) right). This incoherence may be explained by the difference of the initial grain structure as presented in Figure 3-14. In fact, even though for the case V_1K_1CO, considering the grains near the border of the melt pool (zone encompassed by the blue contour in Figure 3-13 (b), the grains in the

experiment (Figure 3-13 (b) left) has more colors compared with the initial texture in blue and green. However, in the simulation, the grain present already red, yellow and pink colors showing a difference in the angular distribution of crystallographic orientations between experiment and simulation. To verify this difference and discuss its consequences, a simulated initial grain texture similar to experimental observations is required, which will be presented in section 3.5.3.

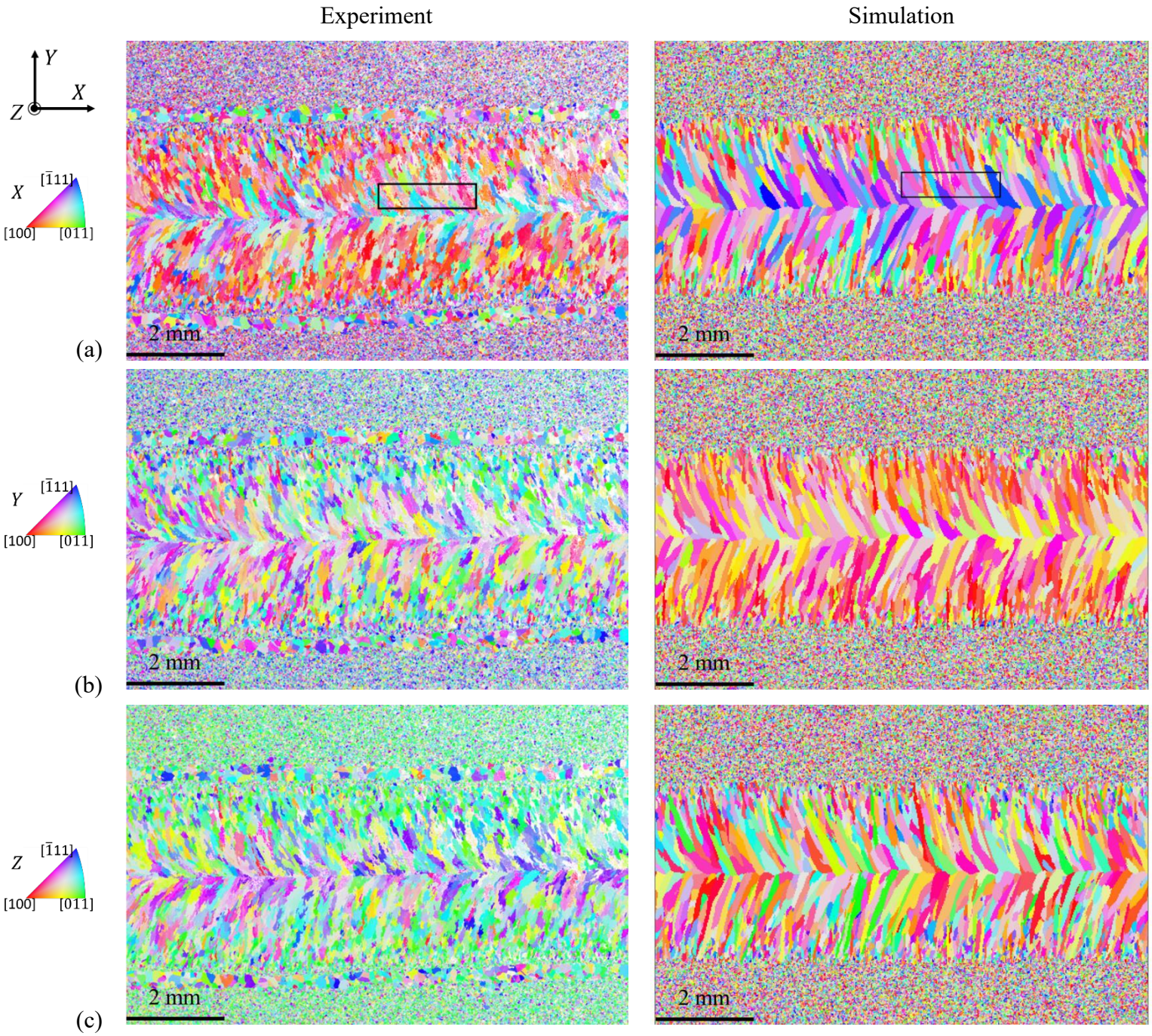

Figure 3-18. RV_2K_1CO simulation. Same as Figure 3-13 caption.

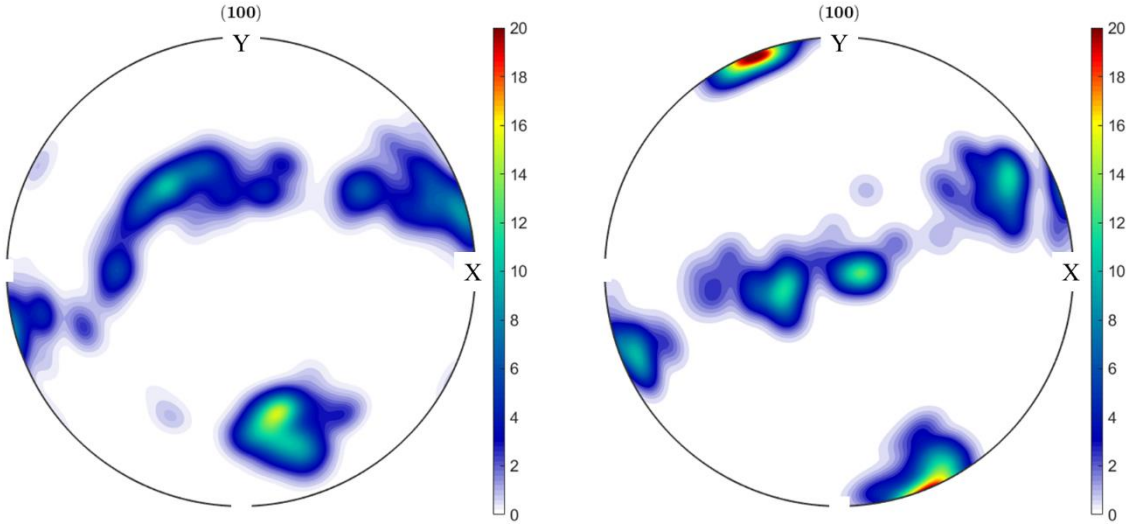

(a) (b)

Figure 3-19. ⟨100⟩ pole figure plotted in the weld bead (black rectangle in Figure 3-18), Same as Figure 3-15 caption.

3.5 Discussion

As stated in section 3.4 , the efficiency of the heat source was first calibrated by comparing the width of the melt pool rather than its length. The reason for this choice is that the growth front at maximum width corresponds to the transition region between remelting and solidification. It should therefore be independent on the growth kinetics law as the local front undercooling tends toward zero at this particular location. So even if the calibration was carried out using simulations RV_1K_1CO and RV_2K_1CO, a similar melt pool width is expected whatever kinetics law is, as long as the velocity is canceled when undercooling is negligible ($v(\Delta T = 0) \simeq 0$). However, the length of the melt pool was clearly retrieved by adjusting the coefficients of the growth kinetics, K_1. In addition, the fact that the same growth law gives close melt pool length for the two welding velocities compared with experiments is again encouraging regarding its relevance, at least for the process conditions investigated in this work.
Hereafter the validity of the second computed dendrite tip growth kinetics, K_2, and its relevance in present simulation is discussed regarding RV_1K_2CO case. Then the practice of chaining rather than coupling is illustrated in simulation RV_1K_1CH. For these two simulations, case RV_1K_1CO serves as the reference. At the end, the influence of initial grain texture is investigated, case TV_1K_1CH and TV_2K_1CH (with T refers to "textured" initial grain structure) are applied to compare with the results presented in section 3.4 .

3.5.1 Welding configuration V_1, kinetics law K_2, coupling scheme, CO

The growth law K_2 reported in Table 3-3 was deduced from PhysalurgY [Phy], a library of physical metallurgy modules coupled with Thermo-Calc [The18] software. Among the modules available in this library, the tool KIND provides access to the growth kinetics of dendritic structure developed in multicomponent alloy. This tool is based on the dendrite tip kinetic

model developed by Hunziker [Hun01]. The present application is coupled with the TCFE9 database [TCFE9] to access thermodynamic equilibrium assumed at the solid/liquid interface and the MOBFE6 database to compute diffusion data in the liquid phase [MOBFE6]. A correlation of the output has been thereafter developed in order to estimate growth kinetics as a simple function of tip undercooling, corresponding to the growth law K_2 (Table 3-3). Figure 3-4, shows that, at a given velocity, a far lower undercooling is computed compared with previous expression K_1.

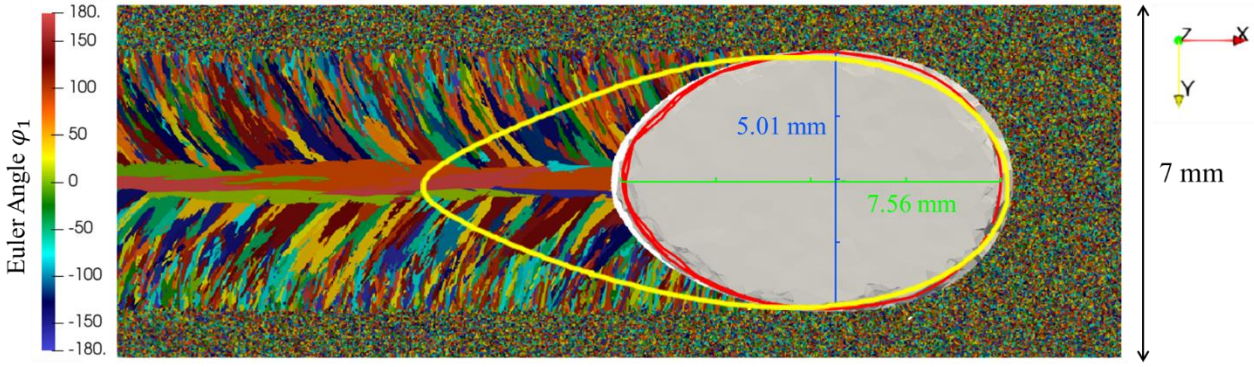

Figure 3-20. RV_1K_2CO simulation at time 14 s. Same as Figure 3-12 (a) caption.

As in Figure 3-12 and Figure 3-17, the region of undercooled liquid computed in case V_1K_2CO reported in Figure 3-20 lies between the growing front delimited by the grains/liquid boundary and the T_{liq} (red contour). It could be noted that two contours can be observed, this is due to the 3D presentation of T_{liq} contours mixed at different thickness at the end of the melt pool. As expected, the undercooled domain is significantly reduced when using the K_2 kinetics law compared to its dimension computed with the K_1 kinetics law (Figure 3-12) and the same welding velocity V_1. As a consequence, the melt pool shape (region colored in grey) does no longer represent the experimental observation (yellow contour). A spectacular consequence is shown on the grain structure development. Because the growth front is close to T_{liq}, it adopts a rounder shape and the temperature gradient at the growth front progressively evolves from the $\pm Y$ −directions at maximum width to the $+X$ −direction at the centerline of weld bead. As a consequence, grain competition is less directional compared to the reference case V_1K_1CO and some grains with a $\langle 100 \rangle$ direction aligned with the $+X$ −direction survive the competition and remain present at the centerline of the weld bead. Figure 3-21 confirms this interpretation. The simulated IPF-Y map (Figure 3-21 (a)) highlights the grains at the centerline with red color. The columnar grain structure is represented mostly with green color. Compared to the experimental EBSD map (Figure 3-21 (a)), the result is clearly not as close as the simulated map using the K_1 kinetics law. Besides, the $\langle 100 \rangle$ pole figure (Figure 3-21 (b)) of the simulation result shows several special points (encompassed by red rectangle) which do not exist in the experiment observation (Figure 3-15 (b)). These points present the grains nearly aligned with the welding direction (X direction). This result shows the importance to propose a relevant representation of the melt pool shape, which in turns required a satisfying growth kinetics law.

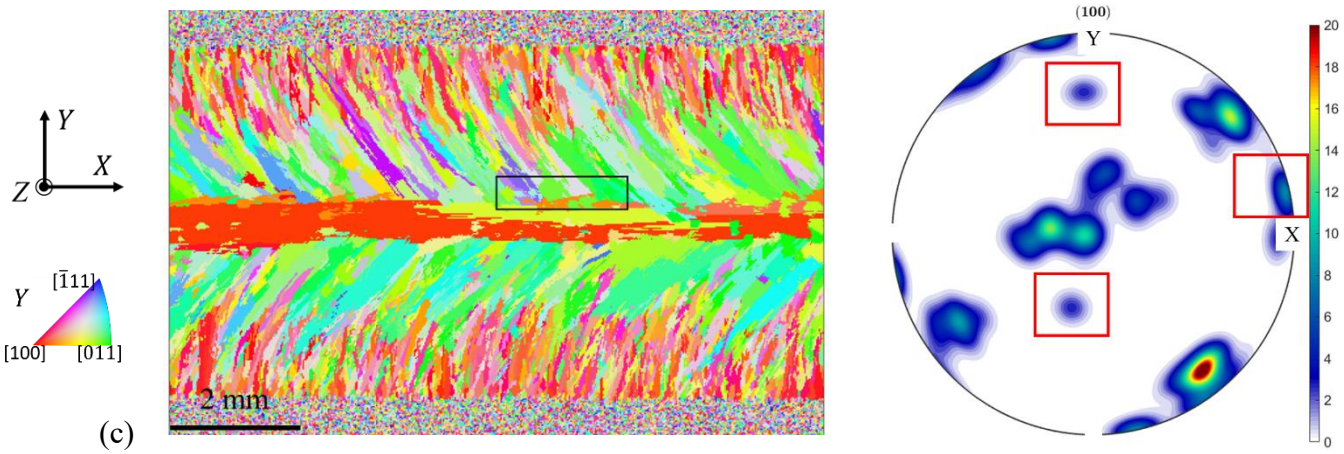

Figure 3-21. RV_1K_2CO simulation. (a) IPF-Y EBSD map, Same as Figure 3-13 (b) caption, (b) $\langle 100 \rangle$ pole figure plotted in the black rectangle in (a).

The relevance of a computed dendrite tip kinetics is then to be discussed. Despite the use of the most recent databases [TCFE9, MOBEFE6], several material parameters of the model are doubtful. They include the diffusion matrix and the ferrite-liquid interfacial energy, as well as the stability constant taken equal to $(2\pi)^{-2}$ [Kur86]. But more questionable are the assumptions of the model that consider no rapid solidification effect. These are solute trapping and kinetics undercooling [Tri94]. Solute trapping is explained by the difficulty of liquid atoms to attach to the solidifying interface while maintaining thermodynamic equilibrium. Kinetics undercooling is linked to the kinetics of attachment of the atoms to the solidifying interface. These contributions are expected to have an influence at high velocity, increasing the solubility of the solid phase as well as the total undercooling of the growth front. Its origin is explained by the difficulty of liquid atoms to attach to the solidifying interface while maintaining thermodynamic equilibrium. So, the present results suggest that more efforts should be developed in order to extend present kinetics model (KIND – PhysalurgY) at high velocity. However, these reasons mentioned above cannot explain completely the difference between the analytical law K_2 and the adapted law K_1, other type of dendrite tip kinetics taking into account the fluid flow [Gan03] may be necessary to apply and test.

Finally, while in-situ observations of the melt pool bring invaluable information, it is regretful that no measurement of the temperature fields was made possible with the present experimental configuration. The main validation of the heat flow is based on the width of the melt pool supposed to correspond to the limits given by the liquidus isotherm. But the use of an infrared camera and well-located thermocouple would have been also very useful. In fact, the computed temperature field suggests that the growth undercooling overpasses 150 °C and is thus of the order of the solidification interval. This again is in favor of high velocity effects that would add on a kinetic contribution to the total undercooling. This effect could have been validated with temperature measurements.

3.5.2 Welding configuration V_1, kinetics law K_1, chaining scheme CH

The chaining scheme of the CAFE model is applied in this section. This is done by comparing the RV_1K_1CH simulation against the corresponding RV_1K_1CO reference case using the coupling scheme. It is worth saying that most direct grain structure simulations in the literature are based on the chaining scheme as it is the simplest to operate [Chi19, Che14-2, Che16, Han14, Han15, Che20].

As detailed in section 2.4.3, with the chaining scheme, the conversion of energy into a temperature makes use of the tabulated phase enthalpies and phase fractions listed in Figure 3-1 whatever the grain structure is. The resulting temperature field is then uniquely defined. It serves to compute the grain structure after its transfer to the CA mesh and the CA grid schematized in Figure 2-12. The predictions using the chaining scheme are presented in Figure 3-23 and Figure 3-24. The melt pool – defined by more than 99 % liquid fraction – is naturally limited to the superheated liquid region and hence includes the T_{liq} isotherm contour (red in Figure 3-23, same as Figure 3-20, two contours of T_{liq} can be observed due to the 3D presentation). The same result is shown when drawing the profiles of temperature and liquid fraction along the centerline of the weld bead in Figure 3-24. The chaining scheme results show that the liquid fraction simply follows the tabulations in Figure 3-1, decreasing below T_{liq} and reaching 0 % below T_{sol}. This position clearly differs from the growth front of the grain structure predicted by the CA method using K_1 in Figure 3-23 in same chaining strategy. It is indeed located ways behind the melt pool predicted by the solution of the heat conservation equations. For this reason, a large region appears behind the melt pool predicted by the conservation equations (in grey), that correspond to CA cells with an index still corresponding to the liquid state (in white). This can be seen as an incoherent result between the CA and FE solutions due to the chaining scheme, that was not present in Figure 3-12 (a) with the coupling scheme: the CA grain structure computed by chaining actually develops in a region where solid is already formed according to the FE solution. Comparison of the profiles for the chaining and coupling schemes is possible in Figure 3-24, also confirming the coherent behavior between CA and FE fields in the coupling scheme where the existence of a mushy zone (non-liquid cells), $g_{\nu^{CA}}^{m}$, is used to convert energy into fraction of phases and hence resulting into a slightly different temperature field (Figure 2-12).

The consequences of the chaining scheme on the grain structure should be discussed. While similitudes exist between the computed grain structures in Figure 3-22 (a) and Figure 3-13 (b) right and also the ⟨100⟩ pole figure in Figure 3-15 (b), the growth front is not as sharp at the rear of the melt pool when using chaining (Figure 3-23 and Figure 3-12 (a)). As a consequence, a small difference exists in the average grain orientation, that is yet merely visible. Thus, despite the highlighted incoherency of the chaining scheme in the resolution stages, it could be considered quite relevant in the present welding simulation. The main reason is due to the high temperature gradient and the constrained growth mode that drives energy through the surrounding cold metal plate. In case of lower temperature gradient processing, for example, casting of thick metal component, the development of the grain structure acts more significantly on the overall temperature field. The most obvious example is the upon formation of an equiaxed grain structure for which recalescence events are regularly reported [Gan94, Car11].

It is also worth noticing that the chaining scheme could have been used to determine the adjusted growth law, K_1, while this was presently done using coupling in simulation RV_1K_1CO. This would have obviously required to compare the shape of the CA computed growth front with the observed melt pool boundary and not the FE computed melt pool (see Figure 3-23). However, this strategy was not pursued as it presents inconsistencies as previously discussed.

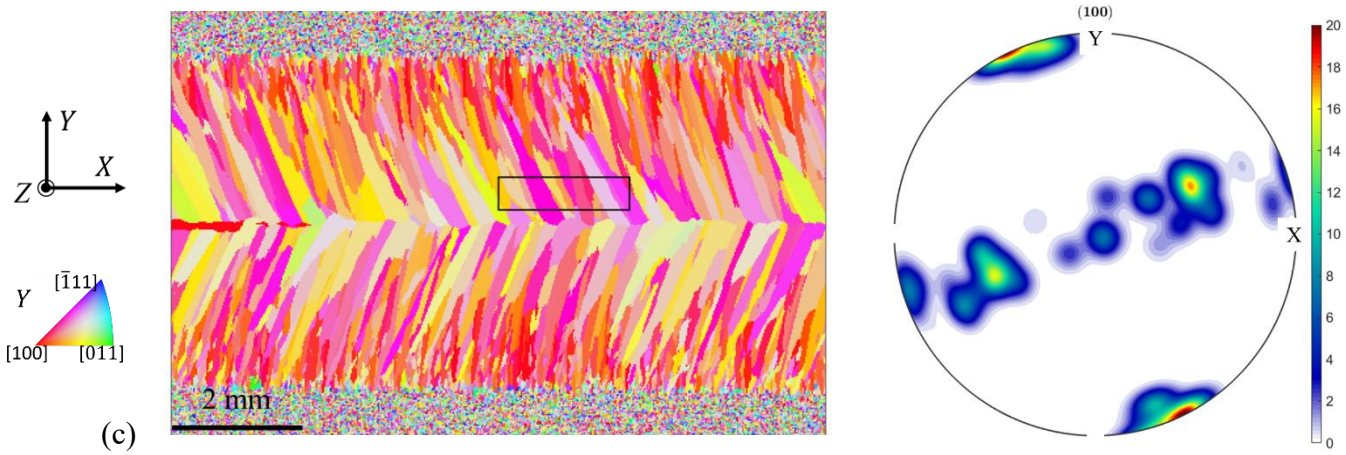

Figure 3-22. RV_1K_1CH simulation. (a) IPF-Y EBSD map, Same as Figure 3-13 (b) caption, (b) $\langle 100 \rangle$ pole figure plotted in the black rectangle in (a).

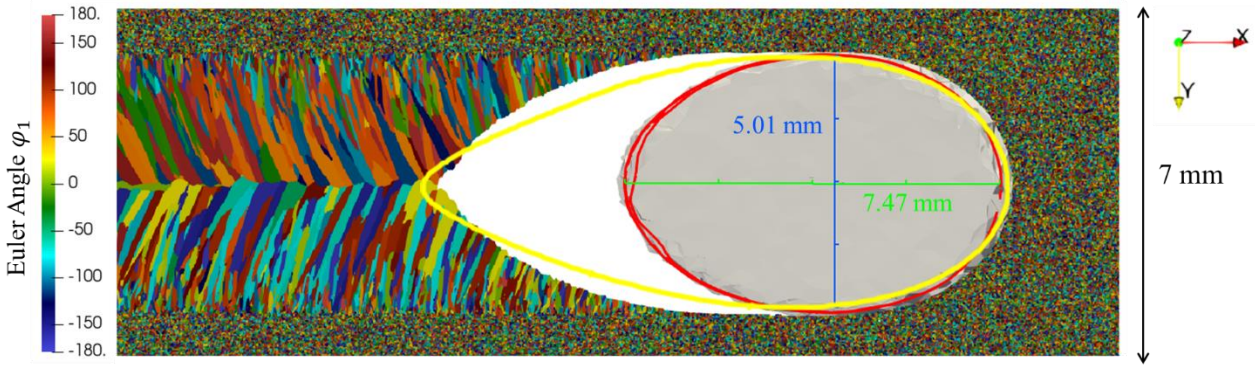

Figure 3-23. RV_1K_1CH simulation at time 14 s. Same as Figure 3-12 (a) caption.

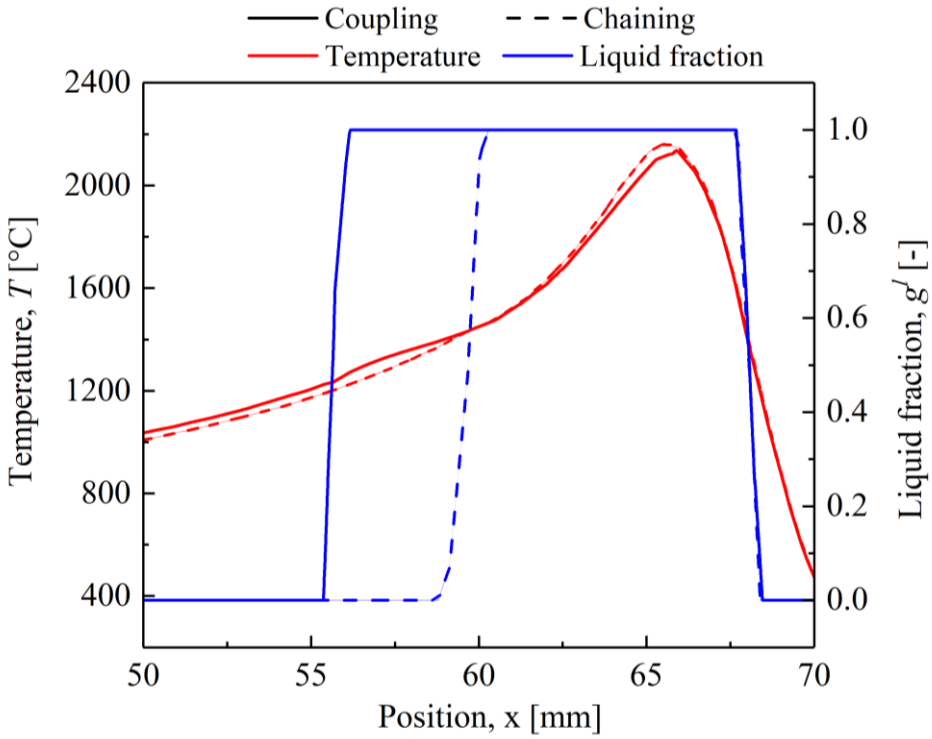

Figure 3-24. Comparison of profiles at time 14 s for (red) the temperature and (blue) the liquid fraction as observed along the centerline ($X-$ line) draw at the center of the melt pool ($Y = 0$ mm) at depth $Z = 0.75$ mm, with (plain lines) the coupling scheme, RV_1K_1CO, and (dashed lines) the chaining scheme, RV_1K_1CH.

3.5.3 Influence of initial texture

As shown in Figure 3-14, the initial grain texture differs from the experiment and the simulation. In order to study its influence on the final microstructure, a simulated grain texture similar to the experiment is carried out. To create this initial texture, some data associated to the base metal are extracted from the experimental EBSD file (for example, within the white rectangle in Figure 3-13 but with a larger domain). This data contains the three Euler angles of a set of grains. During the generation of initial grain texture, the three Euler angles of grains are randomly chosen in this file rather than randomly defined as previously proposed. Consequently, the initial grains (before welding process) have their Euler angles similar to the ones associated to the base metal in experiments. The pole figure of the new initial grain structure is presented in Figure 3-25. This initial grain texture is clearly similar to experimental observations (Figure 3-14 (a)). This initial grain texture creation method is hereafter named ‘texture initiation’, and the previous method using random number for the Euler angles is named ‘random initiation’ hereafter.

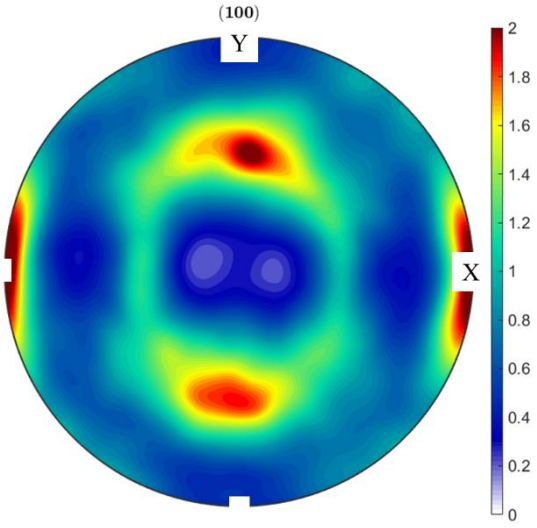

Figure 3-25. ⟨100⟩ pole figure plotted in the base metal, after "texture initiation".

The cases TV_1K_1CH and TV_2K_1CH are applied in the texture initiation base metal, the EBSD map of the two cases are presented in Figure 3-26 at the same zone as in Figure 3-13 for TV_1K_1CH and Figure 3-18 for TV_2K_1CH.

Considering firstly the base metal (white rectangle), the inverse pole figure color codes in the texture initiation is much more similar to the experimental result presented in Figure 3-13 left for TV_1K_1CH than the random initiation presented in Figure 3-13 right. The same observation for TV_2K_1CH can be made by comparing with Figure 3-18. For the grain in the melt pool, the columnar growth of elongated solidification grain structure is nearly the same for the two methods. This columnar growth is mainly related to the temperature gradient during the welding process. Consequently, the change of initial grain texture has a light influence on the growth process as confirmed by present simulations. Considering the case TV_1K_1CH, the IPF-*Y* of the two initial methods present both a color code similar to the experiment, while in the IPF-*X*, more blue and violet color are found in the texture initiation and in the IPF-*Z*, more yellow and green color are presented. However, it is difficult to conclude to an improvement of simulations compared with 'random initiation' case, as both are similar to the experimental observations. Thus, the ⟨100⟩ pole figures of the grains located in the black rectangles windows in Figure 3-26 left is plotted in Figure 3-27 (a). Compared with Figure 3-15, the texture initiation presents a better texture in the center line with two spots at similar position regarding experiments (Figure 3-15 (a)) while the random initiation presents a more homogenous distribution of intensity. However, the grains near the border of the melt pool (zone encompassed by the blue contour in Figure 3-26 (b) left) have the same color code despite the initiation method and different from experimental observation. This may lead to some discussion on temperature field estimation and/or grain growth law.

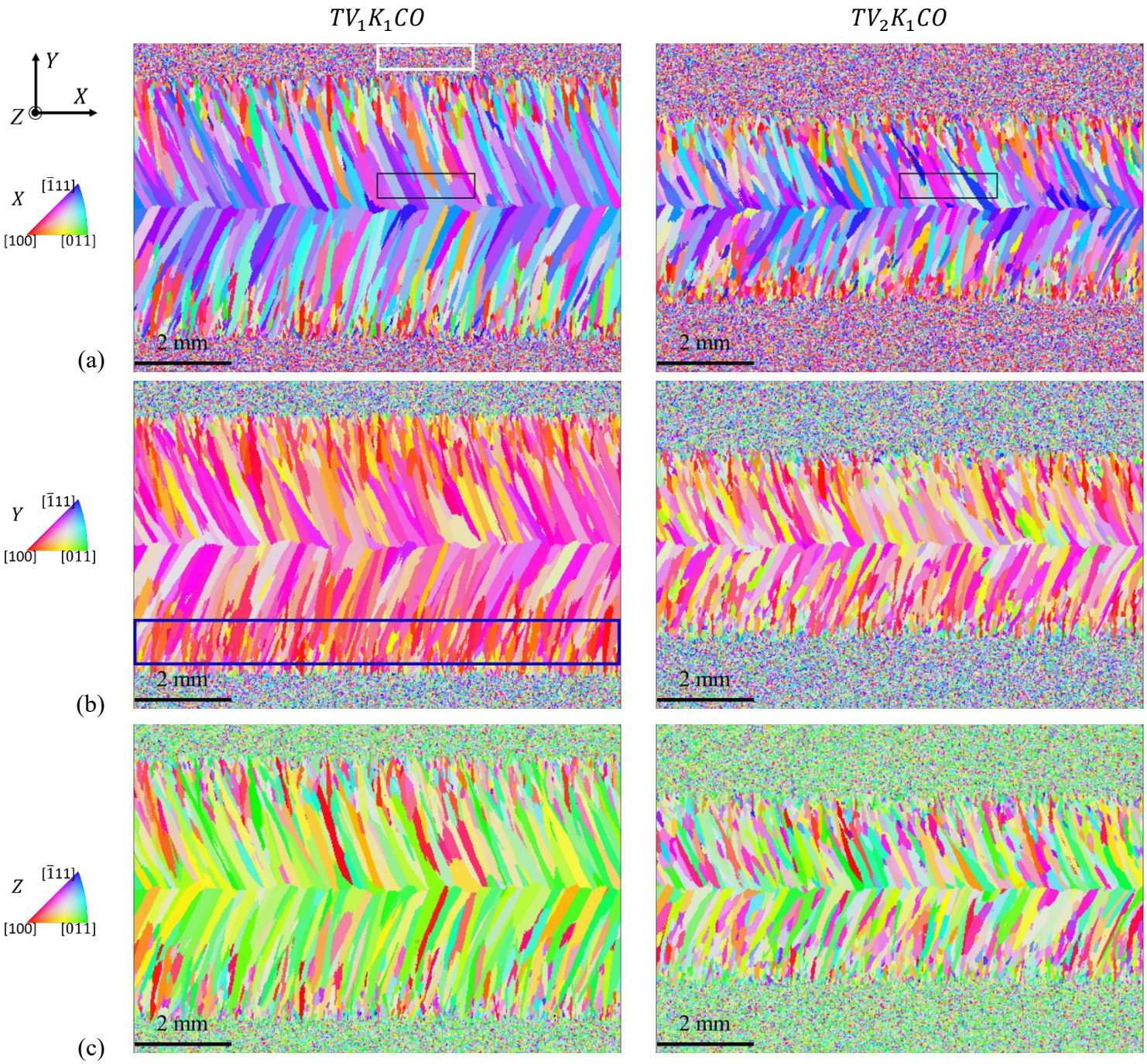

Figure 3-26. TV_1K_1CO and TV_2K_1CO simulation with texture initiation. Same as Figure 3-13 caption.

For case TV_2K_1CH, the IPF-Z color map of texture initiation presents less red color and more green and yellow color than that of the random initiation, which is more similar to the experimental result. For IPF-X, same observations as for case TV_1K_1CH can be made: results of both two methods are similar to the experimental observations. However, for the IPF-Y, the result of the texture initiation always presents a difference of 'cold' color (blue) between the simulation and the experiment. The reason remains unclear, one explanation could be the thermal condition encountered during grain growth during solidification process such as the temperature gradient and the kinetic laws. In this case, experimental temperature field measurement and comparison with simulations could provide better understanding of the

difference in the EBSD color code. The ⟨100⟩ pole figures of the grains in the black rectangles in Figure 3-26 right is plotted in Figure 3-27 (b). The texture presented is closer to the experimental observation especially for the small Z component which is not clearly presented in the random initiation method (Figure 3-19 (b)).

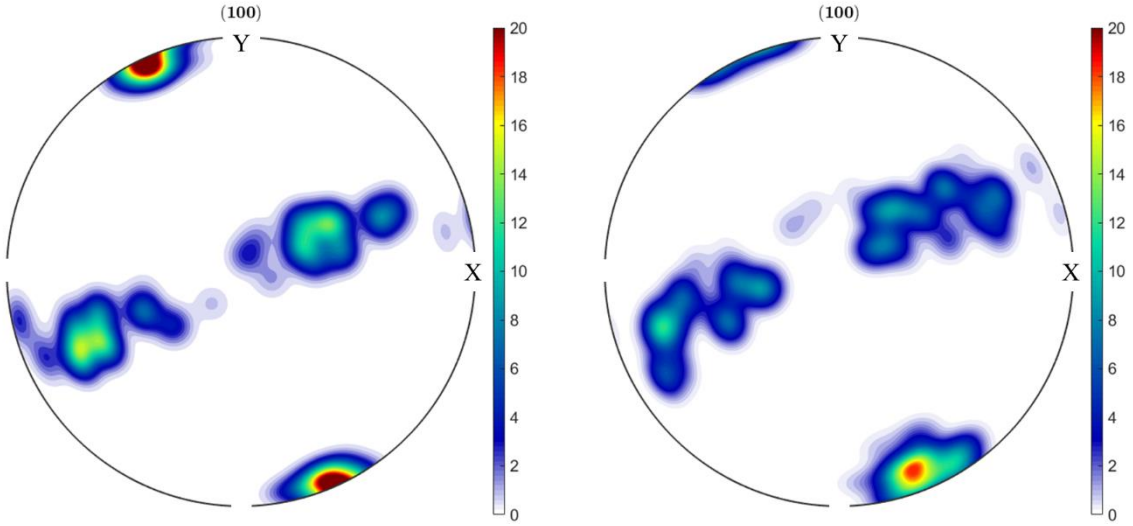

(a) (b)

Figure 3-27. ⟨100⟩ pole figure plotted in the weld bead (black rectangle in Figure 3-26), (a) TV_1K_1CO, (b) TV_2K_1CO.Same as Figure 3-15 caption.

3.6 Conclusions

In this chapter, quantitative comparisons between in-situ observations along with EBSD measurements and CAFE simulations have been carried out on single pass GTAW welding without adding material for metal-sheet plates. Good coherence can be found in the macroscopic fields such as melt pool shape and fluid flow velocity (despite the underestimation of fluid flow caused by numerical limitations). Besides, the overall grain structure and its associated texture can be well reproduced by the CA method providing a satisfying shape of the melt pool with an adjustment of the growth kinetics law. A law retrieving the melt pool shape and the grain structure for two welding velocities is proposed. Another computed dendrite tip growth kinetic law using thermodynamic databases for interface equilibrium and diffusion coefficients is tested, revealing limitations of this analytical computation. Limitations of the chaining scheme compared to the coupling scheme of the CAFE model are also highlighted. Furthermore, the influence of the initial grain structure is also studied. Results show that a “texture initiation” grain structure close to experimental observation gives better pole figure than a “random initiation” while the EBSD map remains quite similar between these two initiation methods despite some slight improvements.

3.7 French summary

Dans ce chapitre, des comparaisons quantitatives entre des observations in-situ de dimension et forme de bain fondu, ainsi que des mesures EBSD et des simulations CAFE ont été effectuées sur un soudage GTAW simple passe sans apport de matière. Une bonne cohérence peut être trouvée dans les champ macroscopiques et la vitesse d'écoulement du fluide (malgré la sous-estimation de l'écoulement du fluide en raison de limitations numériques). De plus, la microstructure globale et la texture de grain associée peuvent être bien reproduites par l'approche CA, fournissant une forme satisfaisante du bain de fusion après ajustement de la loi de cinétique de croissance. La loi proposée permet de retrouver la forme du bain de fusion et la structure des grains pour les deux vitesses de soudage investiguées. Une autre loi de croissance calculée avec les données thermodynamiques (équilibre interfacial et coefficients de diffusion) est testée, révélant les limites de cette approche. De plus, les limites du schéma de chaînage par rapport au schéma de couplage du modèle CAFE sont également mises en évidence. L'influence de la microstructure initiale est également investiguée. Les résultats montrent qu'une structure de grain issues des analyses de la texture expérimentales donne une meilleure texture du métal de base, au travers des figures de pôle, qu'une distribution aléatoire des orientations, bien que les cartes EBSD des domaines resolidifiés soient relativement similaires, au final, entre ces deux méthodes d'initialisation.

4 Multi pass GTAW in narrow chamfer configuration, with added material

In this chapter, the 3D CAFE model is applied to a multi pass GTAW process with material added in a chamfer. Such welding experiments were carried out at Laboratoire Interdisciplinaire Carnot de Bourgogne (ICB) with the 316L stainless steel and have been modeled with the present approach. Three superimposed passes in total are considered. The material of interest considered both for the base metal and the added material. Comparisons of temperature measurement and microstructure between experiment and simulation result are developed. All the material properties are the same as presented in section 3.1, *i.e.* the differences between 316L used in the two experiments are neglected in the simulation. Besides, regarding the conclusion in section 3.5, the kinetic law K_1 and coupling CAFE scheme are considered hereafter.

4.1 Experiment set up

4.1.1 Experimental device and parameters

All the experimental work has been established and achieved in ICB (Laboratoire Interdisciplinaire Carnot de Bourgogne), partner of NEMESIS project. The experimental device is presented in Figure 4-1. The welding process is achieved automatically (*i.e.* welding robot) on the chamfer presented in Figure 4-2, the length of the chamfer is 200 mm and the welding is carried out along the X direction. An argon flow rate of 9 L/min is applied during processing through the welding torch in order to protect the weld pool from oxidation.

(a) (b)

Figure 4-1. Experimental device for multi pass GTAW,
(a) welding machine, (b) zoom of arc and adding wire. [ICB20]

Other welding parameters are presented in Table 4-1. Distance between arc and initial metal surface is fixed at 6.5 mm for each pass. Consequently, after each welding pass, the torch is moved in upper direction from the thickness of added material in the weld bead.

Table 4-1. Welding parameters.

Parameter	Value	Unit
Welding voltage, U	13	V
Welding current, I	220	A
Welding power, UI	2860	W
Welding speed	1.67 (100)	mm s^{-1} (mm min^{-1})
Adding wire radius, R_w	0.45	mm
Adding wire speed, v_w	31.67 (1900)	mm s^{-1}(mm min^{-1})
Distance between arc and initial metal surface for each pass	6.5	mm

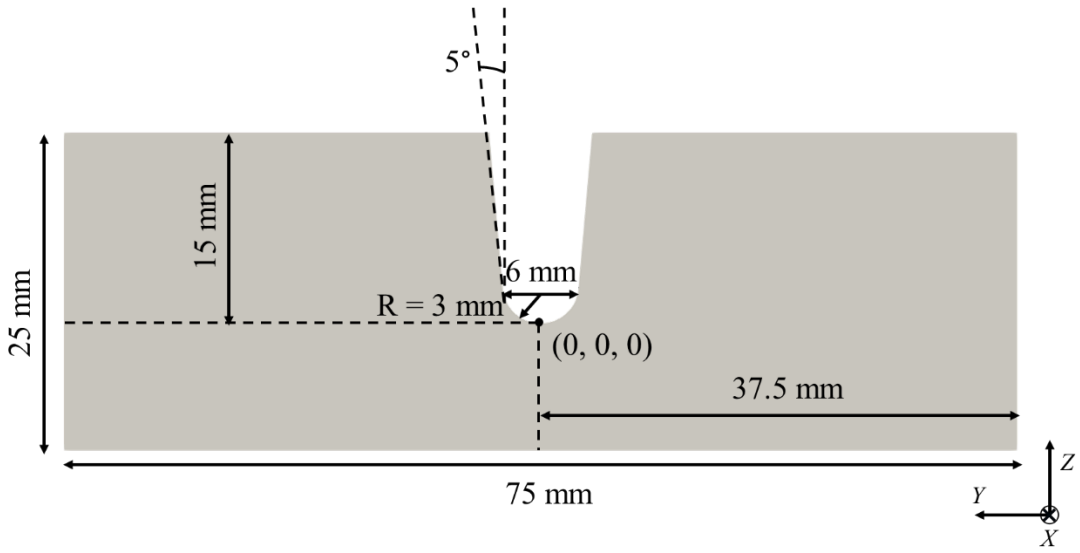

Figure 4-2. Front plane ($X = 0$) of the chamfer configuration.

Two experiments are carried out with the same process parameters presented in Table 4-1. The only difference is the length of the weld bead for the 3 passes. For the first experiment, referred as E1 hereafter, thermocouples are inserted in the chamfer to measure the temperature evolution during the welding process and the cooling stage. For this reason, the weld bead should finish

at the same position for the 3 passes. And the second experiment, referred as E2 hereafter is achieved to get metallographic observations in each of the 3 weld beads requiring a steady regime in each of the 3 beads. The better approach is to develop 3 weld beads who end at different positions in order to leave a sufficient length to achieve a steady regime. Table 4-2 presents the starting point and end point in the two experiments (the position of the torch is the same for X and Y, but 6.5 mm higher in Z) for the 3 passes. It could be noted that the heights along Z direction for the 3 passes are different because of the added material.

Table 4-2. Weld bead starting point and end point of 3 passes in the two experiments.

	E1[mm]	E2[mm]
Pass1 $(X_{S_1}, Y_{S_1}, Z_{S_1}), (X_{E_1}, Y_{E_1}, Z_{E_1})$	$(0,0,0), (200,0,0)$	$(0,0,0), (200,0,0)$
Pass2 $(X_{S_2}, Y_{S_2}, Z_{S_2}), (X_{E_2}, Y_{E_2}, Z_{E_2})$	$(20,0,1.8), (200,0,1.8)$	$(0,0,0), (140,0,1.8)$
Pass3 $(X_{S_3}, Y_{S_3}, Z_{S_3}), (X_{E_3}, Y_{E_3}, Z_{E_3})$	$(40,0,3.5), (200,0,3.5)$	$(0,0,0), (80,0,3.5)$

During the welding process E1, thermocouples are inserted into the chamfer at plane $X = 150$ mm, which could be considered as steady regime for the temperature field over a sufficiently large distance. Coordinates of the thermocouples' positions are presented in Table 4-3 with the position presented in Figure 4-3.

Table 4-3. Thermocouples positions (Y, Z) [mm] in plane $X = 150$ mm.

TC1	TC2	TC3	TC4	TC5
$(9.0, 7.5)$	$(9.5, 4.5)$	$(8.5, 1)$	$(6.5, -2.9)$	$(3.0, -2.9)$
TC6	TC7	TC8	TC9	TC10
$(-9.0, 7.5)$	$(-9.5, 4.5)$	$(-8.5, 1)$	$(-6.5, -2.9)$	$(-3.0, -2.9)$

As presented in Figure 4-3, the positions of thermocouples TC(n) and TC(n + 5) (n ∈ {1,2,3,4,5}) are symmetric with respect to the center plane $Y = 0$. For E2, the metallographic observation plane is chosen 20 mm in front of the end of the weld beads as presented in Table 4-4.

Table 4-4. Metallographic observation planes for E2.

Pass 1	Pass 2	Pass 3
$X = 180$ mm	$X = 120$ mm	$X = 60$ mm

(a)

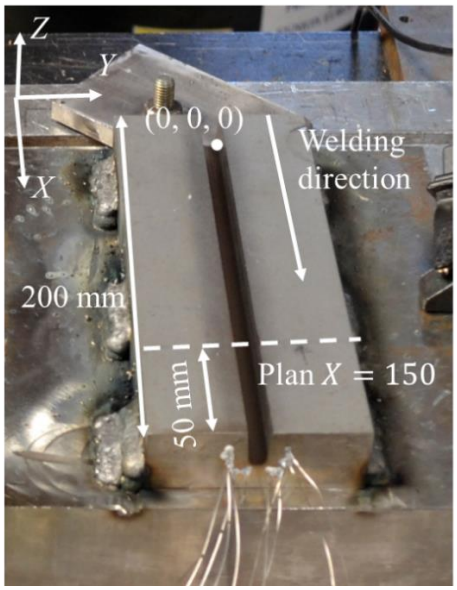

(b)

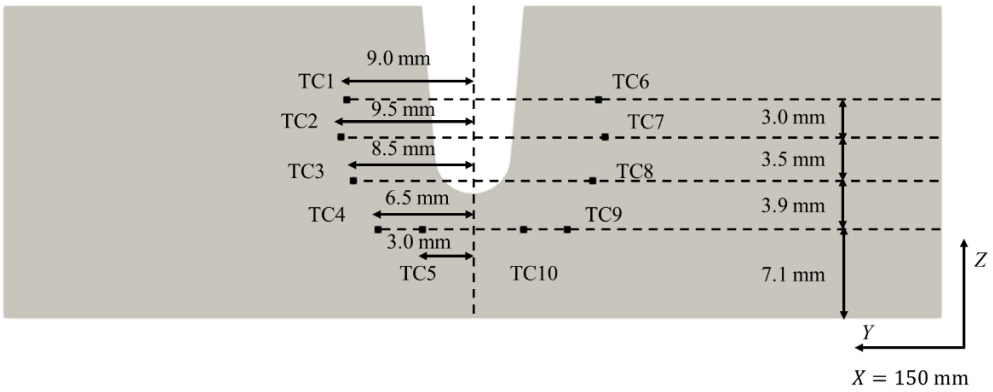

Figure 4-3. Thermocouples positions on plane $X = 150$ mm

(a) position of plane on the chamfer [ICB20], (b) thermocouples positions in plane.

4.1.2 Melt pool shape observation

The melt pool shape is an important parameter to calibrate the thermal parameters especially for the heat source developed in the simulations. The melt pool shapes of the 3 passes are presented in Figure 4-4. Three main parameters are used in the simulations for calibration: L1, the distance between the weld bead surface at the center line and the lowest point of the melt pool, this distance shows the "concentration" of the heat source. L2, the distance between the right top point and the lowest point of the melt pool (at the center line, same point as L1), this distance shows the "distribution" of the heat source. The third parameter is the surface of the melt pool. Detailed values of the measurement are presented in Table 4-5. It can be noted that L2 is chosen at the right side of the melt pool. The reason is the dissymmetry of melt pool shape shown in Figure 4-4 (a) and (b). In fact, in the experiment, it is difficult to maintain the welding torch exactly perpendicular to obtain the symmetric melt pool. Besides, the fusion of the initial chamfer makes it difficult to locate the position of the melt pool (as shown in Figure 4-4). Thus,

for the first pass, the right side where the initial chamfer is clearer is chosen as the reference for L2 and this choice is kept for the 2 next passes. It could be noted that the "right" is defined with respect to Figure 4-4, which can also be defined as the left side with respect to welding direction.

Table 4-5. Main parameters measured for the melt pool shape.

	Pass 1	Pass 2	Pass 3
L1 [mm]	2.67	2.76	3.17
L2 [mm]	5.22	4.61	4.44
Melt pool surface [mm^2]	18.96	23.96	22.94

Another point to be noted is the dispersion of the experimental result. Even through the welding parameters are kept identical for the 3 passes, it could be noted that the melt pool shapes for the first pass are not the same in Figure 4-4 (a), (b) and (c). Besides, the melt pool shape for the second pass is also different in Figure 4-4 (b) and (c). The reason could be the manipulation difficulties during the experiment to always keep the same welding conditions such as welding power and the distance between the torch and the metal surface. In addition, an interaction between the torch and the chamfer is also noticeable on Figure 4-4 as a part of the metal on both sides of the electrode is melted and feeds the melt pool. Consequently, the melt pool sizes are modified depending on the importance of this feeding process.

(a)

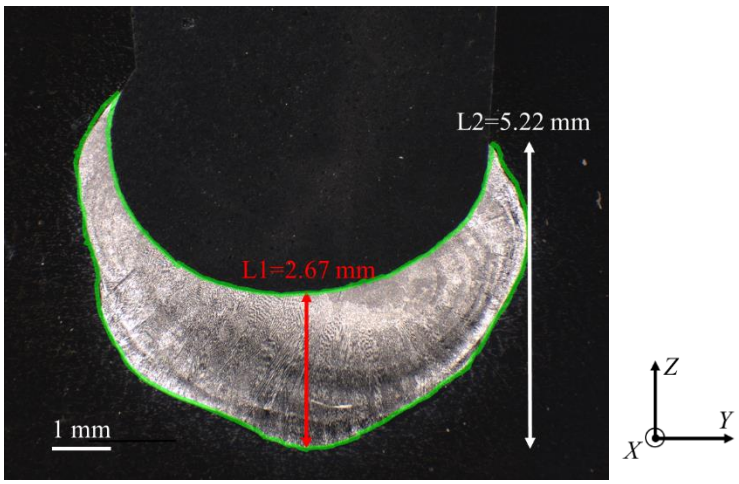

(b)

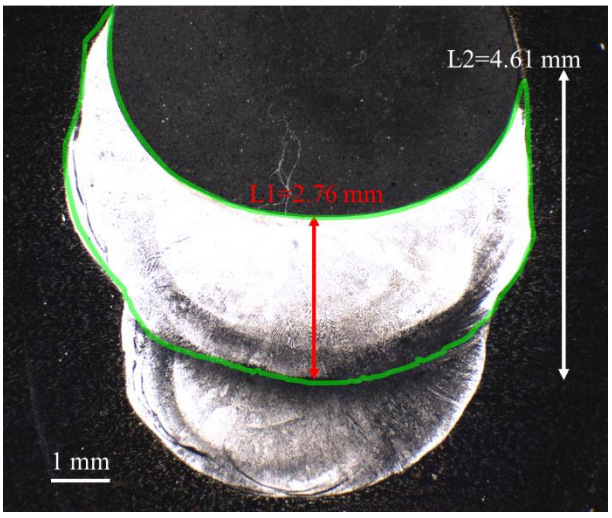

(c)

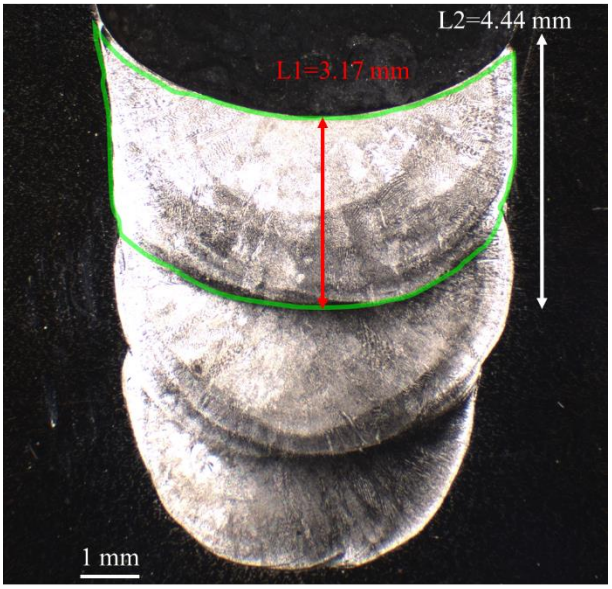

Figure 4-4. Melt pool shape observation, the green contours present the melt pool shape for the 3 passes (a) first, (b) second, (c) third passes, welding direction is X.

4.2 Simulation parameters

Same as for the single pass GTAW simulation, the global simulation domain contains the metal subdomain Ω^M and the surrounding gas subdomain Ω^G on the top of the metal plate. As presented in Figure 4-5, the length of the simulation domain is decreased to 100 mm rather than 200 mm in the experiment to save computation time. Practically, about 20 s are required in the simulation to reach the steady state (see hereafter Figure 4-10). As the welding speed is equal to 1.67 mm s^{-1}, the length of the weld bead is about 34 mm at this step. Consequently, 100 mm is long enough to cover the whole length until this steady state. In the simulation, a weld bead of 60 mm is achieved for the 3 passes, a such simulation of each pass considering the grain structure takes about 60 hours on 56 processors. Thus, the reduction of part length is also necessary to decrease computation time.

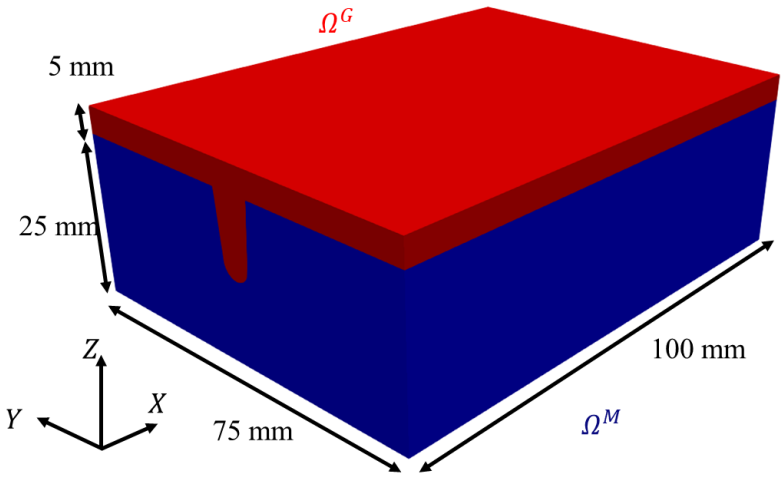

Figure 4-5. Simulation domain Ω with (blue) the metal subdomain, Ω^M, and (red) the upper gas subdomain, Ω^G.

The initial FE mesh is presented in Figure 4-6 (a), and the CA mesh positioned along the weld line, as shown in Figure 4-6 (b). For the same reason, the CA mesh is smaller than the FE mesh. Besides, the CA mesh contains also initial gas domain in order to represent the weld bead induced by the use of an adding wire. Other details of the FE and CA mesh can be found in Table 4-6. As shown in Figure 4-6 (b), the mesh around the heat source is refined to better solve the FE problem in this zone where temperature gradient is large. Same as for the single pass GTAW previously presented, this zone of refined mesh will advance with the heat source during the simulation.

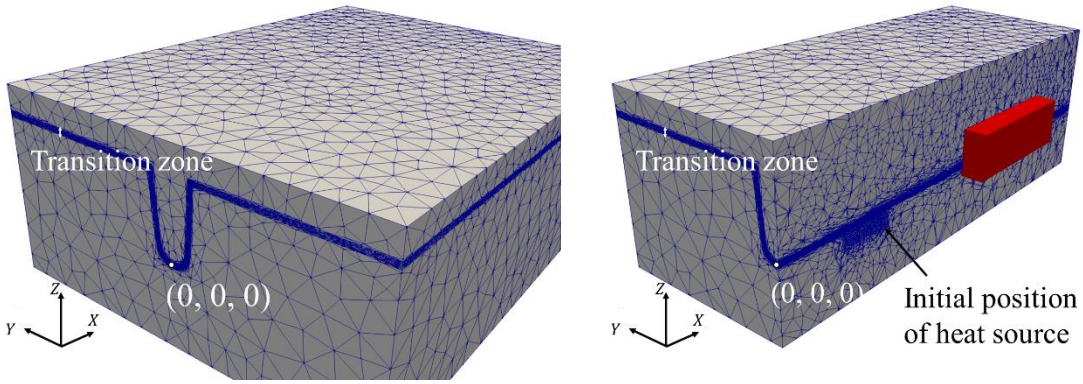

(a) (b)

Figure 4-6. (a) (blue) initial FE mesh
(b) longitudinal cut of the initial FE mesh by plane Y=0 and (red) CA mesh.

Table 4-6. Mesh parameters.

Parameter	Value
Global simulation domain, Ω	$100 \times 75 \times 30$ mm
Metal subdomain, Ω^M	See Figure 4-5 in blue
Top gas subdomain, Ω^G	See Figure 4-5 in red
Half thickness of transition zone, ε	0.5 mm
FE mesh size in the transition zone (Figure 4-6 (a))	50 µm
FE mesh size around the heat source (Zone HS in Figure 4-6 (b))	0.5 mm
FE mesh size elsewhere	5 mm
CA domain Ω^{CA}	$30 \times 10 \times 10$ mm
CA mesh size (fixed)	0.5 mm
CA cell size	20 µm

The welding parameters used in the simulation are the same as in the experiment (Table 4-1), except for the welding length. Each pass takes 36 s in the simulation corresponding to a weld bead at about 60 mm, *i.e.* each pass begins at $X = 20$ mm and ends at $X = 80$ mm. For each pass, the initial condition for the resolution of energy conservation equation (2-21) is to consider the weld piece at room temperature (20°C) and for momentum conservation (Navier Stokes equation (2-59)) is zero velocity for the global system. All the surfaces are considered as adiabatic for energy conservation equation (2-21). For Navier-Stokes equation (2-59), zero velocity and free pressure are applied for all the 4 side surfaces.

4.3 Heat source modeling and thermal simulation result

The purpose of this section is to compare the thermal simulation result (*i.e.* melt pool shape and temperature evolution) with the experimental measurements in terms of melt pool shape and temperature evolution in order to validate the thermal resolution and the heat source model.

4.3.1 Modeling of heat source in chamfer configuration

The configuration of chamfer in multi pass GTAW process leads to more complicated modelling than in the single pass metal plate. In this section, three heat source models will be presented and the associated melt pool shape are compared with the experimental measurements (section 4.1.2). The comparison of these melt pool shape will define thereafter the more relevant heat source model. However, it should be noted that, during the experiment, the chamfer is deformed. For example, the thermal stress during solidification of the first pass can cause the closure of the chamfer which makes its side surface closer to the heat source for the second pass and leads to a higher melt pool. As shown in Figure 4-7, the angle of the chamfer after 3 passes changes from 5° to 2°. Because the solid mechanical resolution is not yet considered, the comparison of melt pool shape is restricted to the first pass to limit the consideration of chamfer deformations.

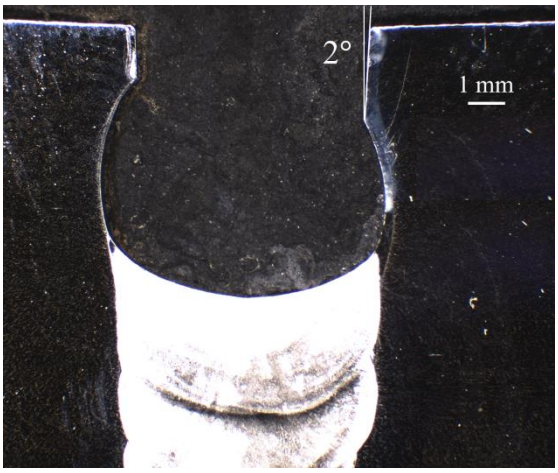

Figure 4-7. Deformation of chamfer after 3 passes.

The three heat sources models considered are defined by the following formulae:

Model 1: Gaussian

$$\dot{Q}_P = \frac{3\dot{Q}_{Plasma}}{K_P\ 2\pi\ d^2\ (1-\cos\alpha)} \mathrm{e}^{-3\left(\frac{\beta}{\alpha}\right)^2} \cos\gamma \qquad (4\text{-}1)$$

Model 1 has the same expression as in equation (2-29), and the definition of the parameters are given in Figure 2-6

Model 2: Uniform disc

$$\dot{Q}_P = \frac{\dot{Q}_{Plasma}}{2\pi\, d^2\,(1-\cos\alpha)}\cos\gamma \tag{4-2}$$

In model 2, the heat source is assumed as homogeneous on a spherical cap (part of sphere) with aperture angle α.

Model 3: Uniform ellipse

$$\dot{Q}_P = \frac{\dot{Q}_{Plasma}}{d^2\, F_p}\cos\gamma \tag{4-3}$$

$$\begin{aligned} F_p = {} & 2\pi\big(1-\cos(\alpha_X)\big) + \pi(\alpha_Y-\alpha_X)\sin(\alpha_X) \\ & - \frac{\pi(\alpha_Y-\alpha_X)^2}{96\cos(\alpha_X)}\big((\alpha_Y-\alpha_X)(\cos(2\alpha_X)-5) \\ & + 6\sin(2\alpha_X)\big)\tan(\alpha_X) \end{aligned} \tag{4-4}$$

Model 3 presents an elliptic heat source defined with two angles α_X and α_Y in order to extend the Model 2. The length and the width are respectively equal to $2d_0\tan(\alpha_X)$ and $2d_0\tan(\alpha_Y)$, where d_0 is the distance between the heat source and the metal surface. Details of the expression of model 3 is presented in Appendix 2. It should be noted that the correct expression of this heat source model is more complex than equation (4-4) but this latter expression is a quite precise approximation based on the limited development of the original expression. Figure 4-8 shows the evolution of $\dot{Q}_P$ as a function of the distance between the considered point B (presented in Figure 2-6) and the projection of heat source on the surface plane S' as shown in Figure 4-9. To present the heat sources, $S'B$ is chosen along the welding direction $+X$ *i.e.* the evolution of $\dot{Q}_P$ in Figure 4-8 correspond to the red segment in Figure 4-9.

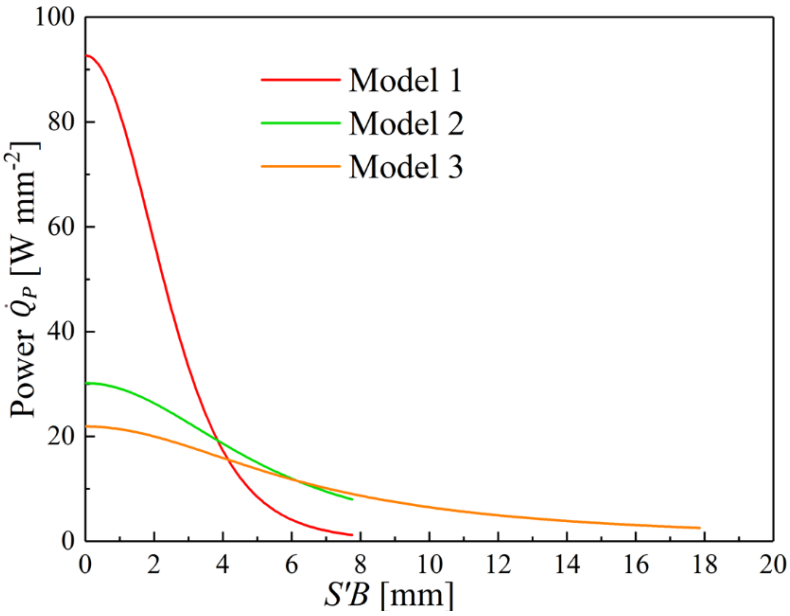

Figure 4-8. $\dot{Q}_P$ in function of distance $S'B$ for the three heat source models on a plane surface, distance of the source $d_0 = 6.5$ mm, $\dot{Q}_{Plasma} = 2860$ W. $\alpha = 50°$ for model 1 and model 2, $\alpha_X = 70°$, $\alpha_Y = 50°$ for model 3.

It should be noted that the power $\dot{Q}_P$ is not constant on the plane surface (Figure 4-8). This is caused by the evolution of the angle γ, defined between SB and the local normal $\boldsymbol{n}$ (Figure 2-6). As the aperture angle α is identical for model 1 and model 2, these two heat sources stop at the same distance $S'B = d_0 \times \tan(\alpha) = 7.74$ mm. For model 2, as the gaussian term is removed, the power is much more homogeneous on the surface compared to model 1. For model 3, the heat source covers a longer distance along the welding direction, X, and stops at $S'B = d_0 \times \tan(\alpha_X) = 17.86$ mm (Figure 4-8). In the transverse direction, the heat source disappears at $S'B = d_0 \times \tan(\alpha_Y) = 7.74$ mm along the Y direction (Figure 4-9).

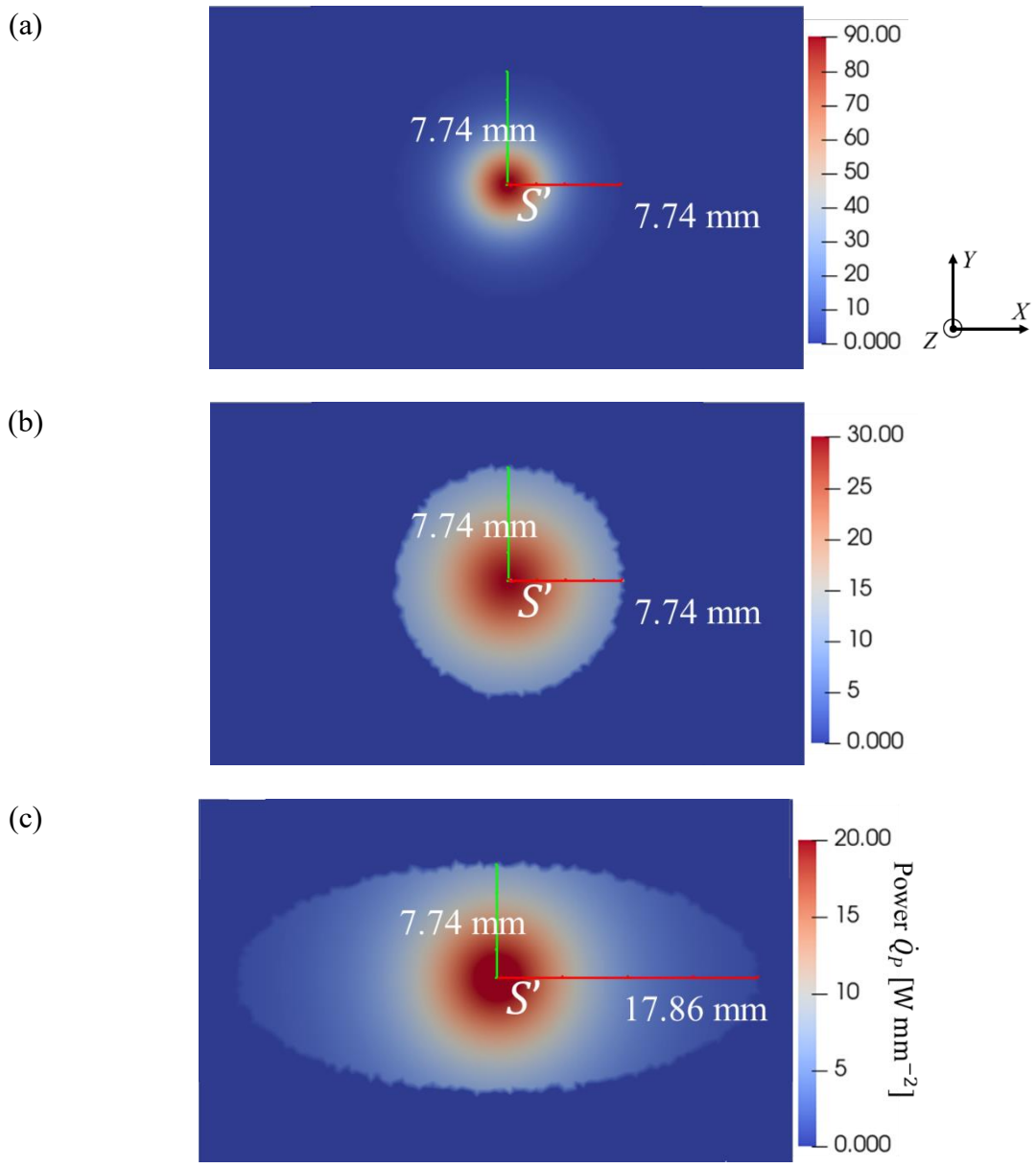

Figure 4-9. Heat source presentation on a plane surface: Model (a) 1, (b) 2, (c) 3. Same parameters are used for heat sources as Figure 4-8. The welding direction is X.

4.3.2 Thermal simulation result

In this section, the determination of steady state in the simulation will be given in detail. As mentioned above, to develop the comparison between simulation and experiment, the steady state of the simulation should be firstly determined as the experimental observation is believed to be achieved in the steady state (section 4.1.1). Figure 4-10 presents the time evolution of melt pool size for the three heat sources models. For a welding duration, t, larger than 20 s the melt pool size is nearly constant in any case and the steady state is considered as achieved (parameters of the three models are presented in Table 4-7, obtained by the calibration by

experimental results, which are different from Figure 4-9). Consequently, the simulation results are hereafter compared for time $t = 27s$ (blue line in Figure 4-10) when complete steady state is observed.

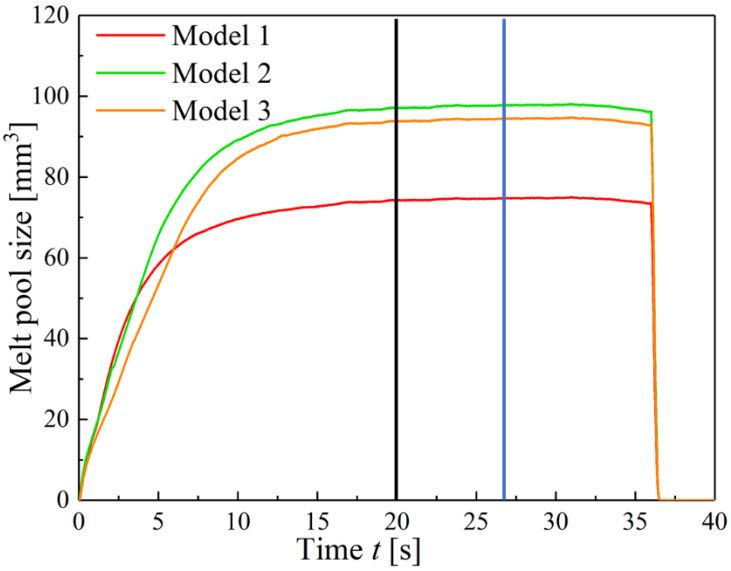

Figure 4-10. Melt pool size evolution during the welding process.

Figure 4-11 presents the evolution of melt pool length during the simulation with model 3. It could be confirmed by the melt pool length that the steady state of the welding process is obtained at $t > 20s$. It should be noted that the melt pool presented in Figure 4-11 is not at the exact position for reason of presenting the different melt pool at the same figure.

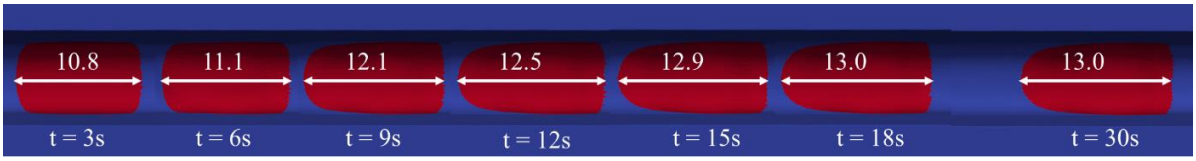

Figure 4-11. Melt pool length evolution (model 3) during the welding process.

4.3.2.1 Melt pool shape comparison

Parameters of the heat sources are calibrated manually for the three models in terms of the lengths L1, L2 (Figure 4-4) for the first pass and the melt pool surface in order to obtain comparable melt pool size. Table 4-7 presents the calibrated heat source proposed for the three models.

Table 4-7. Heat source parameters.

	Model 1	Model 2	Model 3
Efficiency η	0.6	0.68	0.8
Welding power, ηUI [W]	1716	1944	2288
Aperture half angle, α [°]	60	50	$\alpha_X = 70$ $\alpha_Y = 50$

Detailed values of the melt pool shape are summarized in Table 4-8. And Figure 4-12 presents the melt pool shape comparison between experimental measurement (green contour) and the simulation result (red zone defined by more than 99 % liquid fraction). The position along the welding direction X chosen to present the melt pool shape (Figure 4-12) corresponds to the deepest melt pool in center. This position is nearly the same as the position of the heat source at current time step. It could be noted that 2 contours of upper melt pool are presented in Figure 4-12, this is related to the 3D representation of the weld bead containing the completed weld bead (up contour) and the weld bead in development (lower contour). Figure 4-13 shows these two weld beads in details and the cavity of added material inside the melt pool determining the domain where source term of added metal is introduced.

On the one hand, for model 1, L1 is a little longer than the experimental measurement while L2 is shorter which proves that model 1 concentrate more energy in the center zone due to the Gaussian term. This observation is also verified by Figure 4-12 (a). Besides, regarding the concentrated energy distribution, the efficiency of the heat source is decreased to 0.6, leading to a smaller surface of melt pool. On the other hand, for model 2 and 3, as the Gaussian term is removed, the distribution of energy is much more homogeneous and the side surfaces of the chamfer are more heated compared with model 1. The Figure 4-12 (a) shows a nearly straight side surface of the melt pool while the Figure 4-12 (b) and (c) present a rounder side surface which is closer to the experimental observation. Comparing model 2 and 3, the efficiency of the heat source is increased from 0.68 to 0.8 while the L1, L2 and melt pool surface are very close. The reason is the elliptic distribution of model 3 which gives out more energy along the welding direction. Besides, along Y direction, model 2 and 3 present nearly the same melt pool shape, the reason could be the same aperture half angle ($\alpha = \alpha_Y$ in Table 4-7). Another point to be noted is the evolution of chamfer shape compared to its initial position due to the fusion of side surfaces as experimentally observed (green contour). None of the simulation results show the same evolution. The lack of chamfer evolution is mainly due to the viscosity used in the simulations which is much higher than the correct value (Table 3-2). The reason of our choice is to avoid numerical difficulties when using a monolithic solution of the Navier-Stokes equations for the whole system, also as discussed in previous chapter.

Table 4-8. Detailed melt pool shape comparison.

	Exp	Model 1	Model 2	Model 3
L1 [mm]	2.67	2.80	2.65	2.70
L2 [mm]	5.22	5.10	4.95	5.21
Melt pool surface [mm^2]	18.96	16.80	18.85	18.95

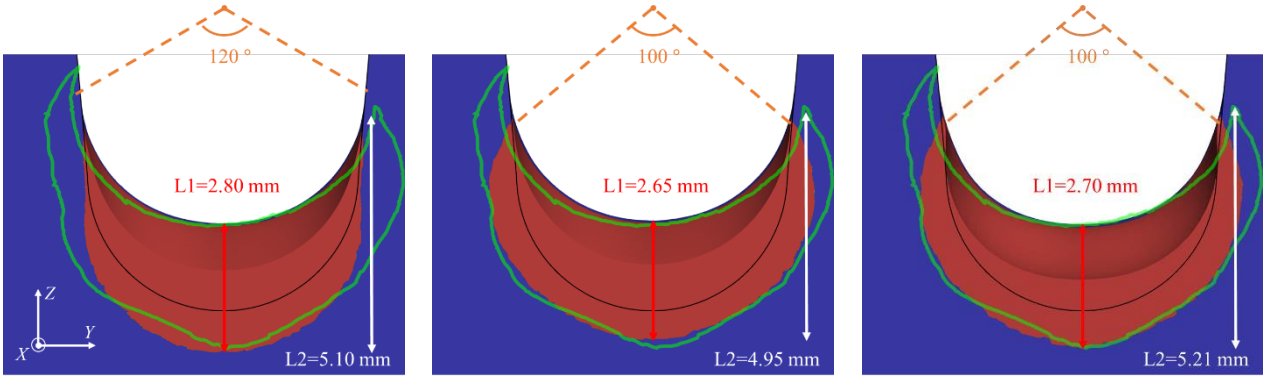

(a) (b) (c)

Figure 4-12. Melt pool shape comparison between three models (red part) and experimental observation (green contour) at t=27s, (a) model 1, (b) model 2, and (c) model 3. Black contour presents the initial chamfer position. Orange point presents the heat source position and the dashed orange line presents the aperture angle 2α.

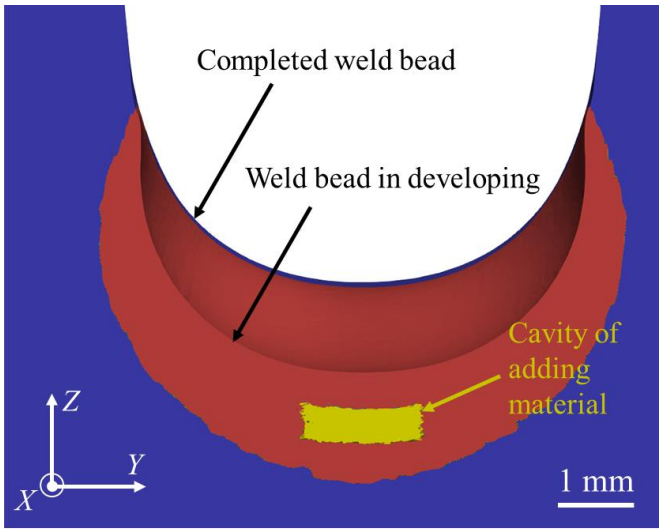

Figure 4-13. Completed weld bead and weld bead in developing with the cavity of added material.

4.3.2.2 Temperature field comparison

As presented in section 4.1 , several thermocouples were installed by ICB partner inside the chamfer during welding experiment to measure the temperature evolution in different positions. This temperature evolution is also compared between experiment and simulation for the three heat source models. However, as the length of the chamfer is different in the simulation and in the experiment, the thermocouples cannot be at the same position in these two different configurations. As presented in Table 4-3, thermocouples are positioned on the plane $X = 150$ mm along the welding direction X in experiment, while in the simulation, this position is $X = 65$ mm along the welding direction X. As the welding begins at $X = 20$ mm, it takes 27 s for the heat source to reach the plane $X = 65$ mm. Thus, a time calibration of temperature is required. This calibration is achieved by putting the maximum temperature of thermocouple TC10 at the same time (for example, experimental time) for different models, and this time gap of TC10 is then applied to other thermocouples. TC10 is chosen as the reference thermocouple as it is the closest to the melt pool. In fact, as the minimum time is necessary for the thermal diffusion at TC10, the measurement could be considered as the most precise for the maximum temperature. Besides, only the thermocouple TC6 – TC10 at the right side of the chamfer are considered in the comparison. One reason is the symmetry of the chamfer in simulations, another reason is associated to the melting of the initial chamfer which increases the uncertainty on the temperature measurement.

Figure 4-14 presents the temperature evolution for the three heat source models compared with experimental measurements. For all the three models, the slope of the heating stage and the cooling stage is coherent with the experimental result showing the relevance of the thermal properties used for 316L steel grade in the simulation. For each thermocouple, the maximum temperature of three models is in the same order: model 3 > model 2 > model 1. The main reason of this evolution between the models is the choice of the efficiencies between models (Table 4-7), as the efficiency is in the same order for the 3 heat sources.

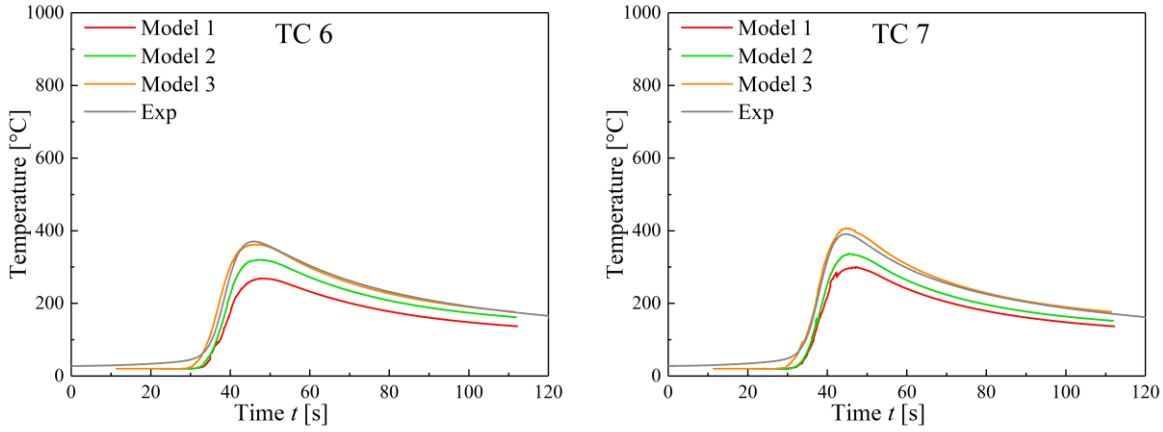

(a)

(b)

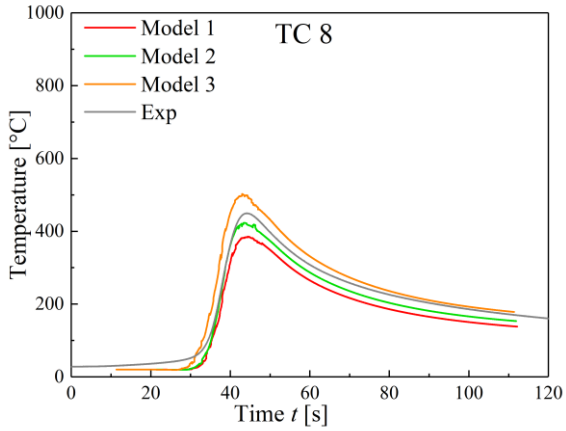

(c)

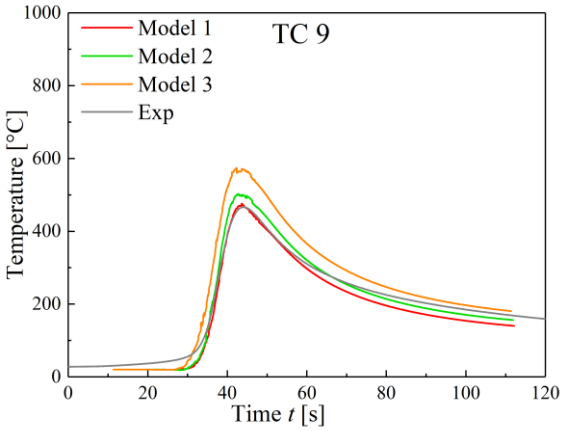

(d)

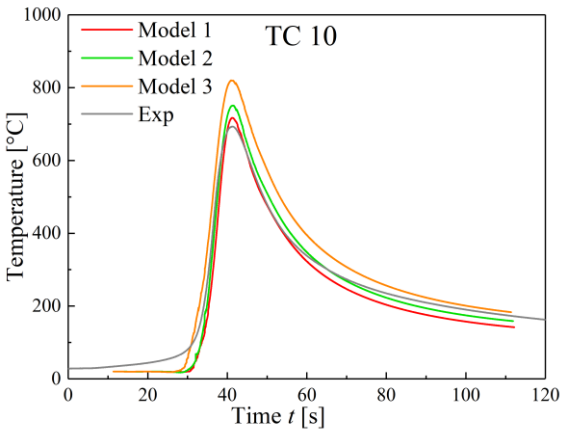

(e)

Figure 4-14. Temperature evolution of thermocouples.

For model 1, the temperature evolution curves are coherent with experiments for the two thermocouples, TC 9 and TC10, close to the melt pool. The differences between curves increase thereafter when the thermocouples are located on the side surface (*i.e.* chamfer surfaces). This difference is induced by the melt pool shape between experiment and simulation as presented in Figure 4-12 (a), indicating the concentration of energy in the center of the chamfer.
Model 2 presents good coherence of temperature evolution curves for TC8 – TC10, even for TC6 and TC7, the difference in temperature evolution is reduced compared with model 1. The main reason is the use of a more homogeneous energy distribution function.
For model 3, the maximum temperature is higher than the experiment for TC8 – TC10, even though good coherence of temperature evolution is found for TC6 and TC7. This could be explained by the heat source efficiency which may be higher than the experimental value even though the melt pool size corresponds to the experiment. In fact, as the main purpose of this simulation is the grain structure evolution taking place inside the melt pool, this efficiency at 0.8 is applied in order to keep the good coherence of melt pool shape. We have also to note that the temperature begins to increase before the two other models, due to the elliptic and elongated shape of heat source which preheat the chamfer on a longer distance compared with the previous models. It could be noted that, in the experiment, the temperature can increase to 40℃ (even 60℃ for TC10) at about 25 s, while in the three simulations, this phenomenon is not observed as the temperature increase is observed later. The experimental increase in temperature could be explained by the circulation of heated gas who heat the chamfer during the welding. This circulation of gas is not considered yet in the simulation which leaves this difference at the beginning of the temperature evolution.

4.3.2.3 Microstructure comparison

As shown in Figure 4-15, the microstructures at the center plane are different between the three heat source models as a consequence of the change in melt pool shapes, especially at the rear. However, Model 3 presents the longest melt pool due to the use of an elliptic shape for the heat source which provides more energy at the rear of the melt pool. Consequently, as the grains develop along the direction of the temperature gradient, normal to the melt pool contour, the solidified grains structure presents a tilted angle (angle θ as presented in Figure 4-15) along the welding direction at about 30°. As the melt pool is shorter at rear for model 1 and model 2, this tilted angle is increased at about 35°. Besides, the melt pool length for model 1 is shorter than model 2 due to the non-homogeneous source, the energy is more focused at the center (as shown in Figure 4-8 and Figure 4-9). Furthermore, considering the melt pool shape near the top metal surface (encompassed in white), model 2 shows a contour nearly perpendicular to the welding direction. As a consequence, a grain with Euler angle $\varphi_1 \approx 0°$ (the green grain with $\langle 100 \rangle$ direction along the welding direction) survives the grain competition and develops along the weld bead in a great distance. For model 1, even though the encompassed part of melt pool shape presents weak difference from that of model 2, the grain competition is strong enough to eliminate the green grain.

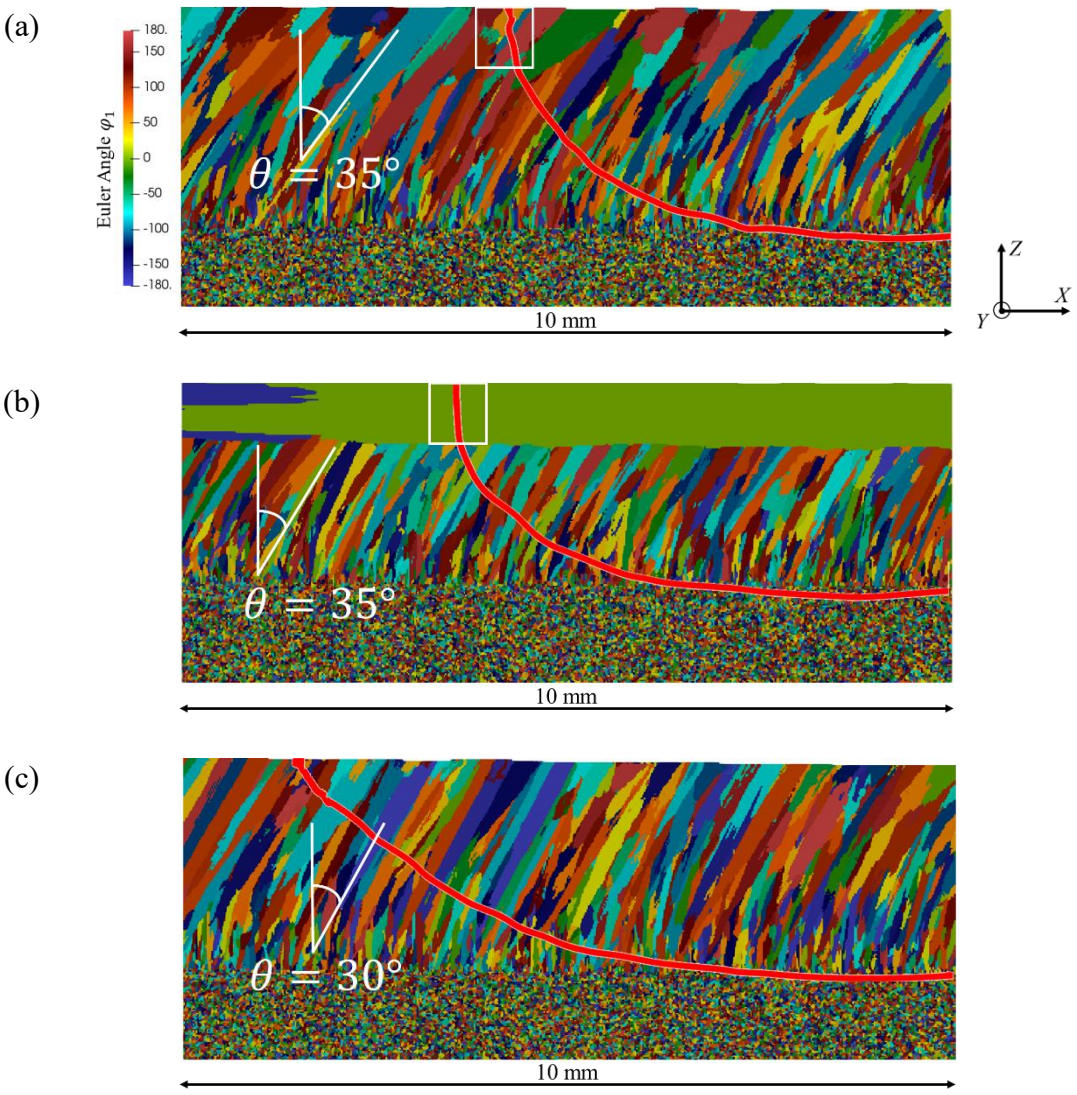

Figure 4-15. Microstructure (presented by Euler angle φ_1) on center plane $Y = 0$ in $X \in [60,70]$ mm after completed solidification for, (a) model 1, (b) model 2, (c) model 3. The corresponding melt pool contour (liquid fraction equals 99 %) is highlighted in red.

4.3.2.4 Choice of heat source model

By considering the melt pool shape (section 4.3.2.1) and temperature evolution (section 4.3.2.2), the model 2 and 3 are more reasonable to be applied. The grain structure (section 4.3.2.3) demonstrates that the model 2 is not appropriate as no grain is experimentally observed along the welding direction (section 4.4). Therefore, model 3 is considered as the more relevant one. This model is used thereafter for pass 1 and applied for the next two passes.

4.4 Simulation results for multi pass welding

4.4.1 Thermal simulation results

As presented in Figure 4-4, the dimensions associated to experimental welding results are dispersed between passes (Length L1, L2, melt pool shape) even though the same welding parameters are kept for the three different passes. Therefore, in the simulation, the comparison and calibration of thermal parameters, especially the heat source parameter, has been developed based on the single upper (*i.e.* last) pass rather than the whole melted domain (see differences between Figure 4-16 and Figure 4-17).

Table 4-9 shows the different parameters proposed to model heat source (model 3) for each pass. Several reasons could explain these differences for the 3 passes: the closure of the chamfer after passes in the experiment which is not considered in the present simulation (Figure 4-7). Besides, the variety of the metal surface after each pass (*e.g.* rugosity) can also leads to a modification of welding parameters.

In the experiment, as the chamfer tends to close after each pass, the melt pool surface tends to increase (Table 4-5, melt pool surface of pass 1 is smaller than that of pass 2 and 3), which leads to an increase of efficiency. Besides, α_Y is decreased to calibrate the height of the melt pool L1 and L2.

Table 4-9. Heat source parameters for 3 different passes.

	Pass 1	Pass 2	Pass 3
Efficiency η	0.8	0.85	0.85
Welding power, ηUI [W]	2288	2431	2431
Aperture angle, α [°]	$\alpha_X = 70$ $\alpha_Y = 50$	$\alpha_X = 70$ $\alpha_Y = 45$	$\alpha_X = 70$ $\alpha_Y = 40$

Table 4-10 presents the comparison of the melt pool shape L1, L2 and the surface for the three different passes with parameters of heat source in Table 4-9. The result for pass 1 is the same as in Table 4-8 for model 3.

Table 4-10. Detailed melt pool shape comparison for 3 different passes.

	Pass 1		Pass 2		Pass 3	
	Exp	Sim	Exp	Sim	Exp	Sim
L1 [mm]	2.67	2.70	2.76	2.88	3.17	3.02
L2 [mm]	5.22	5.21	4.61	4.96	4.44	4.51
Melt pool surface [mm^2]	18.96	18.95	23.96	21.7	22.94	21.5

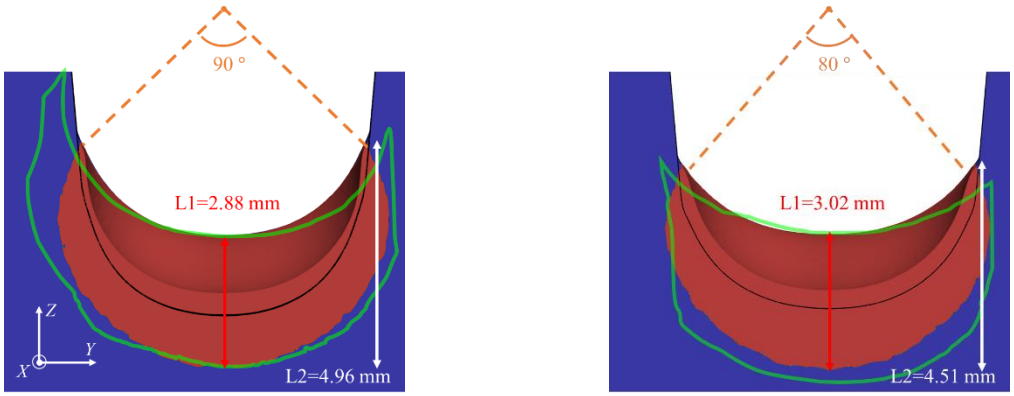

(a) (b)

Figure 4-16. Melt pool shape comparison (red part) and experimental observation (green contour) at t=27s, (a) pass 2, (b) pass 3. Black contour presents the initial weld bead position for each pass, *i.e.* initial weld bead position for pass 2 is the end of pass 1. Orange point presents the heat source position, and the dashed orange line presents the aperture angle in 2α.

Figure 4-16 shows the comparison of melt pool between simulation and experiment. As mentioned previously, L2 is defined at the right side as, in the simulation, less deformation and fusion of side surface occurred on this side. As the simulation do not consider this deformation, the calibration focusses on this right side. For Figure 4-16 (b), the shape of the melt pool is more coherent on the right-hand side than on the left-hand side where more fusion of the chamfer surface is observed. This incoherence at the left side could also explain the weaker melt pool surface in the simulation compared with experiment. Considering Figure 4-16 (c), more difference could be found for the pass 3. In the experiment, the melt pool has a "straight" side surface which is not observed in the simulation. In fact, the melt pool shape observed in the experiment corresponds more to the melt pool of model 1 (Gaussian) as presented in Figure 4-12 (a) where the heat source is more focused. This shape cannot be obtained by the heat source model 3 (elliptic). Besides, in the experiment, we have to mention that the melt pool for the 3 passes do not have a stable shape, especially for the pass 3. Therefore, more metallographic observations at different positions could be useful to investigate the melt pool stability and its evolution in future comparisons.

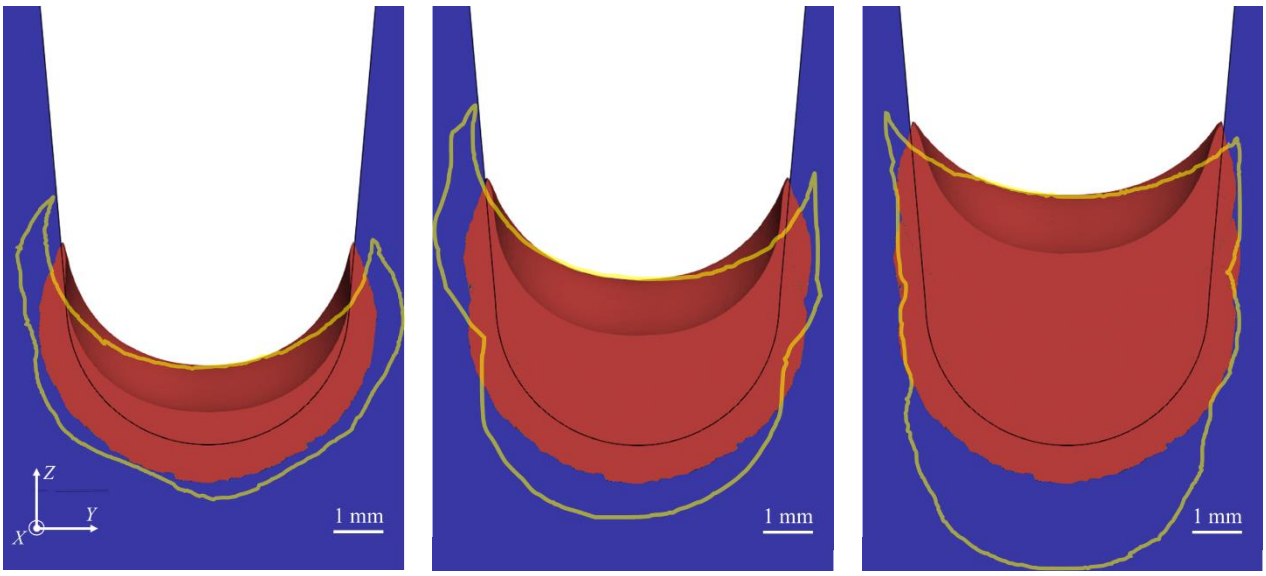

(a) (b) (c)

Figure 4-17. Melt pool shape superposition (red part) and experimental observation (yellow contour) at t=27s, (a) 1 pass, (b) 2 passes, and (c) 3 passes. Black contour presents the initial chamfer position.

Figure 4-17 presents the superposition of the melt pool for different passes and the experimental observations. The experiment contour (yellow) is superposed with the simulation result (red) by positioning the top surface on the weld bead at the same height. A large difference is observed, in the melt pool shape and the melt pool surface. In fact, as presented before, the simulation calibration focusses on each pass rather than the whole melt pool for multi pass, differences could be caused by this calibration strategy restricted to the upper pass. However, in the experiment, the weld bead of multi pass does not conserve the complete information of the precedent pass (for example, the top surface of the weld bead of the precedent pass is merged by the new weld bead), thus the calibration of multi pass weld bead is not possible. Besides, the dispersion of the melt pool shape (presented in Figure 4-4) between different passes can also be an explanation of the large difference. Another explication possible could be the variation of weld bead surface (*e.g.* rugosity), even though the samples (Figure 4-4) obtained are positioned at the steady state, differences of weld bead can always exist which depend on the operation of welding machine.

To better understand this difference, more metallographic observations at different positions would be necessary.

Figure 4-18 presents the temperature evolution of the thermocouples (same position as in Figure 4-14) for the second pass. Same calibration on time scale is achieved with the same strategy as for the first pass. Even though the maximum temperature presents a difference between the simulation and the experiment, the global trends of temperature evolution in the experiment is well presented by the simulation. Besides, the maximum temperature of TC6 and TC7 are increased while that of TC8, TC9 and TC10 are decreased. This evolution is due to the first weld bead (first pass) previously developed. The torch is lifted to keep the same distance between the heat source and the metal surface (6.5 mm). As a consequence, the heat source is

closer to the thermocouple TC6 and TC7 and farther from TC8, TC9 and TC10. This trend of maximum temperature evolution is also observed in the simulations.

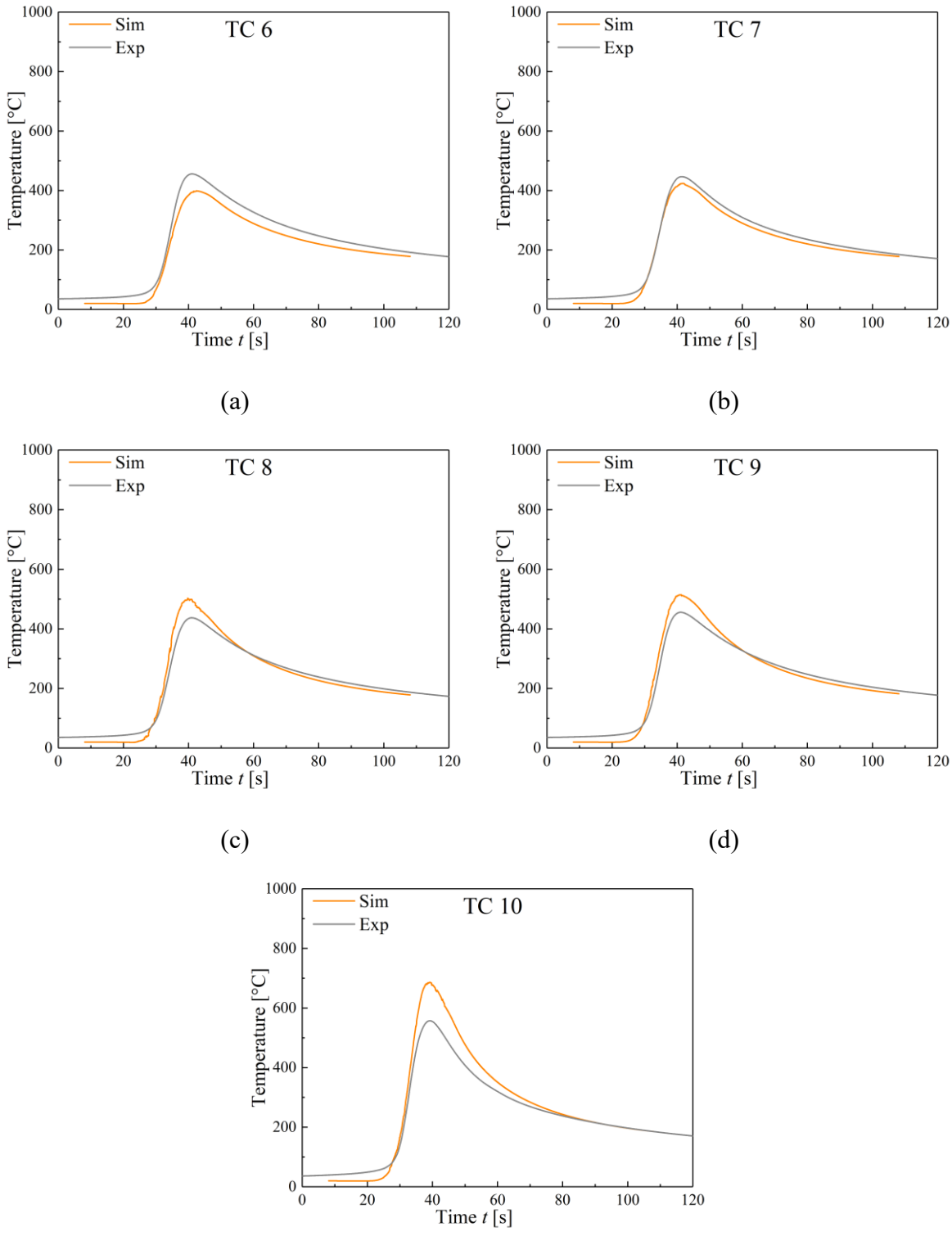

Figure 4-18. Temperature evolution of thermocouples for pass 2.

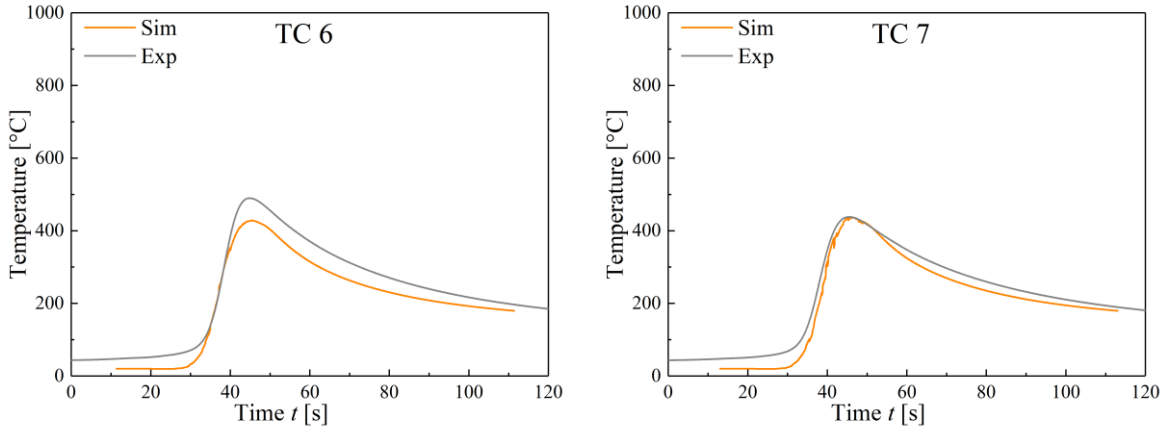

(a)

(b)

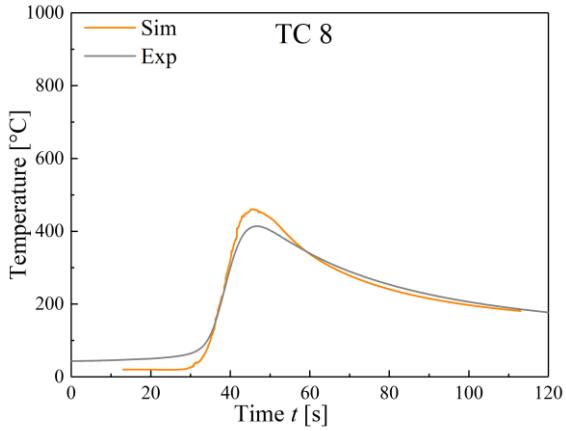

(c)

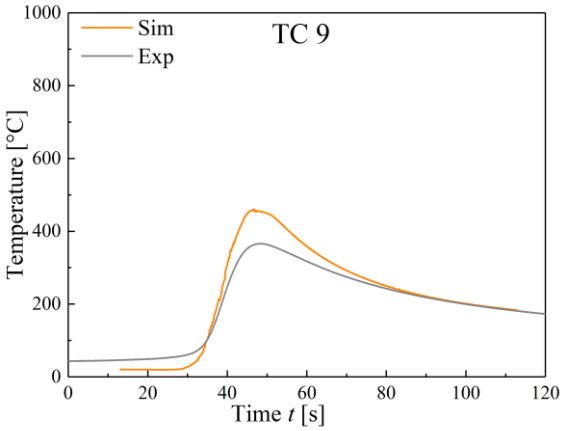

(d)

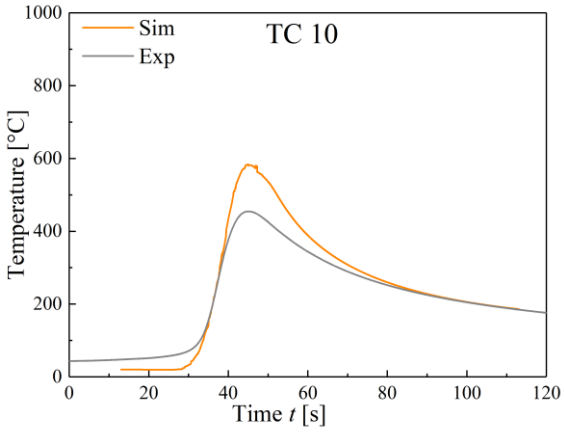

(e)

Figure 4-19. Temperature evolution of thermocouples for pass 3.

The same temperature evolution for the third pass is presented in Figure 4-19. More differences are observed between the simulation and the experiment. This could be due to the cumulated deformation for the multi pass welding as shown in Figure 4-7. Another

explanation could be the difference on the melt pool shape between the simulation and the experiment as presented in Figure 4-16 and Figure 4-17 which have influence on the distance between thermocouples and remelted domain and, consequently, heating stage. Same as for the melt pool shape difference, more experimental observation would be necessary to provide a clear understanding of the temperature evolution. Another point to mention is the beginning of heating in the experiment which is much early than the one observed in the simulation (temperature can increase to 40℃ at about 20 s). As presented before, this could be due to the flow of the heated gas which is not considered.

4.4.2 Comparison of microstructure

Figure 4-20 shows the evolution of grain structure after solidification for the multi pass welding at the center plane $Y = 0$. It should be noted that the initial grain structure is obtained by "random initiation" method mentioned in section 3.5.3, *i.e.* no texture exists for the initial grain structure. The zone between $X \in [60,70]$ along the welding direction corresponding to the time scale $t \in [24,30]$ is chosen as associated to the steady state, as presented by Figure 4-10 and Figure 4-11. For the first pass, the grains begin to develop from the base metal along the temperature gradient (Figure 4-15 (c)). For the two next passes, the grains develop from the existing microstructure (epitaxial grain growth) which presents already a preferred direction. Therefore, these grains continue to develop up to the top of the metal surface leading to the development of long grains through the whole melt zone of all passes. Another point could be noted is the tilted angle (angle θ in Figure 4-15) along the welding direction, this angle is kept and nearly unchanged for the 3 passes. In fact, this angle is a combined phenomenon of melt pool shape at rear and the dendrite develop law. As the heat source along the welding direction ($\alpha_X = 70°$) and the dendrite develop law are not changed between passes, the tilted angle has no reason to change, the grains develop along the same direction.

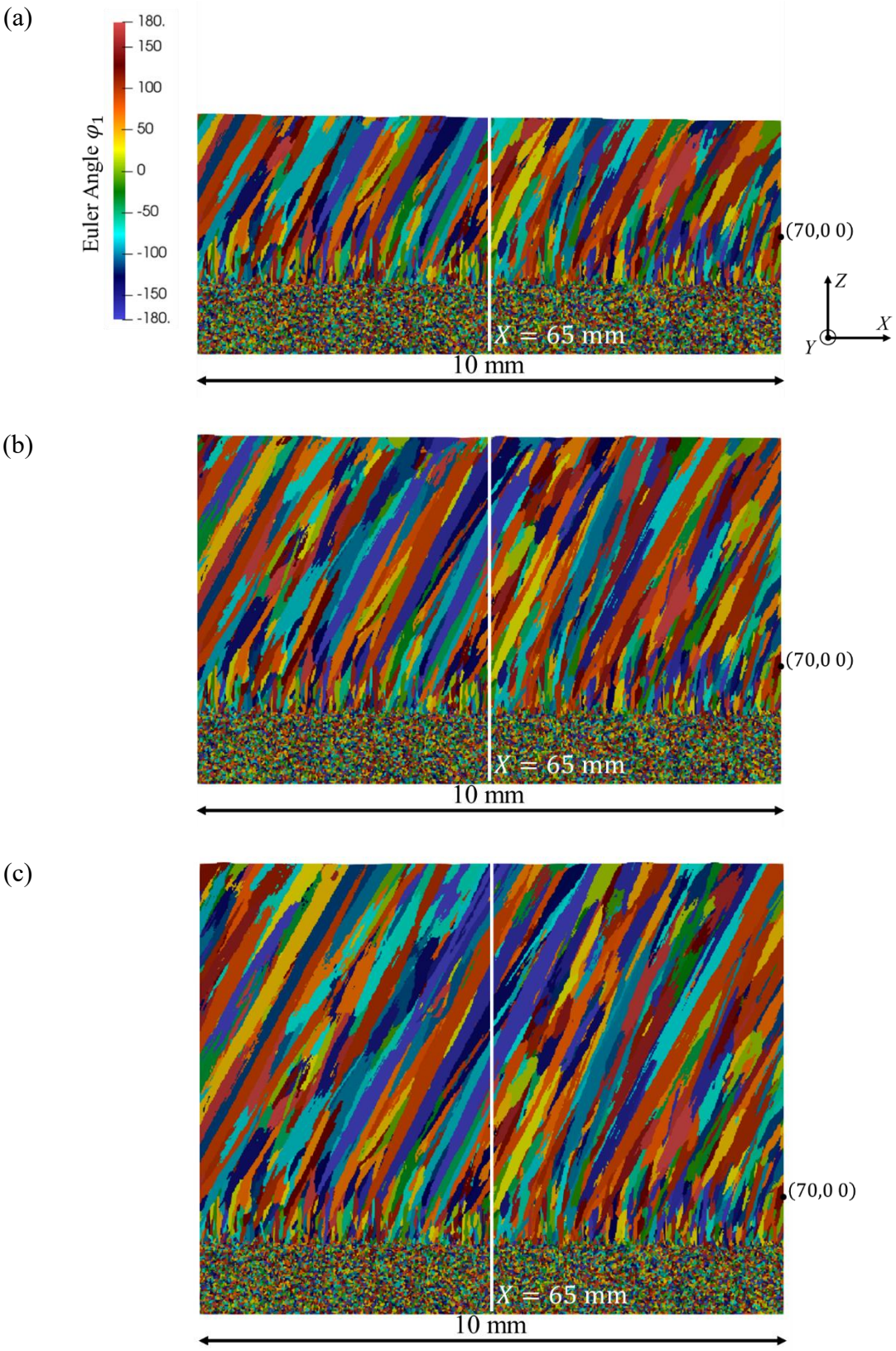

Figure 4-20. Microstructure (presented by Euler angle φ_1) on center plane $Y = 0$ in $X \in [60,70]$ mm after completed solidification of, (a) pass 1, (b) pass 2, and (c) pass 3.

The EBSD map of the grain structure on the plane $X = 65$ mm (white line - Figure 4-20) are presented in Figure 4-21. It should be mentioned that EBSD experimental observations are only reported in transversal planes by ICB. The inverse pole figures (IPF) correspond to orientation of the grains projected along the $Y-$ direction for the 3 passes of weld bead. (The $X-$ and $Z-$ directions IPF are presented in appendix 3). Considering the grain structure of the base metal, the grain size is very fine and well represented by the simulation. However, the color map of the base metal shows some differences in grain structure between simulations and experiments. In fact, the base metal is generated randomly in the simulation while in the experiment, a preference grain structure preexisted before the welding (see base metal color observation in EBSD Figure 4-21). Nevertheless, as discussed in chapter 3, the initial grain structure of the base metal may have few influences on the grain structure inside the weld bead.

Differences could be observed on color maps between simulations and experiments. In the experiment, the dominant color is in red, yellow and orange, meaning that these grains have one of their $\langle 100 \rangle$ directions close to the $Y-$ direction. While in the simulation result, a dominance of blue, green and purple is presented which means the $\langle 111 \rangle$ and the $\langle 011 \rangle$ directions of those grains are closer to the $Y-$ direction. One explanation of this difference is the tilted grain angle (angle θ in Figure 4-15). In the simulation, this tilted grain angle, θ, can reach a maximum of around 30° while in the experiment, this tilted grain angle seems much lower. This could be proved by the grain morphology. In the experiment, especially for the first pass, the grains are longer than the grains presented in the simulation for same X cutting plane. As the observation plane is perpendicular to the welding direction, a longer grain observed indicates a lower tilted angle. This difference is caused by the thermal evolution along the welding direction and, more precisely, the melt pool shape along the welding direction. As mentioned before, this is related to the heat source model along the welding direction (α_X) and the dendrite growth kinetic law. An experimental observation of grain structure along a longitudinal plane (Figure 4-20) would be necessary to identify and verify the cause of this difference in EBSD observations, and an in-situ observation of the melt pool shape would also provide insightful information to discuss these results, as chapter 3. However, we have also to notice the difficulties associated to develop such observation in chamfer during welding process.

Another point to be noted is the grain size increase for the 3 passes especially in the simulation which is less visible in experiments. The origin of this observation is the *initial grain structure* used to develop new columnar structure in an epitaxial grain growth process. The first pass starts at the base metal with a very small grain size. The grain growth competition occurs thereafter during the solidification. The second and the third pass starts at a welded grain structure with elongated columnar grain which are already “selected” by the precedent pass. Bigger grains develop, step by step, as the selection mechanism is enhanced between passes.

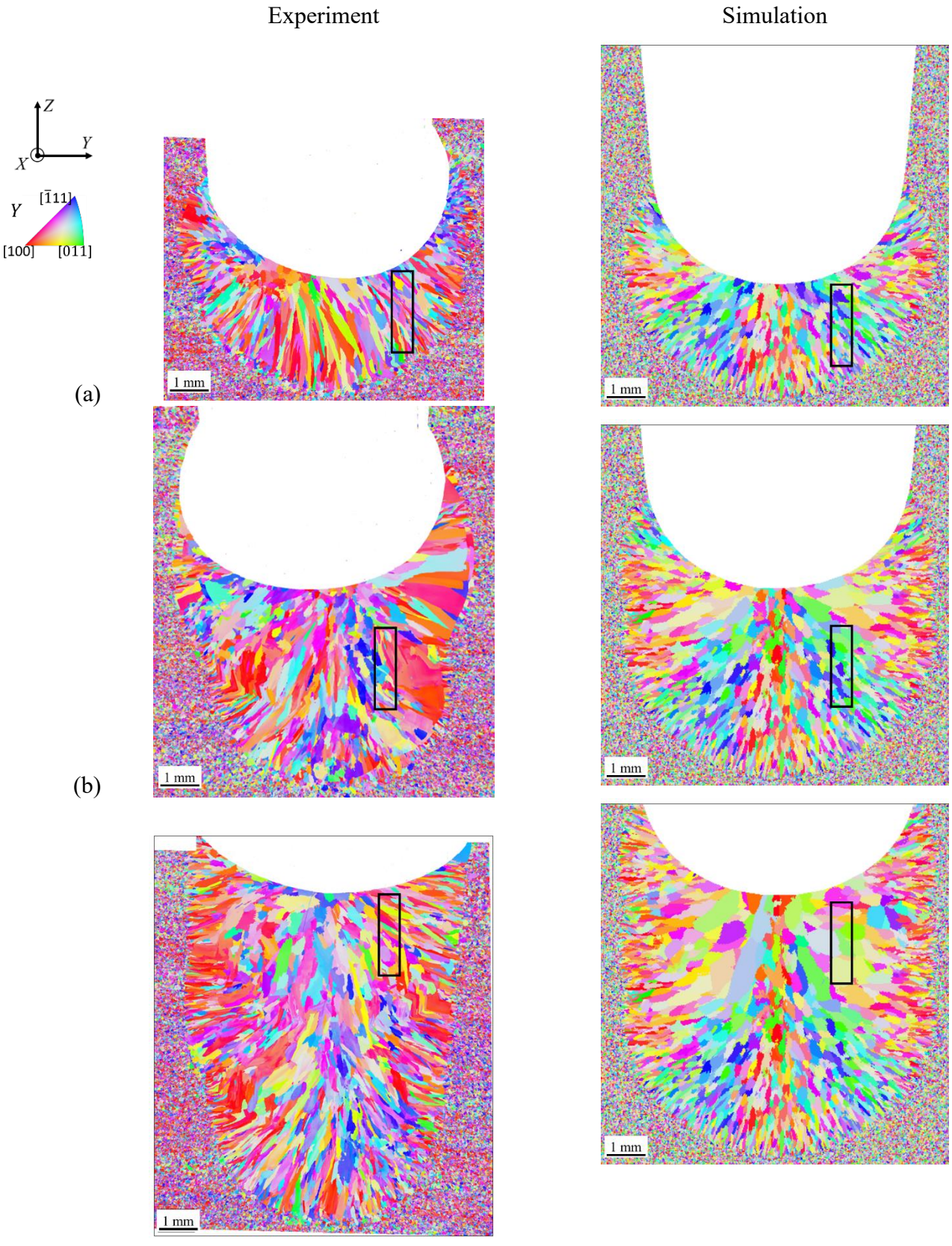

Figure 4-21. EBSD maps of the grain structure on plane $X = 65$ mm (left) measured and (right) simulated with the CAFE model. The inverse pole figure color codes for $Y -$ direction respect to the pass (a) 1, (b) 2 and (c) 3.

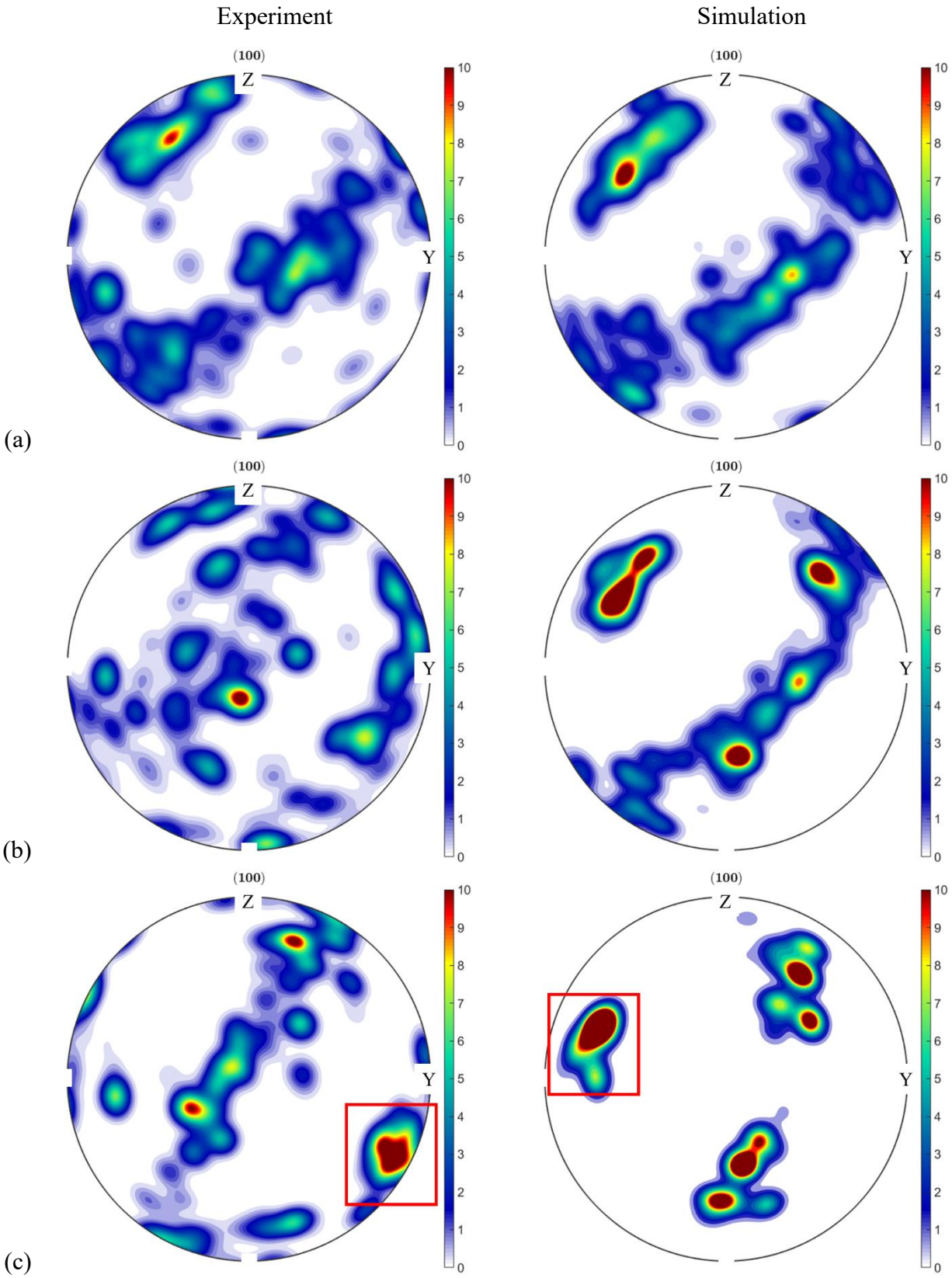

Figure 4-22. ⟨100⟩ pole figure ploted in the weld bead (black rectangle in Figure 4-21) (a) pass 1, (b): pass 2 and (c) pass 3.

The ⟨100⟩ pole figures of the grains located in the black rectangles windows drawn in Figure 4-21 are plotted from (left) the experiment and (right) the simulated orientation maps for the 3 passes. The rectangles are chosen at the right side of the melt pool where the temperature gradient at the grain growth front is positive along Z and negative along Y directions. For the first pass, the fiber texture of the simulation results is coherent with the experimental observation despite the difference of EBSD color (Figure 4-21). However, it may be difficult to have same conclusion for pass 2 as the experiment result does not present a clear texture. Regarding pass 3, the difference position of the spot encompassed in red rectangle indicates that the grains in the simulation have one of the ⟨100⟩ directions closer to the welding direction ($-Y$ direction) which also means a larger tilted grain angle (angle θ in Figure 4-15). This could be a confirmation of the explanation on the differences between EBSD map presented in Figure 4-21 as mentioned before. Another point to be noted is that the spot of the pole figure in the simulation is more and more focused when the weld bead develops from pass 1 to pass 3. This is due to the increasing size of the grain in the melted domain encompassed by the black rectangle in Figure 4-21.

4.5 Conclusions

In this chapter, the quantitative comparisons between experimental observation and the CAFE simulations results are achieved on a multi pass GTAW process with added material. An analyze of heat source in the chamfer configuration is carried out and a uniform elliptic heat source is developed and validated to have good coherence of experimental result regarding thermal resolution (melt pool shape and temperature evolution during the welding). Differences exist at the melt zone for multi pass welding as shown in Figure 4-17. The reason could be the deformation of the initial chamfer during the experiment (Figure 4-7) and also the dispersion of experimental result (Figure 4-4). Future observations at more positions in the weld bead and its neighborhood can be insightful input to check these differences. Besides, the fusion of the side surface of the chamfer in the experiment is not observed in the simulation (Figure 4-12) due to the choice of an increased viscosity to reduce numerical difficulties.
Grain structures of simulation and experiment are also compared by EBSD map and pole figure. Results shows that the tilted grain angle (angle θ in Figure 4-15) is probably larger in the simulation which leads to the difference in EBSD map. An in-situ observation of the melt pool shape as chapter 3 along the welding direction could be useful to calibrate this tilted grain angle and to obtain a more coherent result also regarding the heat source model.

4.6 French summary

Dans ce chapitre, des comparaisons quantitatives entre observations expérimentales et simulations CAFE sont réalisées sur un procédé de GTAW multi-passes avec ajout de la matière. Une discussion sur la source de chaleur pertinente est proposée et une source thermique elliptique uniforme est développée. Elle permet d'obtenir une bonne cohérence des simulations avec les données thermiques expérimentales (forme du bain de fusion et évolution de la température pendant le soudage). Plusieurs différences existent, cependant, au niveau du bain de fusion pour le soudage multi-passes comme le montre la Figure 4-17. La raison pourrait être

la déformation du chanfrein initial au cours de l'expérience (Figure 4-7) et aussi la dispersion du résultat de l'expérience (Figure 4-4). L'observation d’autres positions du cordon pourrait apporter des informations pertinentes pour discuter et comprendre ces différences. De plus, la fusion de la surface latérale du chanfrein dans l'expérience n'est pas représentée dans la simulation (Figure 4-12) en raison du choix fait de la viscosité pour réduire les problèmes numériques.

Les structures de grain sont aussi comparées entre simulations et expériences au niveau des cartographies EBSD et des figures de pôle. Les résultats montrent que l'angle d’inclinaison des grains (angle θ dans Figure 4-15) dans la simulation, au cours de la croissance épitaxiale, est probablement surévalué, ce qui conduit aux différences observées sur les cartes EBSD. Une observation in-situ de la forme du bain de fusion comme présentée au chapitre 3, le long de la direction de soudage, serait nécessaire pour calibrer cet angle et obtenir les résultats plus cohérents.

5 Hot cracking simulation during single pass GTAW

In this chapter, the WYSO criterion presented in chapter 1 is applied to a single pass GTAW to evaluate the hot cracking risk during the process. Note that in this simulation, only the hot cracking criterion is computed, indicating the occurrence of hot cracking (crack initiation), while crack propagation is not simulated.
The partner of NEMESIS project, ICB, has achieved a hot cracking initiation experiment on a static welding configuration with a bi-axial tensile set-up. However, because of the time delay to reach experimental results, this experiment could not be simulated. Thus, the simulation results are compared with experimental results found in the literature [Bel16] in order to validate the criterion. In this work, the WYSO criterion is computed for different cases in order to verify and validate the criterion. Besides, in section 5.5.2, the grain structure simulated by the CAFE method is considered in the WYSO criterion to study the influence of grain structure on hot cracking prediction.

5.1 Material properties

In this hot cracking test, the AISI 321 steel is used [Bel16]. The chemical composition of the AISI 321 steel is presented in Table 5-1.

Table 5-1. Chemical composition of AISI 321 steel [Bel16].

Fe	C	Cr	Mn	Ni	P	S	Si	N	Ti	Unit
balance	0.029	17.15	0.94	9.02	0.021	0.001	0.46	0.011	0.31	wt%

Figure 5-1 presents the transformation path of the AISI 321 steel. Same as for the 316L, this is extracted from the software Thermo-Calc [The18] with the TCFE9 thermodynamic database [TCFE9] considering only liquid, l, ferrite, α, and austenite, γ, phases. However, for the AISI 321 steel, a GS (Gulliver-Scheil) solidification path is applied as in [Bel16]. The liquidus temperature is $T_{liq} = 1457\,°C$, and the solidus temperature is $T_{sol} = 1269\,°C$. The solidus value is chosen for a remaining fraction of liquid lower than 1%.

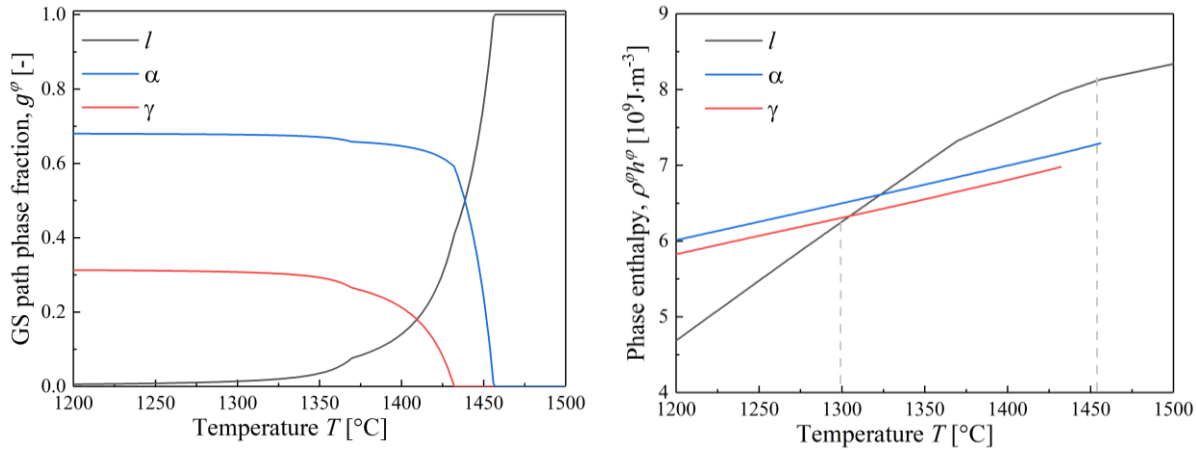

(a) (b)

Figure 5-1. Temperature evolution of GS solidification path, (a) the volume fraction of the phases involved during solidification, g^{φ} with $\varphi = \{l, \alpha, \gamma\}$, corresponding to liquid, l, ferrite, α, and austenite, γ, and (b) their volumetric enthalpy, $\rho^{\varphi}h^{\varphi}$ of AISI 321 [Phy].

The thermal conductivity $\langle\kappa\rangle^{\varphi}$ for all phases $\varphi = \{l, \alpha, \gamma\}$ is shown in Figure 5-2. Note that the thermal conductivity is chosen identical for the three phases [Bel16].

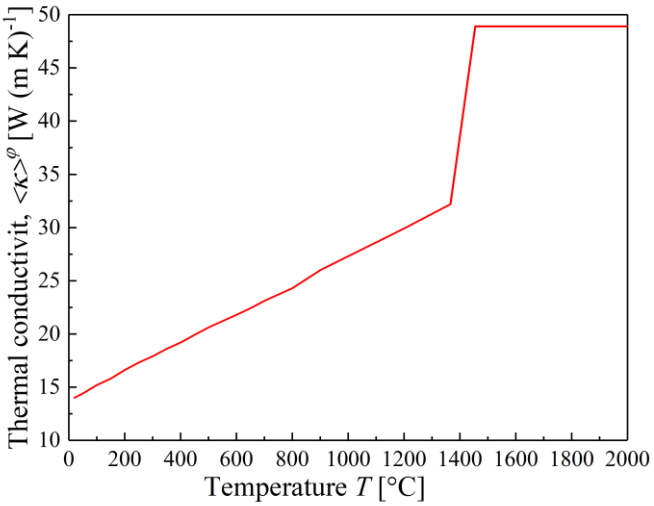

Figure 5-2. Thermal conductivity $\langle\kappa\rangle^{\varphi}$ of AISI 321 steel for $\varphi = \{l, \alpha, \gamma\}$.

In Figure 5-2, a sharp rise of the thermal conductivity can be noted at 1380 °C, between the $T_{sol} = 1269$ °C and $T_{liq} = 1457$ °C. In fact, this change is introduced in [Bel16] to take into account the convective effects in liquid metal. In other words, in the present simulation, the convection term of the energy conservation equation is neglected while the convective effects are accounted for by this rise of the thermal conductivity. This approach is different from the welding simulation presented in chapter 3 and 4. Details of the energy conservation equation will be presented in section 5.3.1.

5.2 Experiment set up

The JWRI test presented in chapter 1 is achieved to determine the condition of hot cracking occurrence. This test consists of carrying out a single fusion line with the GTAW process on a plate (length 140 mm, thickness 2 mm, width 20 or 25 mm). The plate is constrained at one end while the others are free as presented in Figure 5-3 (a) and (b).

(a)

(b)

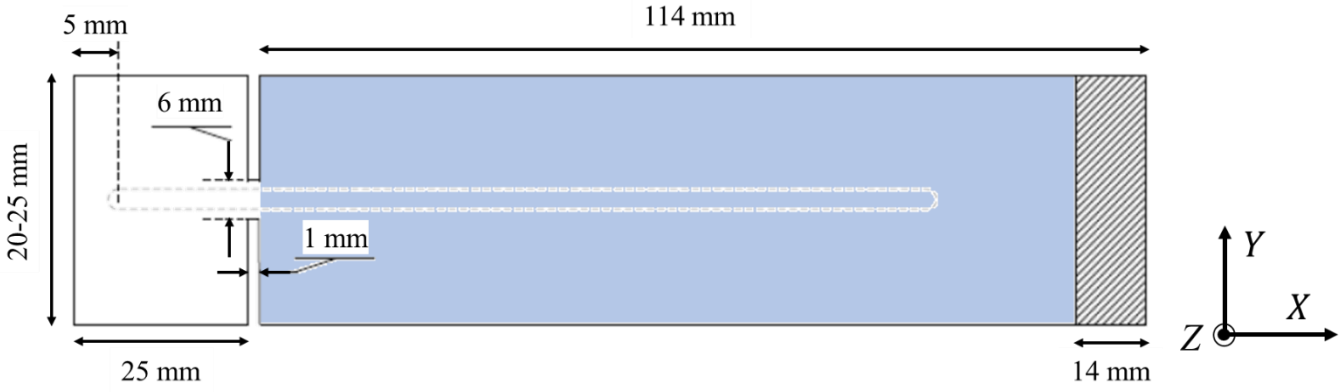

(c)

Figure 5-3. JWRI hot cracking test (a) experimental set-up showing clamping and protection against oxidation on the lower side of the plate, (b) geometry of plate specimens, the blue part presents the simulation domain, (c) example of a crack fully developed throughout the weld bead, test 25C in Table 5-2 [Bel16].

Through-thickness welding is started at 5 mm from the free end and is done without any filler material, so the weld bead is a simple straight fusion line, as indicated in Figure 5-3 (b). The test begins at the 25mm long appendix, this part detaches as the fusion zone passes through the width reduction (notch in the plate). At this moment an enlarged fusion zone is generated temporarily, which favors the initiation of an axial crack. Depending on the welding conditions, the cracks either stops immediately or it progresses in the axial direction as presented in Figure 5-3 (c). No external load is necessary to open the crack: the crack results only from thermal expansion (associated with the clamping effect) at the rear of the mushy zone, where the alloy shows a low mechanical resistance at the end of its solidification (in the BTR interval). The plate is protected from oxidation by argon gas on the upper side and by disposal of very thin copper foils at the lower face (Figure 5-3 (a)).

To study the hot cracking phenomenon, four different welding configurations are investigated including metal plate with 2 different widths (20 and 25 mm). Welding tension is 10 V and linear heat input is about 235 J/mm, with variable welding current and welding speed. The occurrence of hot cracking is indicated in the observation. The crack is started through the notch at the plate edge, as presented in the literature [Cro06], the closure or continuation of the crack is often correlated with the plate width, because the amplitude of transverse tensile stress and strain is related to the plate width. However, in the cases presented in Table 5-2, there is no direct apparent correlation between crack occurrence and one of the operating or geometrical parameters: plate width, welding current, welding speed or heat input. Note that the nomination of the test is the width of the sheet and the observation of the experiment result, *e.g.* 20C represents cracking case on the sheet of width 20 mm.

Table 5-2. Welding test configurations.

Test #	Weld part width [mm]	Welding tension U [V]	Welding current I [A]	Welding speed V [mm s^{-1}]	Linear heat input UI/V [J mm^{-1}]	Observation: crack (C)/non-crack (NC)
20C	20	10	109	4.67	233.4	C
20NC	20	10	102	4.33	235.6	NC
25C	25	10	109	4.67	233.4	C
25NC	25	10	102	4.33	235.6	NC

For the AISI 321 used in the hot cracking simulation and in view of the CAFE simulation, a dendrite tip kinetics law K_3 is computed by PhysalurgY [Phy] with the TCFE9 database [TCFE9] to access thermodynamic equilibrium assumed at the solid/liquid interface and the MOBFE6 database to compute diffusion data in the liquid phase [MOBFE6] as for K_2 in chapter 3.

Table 5-3. Dendrite tip kinetics law.

K_3	$v_3^{\langle 100 \rangle} = 6.72 \cdot 10^{-4} \Delta T^{3.39}$	mm s^{-1}
K_4	$v_4^{\langle 100 \rangle} = 1.0 \cdot 10^{-3} \Delta T^{2}$	mm s^{-1}

As presented in section 3.5.2, the analytic law may be not sufficient to represent the melt pool shape in the experiment. However, to get the adapted law, in-situ observations and measurement are needed, that are not available in this hot cracking experiment. Thus, the analytical dendrite growth law K_3 is applied to prove the possibility of grain structure consideration in the hot cracking modeling.

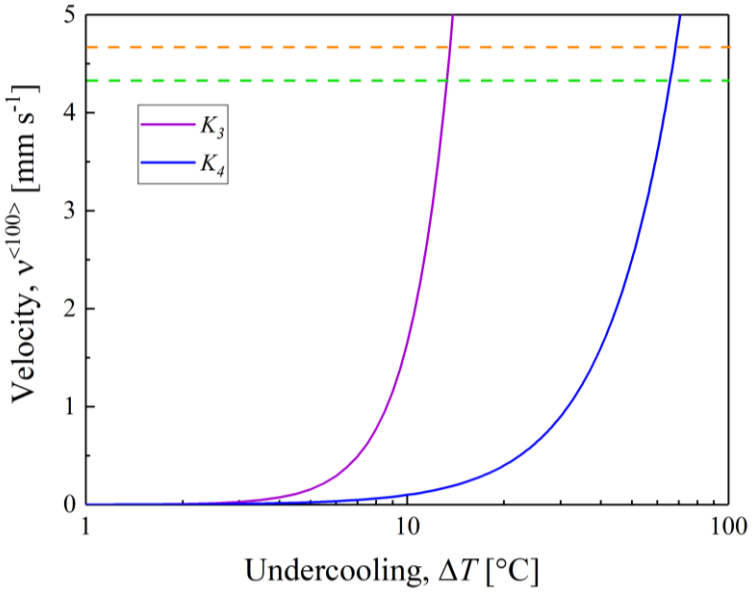

Figure 5-4. Growth velocity, v, as a function of dendrite tip undercooling, ΔT. Evolution of investigated laws K_3 and K_4.

Figure 5-4 presents the relation between the undercooling ΔT and the dendrite tip growth velocity. The orange/green horizontal line presents two welding speed $4.67/4.33$ mm s^{-1}, which are the welding speeds applied (presented in Table 5-2). This gives the corresponding undercoolings $13.3°C/13.6°C$ for law K_3 and $65.8°C/68.3°C$ for law K_4. Note that the difference for different welding speeds is very weak since the difference in critical undercooling is also weak. Except for section 5.6.2, K_3 is applied to all the simulations with grain structure. K_4 is used in section 5.6.2 to study the influence of the microstructure.

5.3 Numerical modeling

For the hot cracking modeling, the global deformation (such as deflection of metal plate which is already neglected in chapter 3 or subsidence as presented in chapter 3) of metal plate is not

considered. Besides, the process studied is GTAW without added material, which means the LS method has no obvious advantage while it increases the demand of mesh quality and computing resource. Thus, the LS method is not applied for the present hot cracking prediction study.

5.3.1 Heat transfer resolution

As no gas domain is considered in the modeling, only the terms in the metal domain for the energy conservation equation of equation (2-20) are kept:

$$\frac{\partial \langle \rho h \rangle^M}{\partial t} + \nabla \cdot \langle \rho h \boldsymbol{v} \rangle^M - \nabla \cdot (\langle \kappa \rangle^M \boldsymbol{\nabla} T) = \dot{Q}^M \tag{5-1}$$

As introduced in section 5.1 , the convective term is not considered in the conservation equation while the convection effect itself is taken into consideration by the rise of thermal conductivity. Thus, equation (5-1) becomes:

$$\frac{\partial \langle \rho h \rangle^M}{\partial t} - \nabla \cdot (\langle \kappa \rangle^M \boldsymbol{\nabla} T) = \dot{Q}^M \tag{5-2}$$

To simplify the expression, $\langle \quad \rangle^M$ is replaced by $\langle \quad \rangle$ hereafter which presents the average volumetric property of metal. Equation (5-2) becomes:

$$\frac{\partial \langle \rho h \rangle}{\partial t} - \nabla \cdot (\langle \kappa \rangle \boldsymbol{\nabla} T) = \dot{Q} \tag{5-3}$$

For a given point $B(x, y, z)$ in the simulation domain, at time t, the heat source $\dot{Q}$ is calculated by the expression:

$$\dot{Q}(B,t) = \frac{3 k_e U I}{\pi e r_s^2} exp\left[-\frac{(x - Vt)^2 + y^2 + f_z\big((e - z)/2\big)^2}{r_s^2} \right] \times H(z - s) \tag{5-4}$$

with k_e the efficiency coefficient of the heat source, e the thickness of the metal plate, r_s the radius of the arc and f_z the thickness attenuation factor. H is a Heaviside function who equals 1 when $z - s \geq 0$ and 0 elsewhere, s is the truncation factor. This Heaviside function is applied to limit the thickness of the heat source as presented in the literature [Wis09]. Figure 5-5 (a) presents an isovalues contour of $\dot{Q}(B,t)$ ($\dot{Q}(B,t) = constant$), and Figure 5-5 (b) presents the truncated isovalues contour in Figure 5-5 (a).

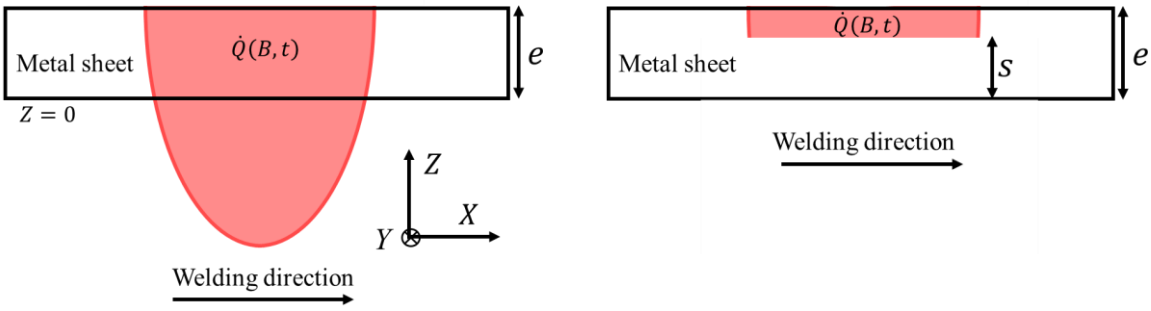

(a) (b)

Figure 5-5. Isovalues contour of the heat source $\dot{Q}(B,t)$ (a) contour complete, (b) contour truncated by the truncation factor s. The metal sheet is represented by the black contour

Table 5-4 presents the parameters of the heat source applied in the simulation. It can be noted that the efficiency coefficient k_e is higher than 1 while the efficiency of a welding process cannot exceed 1. This is because the efficiency coefficient k_e is not the efficiency of heat source (presented by η in chapter 3 and 4). It also takes into account the truncation s and the thickness attenuation f_z. *i.e.* η is therefore lower than k_e.

Table 5-4 Heat source parameters [Qui10]

k_e	e [mm]	r_s [mm]	f_z	s [mm]
1.2	2	5.4	40	1.6

The boundary condition of the thermal resolution is applied to all the surfaces of the weld plate and consists of a mixed convection-radiation condition. The heat flux is defined as:

$$-\langle\kappa\rangle\boldsymbol{\nabla}T\cdot\boldsymbol{n} = h_c(T - T_{ext}) + \varepsilon_r\sigma_r(T^4 - T_{ext}^4) \quad (5\text{-}5)$$

where h_c, the heat transfer coefficient, equals $15\ W\ m^{-2}K^{-1}$ [Bel16], σ_r the Stefan-Boltzmann constant equals $5.67\times10^{-8}\ kg\ s^{-3}K^{-4}$, ε_r is the metal emissivity and $\boldsymbol{n}$ is the unit normal vector. Figure 5-6 presents the emissivity of the AISI 321. It could be noted that the emissivity of the material considered is greater than 1 at temperatures below 1000 °C, which is theoretically impossible since emissivity can never reach that of the black body. This is because the emissivity value is obtained by an inverse method, in which the heat lost by radiation is known [Hae11], *i.e.* $\varepsilon_r\sigma_r(T^4 - T_{ext}^4)$, and the emissivity is deduced by knowing the temperature. The real emissivity could be measured in future experiment and replace the values presented here.

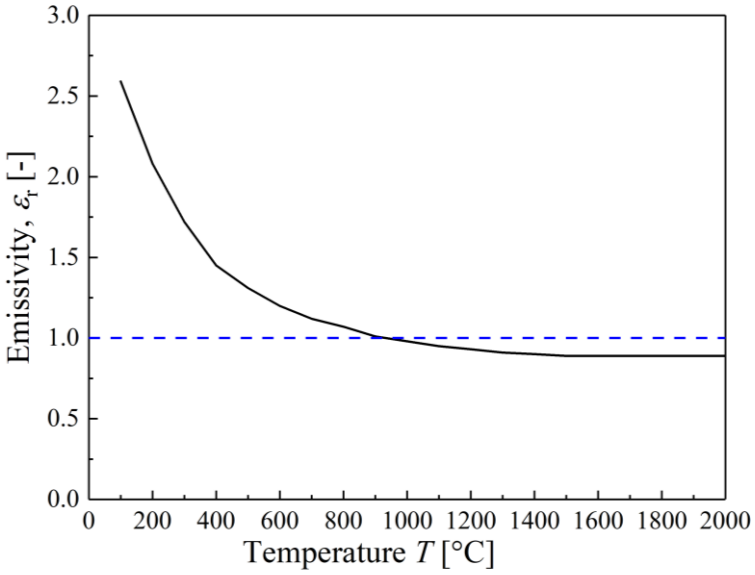

Figure 5-6. Emissivity of the AISI 321 metal plate [Qiu10].

5.3.2 Solid mechanics modeling

5.3.2.1 Momentum conservation equation

Same as for the fluid mechanics presented in chapter 2, the modeling of solid mechanics consists in coupling the conservation equations of momentum and mass. The local momentum conservation equation can be written as:

$$\nabla \cdot \bar{\bar{\sigma}} + \rho \boldsymbol{g} = \mathbf{0} \tag{5-6}$$

where $\bar{\bar{\sigma}}$ is the stress tensor, ρ is the density, $\boldsymbol{g}$ is the gravity vector. The stress tensor, $\bar{\bar{\sigma}}$, can be decomposed into two parts: the deviatoric stress tensor $\bar{\bar{s}}$ and a second term related to the pressure field $p = -\frac{1}{3} tr(\bar{\bar{\sigma}})$, given as follows:

$$\nabla \cdot \bar{\bar{s}} - \nabla p + \rho \boldsymbol{g} = 0 \tag{5-7}$$

5.3.2.2 Constitutive law

The resolution of equilibrium equation is mainly governed by the constitutive law describing the relation between stress and strain. During the welding process, the material endures a large temperature variation from ambient temperature up to melting point. The modeling of solid mechanics requires a suitable constitutive law which can be used in the full temperature range. As viscous phenomena become important at high temperature, a general elasto-viscoplastic model is necessary [Ham08]. In the present model, 3 regimes are distinguished:

- Elasto-viscoplastic (EVP) at temperature T lower than a critical temperature (called also coherency temperature) T_c, which is usually chosen near but lower than the solidus temperature T_{sol} [Che18, Zha20],

- Viscoplastic (VP) in the mushy zone where $T_c < T < T_{liq}$,
- Newtonian in the melt pool where $T > T_{liq}$.

Similar to the model used in welding by Hamide [Ham08] and Desmaison [Des13], the first regime can be modeled by an EVP constitutive law while the other two behaviors can be both described by a VP constitutive law as the Newtonian behavior is just a special case of VP behavior.

In the case of small deformation, the strain rate tensor $\dot{\bar{\bar{\varepsilon}}}$ can then be decomposed into several parts:

$$\dot{\bar{\bar{\varepsilon}}} = \begin{cases} \dot{\bar{\bar{\varepsilon}}}^{th} + \dot{\bar{\bar{\varepsilon}}}^{el} + \dot{\bar{\bar{\varepsilon}}}^{vp} & if\ T < T_c \\ \dot{\bar{\bar{\varepsilon}}}^{th} + \dot{\bar{\bar{\varepsilon}}}^{vp} & if\ T > T_c \end{cases} \tag{5-8}$$

where $\dot{\bar{\bar{\varepsilon}}}^{th}$, $\dot{\bar{\bar{\varepsilon}}}^{el}$ and $\dot{\bar{\bar{\varepsilon}}}^{vp}$ present the thermal, elastic and viscoplastic part of $\dot{\bar{\bar{\varepsilon}}}$, respectively. The thermal strain rate tensor $\dot{\bar{\bar{\varepsilon}}}^{th}$ can be defined by:

$$\dot{\bar{\bar{\varepsilon}}}^{th} = \alpha_T \frac{dT}{dt} \bar{\bar{I}} \tag{5-9}$$

where $\bar{\bar{I}}$ is the unit tensor and α_T is the one dimension thermal expansion coefficient.

Elasto-viscoplasticity

Assuming the material is isotropic, the elastic strain rate $\dot{\bar{\bar{\varepsilon}}}^{el}$ can be written as:

$$\dot{\bar{\bar{\varepsilon}}}^{el} = \frac{1+\upsilon}{E} \dot{\bar{\bar{\sigma}}} - \frac{\upsilon}{E} tr\left(\dot{\bar{\bar{\sigma}}}\right) \bar{\bar{I}} \tag{5-10}$$

where E is the Young modulus, and υ is the Poisson coefficient.

The viscoplastic strain rate $\dot{\bar{\bar{\varepsilon}}}^{vp}$ is expressed by means of a viscoplastic law including kinematic hardening. Denoting F the plasticity criterion and σ_0 the yield stress, we have:

$$F\left(\bar{\bar{\sigma}}, \bar{\bar{X}}\right) = \left(\bar{\bar{s}}, \bar{\bar{X}}\right)_{eq} - \sigma_0 = \sqrt{\frac{3}{2}\left(\bar{\bar{s}} - \bar{\bar{X}}\right) : \left(\bar{\bar{s}} - \bar{\bar{X}}\right)} - \sigma_0 \tag{5-11}$$

$\bar{\bar{X}}$ is the kinematic hardening stress tensor, its expression is given in (5-14). The viscoplastic strain rate $\dot{\bar{\bar{\varepsilon}}}^{vp}$ can then be expressed as:

$$\dot{\bar{\bar{\varepsilon}}}^{vp} = \dot{\lambda} \frac{\partial F\left(\bar{\bar{\sigma}}, \bar{\bar{X}}\right)}{\partial \bar{\bar{\sigma}}} = \frac{3}{2} \frac{\dot{\lambda}}{\left(\bar{\bar{s}}, \bar{\bar{X}}\right)_{eq}} \left(\bar{\bar{s}} - \bar{\bar{X}}\right) \tag{5-12}$$

with $\dot{\lambda}$ the generalized viscoplastic strain rate $\dot{\bar{\varepsilon}}$:

$$\dot{\lambda} = \dot{\bar{\varepsilon}} = \sqrt{\frac{3}{2} \dot{\bar{\bar{\varepsilon}}}^{vp} : \dot{\bar{\bar{\varepsilon}}}^{vp}} \tag{5-13}$$

the kinematic hardening stress tensor $\bar{\bar{X}}$ is given:

$$\bar{\bar{X}} = \frac{2}{3} C \bar{\bar{\alpha}} \tag{5-14}$$

with C a material parameter and $\bar{\bar{\alpha}}$ the tensor of internal variables for kinetic hardening:

$$\dot{\bar{\bar{\alpha}}} = \dot{\bar{\bar{\varepsilon}}}^{vp} - \gamma \dot{\varepsilon} \bar{\bar{\alpha}} \tag{5-15}$$

γ is also a material parameter.
Finally, the Lemaître viscous flow can be described as:

$$\dot{\varepsilon} = \left(\frac{\langle F \rangle}{K} \right)^n \tag{5-16}$$

the Macauley bracket $\langle \cdot \rangle$ expresses the non-zero viscoplastic strain rate only if F is positive:

$$\langle F \rangle = \begin{cases} F & if\ F > 0 \\ 0 & if\ F < 0 \end{cases} \tag{5-17}$$

In the simulation, in order to simplify the constitutive law, the yield stress σ_0 is neglected ($\sigma_0 = 0$) and only the first term of the kinematic hardening internal variables tensor $\bar{\bar{\alpha}}$ is kept which means $\dot{\bar{\bar{\alpha}}} = \dot{\bar{\bar{\varepsilon}}}^{vp}$ [Qiu10, Ker00].

Viscoplasticity
For the purely viscoplastic constitutive law, as the kinematic hardening and the yield stress do not exist anymore, the Lemaître viscous flow becomes:

$$\dot{\varepsilon} = \left(\frac{\bar{\sigma}}{K} \right)^n \tag{5-18}$$

with

$$\bar{\sigma} = \sqrt{\frac{3}{2} \bar{\bar{s}} : \bar{\bar{s}}} \tag{5-19}$$

Table 5-5. Material parameters for AISI 321 [Qiu10, Ker00].

T [°C]	20	200	780	800	900	1000	1100	1200 (T_c)
K [MPa]	149.8	149.8	149.8	141.4	107.9	88	62	58
n [−]	47.1	47.1	47.1	47.25	11.7	7.8	7.1	6.0
T [°C]	1269 (T_{sol})	1300	1325	1350	1400	1415	1456 (T_{liq})	
K [MPa]	49	45	42.7	18.59	1.07	0.0017	0.0017	
n [−]	5.31	5.0	2.5	2.5	2.5	1.0	1.0	

Table 5-5 presents the temperature evolution of material parameters K and n for the AISI 321. As shown, at high temperature in the upper part of the solidification interval, as $n = 1$:

$$\dot{\varepsilon} = \frac{\bar{\sigma}}{K} \tag{5-20}$$

Thus, the Newtonian behavior is retrieved with a consistence coefficient K equivalent to 3 times the dynamic viscosity, *i.e.* $K = 3\mu$.

Other parameters such as thermal expansion coefficient, Young modulus and C are presented in appendix 3.

5.3.3 Implementation of the hot cracking criterion

As presented in chapter 1, the critical strain based hot cracking criterion, WYSO criterion, proposed by Won et al. [Won00] will be applied in this PhD work to compute the risk of hot cracking during welding process.

5.3.3.1 WYSO criterion

The WYSO criterion F^{WYSO} is expressed as:

$$F^{WYSO} = \varepsilon_{BTR} - \varepsilon_c = \int_{BTR} \dot{\varepsilon}(t)dt - \frac{\phi}{\dot{\varepsilon}^{m^*} \Delta T_{BTR}{}^{n^*}} \tag{5-21}$$

where ε_{BTR} presents the cumulated strain in the plane perpendicular to the dendrite growth direction inside the BTR. Note that the BTR is usually chosen for solid fraction g^s between $0.9 - 0.99$. At that stage of solidification, the dendrites nearly finish to develop and the dendrite growth direction is already fixed. In the case where grain structure is not considered, this direction is assumed as the temperature gradient. The characteristic strain rate is noted as $\dot{\hat{\varepsilon}}$. The computation of $\dot{\hat{\varepsilon}}$ is presented hereafter, following the definition established in [Cer07, Bel09] . ε_c denotes the critical strain which itself depends on the strain rate perpendicular to the dendrite growth direction (or the temperature gradient if it's not considered) inside the BTR. ϕ, m^* and n^* are material parameters which are given in [Won00]: $\phi = 0.02821$, $m^* = 0.3131$ and $n^* = 0.8638$. These values are kept in this work for lack of practical value for AISI321. ΔT_{BTR} is chosen as the temperature interval (116℃ in this work) corresponding to $g^s \in [0.9 - 0.99]$.

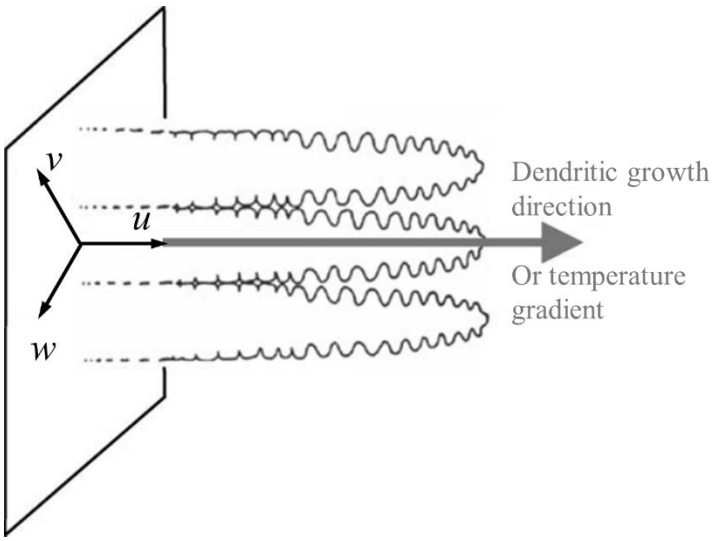

Figure 5-7 Direction presentation for computation of characteristic strain rate $\dot{\hat{\varepsilon}}$.

During the simulation, a reference frame (u, v, w) is established by keeping the direction u as the dendrite growth direction as shown in Figure 5-7. In the next section, we will explain how this direction can be extended from the information provided by the CAFE dendrite growth simulation. (v, w) presents the plane perpendicular to the u direction: where the stress strain following cracking develop. During the simulation, the strain rate $\dot{\bar{\varepsilon}}^{vp}{}_{(i,j,k)}$ computed in solid mechanics related to the global (laboratory) frame (i, j, k), is transferred to the frame (u, v, w) by multiplying the passage matrix P (only the plastic strain are considered for hot cracking because the elastic strain is released when the stress return to 0):

$$\dot{\bar{\varepsilon}}^{vp}{}_{(u,v,w)} = P^T \dot{\bar{\varepsilon}}^{vp}{}_{(i,j,k)} P \tag{5-22}$$

The matrix $\dot{\bar{\varepsilon}}^{vp}{}_{(u,v,w)}$ can be written as:

$$\dot{\bar{\varepsilon}}^{vp}{}_{(u,v,w)} = \begin{bmatrix} \dot{\varepsilon}_{uu}^{vp} & \dot{\varepsilon}_{uv}^{vp} & \dot{\varepsilon}_{uw}^{vp} \\ \dot{\varepsilon}_{uv}^{vp} & \dot{\varepsilon}_{vv}^{vp} & \dot{\varepsilon}_{vw}^{vp} \\ \dot{\varepsilon}_{uw}^{vp} & \dot{\varepsilon}_{vw}^{vp} & \dot{\varepsilon}_{ww}^{vp} \end{bmatrix} \tag{5-23}$$

Considering the sub-matrix $\dot{\bar{\varepsilon}}^{vp}{}_{(v,w)}$ inside the plane (v, w):

$$\dot{\bar{\varepsilon}}^{vp}{}_{(v,w)} = \begin{bmatrix} \dot{\varepsilon}_{vv}^{vp} & \dot{\varepsilon}_{vw}^{vp} \\ \dot{\varepsilon}_{vw}^{vp} & \dot{\varepsilon}_{ww}^{vp} \end{bmatrix} \tag{5-24}$$

The characteristic strain rate $\dot{\hat{\varepsilon}}$ is the maximum positive eigenvalue of $\dot{\bar{\varepsilon}}^{vp}{}_{(v,w)}$. With all the parameters known for equation (5-21), the WYSO criterion F^{WYSO} can then be computed.
In the simulation, as the time is discretized, equation (5-21) becomes:

$$F^{WYSO}(t) = \varepsilon_{BTR}(t) - \varepsilon_c(t) = \sum_{n_{BTR}=0}^{n_{BTR}} \dot{\hat{\varepsilon}}(t)\,\Delta t - \frac{\phi}{\dot{\hat{\varepsilon}}(t)^{m^*} \Delta T_{BTR}{}^{n^*}} \tag{5-25}$$

with Δt the time step of the simulation and n_{BTR} is the number of time step inside the BTR, $n_{BTR} = 0$ corresponding to the entrance in the BTR. For example, at a fixed point of the plate, the entrance in the BTR is at $t = 8\ s$, corresponding to the global time step number $n_{Glo} = 400$ (time step fixed at 0.02 s). Supposing a current time $t = 9\ s$, with global time step number $n_{Glo} = 450$, the time step number inside the BTR is $n_{BTR} = 50$, *i.e.* $450 - 400$.
The $F^{WYSO}(t)$ is updated at each time step, however, only the maximum value of $F^{WYSO}(t)$ is kept and presented:

$$F^{WYSO}(t + \Delta t) = \begin{cases} F^{WYSO}(t) & if\ F^{WYSO}(t) > F^{WYSO}(t + \Delta t) \\ F^{WYSO}(t + \Delta t) & else \end{cases} \tag{5-26}$$

In fact, the decrease of the criterion has no physical sense because the occurrence of hot cracking depends only on the maximum value.
It should be noted that in the critical strain term $\varepsilon_c(t)$, $\dot{\hat{\varepsilon}}(t)$ of the current time instance is applied which is a choice made in [Kos16, Kos16-2]. The choice of different $\dot{\hat{\varepsilon}}$ in $\varepsilon_c(t)$ will be discussed in section 5.6.1.1.

5.3.3.2 Computation of representative grain direction

Thanks to the CAFE model, the dendrite growth direction can be exploited in the hot cracking modeling. However, in the CAFE model, the grain information such as Euler angles is related to the CA cells, which means a post treatment of the grain information is necessary to get the dendrite growth direction related to the FE mesh where solid mechanics is solved, and the hot cracking criterion is computed. This treatment is first achieved on the CA mesh and then transported to the FE mesh. The relation between CA cell, CA mesh and FE mesh together with the field transport between FE and CA mesh are detailed in chapter 2.

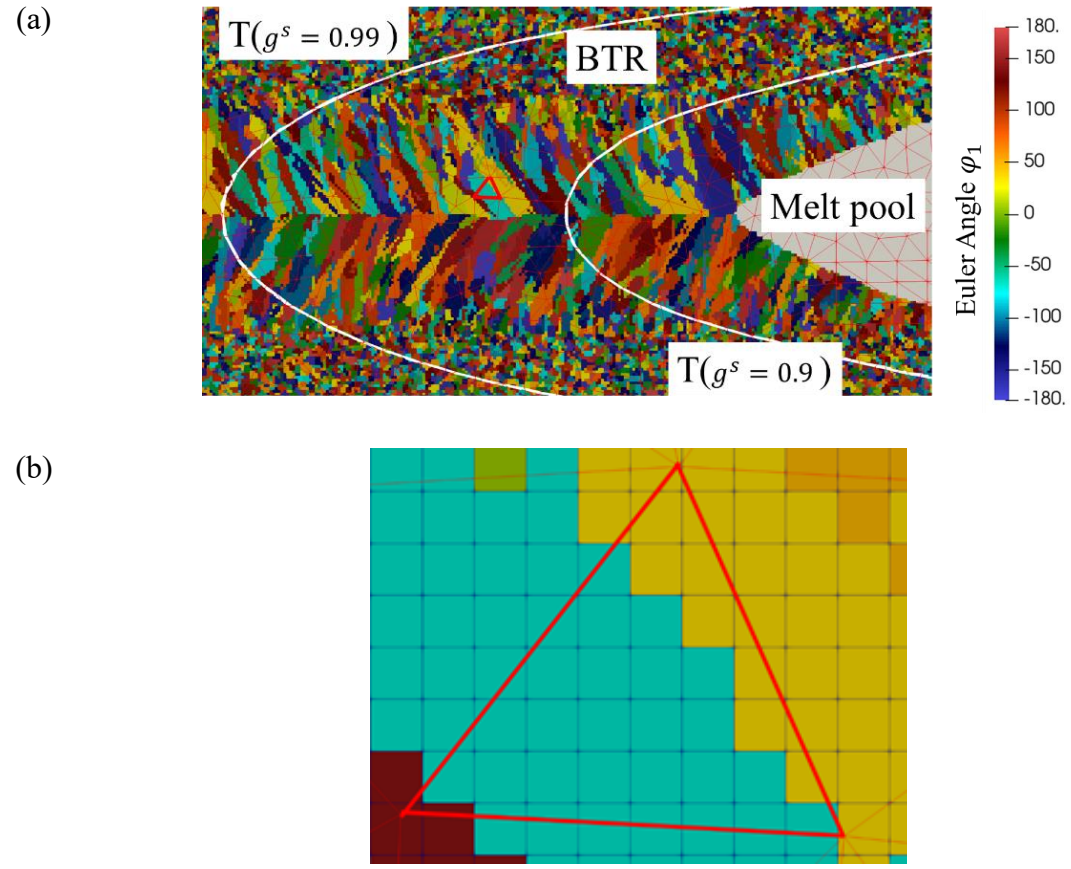

Figure 5-8. Grain structure (first Euler angle φ_1) (a): inside the BTR ($g^s \in [0.9 - 0.99]$) and the corresponding CA mesh in red, (b) zoom of element encompassed in (a) and the corresponding CA grid in blue.

Figure 5-8 (b) presents an element inside the BTR on the CA mesh. It contains several grains as shown (the presentation is 2D while the simulation is in 3D which means more grains could be inside the element). Taking the blue grain which covers the most part of the element as an example, with these 3 Euler angles, the passage matrix P_{C2G} from the crystal reference frame to the global (laboratory) reference frame can be established:

$$P_{C2G} = \begin{bmatrix} P_{11} & P_{12} & P_{13} \\ P_{21} & P_{22} & P_{23} \\ P_{31} & P_{32} & P_{33} \end{bmatrix} \quad (5\text{-}27)$$

with

$$\begin{cases} P_{11} = cos(\varphi_1)cos(\varphi_2) - cos(\phi)sin(\varphi_1)sin(\varphi_2) \\ P_{12} = -cos(\phi)sin(\varphi_1)cos(\varphi_2) - cos(\varphi_1)sin(\varphi_2) \\ P_{13} = sin(\varphi_1)sin(\phi) \\ P_{21} = sin(\varphi_1)cos(\varphi_2) + cos(\phi)cos(\varphi_1)sin(\varphi_2) \\ P_{22} = cos(\phi)cos(\varphi_1)cos(\varphi_2) - sin(\varphi_1)sin(\varphi_2) \\ P_{23} = -cos(\varphi_1)sin(\phi) \\ P_{31} = sin(\phi)sin(\varphi_2) \\ P_{32} = sin(\phi)cos(\varphi_2) \\ P_{33} = cos(\phi) \end{cases} \quad (5\text{-}28)$$

Then the matrix P_{C2G} is multiplied by the 6 ⟨100⟩ crystallographic directions in the crystal reference frame which means the vectors: $[1,0,0], [-1,0,0], [0,1,0], [0,-1,0], [0,0,1], [0,0,-1]$. The 6 result vectors present the 6 ⟨100⟩ crystallographic directions in the global frame. Figure 5-9 presents crystallographic directions $[1,0,0], [-1,0,0], [0,1,0], [0,-1,0]$ for the blue grain considered. Note that, the crystallographic direction [1,0,0] is chosen to represent the grain growth direction.

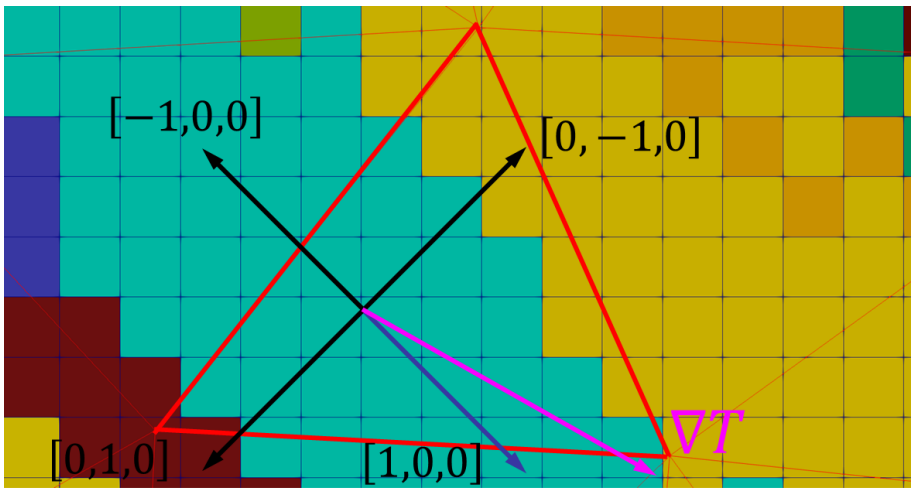

Figure 5-9. Grain direction presentation.

Among the 6 vectors, the closest to the temperature gradient is considered as the dendrite growth direction for the grain.

With the method presented above, the dendrite growth direction for each grain in an element can be deduced, then the weighted average on grain volume in the element is computed and considered as the dendrite growth direction related to the element, $\boldsymbol{D}_e$:

$$\boldsymbol{D}_e = \frac{\sum_i \boldsymbol{D}_i \times n_{cell}^i}{\sum_i n_{cell}^i} \tag{5-29}$$

with $\boldsymbol{D}_i$ the dendrite growth direction computed for grain i in element e and n_{cell}^i is the number of cells contained in grain i in element e.

5.4 Simulation parameters

As mentioned in the beginning of section 5.3 , the simulation considers only the metal subdomain, *i.g.* $\Omega \equiv \Omega^M$. As presented in Figure 5-3, the simulation domain contains only the zone of interest (blue part in Figure 5-3 without the appendix which will detach during welding nor the right part to fix the metal plate).

The FE mesh is presented in Figure 5-10 (a), and the corresponding CA mesh is presented at the center of the FE mesh. As mentioned before, the width of the FE mesh is either 20 or 25 mm depending on the welding configuration. Since the grain structure information (mainly the Euler angles) is necessary along the whole length of the weld bead, the CA mesh has the same length and height as the FE mesh. The difference between the two meshes is the width: the CA mesh needs only to cover the whole width of the melt pool. A 12 mm width of the CA mesh is assigned for all configurations studied in this work.

As shown in Figure 5-10 (a), the center of the FE mesh is refined to better resolve the global function (thermal and solid mechanics) in the zone of interest where the temperature gradient is high, and the melt pool as well as the mushy zone are contained.

Details of the mesh size information are presented in Table 5-6. The initial condition is room temperature (20℃) for the heat flow problem and zero velocity for the momentum conservation equation (solid mechanics, equation (5-7)). The boundary conditions for the thermal resolution is a mixed convection-radiation condition on the 6 surfaces (equation (5-5)) with outside temperature at 20℃. For momentum conservation equation (equation (5-7)), boundary conditions is zero velocity on the plane $X = 100$ mm as presented in Figure 5-10 (a).

The computation algorithm is presented in Figure 5-11. It can be noted that no remeshing is applied on this simulation, the reason being to keep the refined mesh (initial mesh) to present the stress, strain and hot cracking criterion and to reduce the influence of remeshing on the fields of interest.

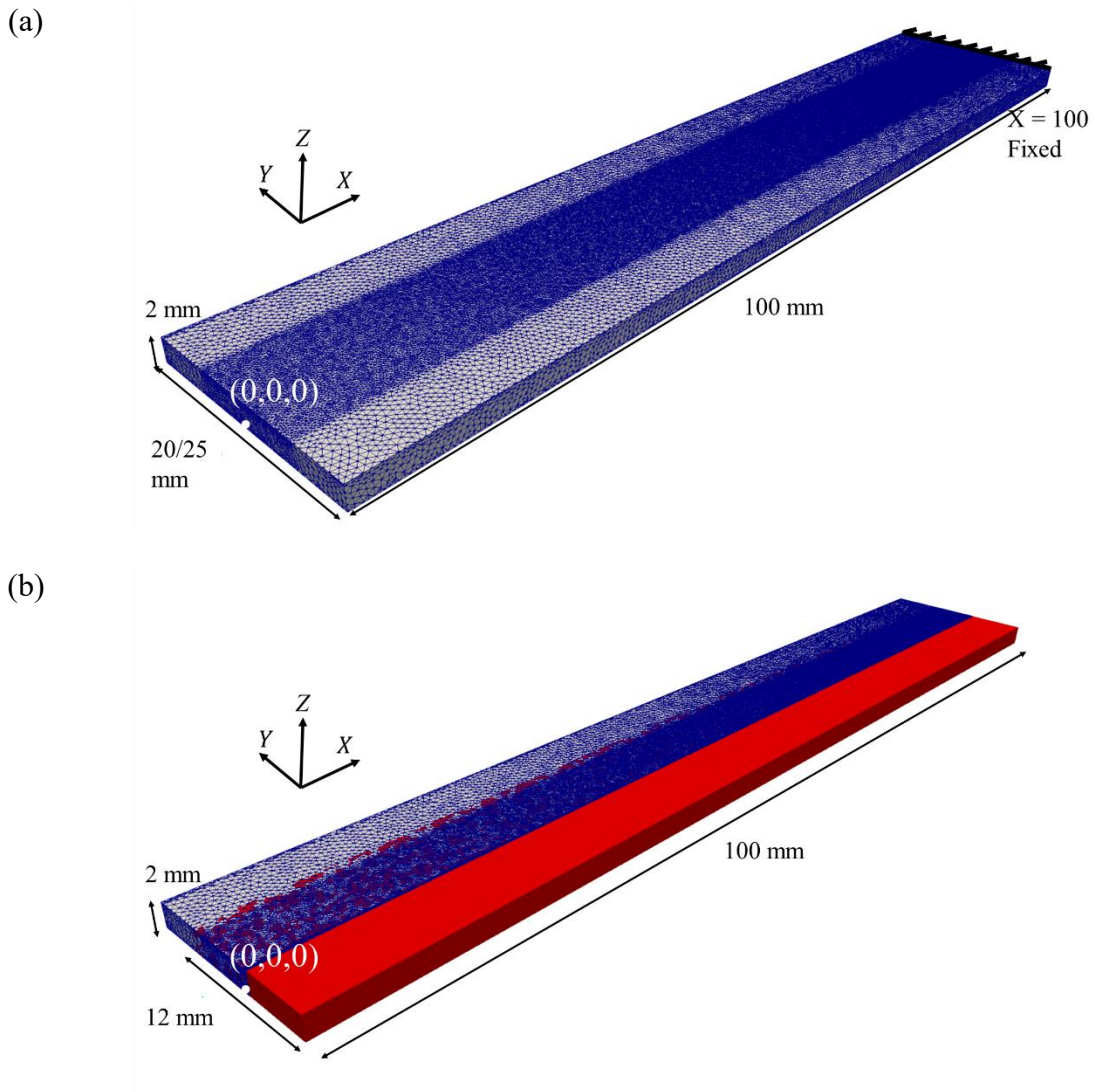

Figure 5-10. (a) FE mesh, (b) cut of initial FE mesh by plane Y=0 in blue and CA mesh in red.

Table 5-6. Mesh parameters.

Parameter	Value
Global simulation domain, Ω	$100 \times 20/25 \times 2$ mm
FE mesh size along the heat source path (center part in Figure 5-10 (a))	0.3 mm
FE mesh size elsewhere	0.5 mm
CA domain Ω^{CA}	$100 \times 12 \times 2$ mm
CA mesh size	0.5 mm
CA cell size	50 µm
Initial grain density	1000 mm^{-3}

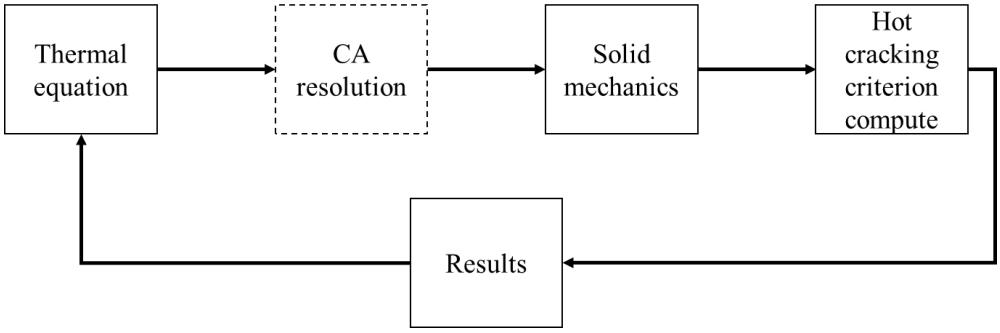

Figure 5-11. Computation process for each time step.

In the simulation, the welding process begins at the center of the top surface of plane $X = 0\ mm$, *i.e.* coordinate $(0,0,2)$. In order to model the existence of the appendix that detaches during the process, the heat source is kept at this initial position for 2 seconds [Bel16], then the heat source advances along the X direction along the center line of the metal plate during 20s, creating a penetrated melt pool and a weld bead of $86.6/93.4$ mm length with different welding speed $4.3/4.67$ mm s^{-1}. Then the heat source is stopped and the plate is left to solidify and cooling until the maximum temperature of the simulation domain becomes lower than the BTR. The whole welding process takes 25 s, (*i.e.* 25 s welding and 5 s cooling). Other welding parameters such as heat source power are presented in Table 5-2. Such a simulation for a 25 seconds welding process takes about 20 hours on 56 processors.

5.5 Simulation results

5.5.1 Hot cracking criterion (F^{WYSO}) without grain structure

For reminding, in the simulation without grain structure, the temperature gradient is applied as the direction u to define the frame (u, v, w) to compute the $\dot{\hat{\varepsilon}}$ in the WYSO criterion F^{WYSO}.
Figure 5-12 shows the computed F^{WYSO} for the different welding configurations as presented in Table 5-2 after complete solidification ($t = 25$s). The representative plane is chosen at $Z = 1$ mm where the F^{WYSO} has the maximum value through the thickness (presented in Figure 5-14). As shown, the non-crack cases have a shorter weld bead than the crack cases because of the lower welding speed.
The first observation focuses on the value of F^{WYSO} at the beginning of the plate along the center line (encompassed by the black contour in Figure 5-12). For all the 4 configurations, F^{WYSO} has a large value indicating a large risk of hot cracking in the center of the plate which is coherent with the experiment observation as shown in Figure 5-3 (c). As mentioned before, cracks propagation (separation of initial mesh) is not simulated. Only the criterion indicating the hot cracking risk is computed. Therefore, F^{WYSO} decreases as the welding process continue along the X direction as shown in Figure 5-12. Another point is the positive value of F^{WYSO} for all 4 configurations, even for the non-crack cases in Figure 5-12 (b) and (d). This observation could justify a modification of WYSO criterion: a threshold value rather than 0 may be possible to define the appearance of the cracks. However, to find this threshold value, more welding

configurations should be tested experimentally which could be a perspective of this PhD project. Until now, the most important explanation of the WYSO criterion is to distinguish between the crack and non-crack cases. As presented in Figure 5-12 (a) and (b), for the plate 20 mm wide, the crack case 20C presents a F^{WYSO} larger than 20NC. However, a similar conclusion is hard to make for the plate 25 mm wide. This is why sensors of computed values are used to make precise comparisons.

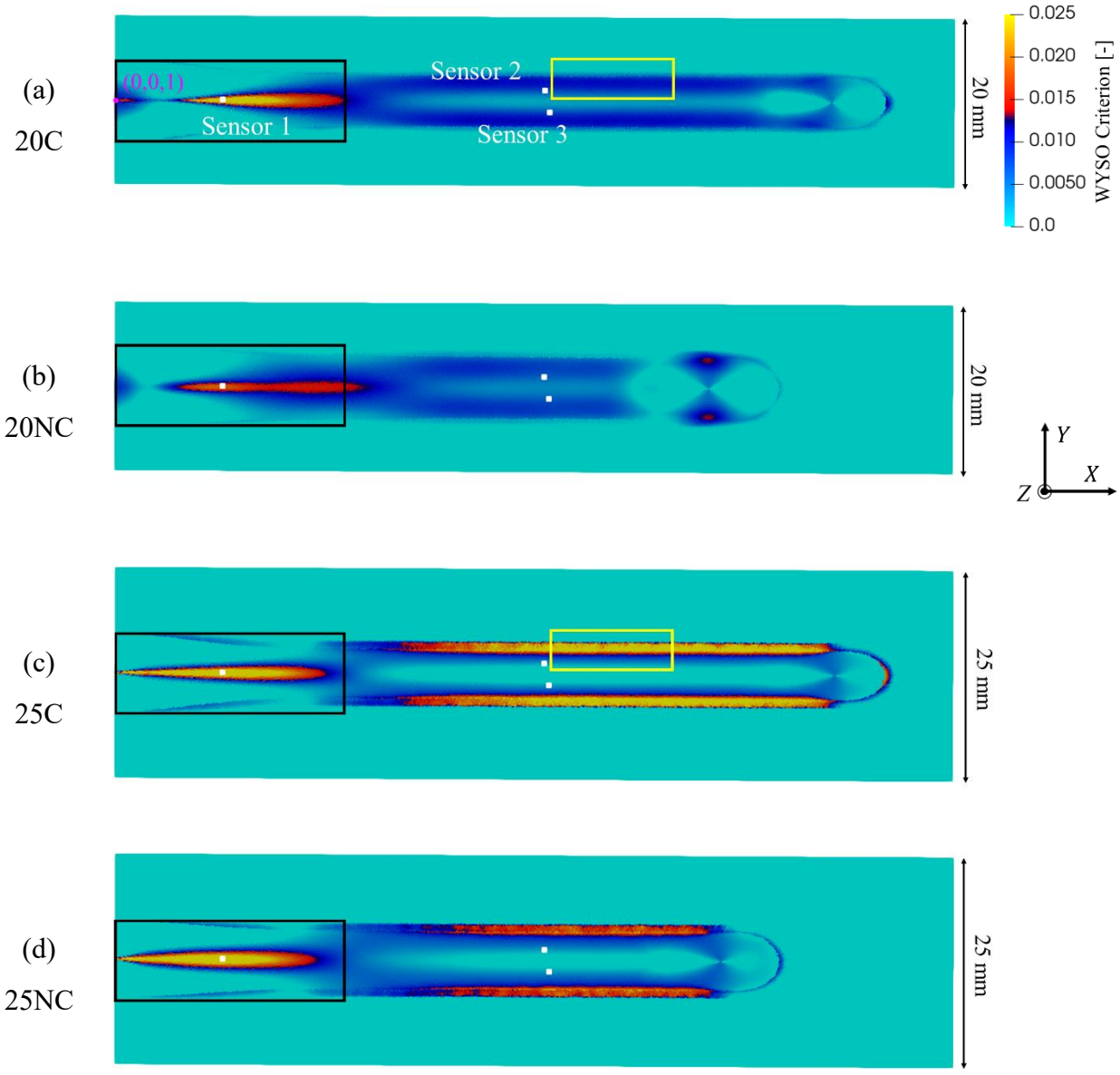

Figure 5-12. WYSO criterion for different welding configurations in Table 5-2 after complete solidification: (a) 20C, (b) 20NC, (c) 25C and (d) 25NC. On plane $Z = 1$ mm at $t = 25$ s.

Before the presentation of sensors measurement, another point of the criterion presented in Figure 5-12 should be mentioned. Values of F^{WYSO} are larger on the 25 mm plate at the side of the weld bead than that on the 20 mm plate (encompassed by yellow contours in Figure 5-12 (a) and (c)).

Figure 5-13 presents the corresponding von Mises equivalent stress $\bar{\sigma}$ (equation (5-19)) and equivalent viscoplastic strain rate $\dot{\bar{\varepsilon}}$ (equation (5-13)) inside the BTR for the welding cases 20C and 25C. As the plate width is different, heat diffusion is different which leads to a different BTR shape, as shown, meaning also a different thermal condition. The cooling is more pronounced in case 25C, which leads to a smaller extension of the BTR zone. As the stress and strain are both related to the thermal condition, the von Mises equivalent stress $\bar{\sigma}$ and especially the equivalent viscoplastic strain rate $\dot{\bar{\varepsilon}}$ of the plate 25C are larger than that of the plate 20C. Since the WYSO criterion is based on the cumulated strain, the criterion values are larger in 25C than in 20C.

However, as mentioned before, the computed WYSO criterion presents the risk of hot cracking without simulation of the propagation of the cracks. The simulation conditions such as thermal condition and solid mechanical condition in the zone presented in Figure 5-13 could be different if the crack exist at the center of the plate as in the experiment. Therefore, the computed result could be less representative than in the zone encompassed by black contours in Figure 5-12.

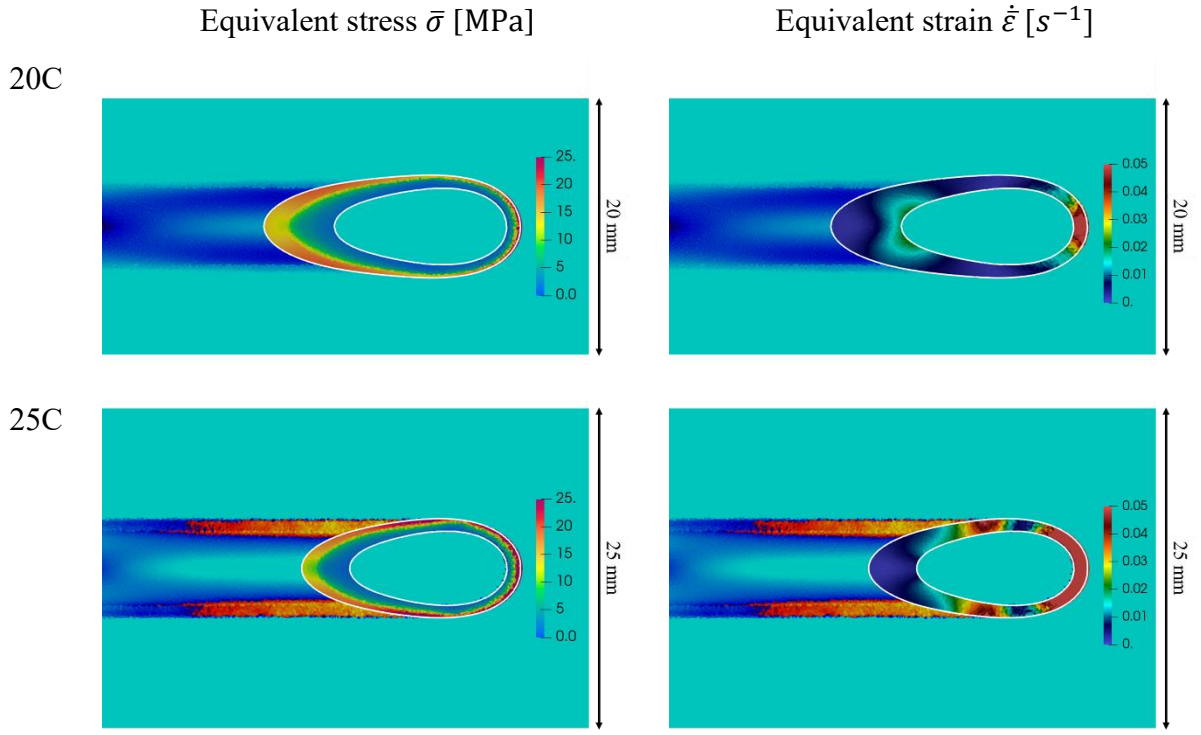

Figure 5-13. Von Mises equivalent stress $\bar{\sigma}$ and equivalent viscoplastic strain rate $\dot{\bar{\varepsilon}}$ in the BTR (between the two white contours) for welding cases 20C and 25C in plane $Z = 1$ mm at $t = 16$ s during the process.

Table 5-7 presents the position of three sensors as shown in Figure 5-12 (a).

Table 5-7. Sensor positions.

	Sensor 1	Sensor 2	Sensor 3
Coordinate $(x, y, z)\ mm$	(12.90,0.05,1.0)	(51.25,1.33,1.0)	(51.80, −1.30,1.0)

Figure 5-14 shows the profile of F^{WYSO} across the thickness for $(x, y) = (12.90,0.05)$ and $(51.25,1.33)$, corresponding to sensor 1 and sensor 2 in Table 5-7. Note that a factor on the 2 scale of F^{WYSO} exists between Figure 5-14 (a) and (b). As presented, F^{WYSO} has its maximum value for $Z = 1$ mm (exact location of sensor 1). However, for sensor 2, the maximum F^{WYSO} is not exactly obtained on the plane $Z = 1$ mm, but considering that the magnitude of the difference is about 10^{-4}, this justifies the observation of F^{WYSO} at sensor 2.

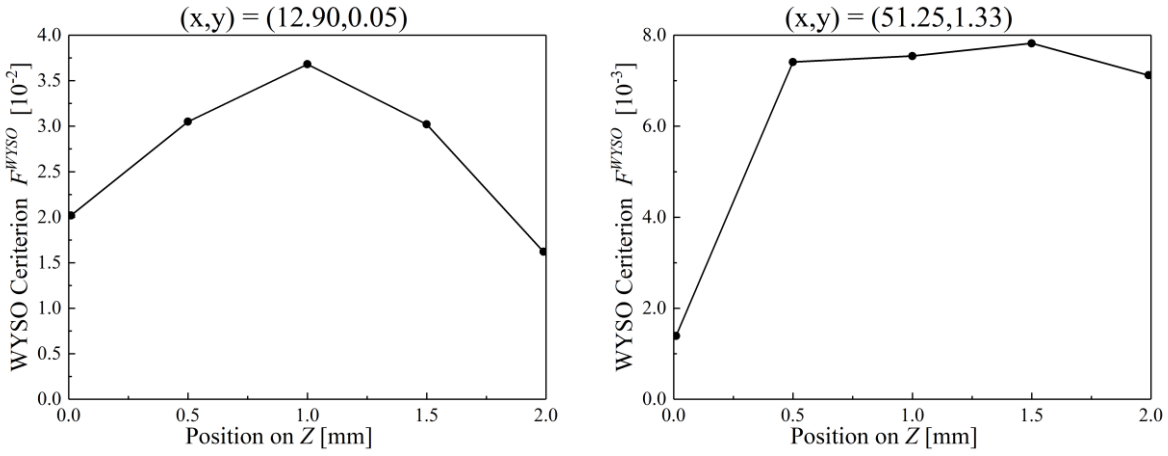

(a) (b)

Figure 5-14. Profile of F^{WYSO} across the thickness for different positions, case 20C at the end of the simulation.

Figure 5-15 presents the evolution of F^{WYSO} across the BTR for the 4 welding configurations presented in Table 5-2, for the different sensors as shown in Table 5-7. Note that the scales of F^{WYSO} are different for the three sensors. The time scale is the time passed inside the BTR and time $t = 0$ s indicates the entrance in the BTR for different cases, which is not the same welding time for the crack and the non-crack cases with different welding speeds. At the beginning of the BTR, the cumulated strain ε_{BTR} may be less than the critical strain ε_c, hence a negative value of F^{WYSO} is found at the beginning of the BTR. It can be noted that all the F^{WYSO} start at the default value -1 (not shown in the figures) at the entrance in the BTR ($t = 0$ s), then at their first time step in the BTR, F^{WYSO} takes the computed values.

As shown in Figure 5-15, for all the three sensors, the 20C presents a lager F^{WYSO} than the 20NC as shown also in Figure 5-12. This is to be noticed that 20NC spends more time inside the BTR, which confirms that the HCS criterion (equation 1-48) proposed by Clyne and David [Cly81] is not sufficient. For sensor 1 (Figure 5-15 (a)), the F^{WYSO} of 25C is also larger than that of 25NC, which confirms the WYSO hot cracking criterion is capable to distinguish the

crack and non-crack cases for different configurations. However, for sensor 2 and sensor 3, the F^{WYSO} can only separate the crack and non-crack case for the plate of 20 mm width, the value of F^{WYSO} is very close and the non-crack case has even a larger value than the crack case for the plate of 25 mm width. One explanation is the threshold value rather than 0 which could be introduced as a modification of WYSO criterion, as explained before. Since the value of F^{WYSO} on sensors 2 and 3 are at least 5 times less than that of sensor 1, it is possible that all the four configurations have non-crack risk at the position of sensor 2 and 3. Another reason could be the lack of crack propagation simulation, as mentioned before, the computed result could be less representative in the zone of sensor 2 and 3. It is important to notice that in the cracking experiments, the hot crack has always been found vertical, aligned with the weld line. Therefore, when it comes to the discussion about F^{WYSO} as a cracking predictor, only the values of F^{WYSO} at sensor 1 are relevant. Some observations of F^{WYSO} at sensors 2 and 3 can be made, but rather discussed from the cracking prediction.

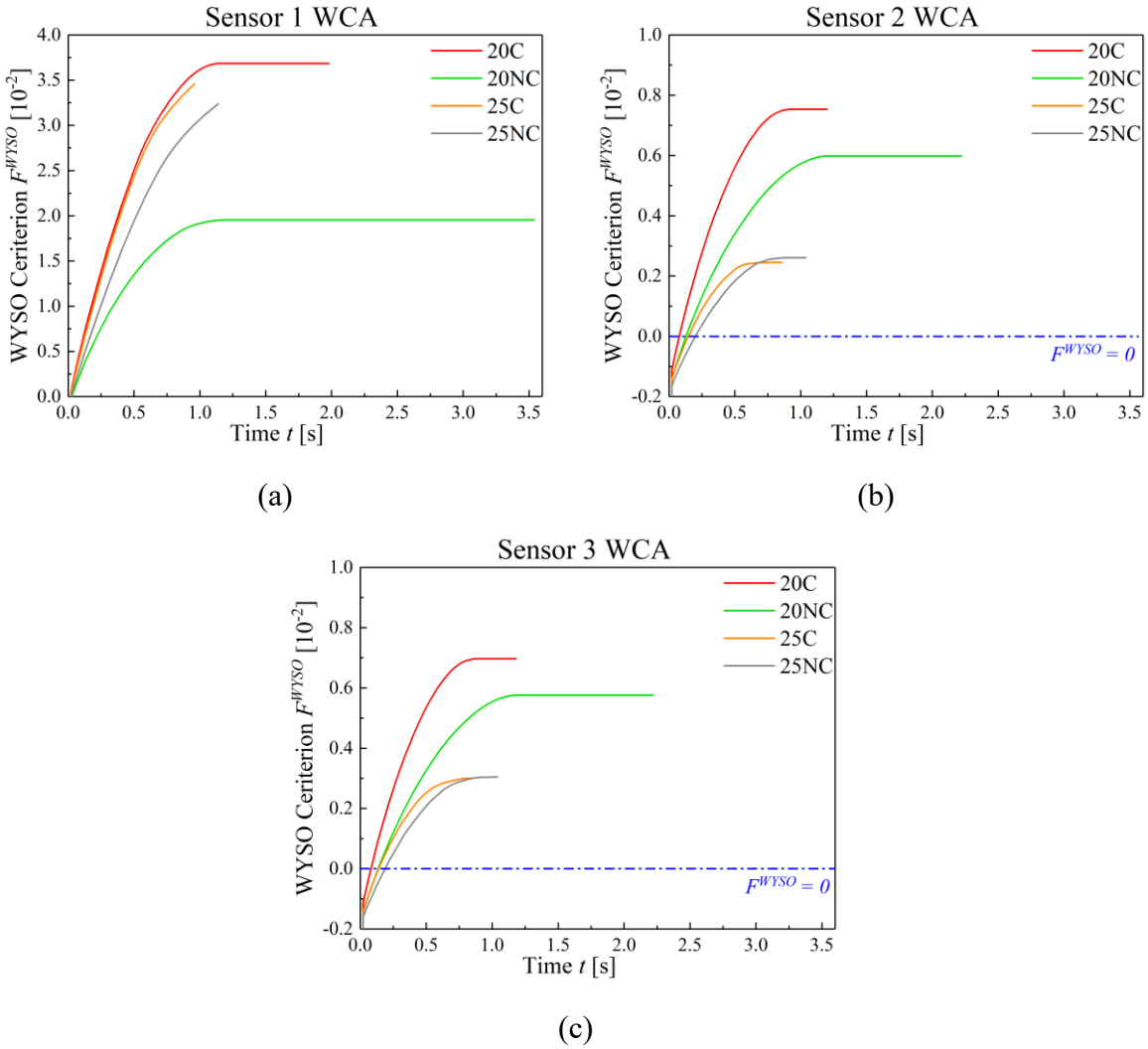

Figure 5-15. Evolution of F^{WYSO} inside the BTR without CA (WCA) calculation for welding configurations presented in Table 5-2 for the three sensors defined in Table 5-7.

Figure 5-16 shows the evolution of the equivalent stress $\bar{\sigma}$, and of the cumulated strain ε_{BTR} inside the BTR for sensor 1. As shown, the case 25NC has a larger equivalent stress than the case 20C. However, the F^{WYSO} and the experimental observation indicate that case 20C has more risk of hot cracking than the 25NC. This demonstrates that the stress may not be a good criterion to determine the hot cracking criterion. Moreover, the cumulated deformation is more coherent with the experiment observation for crack and non-crack cases, confirming the choice of a strain based criterion to compute the hot cracking risk in this PhD work.

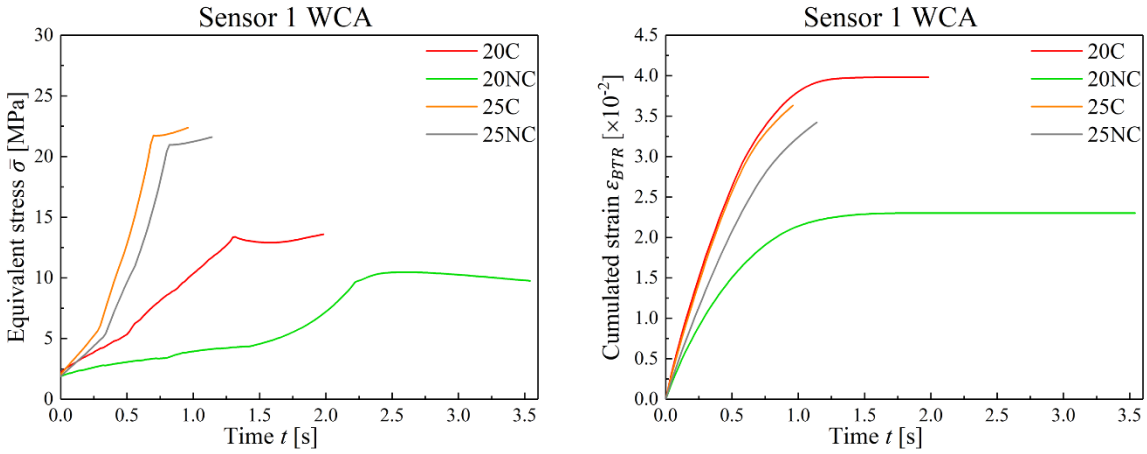

(a) (b)

Figure 5-16. Evolution of: (a) equivalent stress $\bar{\sigma}$, and (b) cumulated strain ε_{BTR} inside the BTR for welding configurations presented in Table 5-2 at sensor 1.

5.5.2 Hot cracking criterion (F^{WYSO}) with grain structure

In this section, the F^{WYSO} is computed by considering the grain structure simulated by the CAFE model, which means the direction u to define the frame (u, v, w) is calculated as presented in section 5.3.3.2. This direction is defined at the entrance of BTR during the simulation and kept unchanged. In fact, the BTR is chosen at $g^s \in [0.9, 0.99]$ in which the grain structure is nearly fixed at such large solid fraction. Note that in the simulation without grain structure, the direction u is the temperature gradient which varies in the BTR interval.
Figure 5-17 shows the F^{WYSO} considering grain structure for the different welding configurations as presented in Table 5-2 after complete solidification ($t = 25\text{s}$) on the plane $Z = 1$ mm. The simulation results with grain structure are similar to that without grain structure. However, the color maps of F^{WYSO} with grain structure Figure 5-17 are not as homogenous as that without grain structure in Figure 5-12. The explanation could be that the distribution of grain direction on the FE mesh is less homogenous than the distribution of temperature gradient which leads to the difference in F^{WYSO} computation.

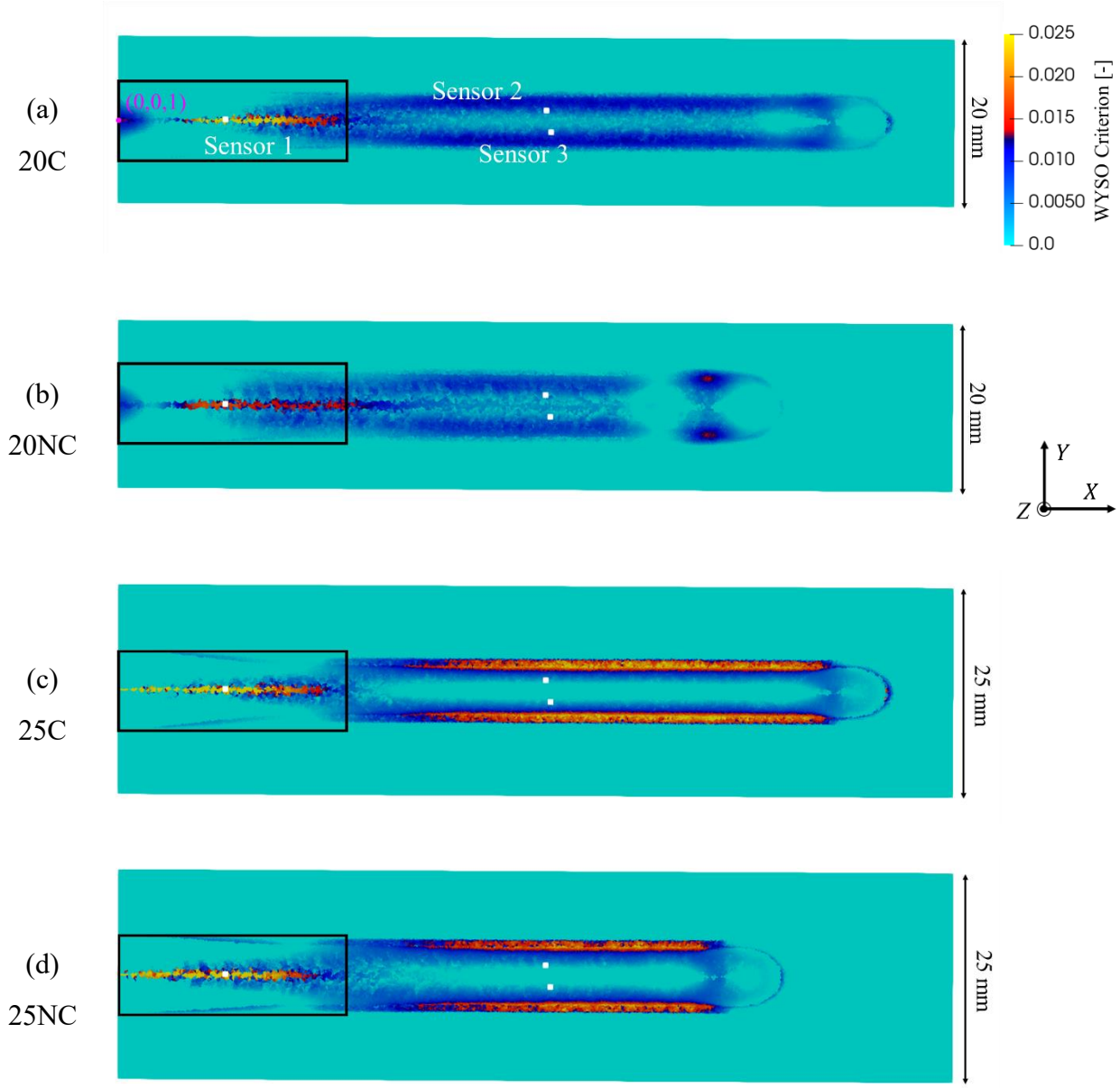

Figure 5-17. WYSO criterion with grain structure for different welding configurations in Table 5-2 after complete solidification: (a) 20C, (b) 20NC, (c) 25C and (d) 25NC.
On plane $Z = 1$ mm at $t = 25$ s.

Figure 5-18 presents the evolution of F^{WYSO} inside the BTR for the four welding configurations in Table 5-2 with and without grain structure (noted as with CA and without CA respectively), in total 8 simulation results. It can be noted that nearly the same evolution curves can be found with and without CA (superposition of curves with CA and without CA), for example, 20NC and 25NC for sensor 1 and 25C for sensor 2. However, for cases 20NC and 20 NC, the computed F^{WYSO} present a large difference for sensors 2 and 3 when considering the grain structure.

As shown in Figure 5-18, the consideration of grain structure does not change a lot the evolution of F^{WYSO} inside the BTR. Besides, the maximum value (the value at the end of BTR) of F^{WYSO} is close for each welding configuration, with and without grain structure (CA). Therefore, the WYSO criterion based on grain structure is still capable to distinguish crack and non-crack cases.

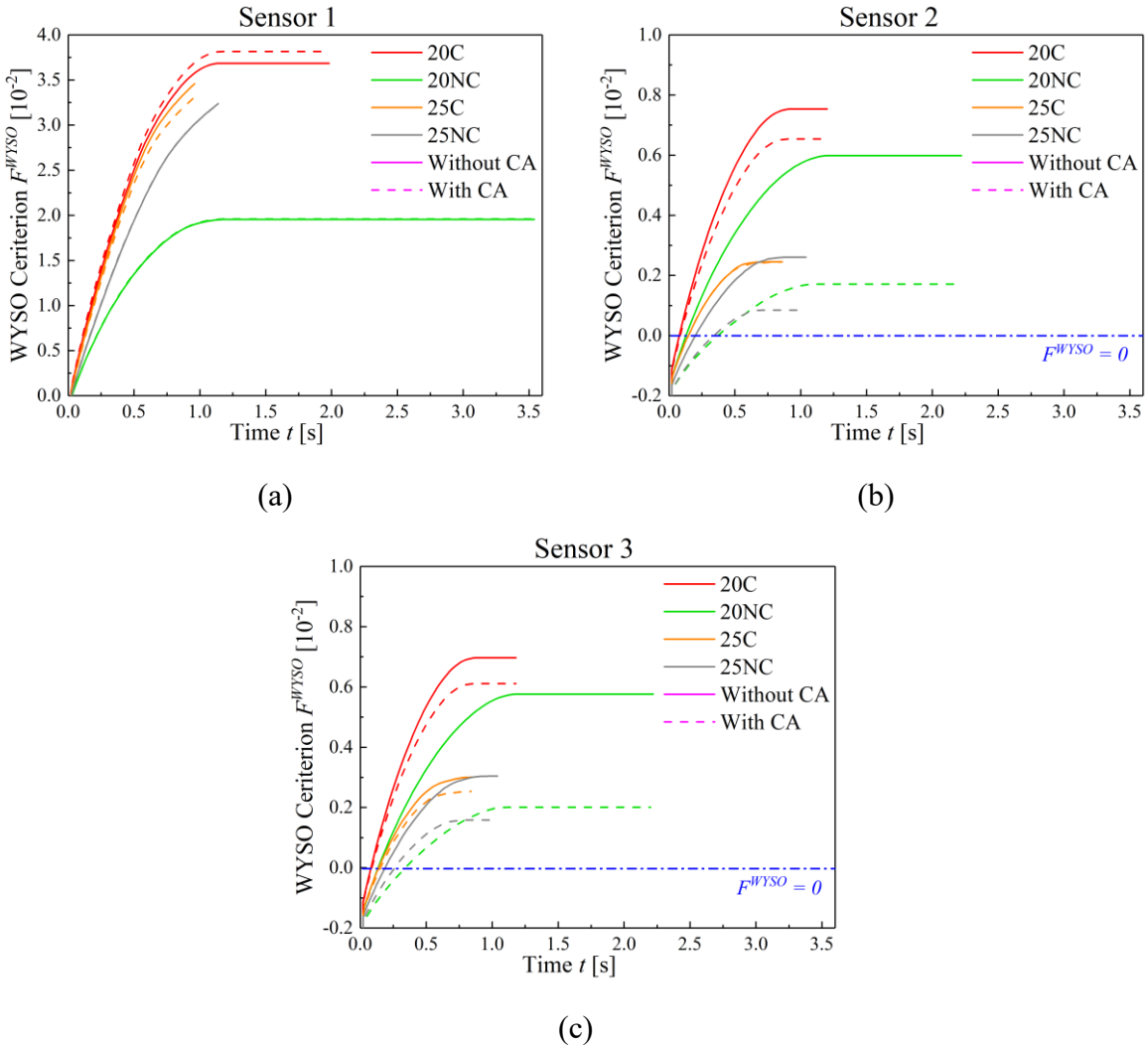

Figure 5-18. Evolution of F^{WYSO} inside the BTR for welding configurations presented in Table 5-2 at the different sensor shown in Table 5-7, with or without consideration of grain structure (with CA or without CA).

According to Figure 5-18, the influence of grain structure on F^{WYSO} is not very clear, the reason could be the similarity of direction u chosen to define the frame (u, v, w) between the cases with CA or without CA.

Figure 5-19 presents the temperature gradient direction (red arrow) and the representative grain direction (blue arrow) inside the BTR for sensor 1 and sensor 2 for cases 20C and 25C. As shown, these two directions are very close to each other, the difference is about $3-4°$ for sensor one and $6-7°$ for sensor 2. It can be noted that for sensor 2, the crystal direction $[1,0,0]$

is chosen (Figure 5-19 top right) as the representative grain direction to compute F^{WYSO} while for sensor 1, the crystal direction chosen is [0,1,0] (Figure 5-19 top left). Note that, as mentioned before, the crystallographic direction [1,0,0] is chosen to represent the grain growth. The reason is that, the crystal direction [1,0,0] is chosen during solidification while the fraction solid g^s is very low (at least $g^s < 0.5$), while the representative grain direction is chosen inside the BTR at $g^s > 0.9$. During the evolution of g^s between $0.5 - 0.9$, the temperature gradient direction may change and as explained in section 0, the chosen representative grain direction could be different from the crystal direction [1,0,0]. As shown in Figure 5-20, the crystal direction [1,0,0] is perpendicular to the melt pool boundary: aligned with the temperature gradient direction. While inside the BTR, the crystal direction [1,0,0] which is already fixed after solidification may be different from the temperature gradient direction. Nevertheless, at least one crystal direction ([1,0,0] or [0,1,0]) is very close to the temperature gradient direction inside the BTR which explains the weak influence of grain structure in F^{WYSO}.

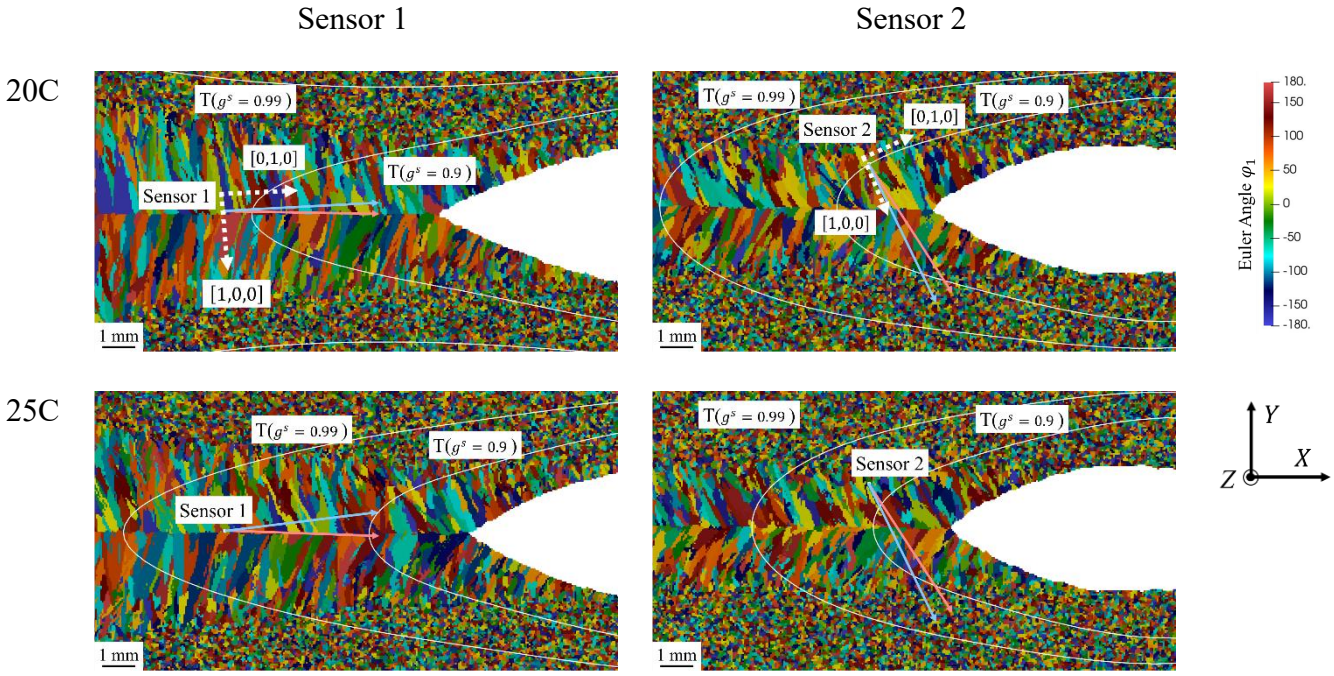

Figure 5-19. Temperature gradient (red) and representative grain direction (blue) inside the BTR for welding case 20C and 25C with grain structure (with CA). At $t = 9$ s for sensor 1 and $t = 16$ s for sensor 2. The grain structure is presented by the first Euler angle φ_1, and the melt pool is in white.

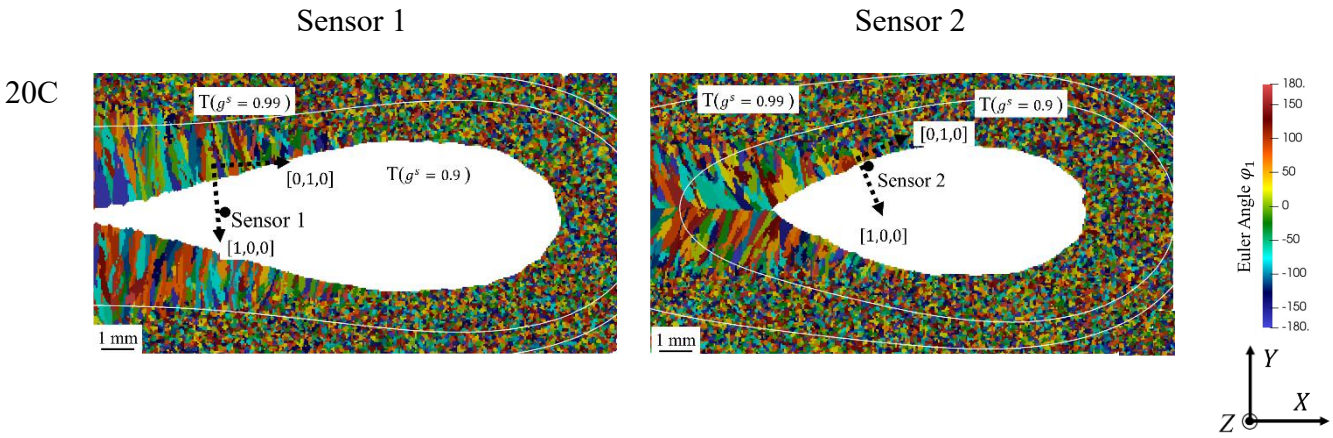

Figure 5-20. Crystal direction for the grain at position of sensor 1 and sensor 2 during solidification. At $t = 7.5$ s for sensor 1 and $t = 14.5$ s for sensor 2. The grain structure is presented by the first Euler angle φ_1, and the melt pool is in white.

Figure 5-21 presents the temperature gradient direction (red) and the representative grain direction (blue) inside the BTR at sensor 2 for cases 20NC and 25NC. As shown, the differences between these 2 directions are larger than that for cases 20C and 25 C (Figure 5-19 sensor 2) which explains the large difference of the computed F^{WYSO} at sensor 2 observed in Figure 5-18 (b).

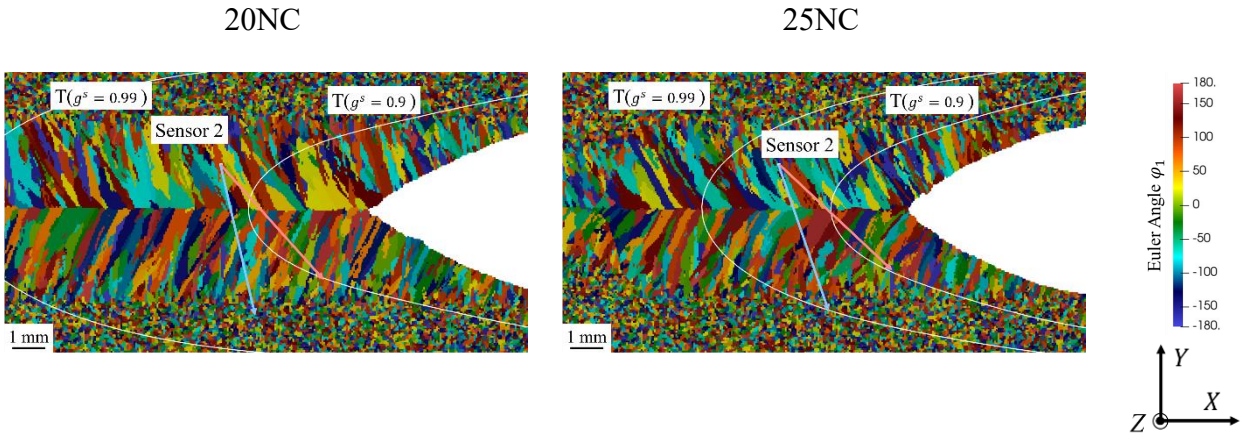

Figure 5-21. Temperature gradient (red) and representative grain direction (blue) inside the BTR for welding case 20NC and 25NC with grain structure (with CA). At $t = 19$ s

One should point out that these simulations present the feasibility of the grain structure influence on the hot cracking criterion. However, the simulated grain structure can be different from the real grain structure as no EBSD map is available for comparison. In order to better understand the influence of grain structure on hot cracking, a discussion is later developed.

5.6 Discussions

5.6.1 Influence of critical strain

The discussions made in this section focus on the simulation without grain structure (WCA).

5.6.1.1 Choice of characteristic strain rate ($\dot{\hat{\varepsilon}}$)

In equation (5-25), the critical strain ε_c is computed using the current strain rate value $\dot{\hat{\varepsilon}}(t)$. However, another choice could be done regarding this characteristic strain rate $\dot{\hat{\varepsilon}}$. Two different choices of $\dot{\hat{\varepsilon}}$ are discussed: the minimum value of $\dot{\hat{\varepsilon}}$ inside the BTR until current time t, $\dot{\hat{\varepsilon}}_{min}$ and the average value of $\dot{\hat{\varepsilon}}$ inside the BTR until current time t, $\dot{\hat{\varepsilon}}_{ave}$.

$$\dot{\hat{\varepsilon}}_{min} = Min_{(0,t),\mathrm{BTR}}\left(\dot{\hat{\varepsilon}}(t)\right) \tag{5-30}$$

$$\dot{\hat{\varepsilon}}_{ave} = \frac{1}{n_{BTR}}\sum_{0}^{n_{BTR}} \dot{\hat{\varepsilon}}(t) \tag{5-31}$$

with n_{BTR} the time step number inside the BTR for the current time t.
Distinction of the different criterion F^{WYSO} is made with the following notations where ${F^{WYSO}}_{cur}$ corresponds to the expression in equation (5-25).

$${F^{WYSO}}_{cur} = \varepsilon_{BTR}(t) - \varepsilon_c(t) = \sum_{n_{BTR}=0}^{n_{BTR}} \dot{\hat{\varepsilon}}(t)\,\Delta t - \frac{\phi}{\dot{\hat{\varepsilon}}(t)^{m^*}\Delta T_{BTR}{}^{n^*}} \tag{5-32}$$

$${F^{WYSO}}_{min} = \varepsilon_{BTR}(t) - \varepsilon_c(t) = \sum_{n_{BTR}=0}^{n_{BTR}} \dot{\hat{\varepsilon}}(t)\,\Delta t - \frac{\phi}{\dot{\hat{\varepsilon}}_{min}{}^{m^*}\Delta T_{BTR}{}^{n^*}} \tag{5-33}$$

$${F^{WYSO}}_{ave} = \varepsilon_{BTR}(t) - \varepsilon_c(t) = \sum_{n_{BTR}=0}^{n_{BTR}} \dot{\hat{\varepsilon}}(t)\,\Delta t - \frac{\phi}{\dot{\hat{\varepsilon}}_{ave}{}^{m^*}\Delta T_{BTR}{}^{n^*}} \tag{5-34}$$

Figure 5-22 presents the time evolution of $\dot{\hat{\varepsilon}}(t)$ and $\dot{\varepsilon}_{YY}$ inside the BTR for sensor 1 as presented in Figure 5-12. $\dot{\varepsilon}_{YY}$ is the transverse component of the strain rate ${\dot{\bar{\varepsilon}}^{vp}}_{(i,j,k)}$ related to the global (laboratory) frame (i,j,k). In fact, for sensor 1, as the temperature gradient is aligned with the welding direction (Figure 5-19), the transverse component of the strain rate ${\dot{\bar{\varepsilon}}^{vp}}_{(i,j,k)}$, $\dot{\varepsilon}_{YY}$, is the component most related to hot cracking. This could also be proved by the similar value of $\dot{\hat{\varepsilon}}(t)$ and $\dot{\varepsilon}_{YY}$ as presented in Figure 5-22.

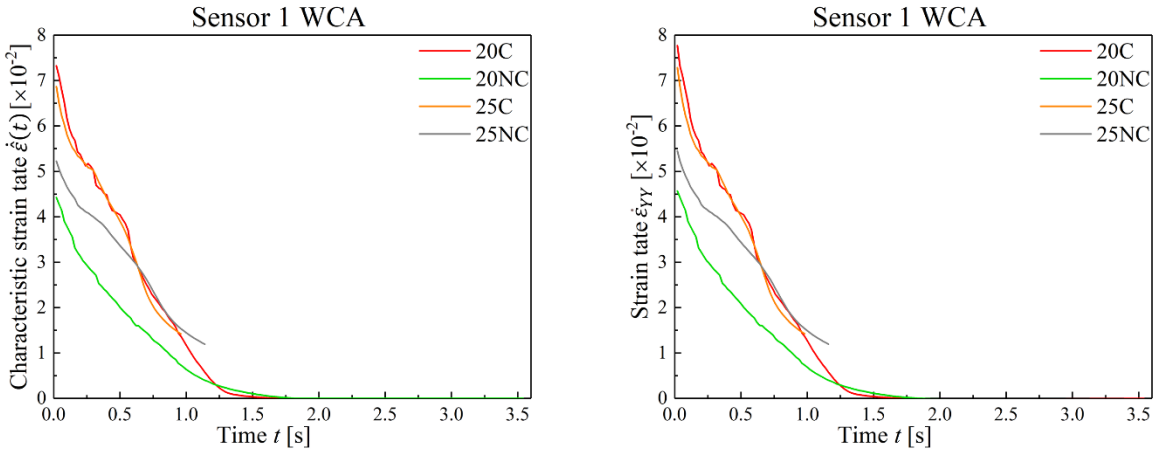

(a) (b)

Figure 5-22. Evolution of: (a) $\dot{\hat{\varepsilon}}(t)$ and (b) $\dot{\varepsilon}_{YY}$ inside the BTR for sensor 1.

As shown in Figure 5-22 (a), $\dot{\hat{\varepsilon}}(t)$ decreases inside the BTR which means that $\dot{\hat{\varepsilon}}(t) = \dot{\hat{\varepsilon}}_{min}$ and thus ${F^{WYSO}}_{cur} = {F^{WYSO}}_{min}$. The first explanation is presented in Figure 5-22 (b), as the strain rate $\dot{\varepsilon}_{YY}$ of global frame (i, j, k) decreases, the characteristic strain rate $\dot{\hat{\varepsilon}}(t)$ of temperature gradient frame (u, v, w) also decreases. Moreover, the further reason is the evolution of material properties during cooling. Inside the BTR, the consistence coefficient K and hardening coefficient n increase to be able to support more stress with less strain.

Figure 5-23 presents the evolution of ${F^{WYSO}}_{cur/min}$ and ${F^{WYSO}}_{ave}$ inside the BTR. The very first observation is that whatever the choice of $\dot{\hat{\varepsilon}}$, the WYSO criterion can always separate the crack and non-crack cases, especially for sensor 1, which is the most interested value to be considered. Besides, for all cases, the ${F^{WYSO}}_{ave}$ is lower than the ${F^{WYSO}}_{cur/min}$. The reason is the decrease of $\dot{\hat{\varepsilon}}(t)$ inside the BTR as presented in Figure 5-22 (a): as $\dot{\hat{\varepsilon}}$ decreases, $\dot{\hat{\varepsilon}}_{ave}$ (that takes into account the precedent values of $\dot{\hat{\varepsilon}}$) is larger than $\dot{\hat{\varepsilon}}(t)$ (equals to $\dot{\hat{\varepsilon}}_{min}$). Thus, the critical strain ε_c is smaller leading to a larger criterion. As shown in Figure 5-23, the choice of $\dot{\hat{\varepsilon}}$ has a weak influence on the discriminating character of the criterion, which means that the WYSO criterion depends more on the cumulated strain than on the critical strain. As shown in Figure 5-24, the difference between ε_{BTR} and ${F^{WYSO}}_{cur/min}$ is weak, indicating that the critical strain ε_c is weak compared with ε_{BTR}.

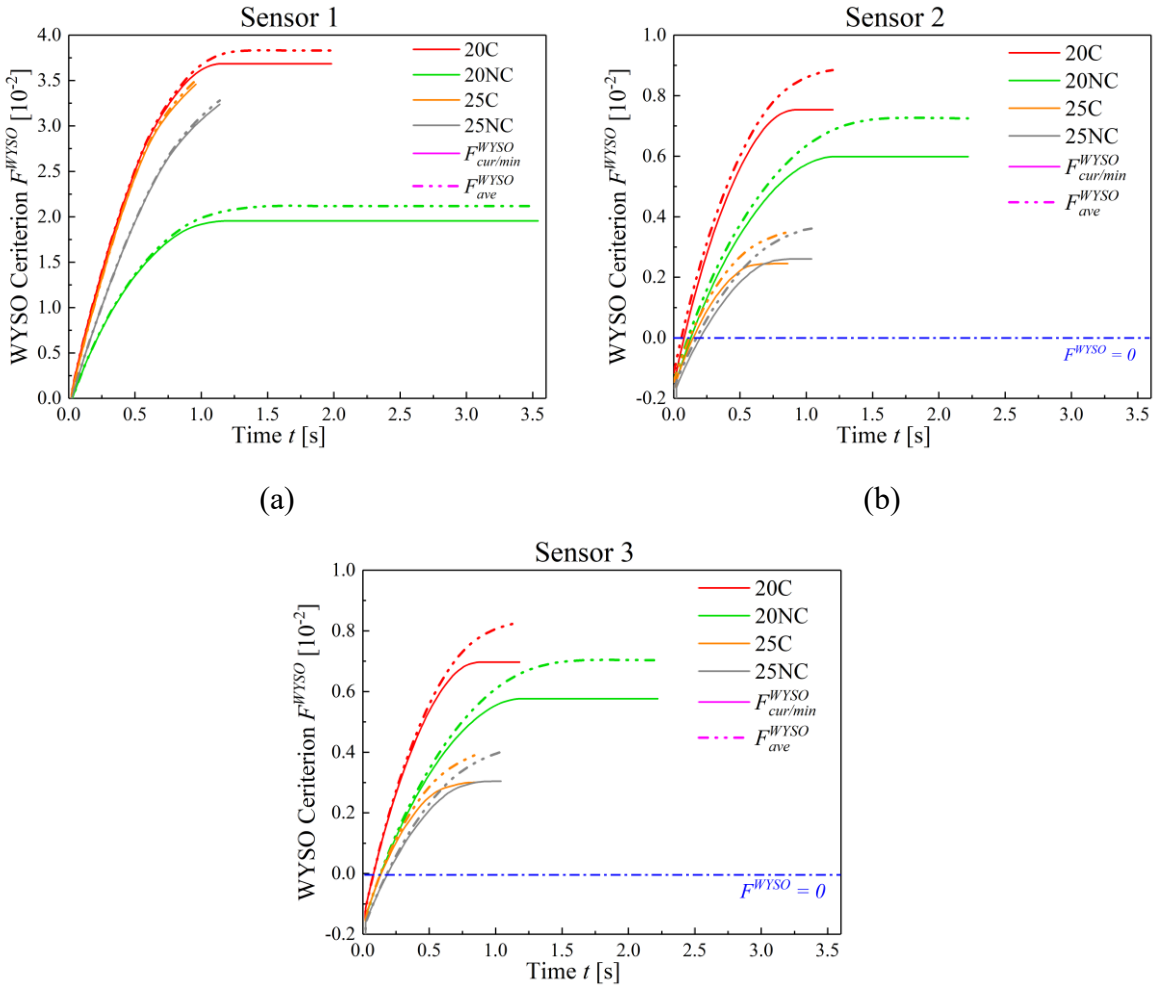

Figure 5-23. Evolution of different F^{WYSO} inside the BTR for welding configurations presented in Table 5-2 at the different sensor shown in Table 5-7.

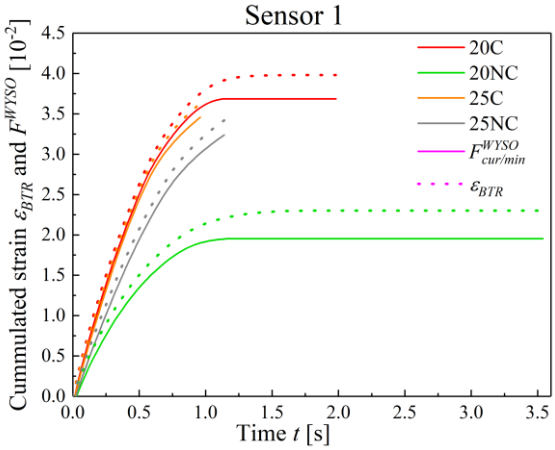

Figure 5-24. Comparison of cumulated strain ε_{BTR} and criterion $F^{WYSO}{}_{cur/min}$ without grain structure for sensor 1.

5.6.1.2 Critical strain considering chemical composition

As presented in section 1.3.2.4, Bellet et al. [Bel09] developed a CBC hot cracking criterion based on the WYSO criterion which takes into account the chemical composition of the steel material. The principle is to modify the critical strain ε_c by multiplying it by a factor (recall of equation 1-67):

$$\varepsilon_c = \frac{\varphi}{\dot{\varepsilon}^{m^*} \Delta T_{BTR}{}^{n^*}} / I_{CBC} \tag{5-35}$$

$$I_{CBC} = \left(a e^{b\, wc} \left(\frac{w_{Mn}}{w_S} \right)^c (w_P)^d \right) \tag{5-36}$$

where $a = 736.5$, $b = 2.195$, $c = -0.857$, and $d = 0.851$. The w values refer to the percentage mass compositions of chemical species. As presented in Table 5-1, for the AISI 321 used in this work, $w_C = 0.029$, $w_{Mn} = 0.94$, $w_S = 0.001$, and $w_P = 0.021$. The calculated $I_{CBC} = 0.083$. It could be noted that the value of I_{CBC} is much smaller than the values presented by the authors [Bel09] which are normally between $0.9 - 3.0$. The reason is the weak content of sulfur. In fact, in the reference [Bel09], the values of w_{Mn}/w_S for all steels considered are less than 100, while in this work, $w_{Mn}/w_S = 940$.
Figure 5-25 presents the CBC criterion F^{CBC} with the following expression:

$$F^{CBC}(t) = \varepsilon_{BTR}(t) - \varepsilon_c(t) = \sum_{n_{BTR}=0}^{n_{BTR}} \dot{\varepsilon}(t)\, \Delta t - \frac{\phi}{\dot{\varepsilon}(t)^{m^*} \Delta T_{BTR}{}^{n^*}} / I_{CBC} \tag{5-37}$$

Same as for the F^{WYSO}, F^{CBC} always takes the maximum value in the BTR interval.

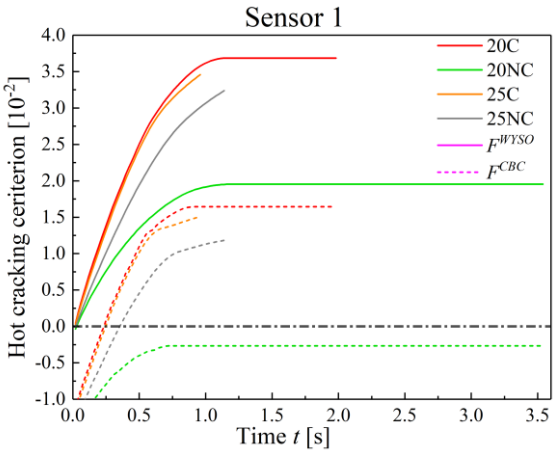

Figure 5-25. Evolution of F^{WYSO} and F^{CBC} inside the BTR for welding configurations presented in Table 5-2 at sensor 1 shown in Table 5-7.

As shown in Figure 5-25, the CBC criterion is also able to distinguish the crack cases and non-crack cases. Besides, as $I_{CBC} = 0.083$, the critical strain of CBC criterion is much larger than that of the WYSO criterion. One advantage of CBC is that it takes negative values for the non-crack case 20NC. However, it remains positive for 25NC, which means that the question regarding the threshold value is still open. Moreover, it is clear that the chemical composition of AISI321 is out of the definition domain of CBC. In total, there is no clear advantage in using CBC instead of the basic WYSO criterion in this work.

5.6.2 Influence of microstructure

In this section, the influence of grain structure is studied by applying another dendrite kinetic law, the law K_4 as presented in Table 5-3 and Figure 5-4. This kinetic law K_4 is chosen arbitrarily which ensure the undercooling $\Delta T < T_{liq} - T(g^s = 0.9) = 1457 - 1385 = 72℃$ at the welding speed, in order not to influence the BTR. In fact, the BTR is chosen for the temperature range between $[T(g^s = 0.99), T(g^s = 0.9)]$, if the undercooling ΔT at the welding speed is too large, $T(g^s = 0.9)$ will be changed and the BTR is also changed. In the first stage of the work, the BTR is chosen to be unchanged.

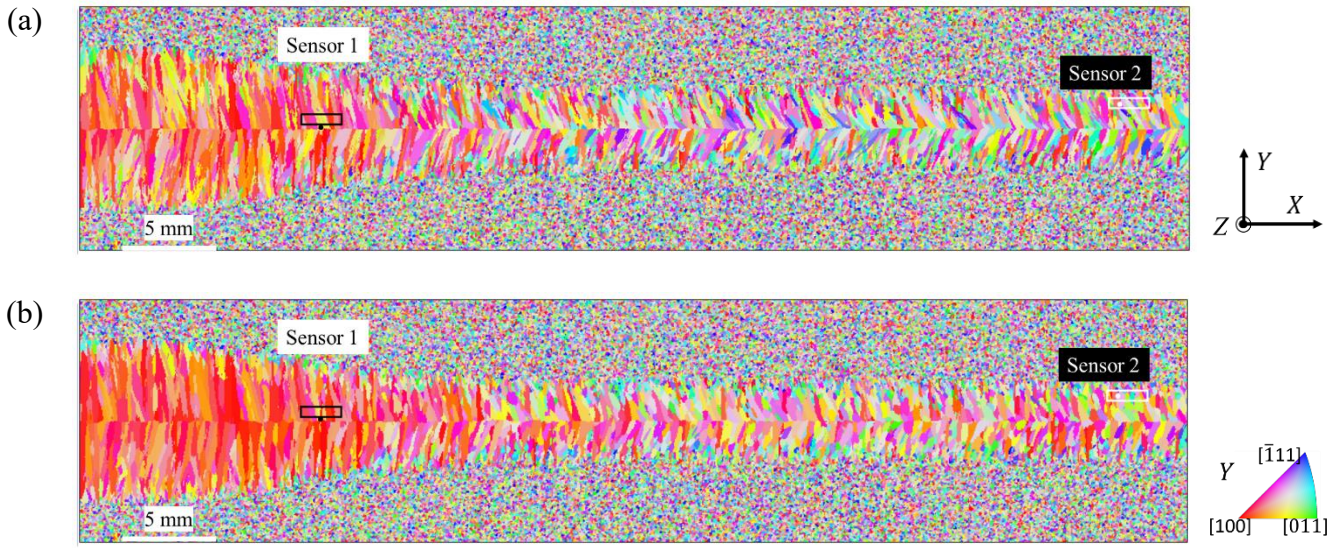

Figure 5-26. $Y-$ direction EBSD maps of the grain structure in plane $Z = 1$ mm between $X \in [0,55]$ mm for the welding case 20C in Table 5-2 for dendrite kinetic law: (a) K_3, (b) K_4 in Table 5-3.

Figure 5-26 presents the computed $Y-$ direction EBSD map of the grain structure after solidification for the different dendrite kinetic law K_3 and K_4 in Table 5-3. As shown, the melt pool is larger at the left side of the plate, the reason is the 2 seconds preheating at the initial position of the heat source before its advancement. The preheating is applied to simulate the welding process on the appendix of the plate in the experiment (as shown in Figure 5-3 (b)). Considering Figure 5-26, the grain simulated by K_4 (b) presents more dominant colors in red than that of K_3 (a), meaning that the $\langle 100 \rangle$ direction of grains of K_4 is closer (nearly aligned with) to the $Y-$ direction. The reason is the different melt pool shape for K_3 and K_4. As shown

in Figure 5-27, the melt pool of K_4 is much longer, especially at the rear than that of K_3. The temperature gradient direction of K_4 also closer to the $Y-$ direction than that of K_3, explaining the difference of grain structure between the two kinetic laws.

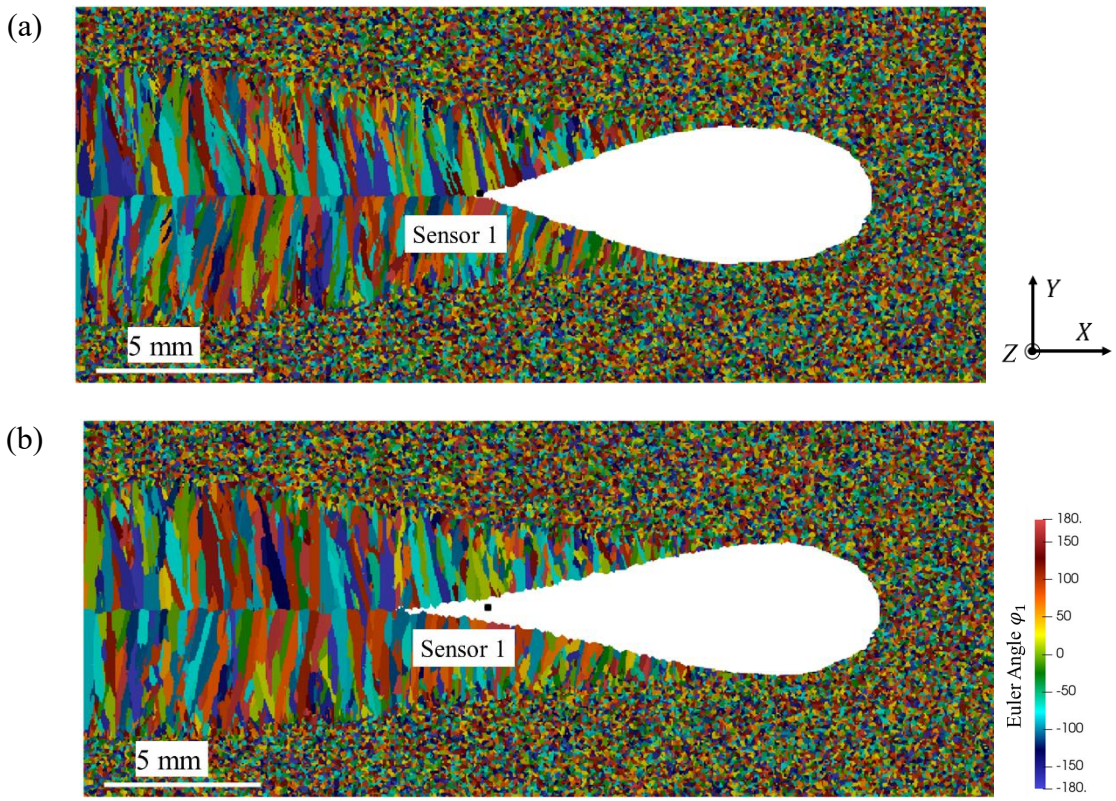

Figure 5-27. Melt pool shape (white domain) during the solidification in plane $Z = 1$ mm for the welding case 20C (Table 5-2) for dendrite kinetic law (a) K_3, and (b) K_4 (Table 5-3) at $t = 8.0$ s. The grain structure is presented by the first Euler angle φ_1.

The $\langle 100 \rangle$ pole figure of the zone around the sensor 1 (black rectangle in Figure 5-26) and sensor 2 (white rectangle in Figure 5-26) is presented in Figure 5-28. The observation around sensor 1 is quite coherent with the EBSD map, the grain structure of K_4 is more aligned to the $Y-$ direction. However, the $\langle 100 \rangle$ pole figure presents not so much difference for the zone around sensor 2 (texture is less).

It could be noted that sensor 1 is not exactely inside the black rectangle in Figure 5-26, this is because the position of sensor 1 is too close to the center of the weld bead and the black rectangle is moved to avoid it.

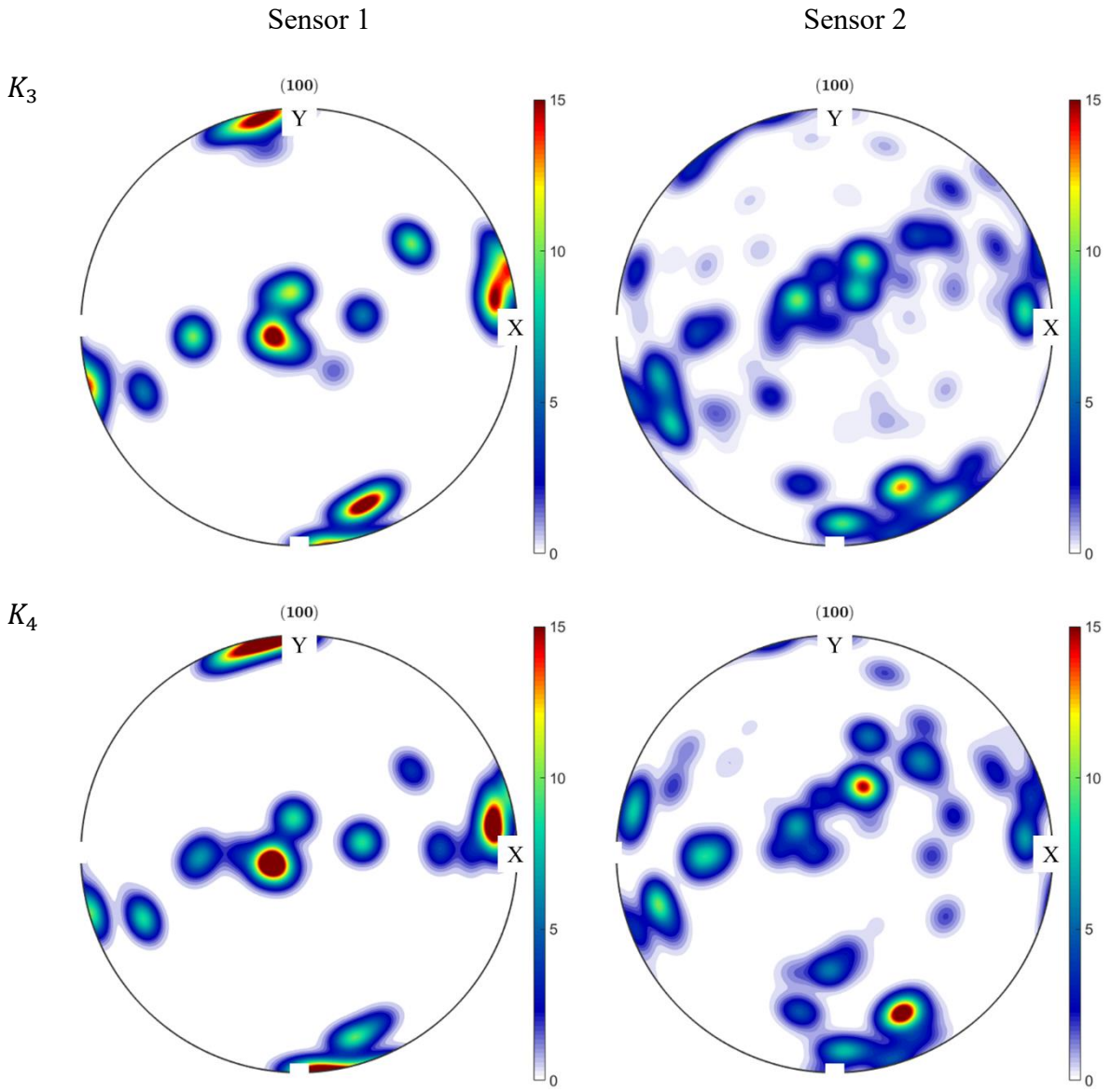

Figure 5-28. ⟨100⟩ pole figure ploted in the weld bead around sensor 1 (black rectangle in Figure 5-26) and sensor 2 (white rectangle in Figure 5-26), the normal direction of the pole figures is the $Z-$ direction.

The WYSO criterion F^{WYSO} after complete solidification ($t = 25$ s) on the plane $Z = 1$ mm for the welding configuration 20C and 20NC with dendrite kinetic law K_4 are presented in Figure 5-29. The results are quite similar with K_4 as presented in Figure 5-17, even though in the zone encompassed by black contour where the grain structures are different for the two kinetic laws. However, the F^{WYSO} computed by kinetic law K_4 is also able to distinguish the crack case and the non-crack case although the values of F^{WYSO} are always positive for both two cases.

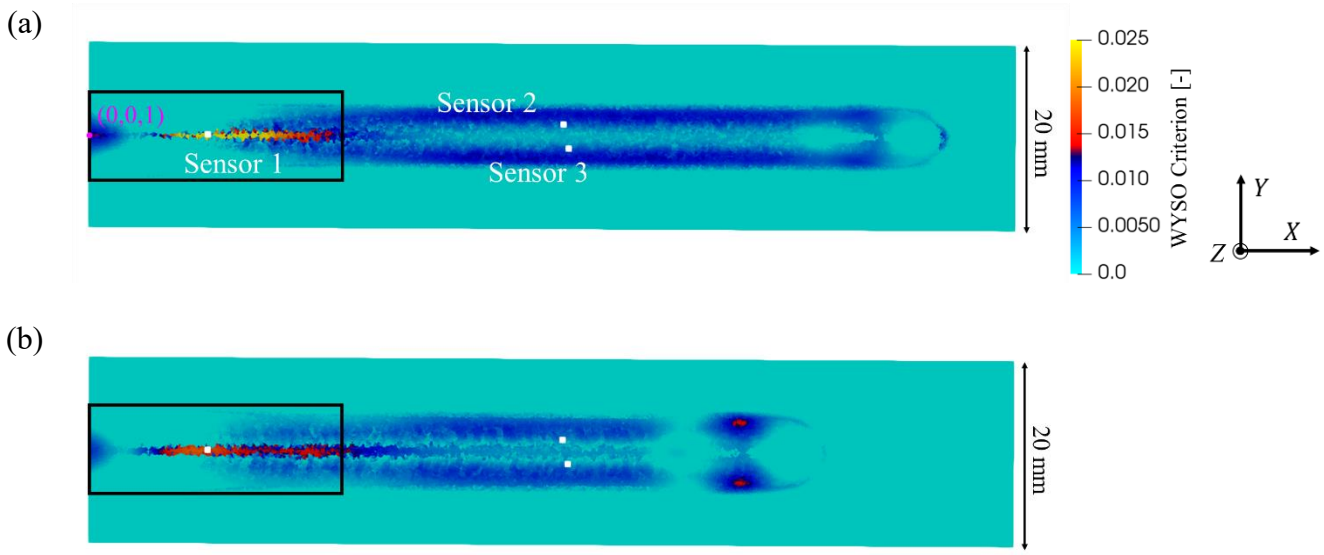

Figure 5-29. WYSO criterion with grain structure for different welding configurations in Table 5-2 after complete solidification with dendrite kinetic law K_4 in Table 5-3:
(a) 20C, (b) 20NC. On plane $Z = 1$ mm at $t = 25$ s.

The evolution of F^{WYSO} inside the BTR at the 3 sensors for the two dendrite kinetic laws are presented in Figure 5-30. Same as presented by Figure 5-29, the differences are weak. The reason could be the similarity of the microstructure as presented above. Even though the dendrite kinetic law K_4 shows an undercooling at about 70 ℃ compared to 13 ℃ for K_3, the grain structure is still very similar, leading to the weak difference of the hot cracking criterion.

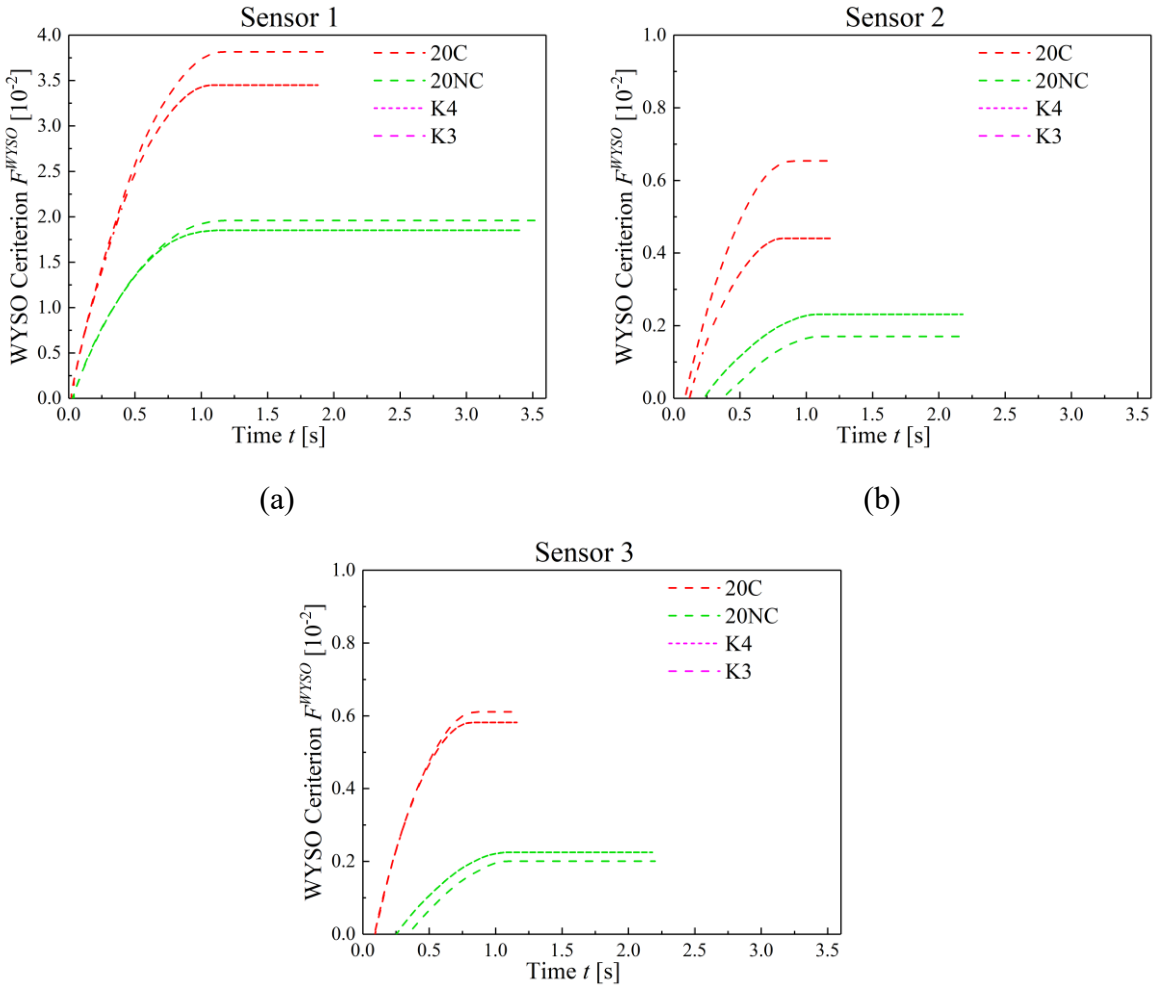

Figure 5-30. Evolution of F^{WYSO} for kinetic law K_3 and K_4 inside the BTR for welding configurations 20C and 20NC presented in Table 5-2 at the different sensor shown in Table 5-7.

This test shows the possibility to study the influence of microstructure on the hot cracking in the simulation. Even though the differences without CA are not very large, the idea could be useful to study the relation between the grain structure and hot cracking. Besides, it should be pointed out that none of these two dendrite kinetic laws is verified with observation or by comparing the grain structure (as done for chapter 3). Thus, further work is still necessary to investigate on the effet of grain structure.

5.7 Conclusions

In this chapter, computation of the hot cracking criterion is carried out on several GTAW configurations. Results show that the strain based WYSO criterion is capable to distinguish the crack and non-crack cases, as observed in the experiment. However, both crack and non-crack cases present a positive value of F^{WYSO}, meaning that the threshold of the criterion may be modified from 0. Besides, the influence of grain structure on the hot cracking criterion is introduced: the cracking plane is defined by the grain development direction calculated by the

CAFE model rather than the temperature gradient direction. Because of the similarity between these two directions, the principal results do not change significantly.
The influence of critical strain is studied. For the WYSO criterion, the change of characteristic strain rate $\dot{\hat{\varepsilon}}$ has a weak influence on F^{WYSO}, the current method as presented in equation (5-25) can be kept. Another CBC criterion reported in the literature [Bel09] is also tested. However, the large difference between the value of w_{Mn}/w_S (less than 100 in [Bel09] and 940 in this work) makes it difficult to conclude that it constitutes a better criterion for the welding process in this work. The influence of grain structure is also studied by applying another dendrite kinetic law. Weak difference is found because of the resemblance of grain structure with the two laws. Further experiments could be necessary to verify the WYSO criterion in different configuration and also verify the grain structure of the simulation with the same procedure as in chapter 3.

5.8 French summary

Dans ce chapitre, le calcul du critère de fissuration à chaud est réalisé sur plusieurs configurations GTAW. Les résultats montrent que le critère WYSO basé sur la déformation est capable de distinguer les cas fissurés et non-fissurés observés dans les expériences. Cependant, les deux cas fissurés et non-fissurés présentent tous une valeur positive de F^{WYSO}, signifiant que le seuil du critère peut être différent de 0. Par ailleurs, l'influence de la structure des grains sur le critère de fissuration à chaud est introduite: le plan de fissuration est défini par la direction de croissance ⟨100⟩ moyenne des grains la plus proche du gradient de température plutôt que par la direction du gradient thermique. En raison de la similarité entre ces deux directions, les principaux résultats du critère de fissuration à chaud ne sont pas changés.
L'influence de la déformation critique est étudiée. Pour le critère WYSO, le changement de vitesse de déformation caractéristique $\dot{\hat{\varepsilon}}$ a une faible influence sur F^{WYSO}. La méthode actuelle présentée dans l'équation (5-25) peut être conservé. Un autre critère CBC rapporté dans la littérature [Bel09] est également testé. En vu de la grande différence du rapport de w_{Mn}/w_S (inférieure à 100 dans [Bel09] et 940 dans ce travail), il est difficile de conclure à l'ontention d'un meilleur critère. L'influence de la structure des grains est également étudiée en appliquant une autre cinétique de croissance des dendrites. Une faible différence est observée en raison de la ressemblance des structures de grains.
Des expériences supplémentaires pourraient être nécessaires pour vérifier le critère WYSO dans différentes configurations et également comparer la structure des grains simulée en suivant la procédure introduite au chapitre 3.

6 Conclusions and perspectives

6.1 Conclusions

The research activities developed during this PhD focused on the development of a relevant numerical 3D model based on the Cellular Automaton – Finite Element (CAFE) method and able to simulate grain structure evolution in GTAW processes applied to stainless steel. These activities follow previous developments done at CEMEF to model microstructure evolution during welding processes. By applying the Level Set method to track the metal-gas interface, the formation of the weld beads in multi pass welding is investigated when added metal is considered, as well as the subsidence of metal plate in a fully penetrating GTAW process.
The model is enhanced by considering fluid and solid mechanics in order to make the comparison between simulation results and experimental observations in terms of microstructure evolution and hot cracking prediction.

Grain structure and melt pool shape comparison

The comparison of microstructure between simulation and experiment requires to obtain similar melt pool shape (width / length) in GTAW process. Once this is achieved, the overall grain structure and its associated texture can be well reproduced by the CA method. This result is obtained when comparing EBSD map and pole figures between simulation and experiment. A good coherence is found between grain orientation in simulation result and experimental observations.

In order to obtain the correct melt pool shape regarding experimental observations, two main points should be considered in a calibration procedure. First, the heat source model and its efficiency which have an influence on the width and the depth of the melt pool, and second, the growth undercooling at the melt pool boundary where dendritic structure develop. This latter evolution is mainly linked to the choice of the dendrite tip kinetic law. It should be mentioned that the law mainly influences the length of the melt pool (especially at rear) rather than its width.

A choice of an angular Gaussian distribution law, as developed by Desmaison [Des13], was done when investigating GTAW process without added metal (chapter 3) as applied to metal sheet. As shown in the chamfer welding configuration (chapter 4), this Gaussian distribution of heat source is not satisfying enough to get the agreement of melt pool shape compared with experiments. Thus, the elliptic heat source is then developed and applied. Better coherences in melt pool shape and temperature evolution are obtained demonstrating the relevance of this choice for application to GTAW in chamfer configuration.

Besides, in GTAW without added metal (chapter 3), the computed dendrite tip kinetic law K_2 [Hun01] based on thermodynamic databases [TCFE9, The18] for interface equilibrium and

diffusion coefficients estimation does not succeed in the prediction of the melt pool shape, which demands an adjustment of the kinetic law based on the experimental observation of melt pool shape. As shown in this work, the sole adapted kinetic law, K_1, can retrieve the melt pool shape and the grain structure for two different welding velocities. To obtain such an adapted law, the coupling scheme of CAFE model is necessary, emphasizing its importance. Furthermore, the limitation of the chaining scheme is pointed out (Figure 3-24): the grain structure computed by the CA model develops in a region where solid is already formed according to the FE solution, which can be considered as an inconsistent result between the CA and FE solutions. The coupling scheme appears consequently as a better approach.

Another point is the exploitation of experimental grain structure for the base metal initiation in the simulation, which can be considered as an improvement for the CAFE model. However, the simulated grain structure shows weak differences between the so-called texture initiation and random initiation. Further simulations could be useful to investigate the influence of initial grain structure in the simulation.

Solid mechanics and hot cracking criterion computation

In the present work, the solid mechanics resolution, as initially developed by Chen [Che18] in additive manufacturing processes modelling, is applied within the context of the welding processes. Thanks to the solid mechanics solver, stress, strain and strain rate evolution during the cooling stage can be computed and then used in the hot cracking criterion calculation. The strain based WYSO criterion [Won00] computed in this work is able to distinguish the crack and no crack cases as in the experiments [Bel09] for the fully penetration JWRI test. However, the values WYSO criterion remain positive for both crack and no crack case, meaning that a modification of the threshold value may be necessary for future applications. Besides, different expressions of critical strain are tested.

Grain structure and hot cracking

Thanks to the CAFE model, the grain structure can be considered in the computation of the hot cracking criterion when computing the direction enduring deformation. Indeed, the temperature gradient direction can be replaced by the grain development direction to define the hot cracking plane. However, no clear enhancement in cracking prediction is obtained when grain structure is considered comparing with cases without grain structure. Nevertheless, the computed criterion is still able to separate the crack and no crack welding cases obtained in experiments. The similarity between the temperature gradient direction and the grain development direction (Figure 5-19) obviously explains this observation. Besides, the simulated grain structure used in the computation of the hot cracking criterion has not been verified by some experimental observations, which could also lead to uncertainties on the computed WYSO criterion applied with grain structure. At least, the feasibility of the consideration of grain structure in the WYSO criterion is proved in this work. In addition, it should be emphasized that applications of hot cracking prediction were not presently dedicated to the results associated to NEMESIS

experimental activities as obtained by partners. Future applications could be consequently foreseen regarding some current developments done at ICB.

Fluid mechanics

The consideration of fluid mechanics in the FE resolution allows the simulation of fluid flow inside the melt pool and the estimation of the subsidence due to the fully penetrated welding configuration compared with experimental observation. Besides, same order of magnitude for fluid flow velocity between simulation and experiment inside the melt pool is obtained (Table 3-8). However, because of some numerical difficulties in the monolithic FE resolution (equation 2-60), an increased viscosity of the liquid metal and the surrounding air is used in this work. This choice causes an underestimation of the fluid flow velocity in the simulation.

6.2 Perspectives

Considering the conclusions presented above, other research activities could be useful to obtain more substantial results and enhance predictions proposed in GTAW welding simulation. These activities would also correspond to future developments associated to the modelling of fusion welding processes.

Grain structure and kinetic law

The present CAFE model is only dedicated to investigate the grain structure evolution inside the weld bead, while the grain structure coarsening in the heat affect zone is observed (Figure 3-14) also as reported in the literature [Elm00, Elm03]. This phenomenon is not considered presently. The simulation of this phenomenon could be necessary for the future comparison of grain structure between simulation and experiment and the enhancement of the CAFE methods. By the way, this simulation is already achieved by using the 3D Monte Carlo method [Yan00] or the Potts model [Rod16, Rod21], which could also be foreseen in the CAFE model.

Another point is the computed dendrite tip kinetic law based on thermodynamic coupling, K_2, that is not satisfying for the quantitative prediction of grain structure. One possible solution is to take into consideration the rapid solidification phenomenon as presented in equation (1-4) which is neglected in this work. In addition, rapid fusion welding processes (*e.g.* laser welding) may also benefit from such evolution. Moreover, the development of relevant kinetic law is necessary for future comparisons with dedicated experiments.

Solid mechanics and hot cracking criterion computation

In the present work for solution of solid mechanics equations (chapter 4 \ GTAW with added metal), the deformation of the weld part after solidification (as shown in Figure 4-8) is not considered and simulated even though the simulation utilities already exist [Che18, Zha20]. The reason is that the main aim of this chamfer configuration was to provide a stable grain

structure compared with the experimental observation of the industrial partners. The chamfer deformation and its importance were only observed after some discussion. In addition, the CAFE model does not consider possible deformation of metal in microstructure modelling and the induced transportation of information between cells. The consideration of this deformation would be surely an asset to enrich the comparison between simulations and experiments. Furthermore, the consideration of this deformation can lead to a more fixed heat source model using identical parameters for the multi pass welding stages. This point is not assumed in present results, as shown previously. Indeed, heat source parameters are changed between passes to calibrate the variation caused by the chamfer deformation (chapter 4.4.1). Besides, the quantitative prediction of grain structure for the complex chamfer configuration can also be improved.

Regarding the computation of hot cracking criterion, both crack and no crack cases present the positive value of WYSO criterion, meaning that the threshold of hot cracking may be modified. To achieve this objective, more welding configurations should be applied, on the one hand to validate the WYSO criterion with more experimental cases and on the other hand to find the threshold conditions leading to crack development (i.e. threshold values) also considering materials properties.

Grain structure and hot cracking

The influence of the grain structure on the computing of the hot cracking criterion is not clearly observed in the present work despite numerical development. Consequently, in future applications, the CAFE structure associated to simulations dedicated to WYSO criterion should be compared with experimental observations. Some procedures presented in chapter 3 or 4 (e.g. in-situ observations or melt pool size measurement) should be thereafter applied to obtain the reliable grain structure and provide better understanding on the influence of grain structure. In such cases, the hot cracking criterion could be computed based on the obtained grain structure and would certainly provide a better understanding on its influence.
Another point is consideration of the grain structure for the constitutive law, which means an anisotropic law at the grain scale. A such law could consider the hot cracking on the grain boundary.

Besides all the perspectives mentioned above for the welding process, the results of the NEMESIS research activity could also be applied in other domains of material research.

Fluid mechanics

In the present project, increased values of liquid metal and gas viscosities were used due to numerical difficulties. Some improvement could be obtained by considering Darcy terms [Aal20, Zha19-2] when solving the momentum conservation equation (equation (2-60)) dedicated to the sole fluid phases. In such condition, no solid viscosity is required as no fluid flow is assumed in the solid region as Darcy term vanishes the fluid velocity. However, the

consideration of Darcy term takes more than 10 times the current simulation time in tests developed in present simulation cases. which makes impossible to lauch nearly 30 simulations to calibrate the heat source parameters (aperture angle, efficiency, etc.) and to fix the dendrite tip kinetic law. Another possible solution is to decrease the difference between the viscosity of solid metal and liquid metal. This approach demands also to launch a large number of simulation. Despite some tests deveveloped at the end of the project until the redaction of the manuscript, no better result were found. However some clear improvements are required in the present model in order to obtain more relevant estimation of fluid flow evolution in the weld pool.

Application of present model on additive manufacturing

Regarding the similarity between manufacturing processes, the CAFE model applied in the welding process could also be carried out for the additive manufacturing process. Besides, the hot cracking during additive manufacturing as reported in the literature [Han20, Che16-2] can be also investigated by the WYSO criterion as done in NEMESIS. In fact, the FE modelling of the LPBF (Laser Powder Bed Fusion) process is well developed by Chen [Che18] and experimentally verified when applied to metallic material (nickel-based alloy) by Queva [Que21]. The coupling to CA model and the study of hot cracking during additive manufacturing would be possible based on all these developments and may correspond to relevant applications.

Application of simulated grain structure on NDT simulation

The simulated grain structure should also be used as an input data of the NDT simulation software (CIVA\Athena) in order to simulate and provide better understanding of the interactions between ultrasonic wave and grain structures. This point corresponds to one of the initial objectives of the NEMESIS project. It is regretful that during the NEMESIS project, limited ultrasonic waves simulations were carried out by the industrial partners on the cases of interest (chamfer configuration) as (Figure 7). However, the simulated grain structure is still useful in the investigation of ultrasonic wave interactions and some applications are expected before the end of the NEMESIS project.

Appendix 1 Grain structure analyses tools

1 Reconstruction of grain structure after welding

The result of grain structure simulations (Figure 1) is necessary to simulate the wave-structure interaction in NDT tools. A file containing this result in a readable format accessible to NDT simulation software is also requested by the industrial partners (EDF, CEA). However, several problems exist to satisfy this demand:

- The present result of CAFE model are included in several .vtu format files (each file corresponds to the cells activated in a time step because of the dynamic allocation),
- These files are not readable by the NDT simulation software,
- A large number of cells are represented (31 640 625 cells in Figure 1 (a)) including cells in the base metal,
- The simulation must be restricted to a reduced domain, for the NDT simulation based on the wave / structure interaction.

Therefore, a new method to reconstruct the grain structure is necessary. Section 2.5.1 presents the storage of the initial grain structure. This file evolves during welding simulation and corresponds to the registered grain structure at a current time. Consequently, the grain structure after welding and complete solidification is similarly registered in the same binary file. Thanks to this file, the reconstruction of the grain structure is made possible. We consider hereafter a simple 3D GTAW process without adding material as presented in Chen [Che14] (Table 1):

Table 1. Parameter of GTAW in 3D.

Parameter	Value
FE (welding) domain $(x \times y \times z, \mathrm{mm})$	$350 \times 150 \times 12$
CA domain $(x \times y \times z, \mathrm{mm})$	$180 \times 60 \times 12$
Initial FE mesh size (mm)	5
CA mesh size (mm)	3
Welding speed $(\mathrm{mm\ s^{-1}})$	2
Heat source power (W)	7500
Kinetic tip law $(\mathrm{mm\ s^{-1}})$	$v^{\langle 100 \rangle} = 10^{-7}\Delta T^2$

The binary file is read after the simulation of welding process in order to reconstruct a file readable by NDT software as corresponding to the require data organization. This file may correspond to a part of interest of the entire grain structure dedicated to NDT analysis. The cells inside the user defined domain (usually a box in 3D and a square in 2D) will be selected and

their information (Euler angle) will be written in a ‘vti’ file. Figure 1 presents the grain structure of the 3D GTAW simulation. With the reconstruction method, the result can be focused on the sole weld bead to register the cell state in the vti file. The grain structure inside the box can also, consecutively, be analyzed. The advantages of the reconstruction method are the following:

- The result (Figure 1 (b)) is contained in a single vti file visualized on Paraview software,
- This file format corresponds to the need for ATHENA's NDT simulation software (EDF),
- An area of interest can be chosen by user to focus on the sole weld bead,
- The number of cells analyzed is reduced (4 668 750 cells in Figure 1 (b) compared to 31 640 625 cells in Figure 1 (a)),
- The result contains the structure inside the weld bead which allows the plan section to generate thereafter 2D presentations,
- Statistical analyzes of grains in the area of interest is made possible (section 2)

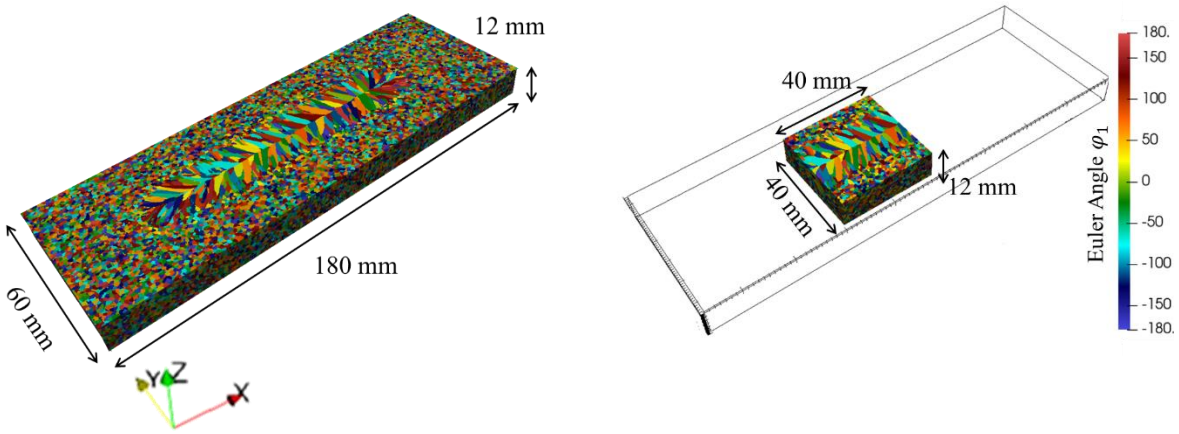

(a) (b)

Figure 1. Simulation of grain structure for 3D GTAW (a) Superposition of result images after reading of the output .vtu files, (b) Reconstruction of the .vti file in the weld bead. Box dimension are provided. The black contour in (b) corresponds to the whole (a) domain.

2 Grain statistical analyses

The reconstruction of the grain structure is made possible to achieve the statistical analyzes in the weld bead (box shown in Figure 1 (b)). The output of the statistical analyses is defined for each grain $\boldsymbol{G}$ as detailed in the following list. Besides, the pole figures (for a 3D structure) can also be obtained corresponding to the defined box. These statistical analyses can also serve to the NDT software to simplify the simulation.

Grain size: Each grain is associated to a group of cells. Hence, the grain size is simply computed by the total number of cells in the grain multiplying the cell volume (cell surface in 2D).

Grain barycenter: The grain barycenter is computed based on the coordinates of cells located inside the grain and presented in a vector form:

$$\boldsymbol{OG^G} = \frac{1}{N_c^G}\sum_{\boldsymbol{\nu}\in G}\boldsymbol{OC_\nu} \tag{1}$$

with O is space origin and C_ν the center of cell ν. N_c^G is the total number of cells in grain $\boldsymbol{G}$.

Main direction (morphological direction): The principle is firstly to find an ellipsoid which encompasses the grain. The main directions of the calculated ellipsoid are then considered as the main directions of grain $\boldsymbol{G}$. We consider the group, Π^G, of all the cell centers associated to grain Π^G

$$\Pi^G = [C_\nu]^T, \nu \in G \tag{2}$$

Then the covariance matrix $\boldsymbol{\mathcal{M}_C^G}$ is defined as:

$$\boldsymbol{\mathcal{M}_C^G} = \begin{bmatrix} Cov(x_{C_\nu}, x_{C_\nu}) & Cov(x_{C_\nu}, y_{C_\nu}) & Cov(x_{C_\nu}, z_{C_\nu}) \\ Cov(y_{C_\nu}, x_{C_\nu}) & Cov(y_{C_\nu}, x_{C_\nu}) & Cov(x_{C_\nu}, z_{C_\nu}) \\ Cov(z_{C_\nu}, x_{C_\nu}) & Cov(z_{C_\nu}, y_{C_\nu}) & Cov(z_{C_\nu}, z_{C_\nu}) \end{bmatrix}, \nu \in G \tag{3}$$

Finally, the eigenvectors of the matrix $\boldsymbol{\mathcal{M}_C^G}$ are assumed as the main directions of the grain $\boldsymbol{G}$.

Feret diameters: Once the main directions are computed, the associated Feret diameters can be calculated as corresponding to the grain elongation in each eigenvector direction considering as *main* directions. For one of the three main directions, the dot product of the vector associated to the cell center belonging to grain $\boldsymbol{G}$ and the normalized eigenvector is made. The value of this dot product presents the projection of cell center along the main direction. Finally, the distance between the maximum and minimum projections provides the Feret diameter along this direction.

Pole figure (3D only): The pole figure is defined using Euler angles. A transfer matrix P_{C2G} as given in equation (5-27 and 5-28) is constructed as associated to the Euler angles. Then the vectors [1 0 0], [$\bar{1}$ 0 0], [0 1 0], [0 $\bar{1}$ 0], [0 0 1]and [0 0 $\bar{1}$] (direction <100>) in the crystal frame of reference are transferred into the global frame of reference using P_{C2G} matrix. These 6 new vectors produce 6 points of intersection with the unit sphere in the global frame of reference, and the projection in the direction defined by the interaction of the unit sphere of the vector <100> and the south pole (X <0) of these 3 points of intersection in the plane X = 0 presents the pole figure for this grain.

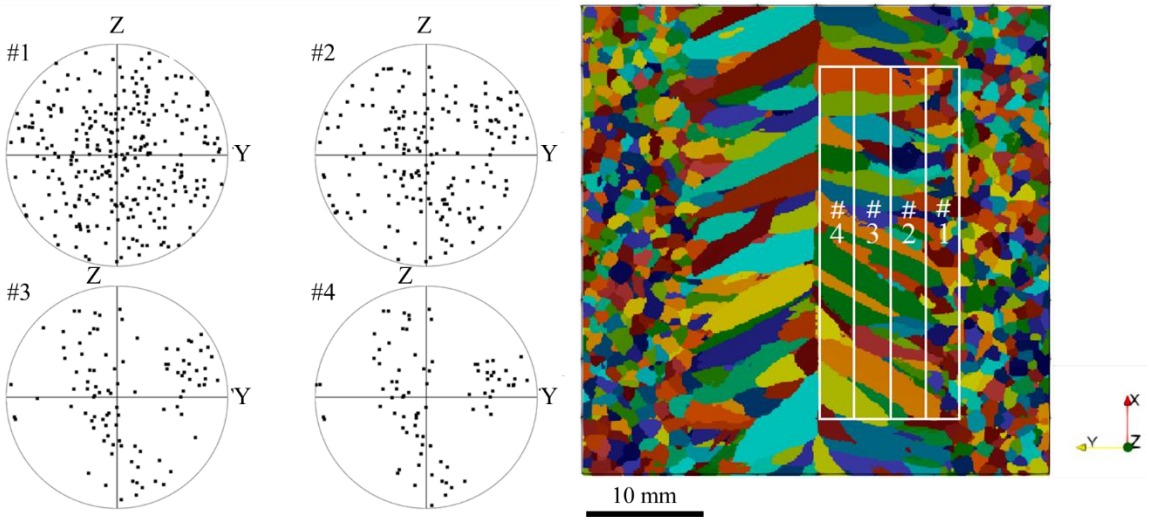

(a) (b)

Figure 2. Analysis of the grain structure by (a): pole figure with different distances to the weld bead identified by (b): number boxes # 1 to # 4.

Figure 2 (a) shows the pole figures for the different areas highlighted by the rectangles in Figure 2 (b) for the top surface of the weld bead presented in Figure 2 (b). The direction of these pole figures corresponds to the welding direction *X*. Zone #1 is located in the base metal region, containing equiaxed grains. Therefore, the points plotted in Figure 2 (a) #1 are associated to a random grain orientation, revealing the initial homogeneous grain structures. However, the points in Figure 2 (a) #2 shows specific orientation. This is due to competition of grain growth in zone (#2). As the selection mechanism is more advanced, with a lower number of grains, in zone (#3), the points are grouped as shown in Figure 2 (a) #3. In addition, the points associated to area (#4) becomes more condensed in Figure 2 (a) #4 due to the advancement of the selection mechanism. The remaining grains have the selected direction <100> gather in a limited angular region. Note that only the south pole figure (***X*** direction) is presented previously, other pole figures are also made accessible in the same simulation tool.

Appendix 2 Modeling of ellipse heat source

In this appendix, the expression of ellipse heat source will be presented in detail, including the expression $\dot{Q}_P$

$$\dot{Q}_P = \frac{\dot{Q}_{Plasma}}{d^2\, F_p}\cos\gamma \tag{1}$$

$$\begin{aligned} F_p = {} & 2\pi\big(1-\cos(\alpha_X)\big) + \pi(\alpha_Y-\alpha_X)\sin(\alpha_X) \\ & -\frac{\pi(\alpha_Y-\alpha_X)^2}{96\cos(\alpha_X)}\big((\alpha_Y-\alpha_X)(\cos(2\alpha_X)-5) \\ & +6\sin(2\alpha_X)\big)\tan(\alpha_X) \end{aligned} \tag{2}$$

with α_X and α_Y the aperture angle of the ellipse along the welding direction (X) and the perpendicular direction (Y).

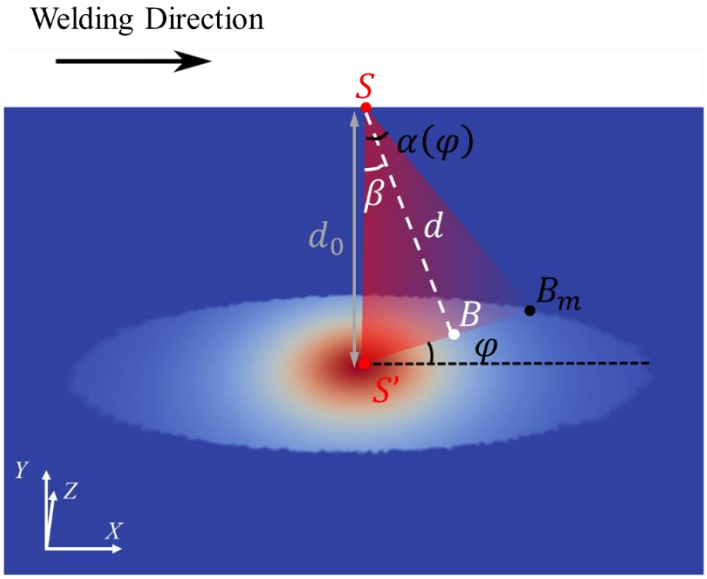

Figure 1. 3D presentation of ellipse heat source.

As shown in Figure 1, S is the position of the heat source with a distance d_0 from the metal surface. S' is the projection of heat source S on the metal surface plan (plan XY here). B is the considered point on the metal surface, with β the angle between the heat source and SB. In Figure 1, B_m locating at the boundary of the ellipse corresponds to the aperture angle $\alpha(\varphi)$ (maximum value of angle β) who itself is in function of φ, the angle between $S'B$ and the welding direction. To simplify the problem, $\varphi \in [0, \pi/2]$ is firstly considered because of the symmetry property of ellipse. It could be noted that $\alpha_X = \alpha(\varphi = 0)$, $\alpha_Y = \alpha(\varphi = \pi/2)$.
To modeling the ellipse shape, the first step is computing the aperture angle $\alpha(\varphi)$.

$$\alpha(\varphi) = \arctan\left(\frac{S'B_m}{d_0}\right) \tag{3}$$

In the parametric representation, the coordinate of point B_m is

$$B_m(x, y) = (a\sin t, b\cos t) = (d_0\tan(\alpha_X)\sin t, d_0\tan(\alpha_Y)\cos t) \tag{4}$$

Then $S'B_m$ can be expressed as:

$$S'B_m = \sqrt[2]{{d_0}^2\tan^2(\alpha_X)\sin^2 t + {d_0}^2\tan^2(\alpha_Y)\cos^2 t} \tag{5}$$

The next step is to express the parameter t in parametric representation by φ.

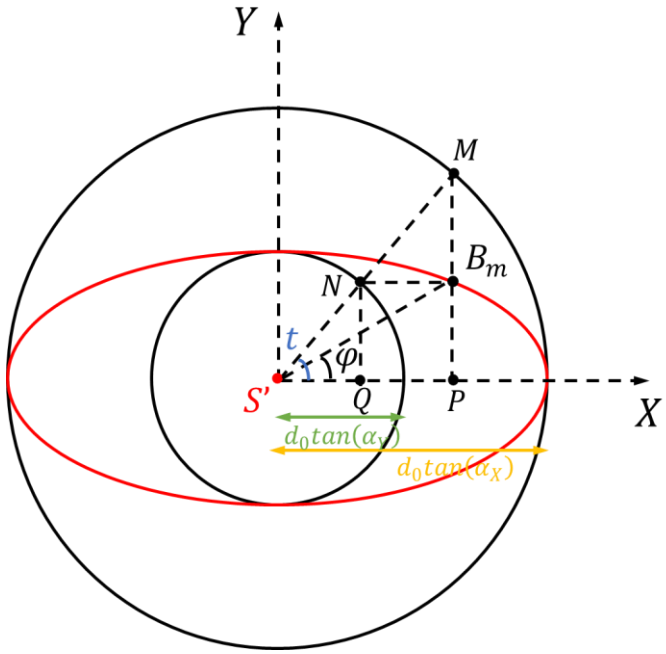

Figure 2. 2D parametric representation of ellipse.

As presented in Figure 2:

$$\tan(t) = \frac{MP}{S'P} \tag{6}$$

$$\tan(\varphi) = \frac{B_mP}{S'P} = \frac{NQ}{S'P} \tag{7}$$

And

$$\frac{NQ}{MP} = \frac{d_0\tan(\alpha_Y)}{d_0\tan(\alpha_X)} = \frac{\tan(\alpha_Y)}{\tan(\alpha_X)} \tag{8}$$

So

$$\tan(t) = \tan(\varphi)\frac{\tan(\alpha_X)}{\tan(\alpha_Y)} \tag{9}$$

By combining equation (3),(5) and (9):

$$\alpha(\varphi) = \arctan\left(\sqrt{\frac{1}{\cot^2(\alpha_Y) + \cos^2(\varphi)\left(\cot^2(\alpha_X) - \cot^2(\alpha_Y)\right)}}\right) \tag{10}$$

Considering the heat source for energy conservation:

$$\dot{Q}_{Plasma}\cos\gamma = 4\int_0^{\frac{\pi}{2}}\int_0^{\alpha(\varphi)} \dot{Q}_P\, d\, \sin(\beta)\, d\, d\beta\, d\varphi \tag{11}$$

And

$$\int_0^{\alpha(\varphi)} \dot{Q}_P\, d\, \sin(\beta)\, d\, d\beta = 1 - \frac{1}{\sqrt[2]{1 + \frac{1}{\cot^2(\alpha_Y) + \cos^2(\varphi)\left(\cot^2(\alpha_X) - \cot^2(\alpha_Y)\right)}}} \tag{12}$$

This term is too complicated to compute the second integer of angle φ, which leads to a limit development at $\alpha_X \to \alpha_Y$. In fact, in the simulation, α_X is close to α_Y, the value chosen is $\alpha_X = 70°$ and $\alpha_Y = 50°$, in radius, the difference is 0.35.
The result of limit development in third order is:

$$\begin{aligned}
&\int_0^{\alpha(\varphi)} \dot{Q}_P\, d\, \sin(\beta)\, d\, d\beta = \\
&\left(4 - 4\cos(\alpha_X)\right) + 4\sin(\alpha_X)\sin^2(\varphi)(\alpha_Y - \alpha_X) \\
&-2\left(\cos(\alpha_X)\sin^2(\varphi)\left(-1 + \cos^2(\varphi)\left(4 + \tan^2(\alpha_X)\right)\right)\right)(\alpha_Y - \alpha_X)^2 \\
&+\frac{2}{3}\cos(\alpha_X)\cot(\alpha_X)\sin^2(\varphi)\Big(-\tan^2(\alpha_X) \\
&\qquad - 3\cos^2(\varphi)\left(4 + \tan^2(\alpha_X) + \tan^4(\alpha_X)\right) \\
&\qquad + 3\cos^4(\varphi)\left(8 + 4\tan^2(\alpha_X) + \tan^4(\alpha_X)\right)\Big)(\alpha_Y - \alpha_X)^3 \\
&\qquad + O(\alpha_Y - \alpha_X)^4
\end{aligned} \tag{13}$$

And the second integer of angle φ gives:

$$\begin{aligned}
\dot{Q}_{Plasma}\cos\gamma = \dot{Q}_P d^2\Bigg(&2\pi\left(1 - \cos(\alpha_X)\right) + \pi(\alpha_Y - \alpha_X)\sin(\alpha_X) \\
&- \frac{\pi(\alpha_Y - \alpha_X)^2}{96\cos(\alpha_X)}\left((\alpha_Y - \alpha_X)(\cos(2\alpha_X) - 5)\right. \\
&\left.+ 6\sin(2\alpha_X)\right)\tan(\alpha_X)\Bigg)
\end{aligned} \tag{14}$$

The expression of equation (1) and (2) is found.

Appendix 3 EBSD maps of the grain structure

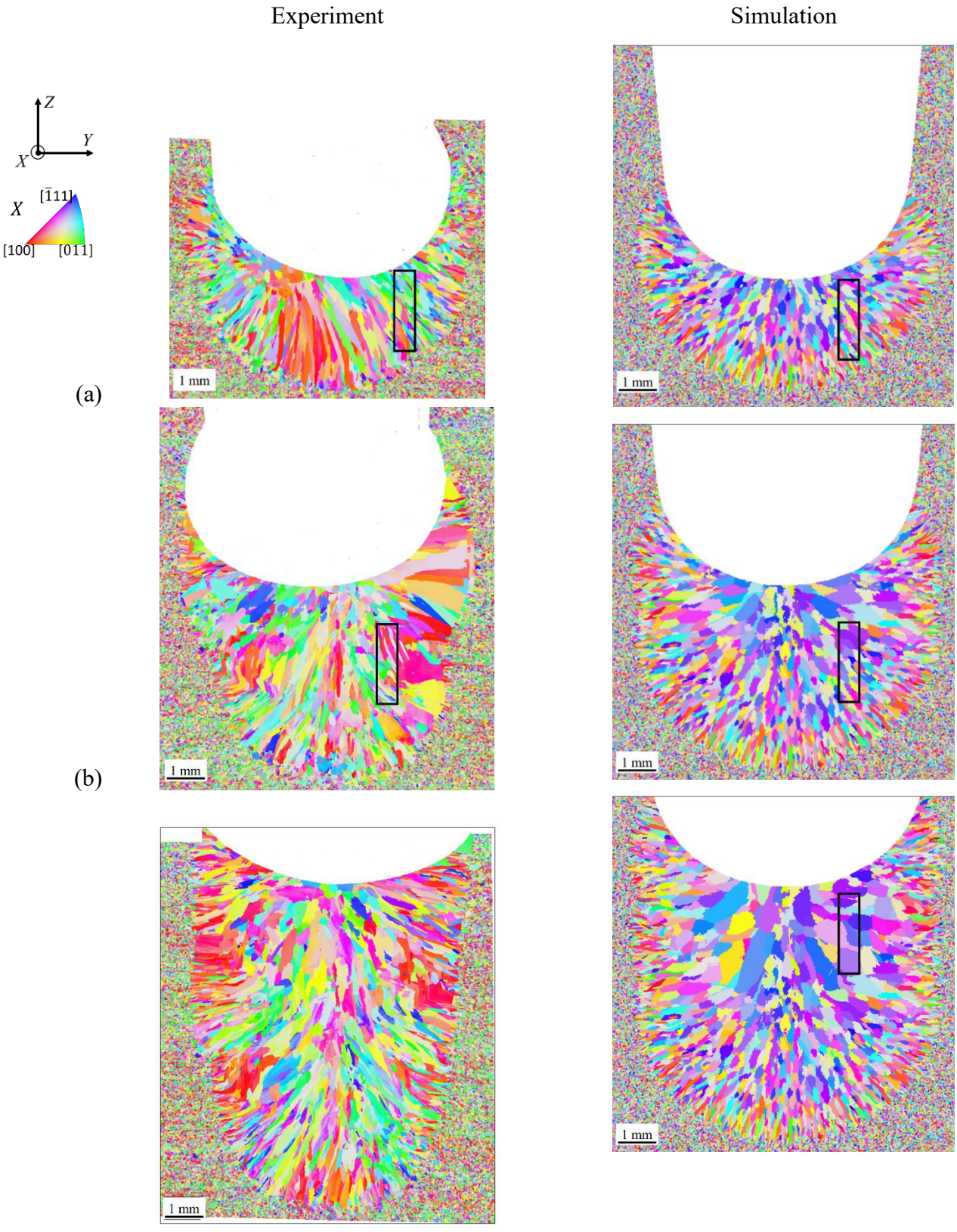

Figure 1. EBSD maps of the grain structure on $X = 65$ mm (left) measured and (right) simulated with the CAFE model. The inverse pole figure color codes for X direction respect to the (a) pass 1, (b) passe 2 and (c) pass 3.

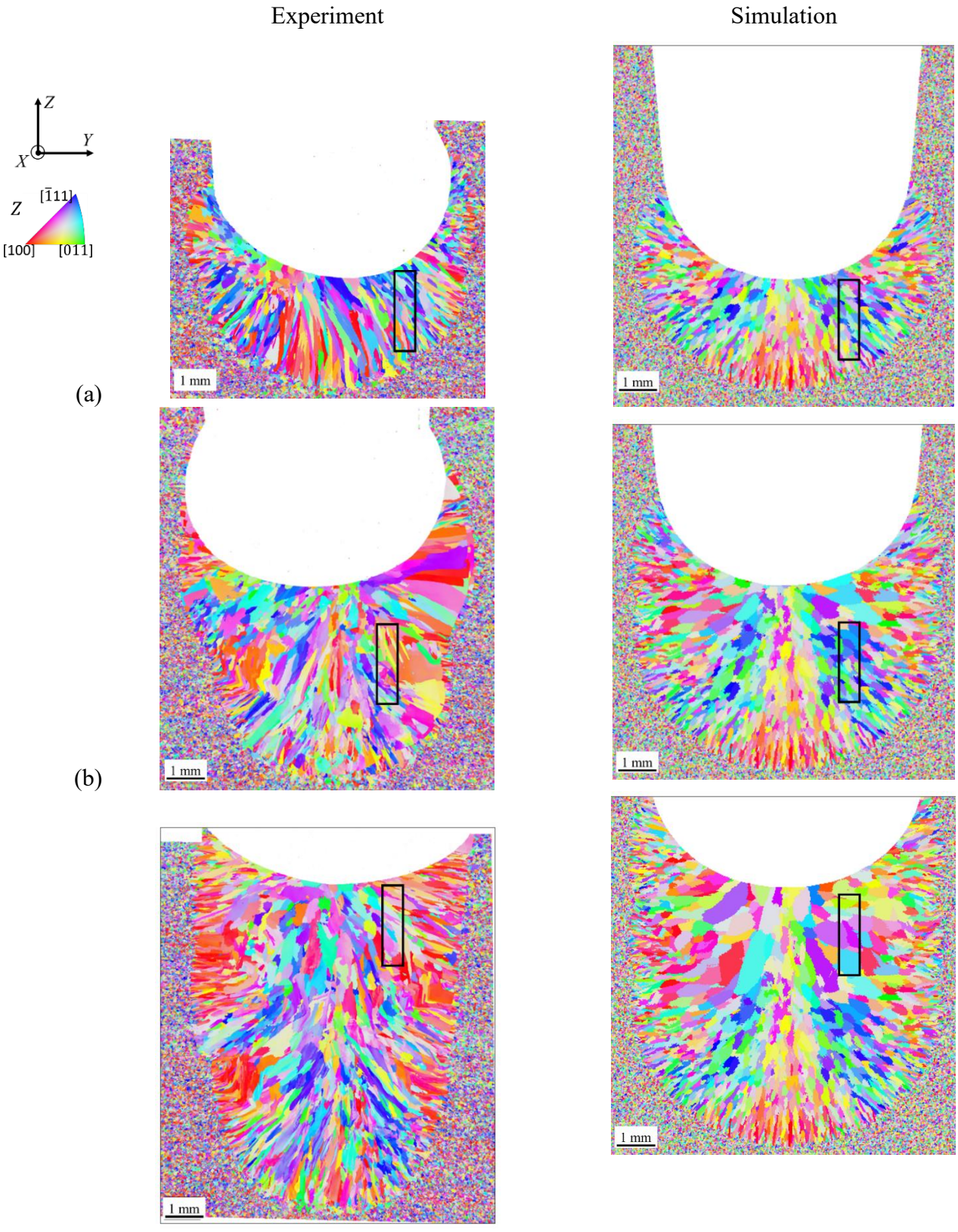

Figure 2. EBSD maps of the grain structure on $X = 65$ mm (left) measured and (right) simulated with the CAFE model. The inverse pole figure color codes for Z direction respect to the (a) pass 1, (b) passe 2 and (c) pass 3.

Appendix 4 Mechanic parameters for AISI 321 [Cer07]

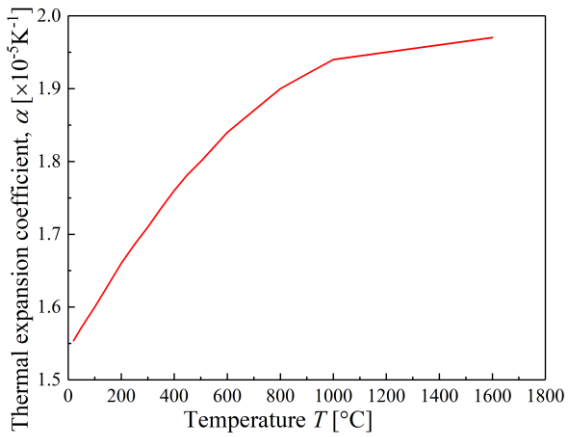

Figure 1. Thermal expansion coefficient α of the AISI 321.

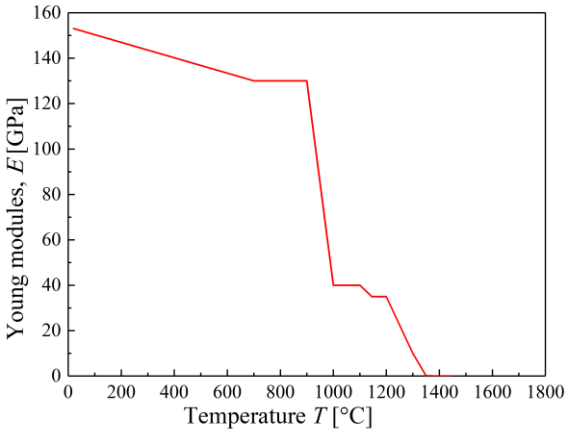

Figure 2. Young modules E of the AISI 321.

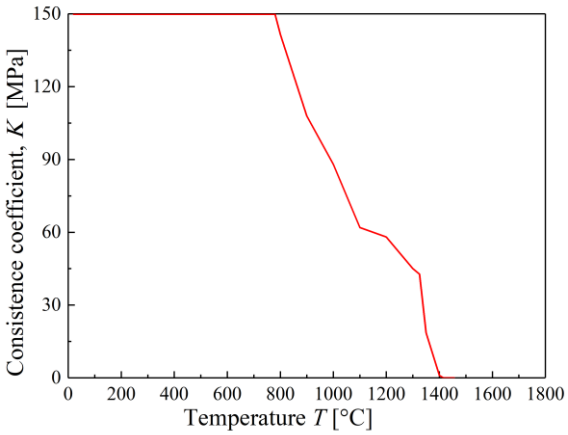

Figure 3. Consistence coefficient K of the AISI 321.

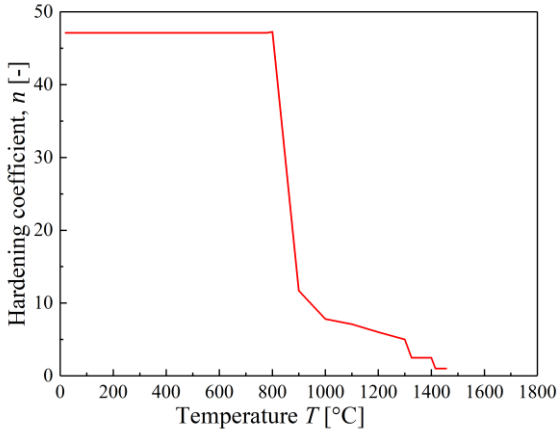

Figure 4. Hardening coefficient n of the AISI 321.

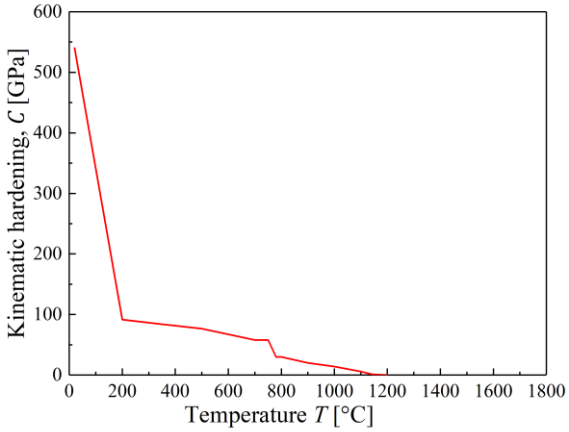

Figure 5. Kinematic hardening parameter C of the AISI 321.

Reference

[Aal20] Aalilija, A., Gandin, Ch.-A., & Hachem, E. (2020). On the analytical and numerical simulation of an oscillating drop in zero-gravity. Computers & Fluids, 197, 104362.

[Adi18] Adiban, S V., Ramu, M. Study on the effect of weld defects on fatigue life of structures[J]. Materials Today: Proceedings, 2018, 5(9): 17114-17124.

[Ahs16] Ahsan, M. R., Kim, Y. R., Kim, C. H., Kim, J. W., Ashiri, R., & Park, Y. D. (2016). Porosity formation mechanisms in cold metal transfer (CMT) gas metal arc welding (GMAW) of zinc coated steels. Science and Technology of Welding and Joining, 21(3), 209-215.

[AISI] American Iron and Steel Institute. "Design Guidelines for the Selection and Use of Stainless Steel". https://nickelinstitute.org/media/1667/designguidelinesfortheselectionanduseofstainlesssteels_9014_.pdf

[Al-R02] Al-Rawahi, N., & Tryggvason, G. (2002). Numerical simulation of dendritic solidification with convection : Two-dimensional geometry. Journal of computational physics, 180(2), 471–496.

[Al-R04] Al-Rawahi, N., & Tryggvason, G. (2004). Numerical simulation of dendritic solidification with convection : Three-dimensional flow. Journal of Computational Physics, 194(2), 677–696.

[All21] Allan, D. B., Caswell, T., Keim, N. C., van der Wel, C. M., & Verweij, R. W. (2021). soft-matter/trackpy: Trackpy v0.5.0. Zenodo.

[Amm14] Ammer, R., Markl, M., Ljungblad, U., Körner, C., Rüde, U. (2014). Simulating fast electron beam melting with a parallel thermal free surface lattice Boltzmann method. Computers & Mathematics with Applications, 67(2), 318-330.

[Ara73] Arata, Y., Matsuda, F., Mukae, S., & Katoh, M. (1973). Effect of weld solidification mode on tensile properties of aluminum weld metal. Transactions of JWRI, 2(2), 184–190.

[Bel09] Bellet, M., Cerri, O., Bobadilla, M., Chastel, Y. (2009). Modeling hot tearing during solidification of steels: assessment and improvement of macroscopic criteria through the analysis of two experimental tests. Metallurgical and Materials Transactions A, 40(11), 2705-2717.

[Bel13] Bellet, M., & Hamide, M. (2013). Direct modeling of material deposit and identification of energy transfer in gas metal arc welding. International Journal of Numerical Methods for Heat and Fluid Flow, 23, 1340-1355.

[Bel16] Bellet, M., Qiu, G., Carpreau, J. M. (2016). Comparison of two hot tearing criteria in numerical modelling of arc welding of stainless steel AISI 321. Journal of Materials Processing Technology, 230, 143-152.

[Bla20] Blanc, N., Bendaoud, I., Bordreuil, C., Deschaux-Beaume, F., Rouquette, S., & Soulié, F. (2020). Observations in-situ des mouvements du bain de fusion et des

mécanismes de solidification au cours de ligne de fusion TIG [Research Report]. Laboratoire de Mécanique et Génie Civil. https://hal.archives-ouvertes.fr/hal-02957986

[Bla21] Blanc, N., Soulié, F., Bendaoud, I., Rouquette, S., Deschaux-Beaume, F., & Bordreuil, C. (n.d.). Fluid flow measurements in fully penetrated 316L TIG welding. Science and Technology of Welding and Joining, 2021.

[Bob88] Bobadilla, M., Lacaze, J., & Lesoult, G. (1988). Influence des conditions de solidification sur le déroulement de la solidification des aciers inoxydables austénitiques. Journal of Crystal Growth, 89(4), 531-544.

[Boe02] Boettinger, W. J., Warren, J. A., Beckermann, C., & Karma, A. (2002). Phase-field simulation of solidification. Annual review of materials research, 32(1), 163–194.

[Bou13] Bouffier, L. (2013). Modélisation de la fissuration à chaud lors du soudage de l'alliage base nickel IN600 (PhD thesis, Université de Grenoble).

[Bra92] Brackbill, J. U., Kothe, D. B., & Zemach, C. (1992). A continuum method for modeling surface tension. Journal of Computational Physics, 100(2), 335-354.

[Bra00] Braccini, M. (2000). Optimisation des pièces moulées: étude des phénomènes de fissuration à chaud dans les alliages Al-Cu (Doctorat , Grenoble INPG).

[Bro78] Brooks, J. A., & Lambert Jr, F. J. (1978). The effects of phosphorus, sulfur and ferrite content on weld cracking of type 309 stainless steel. Welding Journal, 51(5).

[Cam19] Camus, T. (2019). Modélisation des microstructures générées en fabrication additive par fusion laser sélective d'un alliage base nickel [These en préparation, Université Paris sciences et lettres].

[Car95] Cartaud, D. (1995). Essais de fissuration à chaud : Principes et critères d'application. Soudage et techniques connexes, 49(9-10), 17–28.

[Car12] Carozzani, T. (2012). Développement d'un modèle 3D Automate Cellulaire-Éléments Finis (CAFE) parallèle pour la prédiction de structures de grains lors de la solidification d'alliages métalliques (PhD thesis, Ecole Nationale Supérieure des Mines de Paris).

[Car11] Carozzani, T., Digonnet, H., & Gandin, C.-A. (2011). 3D CAFE modeling of grain structures : Application to primary dendritic and secondary eutectic solidification. Modelling and Simulation in Materials Science and Engineering, 20(1), 015010.

[Cer07] Cerri, O. (2007). Rupture à chaud dans les aciers au cours de leur solidification: Caractérisation expérimentale et modélisation thermomécanique [Phdthesis, École Nationale Supérieure des Mines de Paris].

[Cha09] Chassignole, B., Duwig, V., Ploix, M.-A., Guy, P., & El Guerjouma, R. (2009). Modelling the attenuation in the ATHENA finite elements code for the ultrasonic testing of austenitic stainless steel welds. Ultrasonics, 49(8), 653-658.

[Che02] Chen, Q., & Sundman, B. (2002). Computation of partial equilibrium solidification with complete interstitial and negligible substitutional solute back diffusion. Materials Transactions, 43(3), 551–559.

[Che02-2] Chen, L.-Q. (2002). Phase-field models for microstructure evolution. Annual review of materials research, 32(1), 113–140.

[Che14] Chen, S. (2014). Three dimensional Cellular Automaton–Finite Element (CAFE) modeling for the grain structures development in Gas Tungsten/Metal Arc Welding processes(PhD thesis, Ecole Nationale Supérieure des Mines de Paris).

[Che14-2] Chen, S., Guillemot, G., & Gandin, C.-A. (2014). 3D Coupled Cellular Automaton (CA)-Finite Element (FE) Modeling for Solidification Grain Structures in Gas Tungsten Arc Welding (GTAW). ISIJ INTERNATIONAL, 54(2, SI), 401-407.

[Che16] Chen, S., Guillemot, G., & Gandin, C.-A. (2016). Three-dimensional cellular automaton-finite element modeling of solidification grain structures for arc-welding processes. Acta Materialia, 115, 448-467.

[Che16-2] Chen, Y., Lu, F., Zhang, K., Nie, P., Elmi Hosseini, S. R., Feng, K., & Li, Z. (2016). Dendritic microstructure and hot cracking of laser additive manufactured Inconel 718 under improved base cooling. Journal of Alloys and Compounds, 670, 312–321.

[Che17] Chen, Q., Lin, S., Yang, C., Fan, C., & Ge, H. (2017). Grain fragmentation in ultrasonic-assisted TIG weld of pure aluminum. Ultrasonics Sonochemistry, 39, 403–413.

[Che18] Chen, Q. (2018). Modélisation numérique thermomécanique de fabrication additive par fusion sélective de lit de poudre par laser : Application aux matériaux céramiques [These de doctorat, Paris Sciences et Lettres (ComUE)].

[Che19] Chen, S., Ye, X. X., Tsang, D. K. L., Jiang, L., Yu, K., Li, C., Li, Z. (2019). Welding solidification cracking susceptibility and behavior of a Ni-28W-6Cr alloy. Journal of Materials Science & Technology, 35(1), 29-35.

[Che20] Chen, L., Wei, Y., Qiu, S., & Zhao, W. (2020). Macro–Micro Scale Modeling and Simulation of Columnar Grain Evolution During Gas Tungsten Arc Welding of Nickel-Based Alloy GH3039. Metallurgical and Materials Transactions A, 51(2), 887-896.

[Chi19] Chiocca, A., Soulié, F., Deschaux-Beaume, F., & Bordreuil, C. (2019). Study of the effect of growth kinetic and nucleation law on grain structure simulation during gas tungsten arc welding of Cu-Ni plate. Welding in the World, 63(3), 887-901.

[Civ16] Extende-CIVA, EXTENDE S.A., www.extende.com

[Cly81] Clyne, T. W., Davies, G. J. (1981). Influence of composition on solidification cracking susceptibility in binary alloy systems. British Foundryman, 74, 65-73.

[Cou05] Couder, Y., Maurer, J., González-Cinca, R., & Hernández-Machado, A. (2005). Side-branch growth in two-dimensional dendrites. I. Experiments. Physical Review. E, Statistical, Nonlinear, and Soft Matter Physics, 71(3 Pt 1), 031602.

[Cou11] Coupez, T. (2011). Metric construction by length distribution tensor and edge based error for anisotropic adaptive meshing. Journal of Computational Physics, 230(7), 2391-2405.

[Cou13] Coupez, T., & Hachem, E. (2013). Solution of high-Reynolds incompressible flow with stabilized finite element and adaptive anisotropic meshing. Computer Methods in Applied Mechanics and Engineering, 267, 65-85.

[Cro06] Cross, C. E., & Boellinghaus, T. (2006). The effect of restraint on weld solidification cracking in aluminium. Welding in the World, 50(11–12), 51–54. Scopus.

[Dav03] David, S. A., Babu, S. S., Vitek, J. M. (2003). Welding: Solidification and microstructure. Jom, 55(6), 14-20.

[Dan09] Dantzig, J. A., Rappaz, M. (2009). Solidification. EPFL press.

[Deb95] DebRoy, T., & David, S. A. (1995). Physical processes in fusion welding. Reviews of Modern Physics, 67(1), 85-112.

[Dee21] Deepak, J. R., Bupesh Raja, V. K., Srikanth, D., Surendran, H., & Nickolas, M. M. (2021). Non-destructive testing (NDT) techniques for low carbon steel welded joints : A review and experimental study. Materials Today: Proceedings, 44, 3732-3737.

[Del10] Delaleau, P., Beckermann, C., Mathiesen, R. H., & Arnberg, L. (2010). Mesoscopic Simulation of Dendritic Growth Observed in X-ray Video Microscopy During Directional Solidification of Al–Cu Alloys. ISIJ International, 50(12), 1886–1894.

[Del11] Delaleau, P. (2011). Mesoscale Modeling of Dendritic Growth During Directional Solidification of Aluminium Alloys. Norges teknisk-naturvitenskapelige universitet, Fakultet for naturvitenskap og teknologi, Institutt for materialteknologi.

[Des13] Desmaison, O. (2013). Modélisation numérique d'un procédé de soudage hybride arc / laser en approche level set : Application au soudage multi-passes de tôles d'acier de forte épaisseur [Phdthesis, Ecole Nationale Supérieure des Mines de Paris].

[Dre04] Drezet, J. M., Grasso, P. D., Rappaz, M. (2004). Fissuration à chaud: des alliages organiques aux superalliages. Mechanics & Industry, 5(4), 409-417.

[Elm00] Elmer, J., Wong, J., & Ressler, T. (2000). In-situ observations of phase transformations during solidification and cooling of austenitic stainless steel welds using time-resolved x-ray diffraction.

[Elm03] Elmer, J. W., Palmer, T. A., Zhang, W., Wood, B., & DebRoy, T. (2003). Kinetic modeling of phase transformations occurring in the HAZ of C-Mn steel welds based on direct observations. Acta Materialia, 51(12), 3333–3349.

[En09] EN10088-4. (2009). Stainless steels—Technical delivery conditions for sheet/plate and strip of corrosion resisting steels for construction purposes.

[Fra17] Francois, M. M. et al. 2017. “Modeling of Additive Manufacturing Processes for Metals: Challenges and Opportunities.” Current Opinion in Solid State and Materials Science 21(4): 198–206.

[Fle19] Fleurisson, R. (2019). Modélisation multi-échelle parallélisée pour la prédiction de structures de grains dendritiques couplant les éléments finis, un automate cellulaire et un réseau de paraboles [Phdthesis, Université Paris sciences et lettres].

[Gan94] Gandin, C. A., Rappaz, M. (1994). A coupled finite element-cellular automaton model for the prediction of dendritic grain structures in solidification processes. Acta metallurgica et materialia, 42(7), 2233-2246.

[Gan97] Gandin, Ch.-A., & Rappaz, M. (1997). A 3D Cellular Automaton algorithm for the prediction of dendritic grain growth. Acta Materialia, 45(5), 2187-2195.

[Gan03] Gandin, Ch.-A., Guillemot, G., Appolaire, B., & Niane, N. T. (2003). Boundary layer correlation for dendrite tip growth with fluid flow. Materials Science and Engineering: A, 342(1), 44–50.

[Gil96] Gilgien, P. (1996). Calculation of solidification microstructure maps for the system Al-Fe-Si.

[Gor18] Górka, J., & Stano, S. (2018). Microstructure and properties of hybrid laser arc welded joints (laser beam-mag) in thermo-mechanical control processed S700MC steel. Metals, 8(2), 132.

[Gro97] Grong, Ø. (1997). Metallurgical modelling of welding, Institute of Materials (London, England), 2nd.

[Gui04] Guillemot, G. (2004). Formation de structures de grains dans des alliages à solidification dendritique : Modélisation couplée automates cellulaires et éléments finis [Phdthesis, Institut National Polytechnique de Lorraine].

[Gui22] Guillemot, G., Senninger, O., Hareland, C., Voorhees, P., Gandin, Ch.-A. (2022). Thermodynamic coupling in the computation of dendrite growth kinetics for multicomponent alloys, submitted.

[Hac09] Hachem, E. (2009). Stabilized finite element method for heat transfer and turbulent flows inside industrial furnaces [Phdthesis, École Nationale Supérieure des Mines de Paris].

[Hae11] TPLV105 - Thermique non linéaire stationnaire en repère mobile :simulation de l'essai Varestraint, V4.04.105, Doc Code_Aster

[Ham08] Hamide, M. (2008). Modélisation numérique du soudage à l’arc des aciers [Phdthesis, École Nationale Supérieure des Mines de Paris].

[Han14] Han, R., Dong, W., Lu, S., Li, D., & Li, Y. (2014). Modeling of morphological evolution of columnar dendritic grains in the molten pool of gas tungsten arc welding. Computational Materials Science, 95, 351-361.

[Han15] Han, R., Lu, S., Dong, W., Li, D., & Li, Y. (2015). The morphological evolution of the axial structure and the curved columnar grain in the weld. Journal of Crystal Growth, 431, 49-59.

[Han20] Han, Q., Gu, Y., Soe, S., Lacan, F., & Setchi, R. (2020). Effect of hot cracking on the mechanical properties of Hastelloy X superalloy fabricated by laser powder bed fusion additive manufacturing. Optics & Laser Technology, 124, 105984.

[Has14] Hashmi, S. (2014). Comprehensive materials processing. Newnes.

[Hei86] Heintze, G. N., & McPherson, R. (1986). Solidification control of submerged arc welds in steels by inoculation with Ti. Welding Journal, 65(3), 71s–82s.

[Hou55] Houldcroft, P. T. (1955). A simple cracking test for use with argon-arc welding. British Welding Journal, 2(10), 471-475.

[Hoy04] Hoyt, J. J., Asta, M., Haxhimali, T., Karma, A., Napolitano, R. E., Trivedi, R., Laird, B. B., & Morris, J. R. (2004). Crystal–melt interfaces and solidification morphologies in metals and alloys. MRS bulletin, 29(12), 935–939.

[Hug95] Hughes, T. J. R. (1995). Multiscale phenomena : Green's functions, the Dirichlet-to-Neumann formulation, subgrid scale models, bubbles and the origins of stabilized methods. Computer Methods in Applied Mechanics and Engineering, 127(1), 387-401.

[Hun01] Hunziker, O. (2001). Theory of plane front and dendritic growth in multicomponent alloys. Acta Materialia, 49(20), 4191–4203.

[Hys06] Hysing, S. (2006). A new implicit surface tension implementation for interfacial flows. International Journal for Numerical Methods in Fluids, 51(6), 659–672.

[ICB20] Presentation ICB (laboratoire Interdisciplinaire Carnot de Bourgogne) 8 October 2020, NEMESIS internal meeting.

[Iva47] Ivantsov, G. P. (1947), Temperature field around a spheroidal, cylindrical and acicular crystal growing in supercooled melt. Dokl. Akad. Nauk SSSR, 58, 567-73.

[Jar01] Jarvis, B. (2001). Keyhole gas tungsten arc welding : A new process variant. University of Wollongong Thesis Collection 1954-2016.

[JMa] https://www.sentesoftware.co.uk/jmatpro

[Joh04] John. W. M. Bush. MIT Lecture Notes on Surface Tension, lecture 1, 2004.

[Jur96] Juric, D., & Tryggvason, G. (1996). A Front-Tracking Method for Dendritic Solidification. Journal of Computational Physics, 123(1), 127-148.

[Jur98] Juric, D. (1998). Computation of Microsegregation and Microstructure in Solidification with Fluid Convection. MRS Online Proceedings Library, 538(1),

[Kan20] Kang, S., Kang, M., Jang, Y. H., & Kim, C. (2020). Droplet transfer and spatter generation in DC–AC pulse tandem gas metal arc welding. Science and Technology of Welding and Joining, 25(7), 589-599.

[Ker00] Kerrouault, N. (2000). Fissuration à chaud en soudage d'un acier inoxydable austénitique (PhD thesis, Châtenay-Malabry, Ecole centrale de Paris).

[Kha07] Khan, M. I. (2007). Welding science and technology. New Age International.

[Kha16] Khalloufi, M., Mesri, Y., Valette, R., Massoni, E., & Hachem, E. (2016). High fidelity anisotropic adaptive variational multiscale method for multiphase flows

with surface tension. Computer Methods in Applied Mechanics and Engineering, 307, 44–67.

[Kim03] Kim, C.-H., Zhang, W., & DebRoy, T. (2003). Modeling of temperature field and solidified surface profile during gas–metal arc fillet welding. Journal of Applied Physics, 94(4), 2667–2679.

[Koe19] Koepf, J. A., Soldner, D., Ramsperger, M., Mergheim, J., Markl, M., & Körner, C. (2019). Numerical microstructure prediction by a coupled finite element cellular automaton model for selective electron beam melting. Computational Materials Science, 162, 148–155.

[Kou03] Kou, S. (2003). Welding metallurgy. New Jersey, USA, 431(446), 223–225.

[Kos16] Koshikawa, T. (2016). Deformation of steel ingots by punch pressing during their solidification. Numerical modelling and experimental validation of induced hot cracking and macrosegregation phenomena (PhD thesis, PSL Research University).

[Kos16-2] Koshikawa, T., Bellet, M., Gandin, C.-A., Yamamura, H., & Bobadilla, M. (2016). Study of hot tearing during steel solidification through ingot punching test and its numerical simulation. Metallurgical and Materials Transactions A, 47(8), 4053–4067.

[Kot93] Kotecki, D. J. Welding of Stainless Steel, ASM Handbook, Vol.6, 1993, pp. 677-707.

[Kov02] Kovach, Curtis W. (January 2002). "High Performance Stainless Steels". https://nickelinstitute.org/media/1702/highperformancestainlesssteels_11021_.pdf

[Kum94] Kumar, S., & Bhaduri, S. C. (1994). Three-dimensional finite element modeling of gas metal-arc welding. Metallurgical and Materials Transactions B, 25(3), 435-441.

[Kur86] Kurz, W., Giovanola, B., & Trivedi, R. (1986). Theory of microstructural development during rapid solidification. Acta Metallurgica, 34(5), 823-830.

[Lah19] Lahiri, A., & Choudhury, A. (2019). Dendrite tip selection during isothermal free growth in multi-component alloys: Marginal stability theories and insights from phase-field simulations. Computational Materials Science, 158, 209–218.

[Lan78] Langer, J. S., & Müller-Krumbhaar, H. (1978). Theory of dendritic growth—I. Elements of a stability analysis. Acta Metallurgica, 26(11), 1681-1687.

[Les86] LESOULT, G. (1986). Solidification. Cristallisation et microstructures. Techniques de l'ingénieur. Matériaux métalliques, (M58), M58-1.

[Li21] Li, X., Gao, F., Jiao, J., Cao, G., Wang, Y., & Liu, Z. (2021). Influences of cooling rates on delta ferrite of nuclear power 316H austenitic stainless steel. Materials Characterization, 174, 111029.

[Lin01] Lin, Q., Li, X., & Simpson, S. (2001). Metal transfer measurements in gas metal arc welding. Journal of Physics D: Applied Physics, 34, 347.

[Lin13] Lincoln Electric, GMAW Welding Guide. 05-12-2013 visited. http://www.lincolnelectric.com/assets/en_US/Products/literature/C4200.pdf

[Liu12] Liu, Y., Wang, W., Xie, J., Sun, S., Wang, L., Qian, Y., Meng, Y., & Wei, Y. (2012). Microstructure and mechanical properties of aluminum 5083 weldments by gas tungsten arc and gas metal arc welding. Materials Science and Engineering: A, 549, 7-13.

[Liu21] Liu, S., Hong, K., & Shin, Y. C. (2021). A novel 3D cellular automata-phase field model for computationally efficient dendrite evolution during bulk solidification. Computational Materials Science, 192, 110405.

[Lum11] Lumley, R. N. (2011). Introduction to aluminium metallurgy. In Fundamentals of aluminium metallurgy (pp. 1-19). Woodhead Publishing.

[Lhu13] Lhuillier, P. E., TROTTIER, C., SHAHJAHAN, S., ZERIOUH, I., RUPIN, F., CHASSIGNOLE, B., & FOUQUET, T. (2013, October). Overview of the recent developments on grain-scale modeling to simulate ultrasonic scattering with a 2D finite element code. In 10th international conference on NDE in relation to structural integrity for nuclear and pressurized components, Cannes (pp. 1-3).

[Men16] Meng, X., Qin, G., Bai, X., & Zou, Z. (2016). Numerical analysis of undercut defect mechanism in high speed gas tungsten arc welding. Journal of Materials Processing Technology, 236, 225-234.

[Mil98] Mills, K. C., Keene, B. J., Brooks, R. F., & Shirali, A. (1998). Marangoni effects in welding. Philosophical Transactions of the Royal Society of London. Series A: Mathematical, Physical and Engineering Sciences, 356(1739), 911-925.

[Nor06] Norrish, J. (2006). Advanced welding processes. Elsevier.

[Man69] Manz, A. F., Saenger Jr, J. F., Freeman, N. D., & Stanchus, F. T. (1969). U.S. Patent No. 3,483,354. Washington, DC: U.S. Patent and Trademark Office.

[Man88] T MANUAL. (1988). Ultrasonic Testing of Materials at Level-2. (2019, February 28). [Text]. https://www.iaea.org/publications/5736/ultrasonic-testing-of-materials-at-level-2

[Mat82] Matsuda, F., & Nakata, K. (1982). A New Test Specimen for Self-Restraint Solidification Crack Susceptibility Test of Electron-Beam Welding Bead : Fan-Shaped Cracking Test (Materials, Metallurgy & Weldability). Transactions of JWRI, 11(2), 87–94.

[Mat83] Matsuda, F., Nakagawa, H., Nakata, K., Kohmoto, H., & Honda, Y. (1983). Quantitative evaluation of solidification brittleness of weld metal during solidification by means of in-situ observation and measurement (report I) : Development of the MISO technique (materials, metallurgy & weldability). Transactions of JWRI, 12(1), 65–72.

[Market] Welding Materials Market by Type (Electrodes & Filler Materials, Fluxes & Wires, Gases), Technology (Arc, Resistance, Oxy-Fuel Welding), End-use Industry (Transportation, Building & Construction, Heavy Industries), & Region - Global Forecast to 2025, https://www.marketsandmarkets.com/Market-Reports/welding-material-market-165950809.html

[MOBEFE6] MOBFE6 Technical Information. (n.d.). 8.

[Mul64] Mullins, W. W., & Sekerka, R. F. (1964). Stability of a planar interface during solidification of a dilute binary alloy. Journal of Applied Physics, 35(2), 444–451.

[Mur11] Muránsky, O., Smith, M. C., Bendeich, P. J., & Edwards, L. (2011). Validated numerical analysis of residual stresses in Safety Relief Valve (SRV) nozzle mock-ups. Computational Materials Science, 50(7), 2203–2215.

[Nag90] Nagata, S., Matsumiya, T., Ozawa, K., Ohasih, T. (1990). Estimation of critical strain for internal crack formation in continuously cast slabs. Tetsu-to-Hagané, 76(2), 214-221.

[Nie11] Niel, A. (2011). Étude et modélisation du phénomène de fissuration à chaud en soudage à l'arc: Application à l'alliage d'aluminium 6061 (PhD thesis, Université Montpellier II-Sciences et Techniques du Languedoc).

[Olm19] Olmedilla, A., Založnik, M., Fernández, M. C., Viardin, A., & Combeau, H. (2019). Three-dimensional mesoscopic modeling of equiaxed dendritic solidification in a thin sample: Effect of convection flow. IOP Conference Series: Materials Science and Engineering, 529(1), 012040.

[Olympus] Olympus Industrial Resources Application Notes, https://www.olympus-ims.com/en/ultrasonic-testing-faqs/

[Osh88] Osher, S., & Sethian, J. A. (1988). Fronts propagating with curvature-dependent speed : Algorithms based on Hamilton-Jacobi formulations. Journal of computational physics, 79(1), 12–49.

[Ozc03] Ozcelik, S., & Moore, K. (2003). Modeling, sensing and control of gas metal arc welding. Elsevier.

[Pet73] Petersen, W. A. (1973). Fine grained weld structures. Weld. J, 53, 74s–79s.

[Phy] Https://physalurgy.cemef.mines-paristech.fr/.

[Pie07] Pierer, R., Bernhard, C., Chimani, C. (2007). A contribution to hot tearing in the continuous casting process. Revue de Métallurgie–International Journal of Metallurgy, 104(2), 72-83.

[Pin19] Pineau, A. (2019). Modélisation 3D de structures de grains par une approche automate cellulaire. Application à la compétition de croissance dendritique et à la cristallisation du silicium polycristallin [These de doctorat, Paris Sciences et Lettres (ComUE)].

[Que21] Queva, A. (2021). Simulation numérique multiphysique du procédé de fusion laser de lit de poudre—Application aux alliages métalliques d'intérêt aéronautique [Thesis, Université Paris sciences et lettres].

[Qui10] Qiu, G., 2010. Etude de la Modélisation de la Fissuration à Chaud en Soudage d'unAcier Inoxydable Austénitique (Study of Hot Tearing During Welding of anAustenitic Stainless Steel). Mines ParisTech, Paris, pp. 75–80.

[Rai17] Rai, A., Helmer, H., Körner, C. (2017). Simulation of grain structure evolution during powder bed based additive manufacturing. Additive Manufacturing, 13, 124-134.

[Rap93] Rappaz, M., & Gandin, Ch.-A. (1993). Probabilistic modelling of microstructure formation in solidification processes. Acta Metallurgica et Materialia, 41(2).

[Rap99] Rappaz, M., & Boettinger, W. J. (1999). On dendritic solidification of multicomponent alloys with unequal liquid diffusion coefficients. Acta Materialia, 47(11), 3205-3219.

[Rap99-2] Rappaz, M., Drezet, J. M., Gremaud, M. (1999). A new hot-tearing criterion. Metallurgical and materials transactions A, 30(2), 449-455.

[Rap10] Rappaz, M., Bellet, M., & Deville, M. (2010). Numerical Modeling in Materials Science and Engineering (Vol. 32).

[Rod16] Rodgers, T. M., Madison, J. D., Tikare, V., Maguire, M. C. (2016). Predicting mesoscale microstructural evolution in electron beam welding. JOM, 68(5), 1419-1426.

[Rod21] Rodgers, T. M., Moser, D., Abdeljawad, F., Jackson, O. D. U., Carroll, J. D., Jared, B. H., Bolintineanu, D. S., Mitchell, J. A., & Madison, J. D. (2021). Simulation of powder bed metal additive manufacturing microstructures with coupled finite difference-Monte Carlo method. Additive Manufacturing, 41

[Run07] Runesson, K., Skyttebol, A., & Lindgren, L. E. (2007). Nonlinear finite element analysis and applications to welded structures.

[Ruv07] Ruvalcaba, D., Mathiesen, R. H., Eskin, D. G., Arnberg, L., & Katgerman, L. (2007). In situ observations of dendritic fragmentation due to local solute-enrichment during directional solidification of an aluminum alloy. Acta Materialia, 55(13), 4287-4292.

[Rit03] Ritchie, R. O. (2003). Comprehensive structural integrity.

[Saa16] Saad, A. (2016). Modélisation par level set des macroségrégations induites par le retrait à la solidification [These de doctorat, Paris Sciences et Lettres (ComUE)].

[Sah88] Sahoo, P., Debroy, T., & McNallan, M. J. (1988). Surface tension of binary metal—Surface active solute systems under conditions relevant to welding metallurgy. Metallurgical Transactions B, 19(3), 483–491.

[Sak20] Sakane, S., Takaki, T., Ohno, M., Shibuta, Y., & Aoki, T. (2020). Two-dimensional large-scale phase-field lattice Boltzmann simulation of polycrystalline equiaxed solidification with motion of a massive number of dendrites. Computational Materials Science, 178, 109639.

[Sha15] Shakoor, M., Scholtes, B., Bouchard, P.-O., & Bernacki, M. (2015). An efficient and parallel level set reinitialization method – Application to micromechanics and microstructural evolutions. Applied Mathematical Modelling, 39(23), 7291-7302.

[Sha20] Shareef, I., & Martin, C. (2020). Effect of Process Parameters on Weld Spatter in Robotic Welding. Procedia Manufacturing, 48, 358-371.

[Sie13] Sieradzki, L., Madej, L. (2013). A perceptive comparison of the cellular automata and Monte Carlo techniques in application to static recrystallization

modeling in polycrystalline materials. Computational Materials Science, 67, 156-173.

[Sin20] Singh, R. (2020). Applied welding engineering: processes, codes, and standards. Butterworth-Heinemann.

[Sis00] Sista, S., Yang, Z., DebRoy, T. (2000). Three-dimensional Monte Carlo simulation of grain growth in the heat-affected zone of a 2.25 Cr-1Mo steel weld. Metallurgical and Materials Transactions B, 31(3), 529-536.

[Smi13] Smith, P. (2013). The fundamentals of piping design. Elsevier.

[Sun20] Sunny, S., Yu, H., Mathews, R., Malik, A., & Li, W. (2021). Improved grain structure prediction in metal additive manufacturing using a Dynamic Kinetic Monte Carlo framework. Additive Manufacturing, 37, 101649.

[Ste99] Steinbach, I., Beckermann, C., Kauerauf, B., Li, Q., & Guo, J. (1999). Three-dimensional modeling of equiaxed dendritic growth on a mesoscopic scale. Acta Materialia, 47(3), 971–982.

[Ste05] Steinbach, I., Diepers, H.-J., & Beckermann, C. (2005). Transient growth and interaction of equiaxed dendrites. Journal of Crystal Growth, 275(3), 624–638.

[Tak20] Takaki, T., Sakane, S., Ohno, M., Shibuta, Y., & Aoki, T. (2020). Large–scale phase–field lattice Boltzmann study on the effects of natural convection on dendrite morphology formed during directional solidification of a binary alloy. Computational Materials Science, 171, 109209.

[TCFE9] Steel and Fe-Alloys – TCFE. (n.d.). Thermo-Calc Software. Retrieved July 12, 2021, from https://thermocalc.com/products/databases/steel-and-fe-alloys/

[Tef21] Teferra, K., & Rowenhorst, D. J. (2021). Optimizing the cellular automata finite element model for additive manufacturing to simulate large microstructures. Acta Materialia, 213, 116930.

[Tez03] Tezduyar, T., & Sathe, S. (2003). Stabilization parameters in SUPG and PSPG formulations. Journal of computational and applied mechanics, 4(1), 71–88.

[The18] Thermo-Calc-2018-b TCCS manuals Thermo-Calc software AB (Stockholm, SE), 2018.

[Tik10] Tikare, V., Braginsky, M., Bouvard, D., Vagnon, A. (2010). Numerical simulation of microstructural evolution during sintering at the mesoscale in a 3D powder compact. Computational Materials Science, 48(2), 317-325.

[Tou13] Tourret, D., & Karma, A. (2013). Multiscale dendritic needle network model of alloy solidification. Acta Materialia, 61(17), 6474–6491.

[Tou16] Tourret, D., & Karma, A. (2016). Three-dimensional dendritic needle network model for alloy solidification. Acta Materialia, 120, 240–254.

[Tra11] Traidia, A., & Roger, F. (2011). A computational investigation of different helium supplying methods for the improvement of GTA welding. Journal of Materials Processing Technology, 211(9), 1553-1562.

[Tri94] Trivedi, R., & Kurz, W. (1994). Dendritic growth. International Materials Reviews, 39(2), 49–74.

[Via17] Viardin, A., Založnik, M., Souhar, Y., Apel, M., & Combeau, H. (2017). Mesoscopic modeling of spacing and grain selection in columnar dendritic solidification: Envelope versus phase-field model. Acta Materialia, 122, 386–399.

[Vit00] De Vito, S. (2000). Influence de la composition chimique et des conditions de refroidissement sur la fissuration à chaud d'alliages de Nickel (PhD thesis, Institut National Polytechnique de Lorraine).

[Wan04] Wang, N., Mokadem, S., Rappaz, M., Kurz, W. (2004). Solidification cracking of superalloy single-and bi-crystals. Acta Materialia, 52(11), 3173-3182.

[Wan13] Wang, K., Wang, H., Liu, F., & Zhai, H. (2013). Modeling dendrite growth in undercooled concentrated multi-component alloys. Acta Materialia, 61(11), 4254–4265.

[Web1] https://www.livemint.com/Companies/KL0EH2IngyaTOa2IEHrreJ/Fiat-Chrysler-to-recall-18000-Jeep-Wranglers-over-framewel.html

[Web2] https://www.torquenews.com/3769/ford-recalls-nearly-30000-vehicles-repair-variety-problems

[Wei06] Wei, Y., Dong, Z., Liu, R., & Dong, Z. (2006). Modeling the Trans-Varestraint test with finite element method. Computational Materials Science, 35(2), 84-91.

[Wem11] Weman, K. (2011). Welding processes handbook. Elsevier.

[Wis09] Wisniewski, J. (2009). Modélisation thermomécanique de la fissuration à chaud en soudage par faisceau d'électrons d'un alliage CuCrZr. (PhD thesis, Université de Bretagne-Sud).

[Won00] Won, Y. M., Yeo, T. J., Seol, D. J., Oh, K. H. (2000). A new criterion for internal crack formation in continuously cast steels. Metallurgical and Materials Transactions B, 31(4), 779-794.

[Wro16] https://eis.hu.edu.jo/acuploads/10526/ultrasonic%20testing.pdf

[Wro64] Wroth, R. S., Norman, R., & Manz, A. F. (1964). U.S. Patent No. 3,163,743. Washington, DC: U.S. Patent and Trademark Office.

[Xio21] Xiong, F., Huang, C., Kafka, O. L., Lian, Y., Yan, W., Chen, M., & Fang, D. (2021). Grain growth prediction in selective electron beam melting of Ti-6Al-4V with a cellular automaton method. Materials & Design, 199, 109410.

[Xue21] Xue, C., Blanc, N., Soulié, F., Bordreuil, C., DeschauxBeaume, F., Guillemot, G., Bellet, M., & Gandin, C. (2021). Structure and texture simulations in fusion welding processes – comparison with experimental data. Materialia, 101305.

[Yan00] Yang, Z., Sista, S., Elmer, J. W., & DebRoy, T. (2000). Three dimensional Monte Carlo simulation of grain growth during GTA welding of titanium. Acta Materialia, 48(20), 4813–4825.

[Zha10] Zhang, H., Gandin, C.-A., Hamouda, H. B., Tourret, D., Nakajima, K., & He, J. (2010). Prediction of Solidification Paths for Fe–C–Cr Alloys by a Multiphase Segregation Model Coupled to Thermodynamic Equilibrium Calculations. ISIJ International, 50(12), 1859–1866.

[Zha13] Zhang, R., Wang, X., Chen, Z., & Jie, W. (2013). Simulation of constrained dendrite growth of multicomponent alloys using a Calphad method. Materials Science and Technology.

[Zha13-2] Zhang, H., Nakajima, K., Gandin, C.-A., & He, J. (2013). Prediction of Carbide Precipitation Using Partial Equilibrium Approximation in Fe–C–V–W–Cr–Mo High Speed Steels. ISIJ international, 53(3), 493–501.

[Zha16] Zhang, J., Liou, F., Seufzer, W., & Taminger, K. (2016). A coupled finite element cellular automaton model to predict thermal history and grain morphology of Ti-6Al-4V during direct metal deposition (DMD). Additive Manufacturing, 11, 32-39.

[Zha19] Zhang, Y., & Zhang, J. (2019). Modeling of solidification microstructure evolution in laser powder bed fusion fabricated 316L stainless steel using combined computational fluid dynamics and cellular automata. Additive Manufacturing, 28, 750–765.

[Zha19-2] Zhang, S., Guillemot, G., Gandin, C.-A., & Bellet, M. (2019). A partitioned two-step solution algorithm for concurrent fluid flow and stress–strain numerical simulation in solidification processes. Computer Methods in Applied Mechanics and Engineering, 356, 294–324.

[Zha20] Zhang, S. (2020). Numerical simulation of mechanical interactions between liquid and solid phase in solidification processes [PhD Thesis, Université Paris sciences et lettres].

RÉSUMÉ

Le soudage est un processus d'assemblage permanent qui doit assurer la continuité du matériau. Pourtant, pendant la solidification, plusieurs types de défauts comme la fissuration à chaud peuvent se développer, entraînant une diminution de la qualité de la soudure et des performances des pièces. La prise en compte de la structure de grains produite lors du procédé de soudage est ici étudiée pour adapter un critère en déformation cumulée capable de prédire l'occurrence de la fissuration à chaud.
Un modèle tridimensionnel couplant Automate Cellulaire et Éléments Finis (CAFE) est tout d'abord appliqué pour simuler la structure de grain du procédé GTAW (Gas Metal Arc Welding) avec ou sans apport de matière, pour les configurations de tôle et de chanfrein. Toutes les configurations sont dédiées au soudage des aciers inoxydables austénitiques étudiés expérimentalement par les partenaires du projet ANR NEMESIS. Un nouveau modèle de source de chaleur est proposé et pour le soudage en chanfrein. La structure de grain simulée est comparée aux observations expérimentales réalisées par la technique de diffraction des électrons rétrodiffusés (EBSD). Une bonne cohérence est trouvée concernant la texture des grains (cartes EBSD et figures de pôles) une fois que les conditions thermiques correspondantes sont obtenues, validées par la taille et la forme du bain de fusion déduites d'observations in-situ en temps réel.
Des conditions de soudage fissurant et de non-fissurant sont étudiées en exploitant des données expérimentales rapportées dans la littérature. Les résultats des simulations exploitant le critère en déformation cumulée permettent bien de distinguer les cas avec et sans fissuration. L'influence de la structure de grain simulée par l'approche CAFE est considérée. Des résultats similaires sont obtenus, démontrant la faisabilité d'enrichir le critère et une cohérence avec les observations expérimentales.
Des discussions sont finalement proposées comme perspectives pour ces activités. La validation du critère de fissuration à chaud avec plus de configurations de soudage est souhaitable, les contrôles non destructifs (CND) par onde ultrasonore actuellement utilisés pour détecter et localiser la fissuration à chaud pourraient également bénéficier des structures de grains simulées, et une exploitation plus approfondie de la structure dans un critère de fissuration à chaud est envisagée.

MOTS CLÉS

Soudage, fissuration, solidification, modélisation multi-échelles, microstructure, methode CAFE

ABSTRACT

Welding is a permanent assembly process aimed at ensuring the continuity of the material. However, during the solidification stage, several types of defects such as hot cracking develop, leading to a decrease of the weld quality and part performances. Virtual grain microstructure would provide valuable information to enhance literature criterion on defects occurrence and to provide better understanding on their development. In this work, the 3D Cellular Automaton – Finite Element (CAFE) method is applied to simulate the grain structure formation during Gas Tungsten Arc Welding (GTAW) process with or without added material for metal sheet or chamfer configurations. All simulations are dedicated to austenitic stainless steel welding. The simulated grain structure is compared with experimental observations developed in the present partnership of ANR project NEMESIS. New heat source model is also proposed and dedicated to welding in chamfer configuration. A good coherence is found regarding the grain texture (EBSD map and pole figures) once the corresponding thermal conditions (e.g. melt pool shape) are obtained.
Besides, a strain based hot cracking criterion is computed considering a GTAW process developed upon a metal sheet. Both cracking and non-cracking conditions are investigated regarding some experiments reported in the literature. Results of the welding simulations are coherent with these experimental observations to distinguish cases using criterion. Furthermore, the grain structure simulated by CAFE method is considered thereafter in order to investigate the influence of grain structure on hot cracking. Despite similar results as that without grain structure are obtained, a coherency with experimental observations is found.
Some discussions are thereafter proposed as a perspective for these activities, for example, validation of the WYSO hot cracking criterion with more welding configurations. In addition, the current ultrasonic Non Destructive Testing (NDT) used to detect and localize the hot cracking could also benefit from the reliable simulated grain structure to analyze and improve the NDT software performances.

KEYWORDS

Welding, cracking, solidification, multi-scale modelling, microstructure, CAFE method